ERRATA

Page 5, §1.4.1, paragraph 1, line 9: "...assumed that the 5-minute ..." for "...assumed that the the 5-minute ..."

ADDENDUM

Page 5, §1.4: Add at the end of paragraph 1:
"With regard to the interaction of solar p-modes with magnetic field, ring diagram analysis has recently been used to determine that there is a local frequency shift and line width contribution associated with the presence of magnetically active regions (e.g., Hindman et $al.$, 2000, 2001; Rajaguru, Basu, and Antia, 2001). These observations are consistent with the other evidence for the sensitivity of the p-mode frequencies and line widths to the degree of surface magnetic activity (see §1.3); however, they do not have the spatial resolution required to explore small scale features such as sunspots."

page 21, line 9: Delete "...an isotropic magnetic pressure $B^2/2\mu_B$ and a tension B^2/μ_B." and read "...a magnetic pressure gradient $\nabla(\mathbf{B} \cdot \mathbf{B})/2\mu_B$ and a magnetic tension $(\mathbf{B} \cdot \nabla)\mathbf{B}/\mu_B$."

page 23, line 2 and 3: "...Goossens and Poedts (1992); and Goossens, Ruderman, and Hollweg (1995)." should read "...Goossens and Poedts (1992); Erdélyi, Goossens, and Ruderman (1995); Goossens, Ruderman, and Hollweg (1995); and Erdélyi (1997)."

page 26, line 16:
"...and the ($m \neq 0$) kink mode with phase speed $C_K = [(\rho C_A^2 + \rho_e C_S^2)/(\rho + \rho_e)]^{1/2} ...$"
should read "...and the ($m = 1$) kink and higher order ($m > 1$) flute modes with phase speed $C_K = \left[\left(\rho C_A^2 + \rho_e C_{A,e}^2\right)/(\rho + \rho_e)\right]^{1/2} ...$"

The Bibliography, add the following references (in order):

Erdélyi, R.: 1997, *Solar Phys.* **171**, 49

Erdélyi, R., Goossens, M., and Ruderman, M. S.: 1995, *Solar Phys.* **161**, 123

Hindman, B., Haber, D., Toomre, J., and Bogart, R.: 2000, *Solar Phys.* **192**, 363

Hindman, B. W., Haber, D. A., Toomre, J., and Bogart, R. S.: 2001, in A. Wilson (ed.), Proc. SOHO 10/GONG 2000 Workshop, *Helio- and Asteroseismology at the Dawn of the Millennium*, (ESA SP-464), p. 143

Rajaguru, S. P., Basu, S., and Antia, H. M.: 2001, *Astrophys. J.* **563**, 410

THE INTERACTION OF SOLAR OSCILLATIONS WITH MAGNETIC FIELD

Ashley D. Crouch
B. Sc. (Hons)

A thesis submitted for the degree of Doctor of Philosophy

School of Mathematical Sciences
Monash University
Australia

June 2003

Contents

Abstract

In this thesis we investigate the interaction of solar acoustic oscillations, f- and p-modes, with two distinct types of magnetic field structure: sunspots and small-scale intense magnetic fibrils.

Sunspots absorb (and scatter) incident p-modes. The responsible mechanism is uncertain. One possibility is mode conversion to slow magnetoacoustic-gravity waves. In 1994, Cally, Bogdan, and Zweibel determined that, in vertical field, mode conversion can adequately explain the observed f-mode absorption, but is too inefficient to explain the absorption of p-modes. We calculate the efficiency of mode conversion in non-vertical field. In Chapter 3, we assume two-dimensional propagation where the Alfvén waves decouple, computing the efficiency of fast-to-slow magnetoacoustic-gravity wave conversion. It is found that resultant p-mode absorption is significantly enhanced for moderate inclinations at higher frequencies, whereas for p-modes at lower frequencies, and the f-mode in general, there is no useful enhancement. In Chapter 4, we consider the efficiency of mode conversion in non-vertical field with three dimensional propagation, where fast and slow magnetoacoustic-gravity waves and Alfvén waves are all coupled. The resultant damping rates are not substantially different from those in the two-dimensional case (Alfvén waves decoupled). However, broadly speaking, both slow wave leakage and Alfvén wave leakage play an equally significant role in non-vertical field. In addition, a new type of highly damped solution, that mainly exists in highly inclined field, is found.

In Chapter 5, the contribution to p-mode line widths from the excitation of tube mode oscillations on an individual magnetic fibril is computed. An idealised model of the fibril within the photosphere is implemented, consisting of a vertical, thin magnetic flux tube embedded in a plane-parallel isentropic polytrope of index m. In 1996, Bogdan *et al.* considered a similar model, but imposed a stress-free boundary condition at the top of the photosphere which acts to completely reflect any upward propagating tube waves back down into the tube. The stress-free boundary condition neglects a possibly important physical process – the loss of energy to the upper solar atmosphere by the excitation of waves in the chromosphere and corona. Using simple models of the solar chromosphere and corona we explore the consequences of applying various boundary conditions. The resultant upward energy fluxes are not large, but surprisingly the more realistic upper boundary conditions lead to a significant increase in kink mode flux out the bottom. Nevertheless, the sausage mode remains dominant in cases of interest, and is essentially unaffected by the new boundary conditions. Consequently, the resultant total p-mode line width computed here can account for only a few percent of the observed line width.

Statement of authorship

This thesis contains no material which has been accepted for the award of any other degree or diploma in any university or other institution. To the best of my knowledge this thesis contains no material previously published or written by another person except where due reference is made in the text.
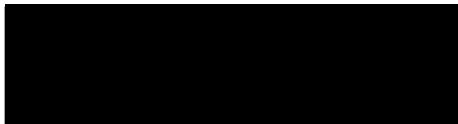
Ashley D. Crouch

Acknowledgements

I would like to thank my friends, family, and colleagues, and also the bar-room philosophers with whom I've shared a laugh over the past few years. I would especially like to thank:

Paul Cally,
for his excellent supervision and support;

and Danielle Nipe,
for her love, compassion and understanding.

Chapter 1

Introduction

1.1 Helioseismology

The normal modes of oscillation of the sun can be categorised as either p-modes ("p" stands for "pressure"), f-modes, ("f" for "fundamental"), or g-modes ("g" for "gravity"). The g-modes are internal gravity waves for which the primary restoring force is buoyancy, and are confined almost totally to the deep solar interior. The f-mode is an incompressive, surface gravity wave with amplitude that decays roughly exponentially with depth away from the solar surface. The p-modes are gravity-modified, acoustic waves, with pressure the primary restoring force.

Figure 1.1 shows the eigenfrequencies of the normal modes as a function of degree l, computed for a spherically symmetric standard solar model (Christensen-Dalsgaard, 1982). The eigenfrequencies for the f-mode and several of the p- and g-modes are shown. The parameter l is the spherical harmonic degree, and it determines the surface horizontal wavenumber $k = [l(l+1)]^{1/2}/R_\odot$ (where $R_\odot$ is the radius of the Sun). For a given degree l, there are discrete set of allowable frequencies. Each of these is characterised by another integer n – the radial order which roughly corresponds to the number of radial nodes in the corresponding displacement eigenfunction (depending on the model). The f-mode has $n = 0$. For the p-modes, with ridges in the upper portion of Figure 1.1, the eigenfrequency increases with increasing radial order n. In contrast, for the g-modes, with ridges in the lower portion of Figure 1.1, the eigenfrequency decreases with increasing radial order.

The p-modes are essentially trapped – bounded below (refracted upward) by the increase in sound speed due to thermal stratification, and bounded above (reflected downward) by the rapid increase in acoustic cutoff frequency near the solar surface. The depth of a p-mode's lower turning point depends on both l and n, and is roughly proportional to the ratio n/l (e.g., Deubner and Gough, 1984). Hence, for a given frequency, p-modes with low degrees have deeper lower turning points, and therefore probe further into the interior, than those with high degree. On the other hand, for fixed degree l, the depth of the lower turning point scales with the radial order n (or the frequency). In simple terms, different p-modes sample different regions of the solar interior. Helioseismology exploits this characteristic to infer the details of the structure of the solar interior.

Figure 1.1: Eigenfrequencies $\nu = \omega/2\pi$, as a function of degree l, for the p-, f-, and g-modes computed for a standard solar model (Christensen-Dalsgaard, 1982). Selected values of the radial order n have been indicated. Reproduced from J. Christensen-Dalsgaard's "Lecture Notes on Stellar Oscillations" (http://astro.phys.au.dk/~jcd/oscilnotes/, p. 72).

The first observations of the oscillations of the solar surface were made by Leighton, Noyes, and Simon (1962) and Evans and Michard (1962). Now both the p- and f-modes are easily and routinely observed at the solar surface, with the peak power centred on a period of roughly five minutes. The observed frequencies are used in both forward and inverse modelling to constrain physical models or to directly infer details of subsurface structure.

2

Helioseismology has been able to determine such features as the sound speed profile (e.g., Christensen-Dalsgaard et al., 1985), the depth of the convection zone (e.g., Christensen-Dalsgaard, Gough, and Thompson, 1991), the differential rotation (e.g., Gough, 1984; Brown et al., 1989; Charbonneau et al., 1999), and the degree of gravitational settling and atomic diffusion (e.g., Proffitt and Michaud, 1991) to name a few. Comprehensive reviews of helioseismology may be found in Deubner and Gough (1984), Christensen-Dalsgaard et al. (1996) and Christensen-Dalsgaard (2002).

1.2 Sunspots

Sunspots are the most prominent magnetic flux concentrations at the surface of the sun. Typically, large sunspots have surface magnetic field strengths as high as 3500 G. Broadly speaking, the magnetic field in sunspots suppresses convection and introduces an additional (magnetic) pressure. Both of these factors act to reduce the temperature of the gas inside sunspots, which is generally 2000 K cooler than the surrounding photosphere. Hence, sunspots appear as dark spots on the surface of the sun.
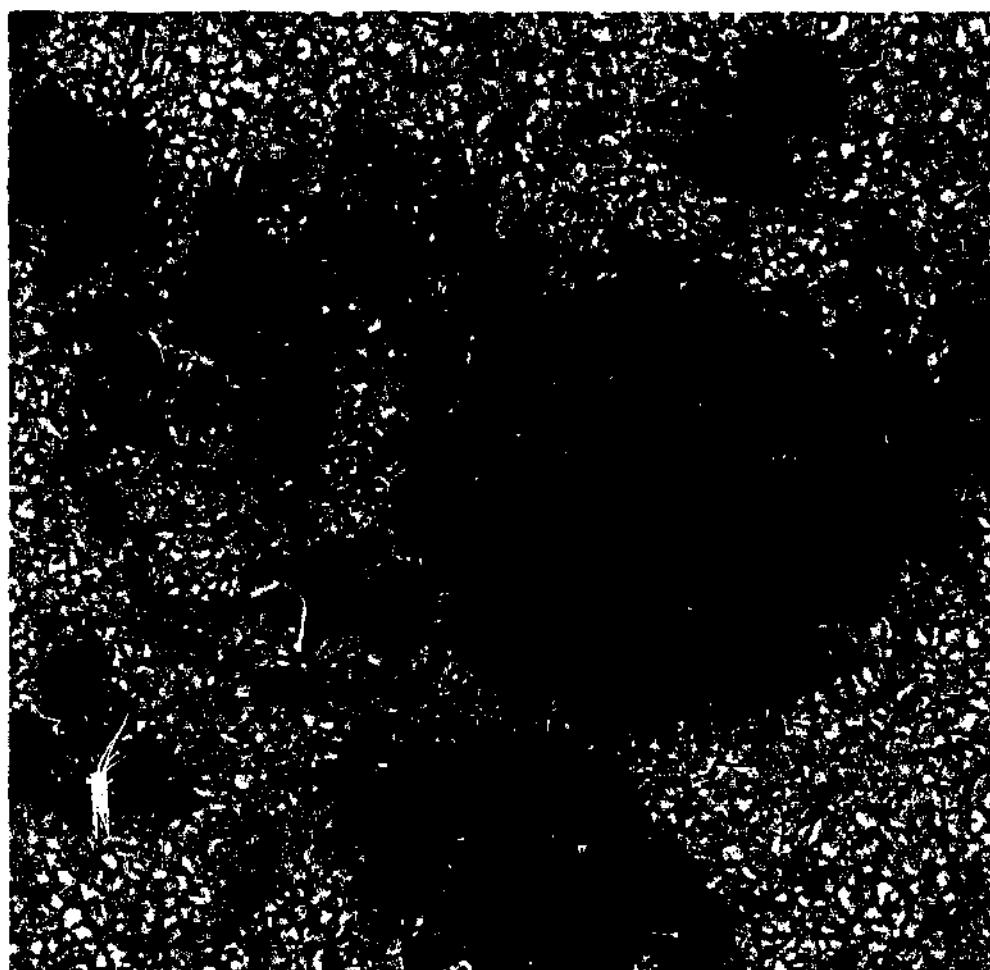

Figure 1.2: A group of sunspots in active region 10030 on 15 July 2002 (courtesy Royal Swedish Academy of Sciences, see also Scharmer et al., 2002).

3

Figure 1.2 shows a group of sunspots in active region 10030 on 15 July 2002. The dominant sunspot in the centre of Figure 1.2 shows the standard features possessed by most large sunspots. These include the central dark core known as the umbra which is surrounded by a region of filamentary appearance known as the penumbra. Typically, the umbral diameter is of order tens of Mm. In the relatively non-magnetic regions (quiet Sun) surrounding the sunspot (Fig. 1.2), convection cells (the solar granulation) are evident.

Currently, the subsurface structure of sunspots is poorly understood. Below the photosphere the sunspot magnetic field may remain as a single monolithic flux tube or, as suggested by Parker (1979), may be composed of a bundle of closely spaced magnetic fibrils. One ultimate goal of sunspot seismology is to discriminate between the two possibilities.

Away from sunspots, the solar magnetic field is in a highly intermittent state. Roughly 90% of the magnetic flux that threads the photosphere is in the form of small-scale intense magnetic flux tubes (or fibrils). These small-scale intense tubes have magnetic field strengths of order 1500 G and diameters of about 100 km (Stenflo, 1978).

For the remainder of this chapter we scrutinise the array of observational evidence for the interaction of solar p-modes with magnetic field. Broadly speaking, the interaction of solar p-modes with magnetic field may be categorised as either global or local, though the two regimes are not necessarily unrelated. The first category refers to the influence of the magnetic field on the global p-mode oscillation frequencies and lifetimes. The second refers to specific magnetic regions on the solar surface, such as sunspots. The theoretical interpretations of the observations are discussed in Chapter 2.

1.3 Global effects

The sun's magnetic cycle of 22 years duration (11 years if polarity is ignored) allows helioseismology to be performed through a wide range of magnetic activity. Woodard and Noyes (1985) were the first to discover that the frequencies of the solar p-modes change during the solar activity cycle. Subsequent investigations (e.g., Libbrecht and Woodard, 1990; Woodard, Kuhn, Murray, and Libbrecht, 1991; Woodard and Libbrecht, 1991; Bachmann and Brown, 1993; Elsworth et al., 1994) established that the p-mode frequencies increase by up to several hundred nHz above solar minimum values as the cycle progresses – with a strong linear correlation found between the frequency shifts and up to six different standard indicators of solar activity (e.g., Bachmann and Brown, 1993; Chaplin et al., 2001). Interestingly, Woodard, Kuhn, Murray, and Libbrecht (1991) and Bachmann and Brown (1993) found that the p-mode frequencies change significantly over periods as short a one month (which also correlate strongly with surface averaged solar activity). The frequency shift is frequency dependent – rapidly increasing from effectively zero at low frequencies (≈ 1 mHz) to a maximum at about 3.5 mHz, and abruptly declining for frequencies above 3.9 mHz (Woodard and Libbrecht, 1991). It has also been shown (e.g., Libbrecht and Woodard, 1990; Woodard and Libbrecht, 1993; Howe, Komm, and Hill, 1999) that the even-index rotational splitting coefficients are sensitive to the solar cycle.

The p-mode line widths (for general observations of these see e.g., Libbrecht, 1988; Korzennik, 1990; Jefferies et al., 1991), which are inversely proportional to the mode lifetimes,

have also been shown to vary with the solar cycle. Jefferies *et al.* (1991) found that the line widths were larger in 1981 (high activity) than in 1987 (low activity), suggesting that the line width increases with increasing activity. Komm, Howe, and Hill (2000) recently confirmed and clarified this result. Komm, Howe, and Hill found that from solar minimum to solar maximum, the p-mode line widths increase by about 7% on average and the associated mode amplitudes decrease by 16%. This array of observational evidence leaves little doubt that the global properties of the p-modes are sensitive to the degree of surface magnetic activity.

1.4 Sunspot seismology

Helioseismology traditionally exploits the characteristics (i.e., the frequencies) of the Sun's free oscillations (p-modes) to infer global properties of the solar interior. Recently, in the last decade or so, local helioseismology has provided promising results on the structure of localised features such as large-scale convection, subsurface flows, emerging active regions, and sunspots. There are several distinct but complementary methods for pursuing local helioseismology. In this section we discuss the techniques relevant to sunspot seismology (Hankel or modal analysis, helioseismic tomography, and helioseismic holography) and the subsequent observational results that have been gained. In passing only we briefly mention ring-diagram analysis, which is another important local helioseismic technique that has been used mainly to infer the structure and evolution of meridional and zonal flows near the solar surface (e.g., Hill, 1988; Patrón *et al.*, 1995; Haber *et al.*, 2000, 2002).

1.4.1 Oscillations inside sunspots

Perhaps the obvious starting point for sunspot seismology is to use the observed characteristics of oscillations inside a sunspot to infer its subsurface structure. Oscillations inside sunspots, first discovered by Beckers and Tallant (1969, see also Bhatnagar, Livingston, and Harvey, 1972; Beckers and Schultz, 1972; Bhatnagar and Tanaka, 1972; Giovanelli, 1972; Zirin and Stein, 1972), can be broadly classified into three categories: 5-minute oscillations in the umbral photosphere, 3-minute oscillations in the umbral photosphere and chromosphere, and running penumbral waves. Recently, Bogdan (2000) suggested that these oscillations are probably just different manifestations of the global oscillations of the entire sunspot. Nevertheless, early approaches often assumed that the the 5-minute umbral oscillations are the passive response of the sunspot to forcing by the (5-minute) p-modes in the surrounding quiet Sun (e.g., Thomas, Cram, and Nye, 1982; Abdelatif, Lites, and Thomas, 1986; Abdelatif and Thomas, 1987; Penn and Labonte, 1993), and the 3-minute umbral modes are resonant oscillations of the sunspot itself.

Thomas, Cram, and Nye (1982) were the first to attempt to use the 5-minute umbral oscillations as a subsurface probe of sunspot structure (see also Abdelatif, Lites, and Thomas, 1986; Abdelatif and Thomas, 1987). Thomas, Cram, and Nye assumed that the sunspot oscillations only respond to the forcing of certain p-modes (i.e., the sunspot flux tube acts as a selective filter), and that the peak response occurs at a wavelength comparable to twice the umbral diameter. Subsequently, Thomas, Cram, and Nye (1982) were able to infer

(conditionally) the radius of the sunspot at the various effective depths probed by the filtered p-modes.

Unfortunately, the development of this technique has been slow. Broadly speaking, observational progress is limited by resolution in both space and time (i.e., precise mode identification is problematic), and theoretical progress is limited by our understanding of the oscillations supported by realistic model sunspots. The recent work by Lites *et al.* (1998) provides an excellent up-to-date example of this technique – using data of exceptionally high quality and employing the best available sunspot model (Cally, Bogdan, and Zweibel, 1994). Comprehensive discussion of the oscillations in sunspots, regarding both observational results and theoretical interpretations, can be found in the reviews by Chitre (1992), Lites (1992), Thomas and Wiess (1992), and Bogdan (2000).

1.4.2 Hankel analysis

An alternative approach is to consider the effect of the sunspot on the incident p-modes as a classical scattering problem. The aim is to determine the amplitude and phases of the p-modes in the quiet Sun surrounding the sunspot, distinguishing those modes propagating toward the spot from those propagating away from it. A comparison of inward and outward amplitudes and phases may then be used to characterise the interaction of the p-modes with the sunspot. This method was first employed by Braun, Duvall, and LaBonte (1987) and further developed by Braun, Duvall, and LaBonte (1988); Braun, LaBonte, and Duvall (1990); Braun *et al.* (1992a); Bogdan *et al.* (1993); Braun (1995); Chen, Chou and the TON Team (1996); Zhang (1997).

Typically, the data (either observed velocity or intensity fields) is analysed in a spherical polar coordinate system (θ, ϕ) centred on the spot or feature of interest $(\theta = 0)$. The analysis is confined to an annulus excluding the sunspot itself (i.e., $\theta_{min} \leq \theta \leq \theta_{max}$). The practical advantages of observing oscillations outside the spot are many and include: increased wavenumber resolution, better mode identification, reduction of scattered light, reduction of line profile distortion, and increased signal-to-noise ratio. In addition, the properties of the oscillations inside the spot are not well understood, whereas the properties of the p-modes in quiet Sun are very well understood. For $\theta \ll \pi$, Hankel functions may be employed as approximations to the more accurate Legendre function decomposition. The observed quantity is expressed as a sum of wave components of the form

$$\Psi_m (\theta, \phi, t) = e^{i(m\phi + \omega t)} \left[A_m (L, \omega) H_m^{(1)} (L\theta) + B_m (L, \omega) H_m^{(2)} (L\theta) \right] , \qquad (1.1)$$

where $H_m^{(1)}$ and $H_m^{(2)}$ are the Hankel functions of the first and second kind, respectively (Abramowitz and Stegun, 1964, Chapter 9), m is the azimuthal order, $L = [l(l+1)]^{1/2}$ (where l is the spherical harmonic degree of the mode), t is time, and ω is the angular frequency. Braun (1995) estimates that the relative error in wave amplitude, introduced by approximating the Legendre functions with Hankel functions, is at worst a few percent. In fact, Bogdan *et al.* (1993, see also Chen, Chou and the TON Team, 1996) employed a decomposition in terms of the Legendre functions. Their results were very similar to those of other studies where Hankel functions were used (e.g., Braun, Duvall, and LaBonte, 1987,

1988; Braun, LaBonte, and Duvall, 1990; Braun, 1995). Because the decomposition (eq. [1.1]) is usually in terms of Hankel functions, this method has come to be known as Hankel analysis.

In equation (1.1), A_m and B_m are complex coefficients that describe the power and phase of waves travelling radially inward and outward, respectively. These may be evaluated from the data by means of an appropriate set of azimuthal (Fourier), radial (Hankel), and temporal (Fourier) transforms (for details see Braun, Duvall, and LaBonte, 1988; Bogdan et al., 1993). The moduli of A_m and B_m correspond to the amplitudes of the incoming and outgoing waves, with any difference reflecting the presence of sinks or sources of acoustic power. Subsequently, the absorption coefficient is defined as

$$\alpha = \frac{P_{in} - P_{out}}{P_{in}} = 1 - \left| \frac{B_m}{A_m} \right|^2 ,$$

where P_{in} and P_{out} are the power of the incoming and outgoing p-modes, respectively. Similarly, scattering – due to horizontal phase speed inhomogeneities – will produce a difference in the phase between A_m and B_m. The phase shift is defined as

$$\delta = \arg(B_m) - \arg(A_m) .$$

The definition of the absorption coefficient must be viewed with some caution as what appears to be actual absorption may be the result of scattering to higher unobservable wavenumbers (e.g., Bogdan and Zweibel, 1987) or mode mixing (where a scatter, excited by an incident wave mode with azimuthal and radial orders m and n, will produce outgoing wave modes with the same temporal frequency but different m and/or n, see Braun, 1995).

Braun, Duvall, and LaBonte (1987) were the first to report that sunspots absorb up to 50% of incident p-mode power. Shortly thereafter, Braun, Duvall, and LaBonte (1988) reconsidered their original observations (of three different spots) in greater detail, improved the data reduction techniques, and also observed an isolated magnetic pore. For the purposes of examining the variation of α with horizontal wavenumber k^*, Braun, Duvall, and LaBonte (1987, 1988) summed over azimuthal orders $-5 \leq m \leq 5$ and the p-modes ridges of radial order $n = 0-6$ (corresponding to 1.5 mHz $\lesssim \nu \lesssim$ 5 mHz). For each of the sunspots observed, Braun, Duvall, and LaBonte found that the levels of absorption are roughly constant (up to 50%) at higher wavenumbers (0.5 Mm$^{-1} \leq k \leq$ 1.5 Mm^{-1}), but drop off rapidly at lower wavenumbers ($k \leq$ 0.5 Mm^{-1}). In contrast, an identical analysis performed on a region of quiet Sun (i.e., a control) shows no significant difference between ingoing and outgoing power, as one would expect. Braun, Duvall, and LaBonte (1988) also analysed the absorption as a function of k along each individual p-mode ridge, this revealed the same trend as for the combined results, including the f-mode. Braun, Duvall, and LaBonte (1988) subsequently concluded, despite the difference in wave properties, that any theoretical interpretation of the absorption mechanism should apply equally for the f-mode (an incompressive surface wave) as well as the p-modes (gravity-modified acoustic waves).

For high-degree p-modes, the depth of the lower turning point scales as n/k (e.g., Deubner and Gough, 1984). Therefore, a mode with a smaller horizontal wavenumber should be less

---

*The horizontal wavenumber, in arc-length coordinates, is related to the spherical harmonic degree, l, by the formula $k = [l(l+1)]^{1/2}/R_\odot$.

7

affected by near-surface phenomena. This lead Braun, Duvall, and LaBonte (1988) to consider the possibility that the observed decrease in α for $k \leq 0.5$ Mm^{-1} may indicate the presence of a shallow, near-surface uniform absorbing layer. The results of their simple computation agree well with the observed variation of α with k. This lead Braun, Duvall, and LaBonte to conclude that some of the decrease in α seen at low wavenumbers may represent a falloff in absorption at depths of $5 - 10$ Mm below the photosphere. However, the corresponding variation of α with radial order n predicted by this model is not observed – suggesting that the variation of α with wavenumber k is actually a characteristic of the absorption mechanism itself, rather than the vertical structure of the absorbing region.

Because the higher order azimuthal components sample an area of larger radius (i.e., higher impact parameter m/k), the variation of α with azimuthal order m can be used to infer information about the horizontal extent of the absorption region. Braun, Duvall, and LaBonte (1988) examined the variation of α with both the azimuthal order (for $-30 \leq m \leq 30$, at a single horizontal wavenumber $k = 1$ Mm^{-1}) and the impact parameter. Braun, Duvall, and LaBonte found that the decrease of α with both m and m/k, for simple isolated spots, is consistent with a uniform absorbing region of radius slightly larger than the visible penumbra. On the other hand, for more complicated active regions and an isolated pore, absorption occurs over a greatly extended region – associated with diffuse magnetic fields in the surroundings.

Braun, LaBonte, and Duvall (1990) performed Hankel analysis at multiple positions rather than just at the centre of the sunspots (as was done in Braun, Duvall, and LaBonte, 1987, 1988). By repeating the Hankel analysis at multiple locations (using only the azimuthally symmetric $m = 0$ mode), Braun, LaBonte, and Duvall (1990) built up spatial maps of the p-mode absorption over several active regions. These maps show that the maximum absorption coincides with the largest spots in the active regions. However, a lesser amount of absorption is also observed over a vast area associated with weak magnetic fields in surrounding plage, in agreement with the observations of Braun, Duvall, and LaBonte (1988). Subsequently, Braun (1995) found that isolated spotless plage does indeed show measurable amounts of p-mode absorption, at a level of 20% of that seen in typical sunspots. Braun, LaBonte, and Duvall (1990) estimate that the absorption efficiency scales roughly with the mean magnetic field strength, although they note the absorption appears to saturate inside the strongest fields (see also Braun and Duvall, 1990).

Observations of a broad range of active regions suggest that the peak value of the absorption coefficient varies with the size of the region. With a small pore exhibiting a maximum of $\alpha = 0.2$ (Braun, Duvall, and LaBonte, 1988). Sunspots with penumbral radii of about 20 Mm show absorption coefficients as high as 0.4 to 0.5 (Braun, Duvall, and LaBonte, 1987, 1988; Bogdan et al., 1993; Braun, 1995). The giant sunspot group of NOAA 5395, with radius of about 60 Mm, exhibited an absorption coefficient of 0.7 (Braun and Duvall, 1990).

Using a technique similar to but distinct from Hankel analysis, Penn and Labonte (1993) examined the spatial distribution of p-mode absorption within two sunspots. The technique consists of measuring the difference between incoming and outgoing power on a circular disk centred on the umbrae. The disk radius is increased incrementally until reaching the sunspot umbral radius. The observed absorption was found to increase linearly with the disk radius, consistent with a model of a uniform distribution of absorption within the sunspot umbrae.

8

Bogdan et al. (1993) were able to attain a high signal-to-noise ratio and high spatial resolution – observing up to $l \approx 1400$ ($k \approx 2$ Mm^{-1}). This allowed them to measure the variation of p-mode absorption as a function of degree l along individual p-mode ridges with radial orders $n = 0,\ldots,5$ (in much greater detail than Braun, Duvall, and LaBonte, 1988). They found that the absorption along each ridge tends to peak at intermediate values of the spherical harmonic degree l in the range $200 \leq l \leq 400$. The highest absorption is found along the p_1 ridge, and the absorption decreases with increasing radial order n. As mentioned above, Bogdan et al. (1993) employed a decomposition in terms of Legendre functions (see also Chen, Chou and the TON Team, 1996). When summed over the same azimuthal orders ($-5 \leq m \leq 5$) and integrated over the same frequencies (1.5 mHz $\lesssim \nu \lesssim 5$ mHz), the absorption coefficient observed by Bogdan et al. (1993) agreed remarkably well with the results of Braun, Duvall, and LaBonte (1987, 1988) for $k \lesssim 0.8$ Mm^{-1}, especially considering that two different sunspots were observed and two quite different techniques for acquiring and reducing the data were employed. However, for larger horizontal wavenumbers (0.8 Mm$^{-1} \lesssim k \lesssim 1.5$ Mm^{-1}), Bogdan et al. found that the absorption coefficient decreases with k – in disagreement with Braun, Duvall, and LaBonte (1987, 1988) who found little if any decrease over this range. Bogdan et al. suggest that the decrease of α with k at high wavenumbers may be due to finite lifetimes of the p-modes, rather than a real change in the absorption properties of the sunspot.

With this in mind, Bogdan and Braun (1995) analysed the observations of the sunspot NOAA 5254 using several different annulus sizes. Bogdan and Braun found that for $l \lesssim 300$, the observed level of absorption was unaffected by the annulus size. On the other hand, for $l \gtrsim 300$, the measured absorption level decreases considerably with increasing annulus radius (for a comprehensive analysis see Chen, Chou and the TON Team, 1996). This result verifies the suggestion of Bogdan et al. (1993) that p-modes with $l \gtrsim 300$ interact strongly with the quiet Sun convection and, therefore, have lifetimes shorter than (or of a similar duration to) the time taken for the modes to travel from the sunspot to the observed annular region. In contrast, modes with $l \lesssim 300$ are more "global" in nature and, hence, do not decay appreciably within the distance to the annulus.

The duration of the aforementioned observations (Braun, Duvall, and LaBonte, 1987, 1988; Braun and Duvall, 1990; Braun, LaBonte, and Duvall, 1990; Bogdan et al., 1993) typically spanned 4-8 hours. This is insufficient to accurately determine the scattering phase shifts, δ. Braun et al. (1992a) analysed a 68 hour data set made from the South Pole in 1988 – enabling the first unambiguous measurement of the scattering phase shifts of p-modes induced by a sunspot. Braun (1995) provided a more detailed discussion of the p-mode scattering analysis initially presented in Braun et al. (1992a), improved the data reduction technique, and presented observations for an additional sunspot and a spotless magnetic plage (also for durations of about 68 hours). The increased temporal duration also provides significantly improved frequency resolution – allowing the measurement of α and δ as a function of degree, radial order, and azimuthal order.

Braun (1995) found that sunspots do not exhibit any significant variation of the measured absorption coefficients over the observed range of azimuthal orders ($-20 \leq m \leq 20$), though there is considerable scatter. The absence of significant variation with m suggests that the absorption is occurring over a region similar in size to, or extended beyond, the inner radius

9

of the annulus θ_{min}. This is consistent with the results of Braun, Duvall, and LaBonte (1988), which showed that absorption also occurs in the diffuse magnetic regions (i.e., plage) surrounding sunspots. This interpretation is reinforced by finding that spotless plage also exhibits absorption, though at a level of 20% of the value seen in sunspots (Braun, 1995).

Due to the lack of significant variation of α with m, Braun (1995) was able to increase the signal-to-noise levels appreciably, without losing information, by computing absorption coefficients averaged over m. Consequently, Braun was able to plot α as a function of l along each p-mode ridge ($n = 0 - 8$). Braun found that the absorption seen in both sunspots exhibited very similar behaviour as a function of l and n, although the larger sunspot exhibited roughly 30% higher peak absorption than the smaller spot. The variation of α with l is broadly consistent with Bogdan et al. (1993) – the absorption along each ridge tends to peak at intermediate values of l, the highest absorption occurs for the f-, p_1-, and p_2-modes, and the absorption decreases with radial order.

Braun (1995) also observed the variation of the absorption coefficient as a function of frequency (see also Braun et al., 1992a). When α, grouped in different bins of degree l, is plotted as a function of frequency a striking pattern emerges. The left panel of Figure 1.3 shows the results for the sunspot NOAA 5254. A similar pattern of behaviour is evident for the other spot observed by Braun, NOAA 5229, despite the drastic difference in surface structure. Figure 1.3 shows there is a broad peak in the absorption coefficient at approximately 3 mHz, a minimum of zero absorption at 5 mHz, and an increase in α with ν at higher frequencies. The plage (results not displayed) showed a similar frequency dependence, though measurable levels of absorption are only observed for the highest l bins. On closer inspection, however, Figure 1.3 is actually slightly misleading. Figure 1.4 (adopted from Braun, 1995) shows the frequency variation of α for the individual radial orders $n = 0 - 8$ and the two different sunspots (NOAA 5229 and NOAA 5254). For each radial order, the frequency variation is different, though all modes show a peak in absorption at lower frequencies, a minimum at moderate frequencies, and a general increase of α with ν for higher frequencies (where the results are shown). Figure 1.4 clearly shows that the location of the absorption maximum and minimum varies with radial order, a feature not evident in Figure 1.3. There are two additional features, evident in Figure 1.4, that are worth noting. Firstly, both sunspots exhibit very similar behaviour despite the difference in appearance at the photosphere. Secondly, the highest levels of absorption occur for the f-, p_1-, and p_2-modes, and the peak absorption decreases with increasing radial order n.

It is apparent from the right hand panel of Figure 1.3 that the quiet Sun control tends to exhibit slight negative values of α – corresponding to emission (i.e., generation of acoustic power). Both Bogdan et al. (1993) and Braun (1995) note that the larger values of the quiet Sun emission tend to correspond to those modes which show the larger levels of absorption in sunspots. Indeed, Braun (1995) showed that there is a significant anti-correlation between the values of α for the spot NOAA 5254 and a region of quiet Sun. Assuming that a statistically steady-state of p-mode generation and decay (i.e., emission and absorption, respectively) is achieved by the turbulent convection, Bogdan et al. (1993) suggest an apparent emission of p-modes observed in an annulus centred on quiet Sun should, in fact, be present for modes sufficiently "global" in nature to interact with nearby magnetic regions (e.g., sunspots and plage).
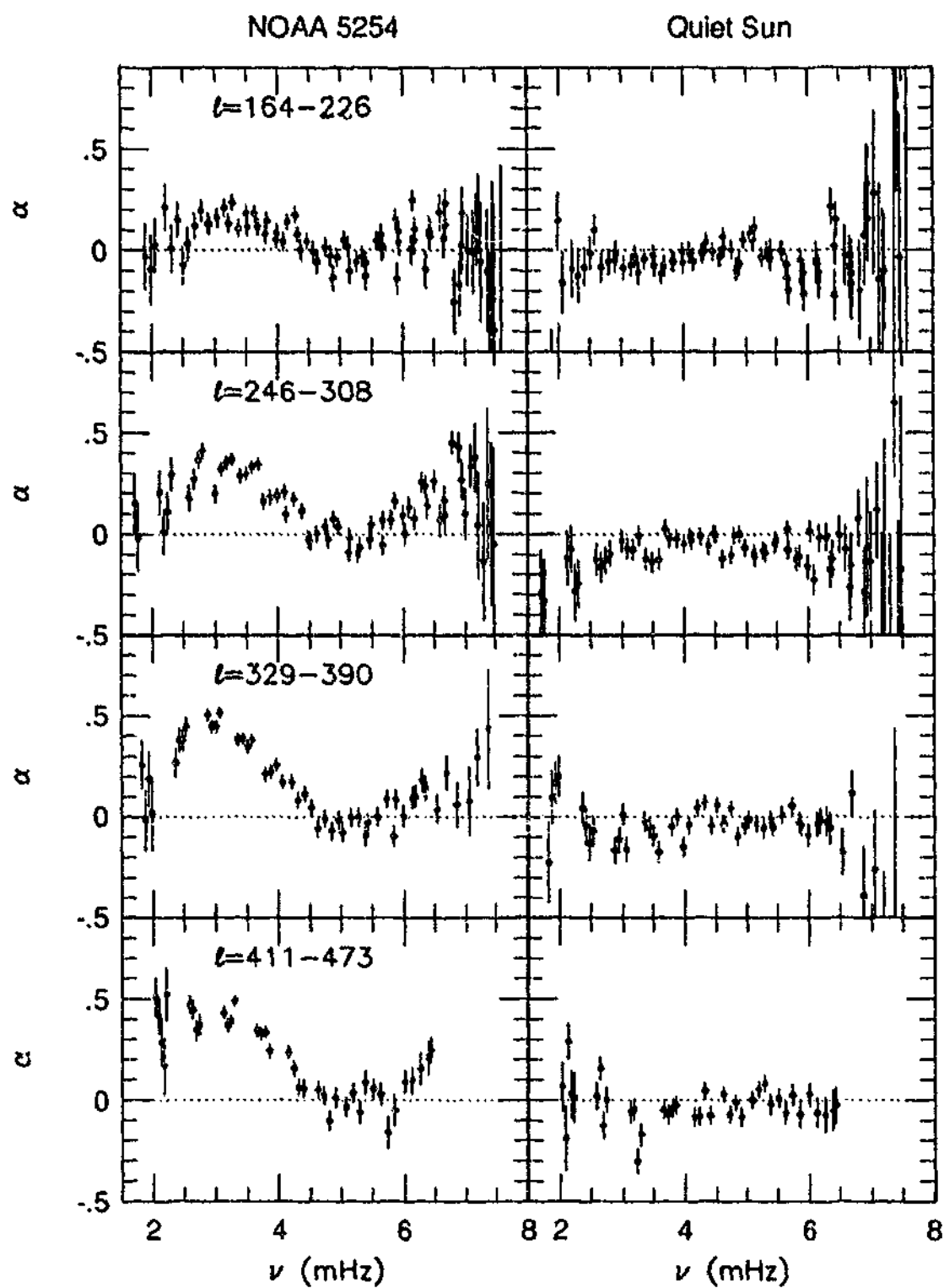
10

Figure 1.3: The "*m*-averaged" absorption coefficient, α, plotted as a function of temporal frequency, ν, for a sunspot (NOAA 5254, *left panel*) and a region of quiet Sun (*right panel*). The vertical panels represent the different values of l into which the absorption data has been binned. Reproduced from Bogdan and Braun (1995, who adopted it from Braun, 1995).

11
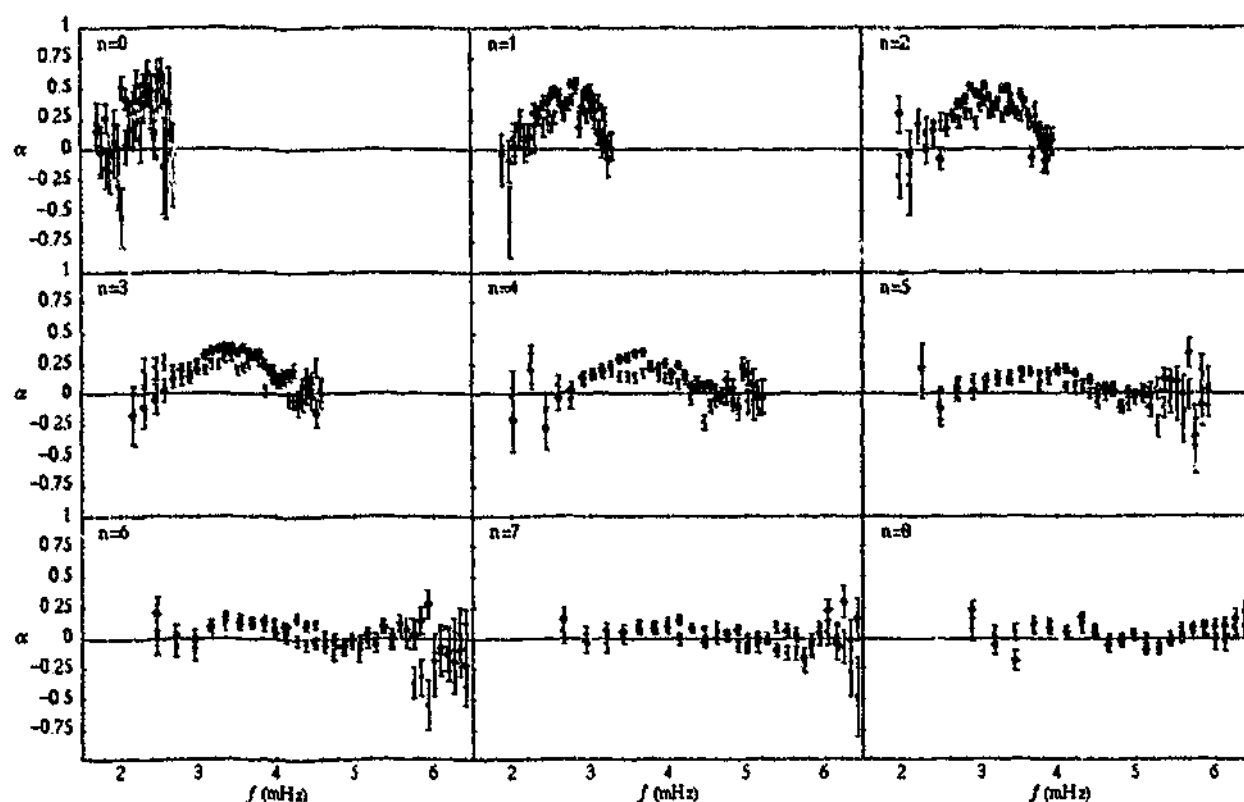
Figure 1.4: The "*m*-averaged" absorption coefficient, α, plotted as a function of temporal frequency, ν, for each of the radial orders $n = 0 - 8$. In this case the results for sunspots NOAA 5254 and NOAA 5229 are displayed (with black and grey diamonds, respectively). Error bars are one standard deviation. Adopted from Braun (1995).

Unlike the absorption coefficient, the scattering phase shifts for both sunspots show a strong dependence on azimuthal order. The scattering phase shift attains a maximum at $m = 0$, and steadily decreases as $|m|$ increases. Coincidently, the maximum observed phase shift is about 150°. The variation of δ with m suggests that the phase shifts are produced within an area about the size of the visible sunspot penumbra. This is in sharp contrast to the absorption measurements, which implied that the absorption is not confined to the sunspots but also occurs in the surrounding plage. Related to this observation is the finding that spotless plage, while absorbing p-modes, produces no measurable phase shifts (less than a few percent of the corresponding value for spots). As expected, the quiet Sun control produces no scattering phase shifts.

Braun (1995) also plotted the phase shifts, averaged over a small range of m, as a function of degree l along each p-mode ridge ($n = 1 - 9$). For both sunspots observed, the m-averaged phase shifts are positive and increase with degree l, with an increase that is faster than linear. Figure 1.5 (adopted from Braun, 1995) shows the scattering phase shifts, δ, as a function of frequency for the individual radial orders $n = 1 - 9$ and the two different sunspots (NOAA 5229 and NOAA 5254). Figure 1.5 shows that δ grows rapidly with increasing frequency, in a similar fashion to the variation with degree l. Figure 1.5 also shows the scattering behaviour of the two disparate sunspots is very similar, as is the absorption behaviour (Fig. 1.4). The

12

frequency dependence of the phase shifts (Fig. 1.5) differs substantially from that of the absorption coefficients (Fig. 1.4). In particular, at frequencies where the sunspots produce essentially no absorption of p-modes, the phase shifts are at a maximum level. This scattering behaviour has been interpreted by Fan, Braun, and Chou (1995) to imply that sunspots are relatively shallow (depth ≈ 1 Mm) acoustic structures (see §2.3).
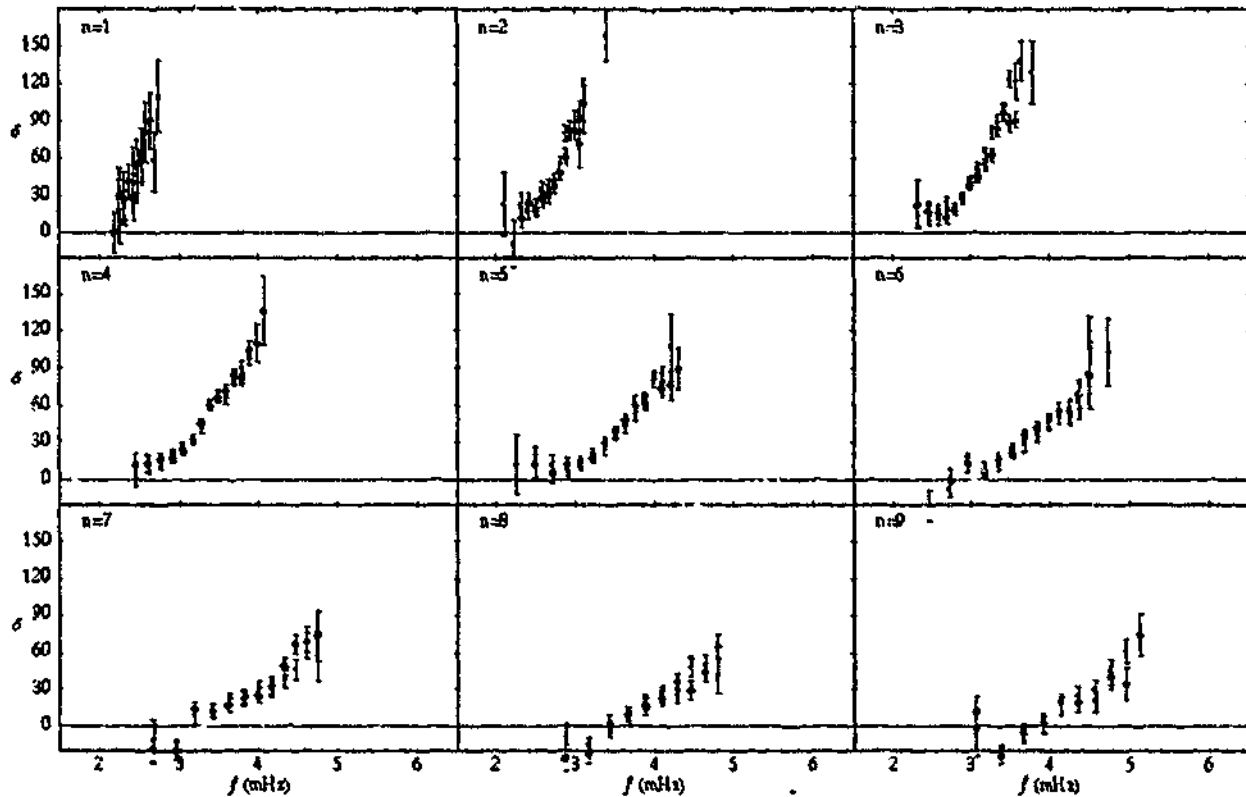
Figure 1.5: The "m-averaged" scattering phase shifts, δ, plotted as a function of temporal frequency, ν, for each of the radial orders $n = 1 - 9$. In this case the results for sunspots NOAA 5254 and NOAA 5229 are displayed (with black and grey diamonds, respectively). Error bars are one standard deviation. Adopted from Braun (1995).

In the two different sunspots observed (NOAA 5229 and NOAA 5254), Braun (1995) found strong evidence that mode mixing occurs between modes of adjacent radial order at the same frequency and same azimuthal order. The frequency variation of the mode mixing phase shifts along each ridge pair is similar to the usual phase shifts (i.e., scattering between identical radial orders), but the mode mixing phase shifts are approximately 90° greater. On the other hand, both the plage and the quiet Sun control exhibited no evidence of mode mixing. The corresponding mode mixing strengths (i.e., the power transferred from an incoming mode n to an outgoing mode n') were not able to be quantified in detail (see Braun, 1995, for discussion).

13

1.4.3 Helioseismic tomography

Helioseismic tomography, also known as time-distance helioseismology, was first proposed by Duvall *et al.* (1993). Again letting Ψ be the observed acoustic oscillation field at the surface (as in §1.4.2, this may be either observed velocity or intensity fields), then the cross-correlation between signals at the surface positions r_1 and r_2, separated by a horizontal distance Δ, is determined by

$$C_0\left(\Delta, \tau\right) = \int_0^T \Psi\left(r_1, t\right) \Psi^*\left(r_2, t + \tau\right) dt,$$

where τ is the time delay between signals, and T is the temporal duration of the observations. Duvall *et al.* found that the cross-correlation, C_0, between fluctuations at two distinct surface locations is maximal along a parabolic curve of the form $\Delta \propto \tau^2$. Dispensing with the modal description (see §1.4.2) altogether, Duvall *et al.* interpreted this behaviour in terms of a ray (or optics) formalism, where the solar acoustic oscillations are regarded as a collection of wave packets that travel along ray paths connecting the two points under consideration. Subsequently, the time delay is interpreted as the time taken for the wave packet to travel between the two surface points.

The basic idea of helioseismic tomography is analogous to an approach commonly applied in both terrestrial and oceanographic seismology. By measuring the travel times between different points on the solar surface, helioseismic tomography aims to use these measurements to infer the variation of the internal properties such as the sound speed, magnetic field, and subsurface flow velocities along various ray paths. For example, in regards to sunspots, helioseismic tomography attempts to distinguish between ray paths which encounter the sunspot and those which merely propagate through undisturbed quiet Sun. The resultant difference in travel time for the two different rays contains diagnostic information about the subsurface structure of the spot.

Indeed, Duvall *et al.* (1996) measured such travel time anomalies (see also Braun, 1997). Duvall *et al.* generated maps of the travel time differences (and averages) over a region of the solar surface. For each point in the region of interest, they used the cross-correlation function C_0 to estimate the travel times between the point and an annulus (of radius Δ) centred on it. In the vicinity of active regions, Duvall *et al.* found that travel times for outward propagating waves (τ^+) are smaller, by approximately one minute, than corresponding inward travel times (τ^-). They interpreted this as evidence of downflows within the spot and in its immediate surroundings – the ray paths are almost vertical near the surface, therefore, a downflow would decrease the travel time for an outgoing wave but increase it for an incoming wave. They estimated that the downflows have velocities of about 2 km s^{-1}, and persist to depths of roughly 2 Mm. Subsequent inversions of the Duvall *et al.* travel time data by Kosovichev (1996) suggest that flows associated with active regions also occur at even greater depths (about 20 Mm). Additionally, Duvall *et al.* observed the mean travel time, which evidently decreases by about 0.4 min at the location of sunspots (corresponding to an average wave speed increase). They concluded that this was consistent with the presence of a vertical magnetic field with strength of 2 kG at the surface, that increases to 4 kG at a depth of 600 km.

14

Braun (1997) applied the methods helioseismic tomography to GONG data, and confirmed the findings of Duvall et al. (1996) that $\tau^+ - \tau^- \approx 1$ minute in the vicinity of sunspots (which is not observed for the control experiment where the sunspot is absent). By varying the radius of the inner annulus, Braun also showed that the radial extent of the region producing the travel time anomalies is coincident with the outer boundary of the sunspot penumbrae. Braun then calculated the cross-correlation function C_2 for points connected by a two-skip trajectory, where the first skip (i.e., surface reflection) occurs at the centre of a sunspot. The resultant two-skip travel times (divided by 2) differ significantly to the single-skip travel times. Braun suggested that the discrepancy probably arises from the use of the oscillation signals within the sunspot in the correlation analysis (with associated limitations alluded to in §1.4.1 and §1.4.2).

It should be noted that the process of calculating the cross-correlation function C_0 and the subsequent construction of the time-distance diagram is completely independent of ray theory. The ray formalism is employed at the level of interpretation and inversion, as a convenient method for extracting information from the observations (e.g., D'Silva, 1994, 1996; D'Silva and Duvall, 1995). Bogdan (1997) clarified the relationship between the time-distance and modal-decomposition (see §1.4.2) approaches to local helioseismology. By considering a model for which analytic solutions are available, Bogdan was able to critically compare the two approaches. He found that a wave-packet composed of a superposition of neighbouring p-modes on the traditional k-ω diagram (for an example of the analogous l-ω diagram, see Fig. 1.1) interferes constructively along the ray path predicted by ray theory. Hence, a cross-correlation curve of the form $\Delta \propto \tau^2$ (Duvall et al., 1993) will always be observed. However, Bogdan found that the wave packet is not localised to the ray path joining the two surface bounce points, except if the radial orders of the constituent p-modes are very large (i.e., $n \gg 1$, corresponding to p-modes with vertical wavelengths much less than the density scale, consistent with the WKBJ approximation). In reality, the spectrum of five minute solar p-modes used in observations (e.g., Duvall et al., 1996) have rather low radial orders. Therefore, the subsequent wave packets are diffuse and sample portions of the solar envelope that are up to $10 - 30$ Mm from the predicted ray path. Bogdan cautions against interpretations drawn in terms of a single ray path description, and suggests techniques that account for ray bundles (a sum of ray paths) should be considered for the analysis of the observed travel time anomalies.

Bogdan et al. (1998) extended the investigation of the relationship between the time-distance and modal-decomposition approaches to sunspot seismology. In particular, they developed a pair of formulae relating the quantities measured by the approaches of time-distance (namely, the cross-correlation function) and modal-decomposition (absorption coefficient and scattering phase shift). Applying these to the observations previously analysed by Braun (1997), along with concurrent observations from the HAO/NSO Advanced Stokes Polarimeter, Bogdan et al. demonstrated that the inferred GONG umbral oscillation signal actually originates from the umbra-penumbra boundary (about 6 Mm from the centre of the spot). Additionally, they found that 5-minute oscillations of the umbra-penumbra boundary lag behind those in the centre of the umbra by roughly 1 minute, agreeing with the travel time differences observed by Duvall et al. (1996) and Bogdan (1997). This observation casts serious doubt on the inference made by Duvall et al. (1996), that the travel time difference

is evidence of steady downflows. Bogdan *et al.* also reported that mode mixing, spontaneous *p*-mode emission from within the sunspot, and the generation of magneto-atmospheric waves in the sunspot are all processes that can produce travel time asymmetries (i.e., $\tau^+ \neq \tau^-$).

Finally, we note the recent tomographical inversions by Kosovichev, Duvall, and Scherrer (2000) and Kosovichev (2002) which have yielded impressive images of the three-dimensional structure of the sound-speed perturbation below sunspots. Kosovichev, Duvall, and Scherrer (2000) report that the typical wave speed perturbations range from $0.3-1$ km s^{-1}, in a region as broad as the surface spot and some 10 Mm beneath it. At a depth of 4 Mm, Kosovichev, Duvall, and Scherrer concluded that the wave speed perturbation may correspond to either a 10% temperature enhancement (about 2800 K) or to a 18 kG magnetic field.

1.4.4 Helioseismic holography

Helioseismic holography treats the acoustic field observed at the two-dimensional solar surface in an analogous fashion to how the eye treats the electromagnetic radiation observed at the two-dimensional surface of the cornea. The acoustic field observed over the solar surface, Ψ, is propagated back (in time) into a model of the solar interior. The resultant three-dimensional acoustic field is then sampled in "focal planes" at depths of interest – rendering an image of the features that gave rise to the observed surface signal. Hence, helioseismic holography can probe the three-dimensional distribution of local acoustic anomalies (sinks, sources and scatterers) within the solar interior – a task Hankel analysis can only perform in a limited fashion.

The acoustic egression, H_+, provides a statistical assessment of the contribution made by an acoustic disturbance emanating from a point in the interior, $(\mathbf{r}, z)$, and time t, to the observed surface acoustic field, Ψ, at $(\mathbf{r}', 0)$ and time t'. The acoustic egression is defined as

$$ H_+ \left(\mathbf{r}, z, t \right) = \int \int_{a < |\mathbf{r} - \mathbf{r}'| < b} G_+ \left(|\mathbf{r} - \mathbf{r}'|, z, t - t' \right) \Psi \left(\mathbf{r}', t' \right) d^2 r' dt', $$

where G_+ is a Green's function that expresses how a point disturbance at $(\mathbf{r}', 0)$ propagates backward in time to $(\mathbf{r}, z)$, or equivalently, forward in time from $(\mathbf{r}, z)$ to $(\mathbf{r}', 0)$. The acoustic ingression, H_-, is the time reverse of the egression (with G_+ replaced by its complex conjugate) and expresses the contribution to the surface acoustic field by waves converging onto the focal point $(\mathbf{r}, z)$. The computational regressions are performed over an annular region, the "pupil", with inner radius a and outer radius b centred on $\mathbf{r}$, the surface location directly overlying the focal point $(\mathbf{r}, z)$.

Helioseismic holography was first proposed as a method for imaging active regions on the far side of the sun by Lindsey and Braun (1990, see also Roddier, 1975). However, this has only come to fruition in the last few years (e.g., Lindsey and Braun, 2000a; Braun and Lindsey, 2001). In the interim, helioseismic holography was developed as a technique for local helioseismology (e.g., Braun *et al.*, 1992b; Lindsey and Braun, 1997; Braun *et al.*, 1998; Lindsey and Braun, 1999). The application of helioseismic holography to observations from the SOHO Michelson Doppler Imager has resulted in the discovery of a remarkable array of new solar acoustic phenomena, a comprehensive review of these can be found in Braun and

Lindsey (2000a). Recent additional analysis of helioseismic holography has been performed by Barnes and Cally (2001) and Skartlien (2001, 2002).

In general, the results obtained with helioseismic holography are in excellent agreement with those of Hankel analysis (e.g., Braun, Duvall, and LaBonte, 1987, 1988; Bogdan *et al.*, 1993; Braun, 1995, see also §1.4.2). In particular, sunspots absorb energy from and substantially shift the phase of p-modes incident upon them. For example, when the acoustic egression power (i.e., $|H_+|^2$ integrated over time and normalised with a smoothed ingression, see Lindsey and Braun, 1999) is calculated for a set of observations containing regions which absorb p-modes, such as sunspots and plage, the absorbers shows up as regions of deficit in the acoustic egression power (e.g., Chang *et al.*, 1997; Lindsey and Braun, 1998a,b, 1999; Braun and Lindsey, 1999, 2000a). It should be noted that Chang *et al.* (1997) were the first to apply holography to actual solar data and confirm the localised absorption of p-modes by sunspots, though they refer to the technique as "acoustic imaging" (for details and discussion of the minor technical differences see Braun *et al.*, 1998; Chou, 2000; Lindsey and Braun, 2000b). As alluded to above, holography can do more. We discuss some of the discoveries relevant to sunspots and their immediate surroundings (other notable successes include the first seismic images of a solar flare by Donea, Braun, and Lindsey, 1999).

By performing depth diagnostics, Braun *et al.* (1998) and Lindsey and Braun (1998a,b) found that the depth dependence of the 3 mHz egression power deficits in sunspots are consistent with absorption (in models) that occurs predominantly within a few Mm or less of the photosphere. This is consistent with the p-mode absorption by sunspots measured using Hankel analysis (e.g., Braun, Duvall, and LaBonte, 1987, 1988; Bogdan *et al.*, 1993; Braun, 1995, see also §1.4.2), where α was found to decline with decreasing horizontal wavenumber (i.e., increasing depth of the p-mode lower turning point) in the range $k \leq 0.5$ Mm^{-1}.

In addition to the egression power deficits coinciding with the sunspots and plage, Braun *et al.* (1998), Lindsey and Braun (1998a), and Lindsey and Braun (1999) uncovered a region showing a general deficit of 10-30% in $3-4$ mHz acoustic emission (i.e., an apparent absorbing region) which extends far beyond the sunspot, to distances of $30 - 70$ Mm. This region is referred to as the "acoustic moat". The outer boundary of the acoustic moat roughly coincides with plages in the neighbourhood of the sunspot (which are known p-mode absorbers, Braun, 1995) but often extends into regions that are non-magnetic (Braun and Lindsey, 2000a). It should be noted that the spatial resolution of the Hankel absorption maps (Braun, LaBonte, and Duvall, 1990) was insufficient to detect the presence of such a moat. The acoustic moat was discovered using acoustic power holography, which is sensitive to acoustic sinks and sources, but may only render images of scatters if they are illuminated by nearby sinks or sources. On the other hand, phase-sensitive holography (Lindsey and Braun, 1997; Braun and Lindsey, 2000b), which computes a temporal correlation between the egression and ingression, can detect subsurface features that scatter acoustic waves. While the acoustic moat may have its own absorption mechanism, Lindsey and Braun (1998a) and Braun *et al.* (1998) note that it may simply be a region that scatters the depleted waves emanating from the nearby sunspot, such as a convection cell (driven by the accumulation of heat blocked by the sunspot photosphere). The results of Braun and Lindsey (2000b) using phase-sensitive holography support this hypothesis. They found signatures of an extended, near-surface, rapid outflow (though these results are in apparent conflict with the downflows inferred from helioseismic

17

tomography by Duvall et al., 1996).

By taking the temporal Fourier transform of the egression and ingression the analysis can be shifted to the "spectral perspective" ("chromatic holography" in the terminology of Lindsey and Braun, 1999), where the observations may be viewed as a function of frequency. Using this technique, Lindsey and Braun (1999) found that the acoustic deficit (absorption of p-modes) rendered by the sunspot itself actually persists approximately uniformly over the range $3-7$ mHz. This result is in apparent contradiction with the results of Hankel analysis (see Figure 1.3 and Braun, 1995), which show a distinctive absorption minimum at frequencies near 5 mHz, depending on the radial order (see Fig. 1.4). Instead, Lindsey and Braun (1999) find a 2.5% enhancement of quiet Sun egression (i.e., localised generation of acoustic power) at about 5 mHz in a region surrounding the sunspot that extends far beyond the spot and the acoustic moat. Lindsey and Braun (1999) estimate that the contribution of this small enhanced emission at 5 mHz, over the broad range for which it exists, is sufficient to cancel the acoustic deficit (absorption) caused by the sunspot and, therefore, obscures the Hankel analysis results (Braun, 1995).

The region of enhanced emission surrounding the sunspot, revealed by Lindsey and Braun (1999), is a relatively weak, diffuse "acoustic glory". Acoustic glories (e.g., Braun and Lindsey, 1999, 2000a; Donea, Lindsey, and Braun, 2000) are halos of sharply enhanced higher frequency (above 4.5 mHz) acoustic emission in the regions surrounding multipolar active regions. Acoustic glories are largely comprised of small, discrete emitters that may generate acoustic power 1.5 times that of the average quiet Sun. Donea, Lindsey, and Braun (2000) show that these small emitters are nearly all confined to regions of quiet Sun, but have a remarkable tendency to border weak magnetic regions.

Depth diagnostics reveal the existence of submerged "acoustic condensations" indicating the presence of compact acoustic deficits $10-20$ Mm below isolated sunspots (Lindsey and Braun, 1998b) and multipolar active regions (Braun and Lindsey, 1999). These acoustic condensations generally do not lie directly below the sunspots, but can appear tens of Mm away from any sunspot. The reason for this is not currently understood. In a similar fashion to the acoustic moat, Braun and Lindsey (1999) suggest these features may not be absorbers at all, as they appear in the observations, but simply scatterers (associated with subsurface thermal or Doppler perturbations).

Using multiple-skip chromatic holography Lindsey and Braun (1999, see also Lindsey and Braun, 2000b) confirmed that the quiet sun photosphere is poor specular reflector for frequencies above its acoustic cutoff frequency (this result is consistent with the observations obtained using helioseismic tomography by Duvall et al., 1993). In contrast, the photosphere of active regions, including sunspots, efficiently reflects high frequency acoustic waves. This somewhat surprising behaviour was revealed recently using phase-sensitive holography (Braun and Lindsey, 2000a,b). Additionally, observations using phase-sensitive holography indicate that all magnetic regions, including plage, induce sound travel time perturbations (consistent with the presence of Wilson-like depressions with depths proportional to the surface magnetic pressure). This is in contradiction with the results found using Hankel analysis, in which case plage apparently absorbs but does not scatter incident p-modes (Braun, 1995, see also §1.4.2). The reason for this discrepancy is unclear.

18

1.5 Outline

In Chapter 2 we discuss several theoretical models for the interaction of solar oscillations (p-modes) with various magnetic field structures, which have been proposed to interpret the aforementioned observations. In this thesis, we focus on two observational facts: sunspots absorb (and scatter) incident p-modes, and p-modes have finite lifetimes (i.e., non-zero line widths). Chapters 3 and 4 are devoted to modelling the absorption of solar p-modes by sunspots, in particular, for regions with non-vertical magnetic field. In Chapter 5 we model the global damping of solar p-modes by fibril field, calculating the p-mode lifetimes resulting from energy escaping into both the solar interior and the upper atmosphere. Conclusions are discussed in Chapter 6.

Chapter 2

Modelling the interaction of solar p-modes with magnetic field

From a theoretical perspective, the interaction of solar p-modes with magnetic field (observational evidence outlined in Chapter 1) is generally not well understood. In this chapter, we briefly discuss the magnetohydrodynamic approximation, which is central to modelling the interaction. We then survey several candidate mechanisms for the interaction of solar p-modes with the Sun's magnetic field.

2.1 Magnetohydrodynamics

Magnetohydrodynamics (MHD) is a synthesis of fluid dynamics (as described by the Navier-Stokes equations) and electromagnetism (Maxwell's equations and Ohm's law) in the non-relativistic approximation. The fluid is considered to be highly electrically conducting (meaning at least partial ionisation has taken place), and adequately describable as a single component fluid (i.e., charge separation is negligible over all the length scales of interest). These assumptions are valid for most (though not all) solar phenomena. For the purposes of this investigation these assumptions are reasonable.

Ideal MHD treats the plasma as a perfectly conducting fluid interacting with a magnetic field. Ideal MHD neglects: viscosity, energy losses due to non-adiabatic effects (such as thermal conduction and radiation), and Ohmic diffusion (i.e., electrical resistance). The equations of ideal MHD are the equations for: continuity (conservation of mass),

$$\frac{\partial \rho}{\partial t} + \mathbf{v} \cdot \nabla \rho + \rho \nabla \cdot \mathbf{v} = 0 \, ,$$

conservation of momentum,

$$\rho \left(\frac{\partial \mathbf{v}}{\partial t} + \mathbf{v} \cdot \nabla \mathbf{v} \right) = -\nabla p + \frac{1}{\mu_B} \left(\nabla \times \mathbf{B} \right) \times \mathbf{B} - \rho g \hat{\mathbf{e}}_z \, ,$$

conservation of energy,

$$\frac{\partial p}{\partial t} + \mathbf{v} \cdot \nabla p = \frac{\gamma p}{\rho} \left(\frac{\partial \rho}{\partial t} + \mathbf{v} \cdot \nabla \rho \right),$$

the induction equation (which follows from Ampère's, Faraday's and Ohm's Laws),

$$\frac{\partial \mathbf{B}}{\partial t} = \nabla \times (\mathbf{v} \times \mathbf{B}),$$

and the solenoid condition (expressing the absence of magnetic monopoles),

$$\nabla \cdot \mathbf{B} = 0,$$

where ρ is the mass density, $\mathbf{v}$ is the velocity, p is the gas pressure, $-g\hat{\mathbf{e}}_z$ is the acceleration due to gravity, $\mathbf{B}$ is the magnetic field, and μ_B is the magnetic permeability. The continuity and energy equations are just the usual (non-magnetic) fluid equations, whereas the momentum equation contains an extra term, the Lorentz force, introduced by the presence of the magnetic field. The Lorentz force can be split into two components,

$$\frac{1}{\mu_B} (\nabla \times \mathbf{B}) \times \mathbf{B} = \frac{1}{\mu_B} [\mathbf{B} \cdot \nabla] \mathbf{B} - \frac{1}{2\mu_B} \nabla [\mathbf{B} \cdot \mathbf{B}],$$

indicating that the magnetic field introduces two forces that are absent in the non-magnetic case: an isotropic magnetic pressure $B^2/2\mu_B$ and a tension B^2/μ_B. The Lorentz force has no component in the direction along the field lines. Therefore, the magnetic pressure gradient in the direction along the field lines must exactly balance the magnetic tension component along the field lines. Another important consideration arises from the induction equation. When the fluid is perfectly conducting, as in ideal MHD, Alfvén's theorem implies that magnetic flux is frozen into the fluid (i.e., magnetic field lines move with the fluid). Comprehensive discussion of magnetohydrodynamics can be found in several textbooks (e.g., Ferraro and Plumpton, 1966; Priest, 1982).

2.2   Possible interaction mechanisms

This section is devoted to surveying several mechanisms for the interaction of solar p-modes with a range of magnetic structures. These are for example: sunspots, plage, pores, intense photospheric flux tubes, and canopy field. The survey is not intended to be exhaustive, we emphasise the topics central to this thesis. The interaction of p-modes with magnetic flux concentrations can be decomposed into two distinct components -- absorption and scattering (though the interaction with canopy field lies outside of this categorisation). We focus on absorption, though scattering mechanisms are also briefly discussed. From a theoretical perspective, it is fair to say, the interaction of solar p-modes with magnetic field is not well understood. At present, theoretical models do not adequately explain the observations (outlined in Chapter 1). However, recent advances using the results of this thesis (Appendix F) are extremely promising.

Broadly speaking, the various theoretical attempts employ two distinct approximate models of a magnetic flux concentration: (1) inhomogeneity primarily in the horizontal direction, neglecting gravitational stratification (e.g., resonant absorption and the interaction with bundles of flux tubes); (2) inhomogeneity primarily in the vertical direction (gravitational stratification), neglecting horizontal variations (e.g., mode conversion). There are also phenomenological models for sunspots, and we discuss these first.

2.3 Phenomenological models

A handful of phenomenological models for sunspots have been developed (e.g., Brown, 1990; Fan, Braun, and Chou, 1995; Chou et al., 1996; Chen, Chou and the TON Team, 1997; Barnes and Cally, 2000). By assuming that the effect of the sunspot's magnetic field can be parametrised in some simple manner, such as by a modified sound speed (e.g., Fan, Braun, and Chou, 1995; Chou et al., 1996; Chen, Chou and the TON Team, 1997) or modified upper boundary condition (e.g., Barnes and Cally, 2000), phenomenological models avoid the complications involved with calculating the full Lorentz force. This approach enables the forward (Fan, Braun, and Chou, 1995; Chou et al., 1996) and inverse (Chen, Chou and the TON Team, 1997) problems in sunspot seismology to be tackled.

For example, Fan, Braun, and Chou (1995) calculate the scattering phase shifts for a model "sunspot". The model consists of a near-surface, disk-shaped inhomogeneity in which the sound speed smoothly increases to it's peak value $\sqrt{2}$ times the external sound speed at the same depth. Fan, Braun, and Chou (1995) find a substantial agreement between the observations of sunspot NOAA 5254 (Braun, 1995) and their model when a disk of radius 25 Mm[1] extending over a depth of 1 Mm is employed.

Another example, Chou et al. (1996); Chen, Chou and the TON Team (1997) assume the presence of the magnetic regions can be represented by a complex sound speed – such a model can both absorb and scatter incident p-modes. Chen, Chou and the TON Team (1997) invert the measured absorption coefficients in two sunspots NOAA 5254 (Braun, 1995) and NOAA 7887 (Chen, Chou and the TON Team, 1997), and infer the depth dependence of the real part of the interaction parameter (which corresponds to the absorption of waves). The depth dependences are similar for both sunspots: the real part of the interaction parameter increases rapidly with increasing depth, reaches a maximum value at a depth of about 7 Mm, then gradually drops off to zero at a depth of about 28 – 35 Mm.

Phenomenological models deliberately ignore the details of the interaction mechanism. However, if one can ascribe some physical interpretation to the chosen parametrisation, phenomenological models may provide a bridge between the theory of the interaction mechanism and observations.

2.4 Resonant absorption

Resonant absorption of acoustic oscillations occurs as a result of cross-field inhomogeneity in regions with non-uniform magnetic field. In the context of sunspots, this was first suggested

---

[1]The observed penumbral radius of sunspot NOAA 5254 was 18 Mm (Braun, 1995).

by Hollweg (1988)[2] and further developed by Lou (1990); Rosenthal (1990, 1992); Sakurai, Goossens, and Hollweg (1991a,b); Goossens and Poedts (1992); and Goossens, Ruderman, and Hollweg (1995). Resonant absorption occurs when, in horizontally inhomogeneous regions, the frequency of the oscillation coincides with the local Alfvén (or local cusp) frequency on a particular magnetic surface (corresponding to a singularity in the ideal MHD limit). Enhanced dissipation ultimately occurs at the resonant surface due to non-ideal effects, such as viscosity and electrical resistivity though the rate of absorption is independent of these (Goossens and Poedts, 1992; Erdélyi and Goossens, 1994). Resonant absorption of sound waves is very efficient across a broad range of circumstances (even for weakly dissipative media), for example, straight (monolithic) magnetic flux tubes (e.g., Hollweg, 1988; Lou, 1990; Sakurai, Goossens, and Hollweg, 1991a,b; Keppens, 1995), twisted monolithic flux tubes (e.g., Chitre and Davila, 1991; Goossens and Poedts, 1992; Stenuit, Poedts, and Goossens, 1993; Stenuit, Erdélyi, and Goossens, 1995), and fibril-type field (e.g., Rosenthal, 1990, 1992; Keppens, Bogdan, and Goossens, 1994, discussed further in §2.6). Resonant absorption may operate in a gravitationally stratified atmosphere (e.g., Goossens, Poedts, and Hermans, 1985), though the efficiency remains uncertain.

2.4.1 Resonant absorption in canopy field

In general, gravitationally stratified atmospheres permeated by exactly horizontal magnetic field also possess the Alfvén and cusp resonant layers (Cally 1984, also see §3.1.2). Therefore, resonant absorption (as outlined in §2.4) may take place in canopy field (in the chromosphere and corona) overlying the non-magnetic convection zone. Zhukov (1997); Tirry et al. (1998); Pintér and Goossens (1999); Vanlommel and Goossens (1999); Vanlommel et al. (2002) consider the interaction of the solar p-modes with resonant oscillations in the magnetic canopy. This interaction results in a frequency shift, as well as p-mode damping. Rough agreement with observations can be obtained, depending on the choice of model parameters. The influence of canopy field on the p-modes was also studied by Campbell and Roberts (1989); Evans and Roberts (1990); Jain and Roberts (1994a,b,c). However, the canopy resonances were avoided by a special choice of magnetic field and temperature profiles.

2.5 Mode conversion

Mode conversion occurs as a result of vertical gravitational stratification in atmospheres with a uniform, non-horizontal magnetic field. The damping of global oscillations in stars by conversion to slow modes was first considered by Biront et al. (1982) and subsequently by Roberts and Soward (1983) and Campbell and Papaloizou (1986). This mechanism was first applied to sunspots by Spruit and Bogdan (1992) and further developed by Cally and Bogdan (1993, hereafter CB93); Cally, Bogdan, and Zweibel (1994, CBZ); Cally (1995); Hindman, Zweibel, and Cally (1996); Bogdan and Cally (1997, BC97); and Lites et al.

---

[2]Though resonant absorption of Alfvén waves was originally studied in thermonuclear fusion research as a mechanism for heating laboratory plasmas (see e.g., Chen and Hasegawa, 1974; Hasegawa and Chen, 1976), and later in the heating of solar coronal loops (see e.g., Ionson, 1978; Poedts, Goossens, and Kerner, 1989, 1990).

(1998). Mode conversion occurs because, in a gravitationally stratified atmosphere with a uniform, non-horizontal magnetic field, the fast and slow magnetoacoustic-gravity (MAG) waves interact (predominantly in the region where the sound speed, C_S, and Alfvén speed, C_A, are comparable). In uniform, vertical magnetic fields, the Alfvén waves decouple. In fact, due to the interaction of the fast and slow MAG waves, it is not appropriate to use the terms "fast" and "slow" – these only have meaning when the sound and Alfvén speeds differ greatly. The resultant oscillations, governed by a fourth order system of differential equations, are called π-modes (as distinct from p-modes, in recognition of the role played by the magnetic field). However, at great depth (where $C_A \ll C_S$), the fast and slow MAG wave components of the π-modes are locally decoupled. There, the fast modes are essentially acoustic, trapped oscillations much like the non-magnetic p-modes; and the slow modes are essentially Alfvénic (transverse and incompressive), downward-travelling waves. Consequently, the slow modes can leak energy away from the fast mode resonant cavity.

It is worthwhile noting that the concept of mode conversion is broadly consistent with the observed absorption of p-modes by sunspots, pores and plage (see §1.4.2). In particular, absorption occurs uniformly across the sunspot umbrae and penumbrae (e.g., Braun, Duvall, and LaBonte, 1988; Braun, LaBonte, and Duvall, 1990; Penn and Labonte, 1993; Braun, 1995), and absorption scales roughly with both the size of the magnetic region (e.g., Braun, Duvall, and LaBonte, 1988; Braun and Duvall, 1990; Braun, 1995) and the mean magnetic field strength (e.g., Braun, LaBonte, and Duvall, 1990). The results from helioseismic holography (see §1.4.4) indicate that absorption in sunspots occurs predominantly within a few Mm or less of the photosphere (e.g., Braun et al., 1998; Lindsey and Braun, 1998b; Braun and Lindsey, 2000a). This finding is in qualitative agreement with mode conversion occurring in the layers where $C_S \approx C_A$ (i.e., near the surface).

The efficiency of fast-to-slow mode conversion, in gravitationally stratified, plane parallel, atmospheres permeated by uniform, vertical magnetic fields, has been addressed by CB93, CBZ, Cally (1995) and BC97. The fourth order boundary value problem, consisting of the fourth order MAG wave equation and four boundary conditions, results in an eigenvalue problem. The eigenvalue is necessarily complex due to the leakage of energy by the slow modes – the imaginary part quantifies the efficiency of the mode conversion. CB93 and BC97 consider the temporal evolution of free linear oscillations, calculating complex (angular) frequency eigenvalues ω for given real horizontal wavenumber k. The imaginary part of the frequency eigenvalue indicates temporal decay of the π-modes. CBZ and Cally (1995) carried out the complementary study, the spatial evolution of driven linear oscillations – specifying real angular frequency ω and calculating complex wavenumber eigenvalues k. The imaginary part of the wavenumber eigenvalue indicates horizontal spatial decay of the π-modes. The latter approach is more suitable for the situation where external p-modes of a given frequency drive oscillations inside the sunspot.

To quantify the driving of the internal π-modes by external p-modes, and hence p-to-slow mode conversion, requires matching oscillations (total pressure and radial velocity) across the boundary between the non -magnetic and magnetic regions. In particular, in the non-magnetic region surrounding the sunspot, oscillations need to be decomposed in terms of both a discrete spectrum of horizontally travelling p-modes and a continuous spectrum of horizontally evanescent jacket modes (see Bogdan and Cally, 1995, for details). The matching

24

problem, including the jacket modes, has been addressed by Barnes and Cally (2000) for a (phenomenological) thin-disk scattering model consisting of two non-magnetic regions of finite depth[3], with different upper boundary conditions. The mathematical complications are severe (especially for semi-infinite atmospheres), hence, the eigenvalue analyses do not incorporate the matching problem.

Cally and Bogdan (1997) and Rosenthal and Julien (2000) carried out complementary numerical simulations of non-magnetic p-modes encountering a vertical magnetic flux concentration – this naturally includes the matching across the interface between the magnetic and non-magnetic regions. Both eigenvalue analysis and numerical simulations agree that f-modes are easily absorbed sufficiently to explain observations, whereas p_n-modes (especially $n \geq 2$) are definitely not absorbed sufficiently by this mechanism. In fact, p-to-slow mode conversion becomes very inefficient with increasing radial order, n.

One obvious limitation of the vertical field models is the magnetic field geometry. For example, the observations of Braun, Duvall, and LaBonte (1988), Braun, LaBonte, and Duvall (1990), and Braun (1995) indicate that p-mode absorption is not isolated to the umbrae of sunspots (where the field is primarily vertical), but instead occurs nearly uniformly across a region slightly larger than the penumbrae (where the field is highly inclined). The oscillations supported by a spreading magnetic field are not well understood. Theoretical progress is held back by the presence of both vertical and radial gradients (see Bogdan, 1999, for the outline of a method of solution).

Recently, Cally (2000) carried out two-dimensional finite difference simulations of non-magnetic p-modes encountering a sunspot model with a spreading magnetic field. Cally found that p-mode absorption is greatly enhanced by field spread, though numerical limitations precluded the investigation of models with sufficient spread to fully explain the observations. There are several possible reasons for enhanced absorption to occur in spreading field, for example: the deformation of the $C_A \approx C_S$ conversion region (broadened and deepened – higher radial order p_n-modes carry much of their energy at greater depths than the f-mode); internal mode mixing (scattering of higher order p_n-modes to more lossy low order modes); or inclination of the magnetic field increases the excitation of the downward-radiating slow-mode.

The purpose of Chapters 3 and 4 is to determine the effect of the magnetic field inclination on the efficiency of MAG wave conversion. This is done by generalising the vertical field eigenvalue analysis of CBZ to a non-vertical magnetic field. In Chapter 3 we restrict ourselves to two-dimensional propagation, and concentrate on fast-to-slow MAG wave conversion. In Chapter 4 we consider propagation in three dimensions, where conversion between all three types of waves (fast and slow MAG waves, and Alfvén waves) is possible.

2.6   Flux tubes

In the absence of gravity, the theory of waves travelling in and on isolated, uniform magnetic flux tubes (referred to as tube modes) is well developed. Several early papers made the

---

[3]In atmospheres of finite depth, the p-modes reduce to a finite set and the jacket modes to an infinite but discrete set.

thin flux tube approximation (e.g., Ryutov and Ryutova, 1976; Roberts and Webb, 1979; Wilson, 1979; Spruit, 1982), some of which included gravitational stratification (e.g., Defouw, 1976; Roberts and Webb, 1978; Spruit, 1981). Flux tubes of arbitrary radius were considered shortly thereafter (e.g., Wentzel, 1979; Wilson, 1981; Edwin and Roberts, 1983). If dissipative processes can be neglected, the tube modes will propagate along the flux tube maintaining a constant amplitude provided the disturbance they induce in the surrounding fluid is laterally evanescent. In this case real frequencies are appropriate. However, Roberts and Webb (1979); Wilson (1981); and Spruit (1982) realised that when the tube mode couples to a laterally propagating wave (in the surrounding fluid), its amplitude will decay as energy is carried away by the external waves. In this case, the tube mode is said to be "leaky" (Cally, 1985, 1986) or "acoustically damped" (Spruit, 1982), and complex frequencies are required. Cally (1985, 1986) carried out an extensive analysis of the leaky and non-leaky modes (allowing for complex frequencies) for tubes of arbitrary width and with magnetic field in the external environment. In the thin flux tube limit only two modes survive: the axisymmetric ($m = 0$) sausage mode with characteristic phase speed (along the tube) $C_T = C_A C_S / \left(C_A^2 + C_S^2 \right)^{1/2}$; and the ($m \neq 0$) kink mode with phase speed $C_K = \left[\left(\rho C_A^2 + \rho_e C_S^2 \right) / \left(\rho + \rho_e \right) \right]^{1/2}$ (e.g., Defouw, 1976; Ryutov and Ryutova, 1976; Roberts and Webb, 1978, 1979; Wilson, 1979; Spruit, 1982; Cally, 1985, 1986; Bogdan, 1989). Here, the subscript "e" refers to quantities external to the tube, whereas unsubscripted quantities are internal. Recently, tube mode theory has been extended to non-uniform flux tubes (in unstratified atmospheres) exhibiting resonant absorption at critical surfaces (e.g., Keppens, 1995, 1996; Stenuit, Keppens, and Goossens, 1998; Stenuit et al., 1999).

Associated with the phenomena of acoustic damping of tube modes is the complementary process of resonance scattering, where the tube modes are excited by waves in the surrounding fluid. For example, the scattering resonances of a thin magnetic flux tube occur when the frequency of the incident acoustic wave coincides with one of the natural tube frequencies (corresponding to the characteristic phase speeds of the thin tube modes C_T or C_K). When the flux tube is driven at these frequencies, fluid motions in and around the tube are greatly enhanced over their typical non-resonant level (e.g., Ryutov and Ryutova, 1976; Bogdan, 1989; Ryutova and Priest, 1993a,b).

2.6.1 Ensembles of diverse flux tubes

The absorption of acoustic oscillations by resonance scattering in horizontally inhomogeneous regions has been investigated by Ryutov and Ryutova (1976) and Ryutova and Priest (1993a,b). In this case, acoustic oscillations are absorbed by an ensemble of widely separated, uniform thin magnetic flux tubes randomly distributed in space and over their parameters (e.g., magnetic field strength, density and radius). During the transient phase, absorption occurs because the frequency of the incident sound wave will nearly always coincide with a (natural) resonant frequency in a fraction of the flux tubes. When this occurs, energy is extracted from the acoustic waves as the enhanced response is built up in the resonantly excited flux tubes. At later times, this energy is re-emitted as secondary acoustic waves in higher layers of the atmosphere. Energy will be lost even in the absence of viscosity, thermal

conduction and ohmic losses. However, in densely packed ensembles such as sunspots, large localised gradients will develop due to the small scale inhomogeneities, and classical dissipation will be enhanced (Ryutova and Persson, 1984; Ryutova, Kaisig, and Tajima, 1991; LaBonte and Ryutova, 1993; Lazzaro, Lontano, and Ryutov, 2000). The major limitation of this mechanism is that thin flux tubes in gravitationally stratified atmospheres do not have global resonant frequencies (e.g., Bogdan et al., 1996; Hasan and Bogdan, 1996; Hasan, 1997; Crouch and Cally, 1999; Tirry, 2000, also see discussion in Cally, 2001b). In fact, Tirry (2000) also showed that resonant frequencies (including multiple scattering resonances exhibited by bundles of closely spaced tubes, see Bogdan and Fox, 1991; Keppens, Bogdan, and Goossens, 1994) are absent in an unstratified cavity when one end of the flux tube is open to wave leakage.

2.6.2 Bundles of identical flux tubes

At late times, the enhanced motions of any resonantly excited flux tubes will saturate at their asymptotic level, the balance between excitation and re-emission results in zero net absorption. The steady-state (late time) scattering of acoustic waves by bundles of identical, randomly distributed, uniform magnetic flux tubes in unstratified atmospheres has been investigated in considerable detail (e.g., Bogdan and Zweibel, 1985; Zweibel and Bogdan, 1986; Bogdan and Zweibel, 1987; Bogdan, 1987a,b; Bogdan and Cattaneo, 1989; Bogdan and Fox, 1991; Bogdan, 1992; Tirry, 2000, but for generalisations to stratified atmospheres see Zweibel and Däppen, 1989 who develop a mean field theory approach, and Rosenthal, 1995 who employs the Born approximation). In these studies, as the individual flux tubes are uniform, they – as well as the bundles they belong to – do not absorb acoustic power (at late times). Keppens, Bogdan, and Goossens (1994), however, applied the theory of multiple scattering (the T-matrix formalism developed by Bogdan and Fox, 1991) to incorporate resonant absorption by bundles of closely spaced, non-uniform tubes (where the resonant layer in each tube is modelled using the method of Sakurai, Goossens, and Hollweg, 1991a). For a fixed amount of magnetic flux, Keppens, Bogdan, and Goossens found that fibril sunspots (e.g., the "spaghetti" model suggested by Parker, 1979) absorb much more acoustic power than their monolithic (non-uniform) counterparts. On the other hand, both (monolithic and fibril) sunspot models scatter comparable amounts of incident acoustic energy. There are several major limitations of this mechanism: it neglects tube modes not found in the thin tube limit (e.g., Cally, 1985, 1986; Stenuit, Keppens, and Goossens, 1998; Stenuit et al., 1999); as mentioned in §2.4, the efficiency of resonant absorption in gravitationally stratified atmospheres is not well understood; and multiple scattering resonances (responsible for the enhanced absorption found by Keppens, Bogdan, and Goossens, 1994 in fibril sunspots) are absent when one end of the flux tube is open (Tirry, 2000, see also Cally, 2001b).

2.6.3 The absorption of p-modes by thin magnetic flux tubes

The observed p-mode line widths (e.g., Libbrecht, 1988; Korzennik, 1990; Jefferies et al., 1991) cannot be accounted for by mechanical and thermal processes alone. Various modelling along these lines includes the excitation and damping of p-modes by turbulent convection (e.g.,

Christensen-Dalsgaard, Gough, and Libbrecht, 1989; Goldreich and Kumar, 1991; Goldreich, Murray, and Kumar, 1994) and the scattering of p-modes by convective eddies (Goldreich and Murray, 1994). As discussed in §1.4, it is now well established that sunspots and plage absorb substantial amounts of energy from p-modes incident upon them (Braun, Duvall, and LaBonte, 1987, 1988; Braun, LaBonte, and Duvall, 1990; Braun et al., 1992a; Bogdan et al., 1993; Braun, 1995; Chen, Chou and the TON Team, 1996). This prompted Jefferies et al. (1991) to suggest that the absorption of high degree p-modes by active regions may provide an additional (unmodelled) component of the p-mode line widths. Recent observations by Komm, Howe, and Hill (2000, as discussed in §1.3) also indicate (though not conclusively) that a component of p-mode damping is magnetic in nature.

Bogdan et al. (1996, hereafter BHCC) investigate the possibility that the interaction of p-modes with isolated, thin magnetic flux tubes may represent another unmodelled process capable of explaining the observed p-mode line widths (e.g., Libbrecht, 1988; Korzennik, 1990; Jefferies et al., 1991). BHCC developed a model for a (non-resonant) thin magnetic flux tube, embedded in a gravitationally stratified atmosphere. They consider the tube to be in thermal equilibrium with its surroundings – a reasonable assumption if the tube is thin enough (see §5.1.3). Consequently, the plasma-β[4] is independent of depth, and the excitation of the tube modes by the p-modes in the surrounding atmosphere may occur over the entire length of the tube. The tube modes then travel down into the solar interior.

Above the photosphere the flux tube begins to flare out to such an extent that the thin flux tube model becomes unrealistic. To overcome this difficulty, BHCC imposed a stress-free boundary condition at the photosphere, which acts to reflect any upward-propagating tube waves completely back down into the tube. The stress-free boundary condition deliberately neglects a possibly important physical process: the loss of energy to the upper solar atmosphere by the excitation of waves in the chromosphere and corona. In Chapter 5, we use simple models of the solar chromosphere and corona to explore the consequences of applying various boundary conditions.

Spruit (1981) determined the two completely uncoupled modes of oscillation for a thin magnetic flux tube: the *kink modes*, which describe transverse, incompressive motions of the tube, and the *sausage modes*, which are longitudinal, compressive motions. At the top of the convection zone the longitudinal, compressive motions of the thin magnetic flux tube (sausage mode) match onto longitudinal, compressive motions in the overlying chromosphere – MAG waves. The transverse, incompressive motions of the thin magnetic flux tube (kink modes) match onto transverse, incompressive motions in the overlying chromosphere – Alfvén waves. With this in mind, plausible boundary conditions at the photosphere can be constructed.

The theoretical results of BHCC fall well short of the observations (Korzennik, 1990), by an order of magnitude or more. In Chapter 5, we determine the contribution to the p-mode line width from both the tube modes (sausage and kink modes) escaping deep into the solar interior, and the MAG and Alfvén waves escaping into the upper solar atmosphere.

---

[4]The plasma-β is defined as the ratio of the gas and magnetic pressure, $\beta = 2\mu_B p/B^2$.

Chapter 3

Mode conversion of solar p-modes in non-vertical magnetic fields: Two-dimensional model

In this chapter we consider the oscillations supported by a gravitationally stratified atmosphere permeated by a uniform, non-vertical magnetic field. We derive the equations governing propagation in arbitrary directions. However, in this chapter, we assume two-dimensional propagation where the Alfvén waves decouple. We calculate the efficiency of fast-to-slow MAG wave conversion in non-vertical field for a complete polytrope.

3.1 The governing equations

The unperturbed model atmosphere consists of an inviscid, compressible, perfectly electrically conducting, ideal gas. The atmosphere is plane-stratified[1] by the constant gravitational acceleration, $-g\hat{e}_z$, and permeated by a straight, uniform, non-vertical magnetic field inclined in the (x, z)-plane,

$$\mathbf{B} = B\left(\sin\theta\,\hat{e}_x + \cos\theta\,\hat{e}_z\right),\qquad(3.1)$$

where θ is the angle between the magnetic field vector and the vertical, $\hat{e}_z$ (see Fig. 3.1). We consider the steady-state[2], linear[3] adiabatic oscillations of this atmosphere.

As the unperturbed atmosphere is in hydrostatic equilibrium, the mass density, ρ, and gas pressure, p, are related by $dp/dz = -\rho g$. Consequently, the coefficients of the governing PDEs (the linearised equations of ideal MHD) only depend on the vertical spatial coordinate,

---

[1] For features with horizontal extent greatly exceeded by the solar radius, such as sunspots and small-scale intense magnetic flux tubes, the curvature of the solar surface may be safely neglected.

[2] In quiet Sun, the solar p-modes have periods of the order five minutes and lifetimes of order hours to days. Therefore, it is reasonable to neglect transients and focus on the steady-state oscillations.

[3] In quiet Sun, the typical surface velocity amplitude associated with an individual p-mode is at most about 10 cm s^{-1} (Christensen-Dalsgaard, 2002), whereas the sound speed in the near surface layers is of order 10 km s^{-1}. Hence, the small amplitude assumption is valid.
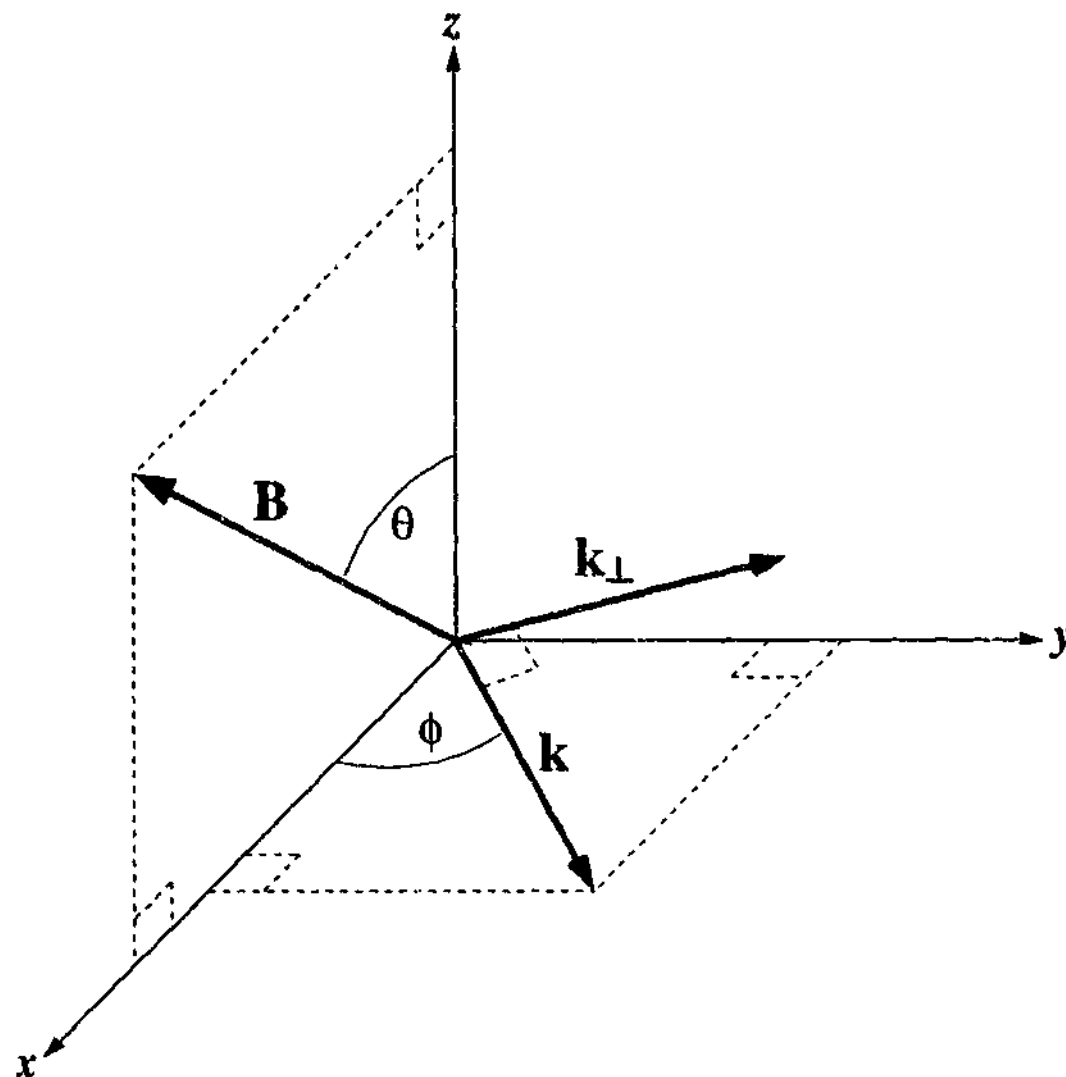
Figure 3.1: The magnetic field vector, **B**, the wave-vector, **k**, the perpendicular wave-vector, $\mathbf{k}_\perp$, and the angles θ and ϕ in three-dimensional Cartesian space.

z. It is, therefore, appropriate to use the method of separation of variables and we assume that all perturbed quantities depend on the horizontal spatial coordinates, x and y, and temporal coordinate, t, according to $\exp\left[i\left(\mathbf{k}\cdot\mathbf{r}-\omega t\right)\right]$, where $\mathbf{k}=k\left(\cos\phi\,\hat{\mathbf{e}}_x+\sin\phi\,\hat{\mathbf{e}}_y\right)$ is the wave-vector, ϕ is the angle between the wave-vector and the x-axis, $\mathbf{r}=x\hat{\mathbf{e}}_x+y\hat{\mathbf{e}}_y$ is the position vector and the angular frequency, ω, is real and non-negative. Figure 3.1 shows the magnetic field vector, **B**, and the wave-vector, **k**, and the angles θ and ϕ in three-dimensional Cartesian space.

The Lagrangian fluid displacement, $\boldsymbol{\xi}=\xi_x\hat{\mathbf{e}}_x+\xi_y\hat{\mathbf{e}}_y+\xi_z\hat{\mathbf{e}}_z=\zeta\hat{\mathbf{k}}+\eta\hat{\mathbf{k}}_\perp+\xi_z\hat{\mathbf{e}}_z$, where $\hat{\mathbf{k}}_\perp=-\sin\phi\,\hat{\mathbf{e}}_x+\cos\phi\,\hat{\mathbf{e}}_y$ (see Fig. 3.1), then satisfies a system of three coupled, second order, ordinary differential equations:

$$C_A^2\left[\cos^2\theta\,\frac{d^2}{dz^2}-\left(\sin^2\phi\,\sin^2\theta+\cos^2\theta\right)k^2\right]\zeta+\left(\omega^2-k^2C_S^2\right)\zeta$$

$$- \sin \theta\, C_A^2 \left[\cos \phi \cos \theta \frac{d^2}{dz^2} - ik \sin^2 \phi \sin \theta \frac{d}{dz} - \cos \phi \cos \theta\, k^2 \right] \xi_z$$

$$+ ik \left[C_S^2 \frac{d}{dz} - g \right] \xi_z = -ik \sin \phi \sin \theta\, C_A^2\, \partial_\parallel \eta , \tag{3.2}$$

$$\left[C_A^2 \partial_\parallel^2 + \omega^2 \right] \eta = - \sin \phi \sin \theta\, C_A^2\, \partial_\parallel \left[\nabla \cdot \xi \right] , \tag{3.3}$$

$$\sin^2 \theta\, C_A^2 \left[\frac{d^2}{dz^2} - \cos^2 \phi\, k^2 \right] \xi_z + \left[C_S^2 \frac{d^2}{dz^2} - \gamma g \frac{d}{dz} + \omega^2 \right] \xi_z$$

$$- \sin \theta\, C_A^2 \left[\cos \phi \cos \theta \frac{d^2}{dz^2} - ik \sin^2 \phi \sin \theta \frac{d}{dz} - \cos \phi \cos \theta\, k^2 \right] \zeta$$

$$+ ik \left[C_S^2 \frac{d}{dz} - (\gamma - 1) g \right] \zeta = - \sin \phi \sin \theta\, C_A^2\, \partial_\parallel \left[\frac{d\eta}{dz} \right] , \tag{3.4}$$

where $\partial_\parallel = \hat{\mathbf{B}} \cdot \nabla = ik \cos \phi \sin \theta + \cos \theta \frac{d}{dz}$ is the directional derivative in the direction parallel to the equilibrium magnetic field, $C_A(z) = B/(\mu_n \rho)^{1/2}$ is the Alfvén speed, and $C_S(z) = (\gamma p/\rho)^{1/2}$ is the adiabatic sound speed. The sixth order system of differential equations (3.2)-(3.4) completely describes the propagation and linear interaction of all types of magnetoacoustic-gravity (MAG) waves – the fast and slow MAG waves and the Alfvén waves (where the distinction is valid). In equations (3.2)-(3.4) the temperature stratification is arbitrary. It can be verified that in the isothermal case, the equations are equivalent to those derived by Leroy and Bel (1979) and Zhugzhda and Dzhalilov (1984a) in terms of the standard Cartesian displacements ξ_x, ξ_y, and ξ_z.

3.1.1 Vertical field

When the equilibrium magnetic field is exactly vertical (i.e., $\theta = 0$), ϕ-dependence vanishes and equations (3.2)-(3.4) reproduce the governing equations first derived by Ferraro and Plumpton (1958). In this case, the MAG waves (fourth order, with fluid displacement $\zeta \hat{\mathbf{k}} + \xi_z \hat{\mathbf{e}}_z$, eqs. [3.2] and [3.4]) and the transverse Alfvén waves (second order, with displacement $\eta \hat{\mathbf{k}}_\perp$, eq. [3.3]) decouple. The vertical field MAG waves equations have received considerable attention from many authors, often in the context of umbral oscillations in sunspots (e.g., Scheuer and Thomas, 1981; Thomas and Scheuer, 1982; Leroy and Schwartz, 1982; Schwartz and Leroy, 1982; Zhugzhda and Dzh 'ilov, 1982; Zhugzhda, 1984; Hasan and Christensen-Dalsgaard, 1992; Spruit and Bogdan, 1992; CB93; CBZ; Banerjee, Hasan, and Christensen-Dalsgaard, 1995; Cally, 1995; Hindman, Zweibel, and Cally, 1996; BC97; Lites et al., 1998; Cally, 2001a). The vertical field Alfvén wave equation has also been studied extensively in various contexts (e.g., Ferraro, 1954; Ferraro and Plumpton, 1958; Hollweg, 1978; Thomas, 1978; Leroy, 1980, 1981; Bel and Leroy, 1981; Leroy and Schwartz, 1982; An et al., 1989).

The vertical field equations have also been studied with non-adiabatic effects included, incorporating either Newton's law of radiative cooling (e.g., Banerjee, Hasan, and Christensen-Dalsgaard, 1997; Birch et al., 2001; Banerjee et al., 2002) or thermal conduction (e.g., Antia

31

and Chitre, 1979; Gore, 1997, 1998). Recently, Settele, Zhugzhda, and Staude (1999) and Settele, Staude, and Zhugzhda (2001) have extended the vertical field equations to include depth dependence of both the turbulent pressure and the adiabatic coefficient.

3.1.2 Horizontal field

When the equilibrium magnetic field is exactly horizontal (i.e., $\theta = 90°$) equations (3.2)–(3.4) reduce to the second order differential equation first derived by Nye and Thomas (1976a), or Nye and Thomas (1974) in the $\phi = 0$ case. In general, this ODE possesses two singularities or critical layers, associated with the Alfvén and cusp resonances, across which wave energy flux is discontinuous (e.g., Cally, 1984). It is worth noting that specific atmospheres may not possess any of these critical layers. For example, atmospheres where both the sound and Alfvén speeds are constant (e.g., Yu, 1965, see also Campbell and Roberts, 1989; Jain and Roberts, 1994b). The critical layers are not present for $\theta \neq 90°$ (see §3.5 for details), however, the horizontal field limit ($\theta \to \pm 90°$) is singular, and for highly inclined fields (e.g., Kamp, 1989, 1990; Zhukov, 1988, 1989a,b, 1990) perturbation methods should be considered.

The horizontal field wave equation has been central to a great number of investigations. For example, modelling canopy field in the chromosphere and corona (Campbell and Roberts, 1989; Evans and Roberts, 1990; Jain and Roberts, 1994a,b,c), including cases where resonant absorption occurs at the critical layers (Zhukov, 1997; Tirry et al., 1998; Pintér and Goossens, 1999; Vanlommel and Goossens, 1999; Vanlommel et al., 2002). The horizontal field wave equation has also been used to model running penumbral waves in sunspots (Nye and Thomas, 1974, 1976b; Cally and Adam, 1983; Small and Roberts, 1984).

3.1.3 Outline – inclined field

With the exception of Leroy and Bel (1979) and Zhugzhda and Dzhalilov (1984a), the sixth order system of equations (3.2)–(3.4) has received little attention. When the oscillations propagate solely in the direction parallel to the (x, z)-plane (i.e., $\phi = 0$, or $k_y = 0$), the Alfvén waves (eq. [3.3]) and the fast and slow MAG waves (eqs. [3.2] and [3.4]) decouple. The less complicated $\phi = 0$ case has been investigated by several authors, for both the MAG waves (e.g., Zhugzhda and Dzhalilov, 1984a,b,c; Schwartz and Bel, 1984a,b; Goossens, Poedts, and Hermans, 1985; Campos and Saldanha, 1991) and the Alfvén waves (e.g., Schwartz, Cally, and Bel, 1984), though mainly for isothermal stratification. The finite difference simulations of Cally (2000), which exhibit enhanced p-mode absorption, are two-dimensional, suggesting that the $\phi = 0$ case is of interest. The remainder of this chapter is devoted to two-dimensional propagation, focusing on the domain $\phi = 0$, $-90° < \theta < 90°$.

Propagation in directions oblique to the (x, z)-plane (i.e., the full sixth order system of equations (3.2)–(3.4) with $\phi \neq 0$) is addressed in Chapter 4. In this case, without loss of generality, the parameter search need only focus on the domain $0 \leq \phi \leq 180°$, $0 \leq \theta < 90°$.

32

3.2 The complete polytrope

The model atmosphere is now specialised to a complete isentropic polytrope, with the surface situated at $z = 0$, and the ideal gas filling the semi-infinite half-space $z < 0$. The mass density, ρ, and gas pressure, p, vary as

$$\rho(z) = \rho_0 \left(-\frac{z}{L}\right)^m , \quad \text{and} \quad p(z) = \frac{\rho_0 g L}{m+1} \left(-\frac{z}{L}\right)^{m+1} , \tag{3.5}$$

where $m = 1/(\gamma - 1)$ is the polytropic index ($\gamma = c_p/c_v$ is the ratio of specific heats)[4].
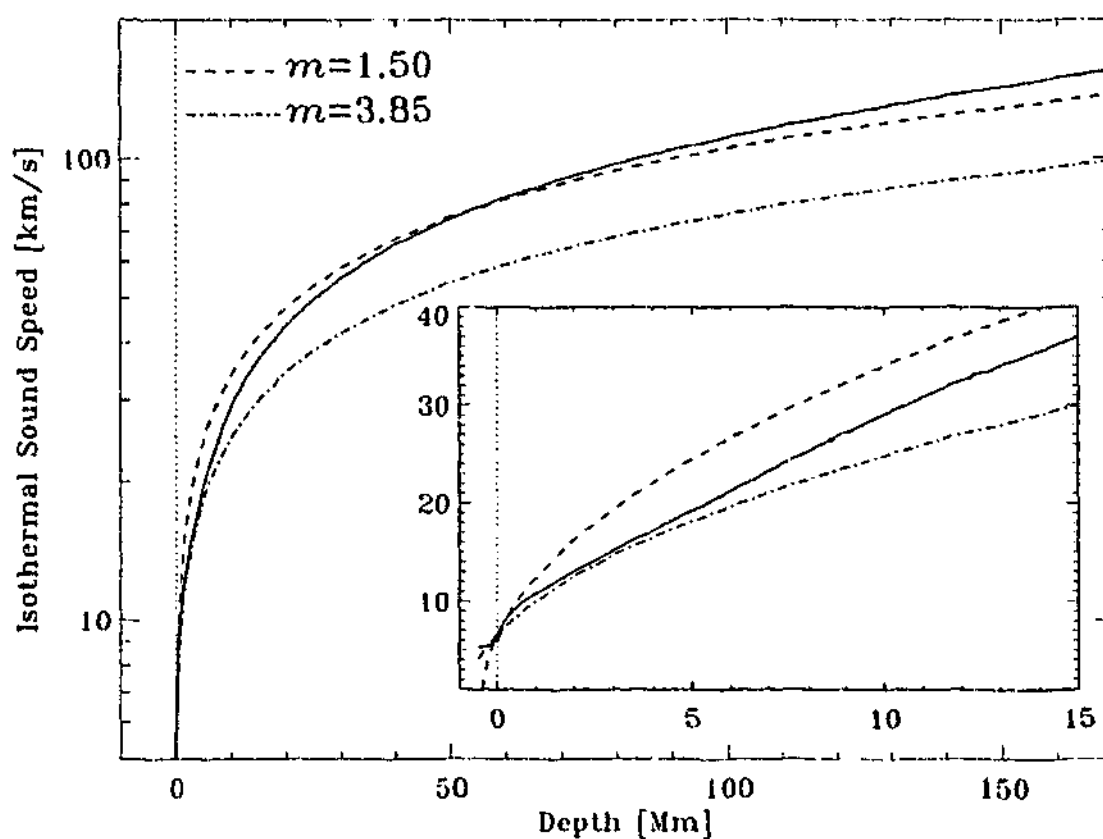

Figure 3.2: Variation of the isothermal sound speed $(p/\rho)^{1/2}$ as a function of depth. The solid curve is obtained from seismic solar model of Christensen-Dalsgaard, Proffitt, and Thompson (1993). The broken curves represent isentropic polytropes constrained to pass through $\rho_0 = 2.78 \times 10^{-4}$ kg m^{-3} and $p_0 = 1.21 \times 10^4$ kg m^{-1}s^{-2} (corresponding to $(p_0/\rho_0)^{1/2} = 6.60$ km s^{-1}) at zero depth. The *inset* provides a detailed view of the surface layers. Reproduced courtesy of BHCC.

The complete polytrope is a very simple approximation to the solar convection zone. To evaluate the merits of the polytropic approximation, we temporarily ignore the magnetic field and take the depth $z = -L$ to coincide with the $\tau_{0.5} = 1$ level of the photospheric reference model provided in Table 11 of Maltby *et al.* (1986). So $\rho_0 = 2.78 \times 10^{-1}$ kg m^{-3},

---

[4]Isentropic polytropes are convectively neutral as the radiative and adiabatic temperature gradients coincide. Consequently, the Brunt-Väisälä frequency vanishes and the atmosphere does not support internal gravity waves (g-modes).

$p_0 = 1.21 \times 10^4$ kg m^{-1}s^{-2} and $g = 2.775 \times 10^2$ m s^{-2} are adopted as the characteristic physical scales at $z = -L$, where $p_0 = \rho_0 gL/(m+1)$, and, therefore L varies as $m+1$. Figure 3.2 (reproduced courtesy of BHCC) shows the variation of the isothermal sound speed $(p/\rho)^{1/2}$ with depth for a solar model computed by Christensen-Dalsgaard, Proffitt, and Thompson (1993)[5], along with the $m = 3/2$ and $m = 3.85$ polytropes. BHCC use these two values of m to bracket the range of solar possibilities. For example, the $m = 3.85$ polytrope provides an acceptable fit to the model in the near surface layers (within the first 5 Mm below the photosphere, see inset). On the other hand, the $m = 3/2$ polytrope provides a more reasonable approximation for the whole of the convection zone.

In the vertical field studies of CB93, CBZ and BC97, attention was restricted exclusively to the $m = 3/2$ polytrope. Hunter (1999) relaxed this restriction. In his doctoral thesis, Hunter considered the oscillations of complete polytropes, permeated by exactly vertical magnetic field, for the cases $m = 3/2, 2, 5/2, 3, 7/2, 4$. Hunter found that the eigenvalues (including the efficiency of mode conversion) are only weakly influenced by changes in the polytropic index, m (Hunter also calculated the eigenvalues for the magnetised solar model of Christensen-Dalsgaard, Proffitt, and Thompson (1993) with a similar outcome). Consequently, in this investigation (as in CB93, CBZ and BC97), we are justified in concentrating solely on the $m = 3/2$ polytrope.

Models with more realistic vertical stratification including chromosphere and corona (such as those employed by CBZ; Cally 1995; Hindman, Zweibel, and Cally 1996; Lites et al. 1998 with vertical magnetic fields) offer a potentially interesting extension to the current problem. However, evaluating the efficiency of p-to-slow mode conversion in non-vertical magnetic fields, with a simple yet reasonable stratification, is the purpose of this exploratory investigation.

Returning to the magnetised complete polytrope, we now define the length scale, L, to be the depth into the complete polytrope where the Alfvén speed, C_A, equals the sound speed, C_S, i.e.,

$$C_A(z) = \sqrt{\frac{gL}{m}} \left(-\frac{L}{z}\right)^{m/2}, \quad \text{and} \quad C_S(z) = \sqrt{\frac{g|z|}{m}}. \tag{3.6}$$

Determination of the solar parameters ρ_0, p_0, g and L is deferred to §3.7.2.

Following the approach of CBZ, without loss of generality, we assume Re $(k) \geq 0$ throughout the remainder of our analysis (i.e., travelling waves propagate in the positive x-direction). We focus on the spatial evolution of the free linear oscillations, hence, we calculate complex wavenumber eigenvalues, k, for specified real angular frequencies, ω, and angle, θ. In this case, it is appropriate to adopt the same nondimensionalisation as CBZ,

$$s = -\frac{z}{L}, \quad \kappa = 2kL \quad \text{and} \quad \nu^2 = \frac{m\omega^2 L}{g}. \tag{3.7}$$

This transformation is singular in the non-magnetic limit ($L \to 0$), but this is of no concern as

---

[5]As the model of Christensen-Dalsgaard, Proffitt, and Thompson (1993) is for quiet Sun, it is unclear how accurately this model represents the interior of a sunspot. Unfortunately, the sunspot umbral core models M, L and E of Maltby et al. (1986) are not tabulated to large depths below the photosphere.

the non-magnetic limit is itself singular (i.e., the second order non-magnetic p-mode equation does not provide a uniform asymptotic approximation to the true solution of the fourth order MAG wave equation in the weak field limit). The nondimensionalised governing equations with $\phi = 0$ are then

$$\cos^2 \theta\, s^{-m} \left[\frac{d^2}{ds^2} - \frac{\kappa^2}{4}\right] \xi_x + \left(\nu^2 - \frac{\kappa^2}{4}s\right) \xi_x$$
$$= \sin\theta \cos\theta\, s^{-m} \left[\frac{d^2}{ds^2} - \frac{\kappa^2}{4}\right] \xi_z + \frac{i\kappa}{2} \left[s\frac{d}{ds} + m\right] \xi_z\,, \tag{3.8}$$

$$\sin^2 \theta\, s^{-m} \left[\frac{d^2}{ds^2} - \frac{\kappa^2}{4}\right] \xi_z + \left[s\frac{d^2}{ds^2} + (m+1)\frac{d}{ds} + \nu^2\right] \xi_z$$
$$= \sin\theta \cos\theta\, s^{-m} \left[\frac{d^2}{ds^2} - \frac{\kappa^2}{4}\right] \xi_x + \frac{i\kappa}{2} \left[s\frac{d}{ds} + 1\right] \xi_x\,, \tag{3.9}$$

where $\xi_x = \zeta$ is the component of the displacement in the x-direction. The decoupled Alfvén wave equation (second order in η) will not be discussed further. As discussed above, from now on we restrict our attention exclusively to the case $m = 3/2$.

3.3 The lower boundary

The lower boundary, $s = \infty$ ($z = -\infty$), is an intrinsically irregular singular point of the governing equations (3.8) and (3.9). Imposing the appropriate boundary conditions requires knowledge of the asymptotic behaviour of the solutions of the governing equations as $s \to \infty$ ($z \to -\infty$). The method of dominant balance (e.g., Bender and Orszag, 1978, Chapter 3) is the standard approach for determining the asymptotic behaviour of solutions of linear ordinary differential equations (ODEs) of arbitrary order in the vicinity of irregular singular points. The method of dominant balance for a system of coupled ODEs is much more complicated. When the background magnetic field is exactly vertical ($\theta = 0$), the governing equations (3.8) and (3.9) can be simplified and the resultant system (CBZ, their eqs. [2.8]–[2.10]) can be readily analysed using the method of dominant balance. The simplification is not valid for the non-vertical field case, subsequently, application of the method of dominant balance alone to the governing equations (3.8) and (3.9) is troublesome.

However, the physical nature of the solutions in the vicinity of the lower boundary (where $C_A \ll C_S$) is well known (e.g., Zhugzhda and Dzhalilov 1982, 1984a,b,c; Zhugzhda 1984; Spruit and Bogdan 1992; CB93; CBZ; BC97; Bogdan 2000; Cally 2001a; Rosenthal et al. 2002; Zhukov 2002). When the sound speed, C_S, and the Alfvén speed, C_A, differ greatly (i.e., $C_A \ll C_S$, as $s \to \infty$) the fast and slow MAG waves (and the Alfvén waves in the $\phi \neq 0$ case) decouple. The reason for this is the large difference between the vertical wavelengths of the fast and slow MAG waves. Hence, in the region where $C_A \ll C_S$ we can address each mode of oscillation separately. In this region, the fast MAG wave is asymptotically an

35

evanescent acoustic wave (compressive and longitudinally polarised), with a vertical wavelength comparable to the local density scale height. The propagation of the fast MAG wave is asymptotically unaffected by the presence of the magnetic field. On the other hand, the slow MAG wave is strongly affected by the presence of the magnetic field. The slow MAG wave is asymptotically a travelling Alfvén wave (incompressive and transversely polarised), with a vertical wavelength very much smaller than the local density scale height.

The physical characteristics of each mode, combined with the method of dominant balance, guide us to consistent asymptotic behaviours for the fast and slow MAG waves. The details are outlined in the next two subsections.

3.3.1 Fast MAG wave asymptotics

Asymptotically, as $s \to \infty$ ($z \to -\infty$) where $C_A \ll C_S$, the fast MAG waves are unaffected by the magnetic field. For the fast MAG wave solution, this characteristic motivates the assumption that, in the governing equations (3.8) and (3.9), the magnetic terms (i.e., terms multiplied by the squared Alfvén speed, $C_A^2 \propto s^{-m}$) are dominated by the non-magnetic terms. This assumption must be checked later. Neglecting the magnetic terms in governing equations (3.8) and (3.9) leaves

$$\left[s \frac{d^2}{ds^2} + m \frac{d}{ds} \right] \xi_x \sim \left(\frac{\kappa^2}{4} s - \nu^2 \right) \xi_x, \quad s \to \infty, \tag{3.10}$$

$$\frac{d\xi_x}{ds} \sim -\frac{i\kappa}{2} \xi_z, \quad s \to \infty. \tag{3.11}$$

Asymptotic relation (3.11) implies that the displacement associated with the fast MAG waves is asymptotically irrotational. Asymptotic relation (3.10) results from eliminating ξ_z from equation (3.9) and the derivative of equation (3.8), then setting the magnetic terms to zero. For the non-magnetic p-modes (see Appendix A for details), the asymptotic relations (3.10) and (3.11) are equalities.

The method of dominant balance applied to relation (3.10) yields the two controlling factors $\xi_x \sim \exp\left(\pm \frac{\kappa}{2} s \right)$. It can be easily verified, by substituting the controlling factors into equations (3.8) and (3.9), that the magnetic terms are dominated (asymptotically) by the non-magnetic terms. Consequently, the initial assumption characterising the fast MAG wave solution, is self-consistent. We impose the boundary condition that evanescent modes be decreasing – retaining the exponentially decaying solution and discarding the exponentially increasing solution. This boundary condition is equivalent to that employed by CB93, CBZ and BC97 for vertical field. Further developing the exponentially decaying asymptotic solution we find

$$\xi_{x_f} \sim s^{(\nu^2/\kappa)-(m/2)} \exp\left[-\frac{\kappa}{2} s \right] U_f(s), \quad s \to \infty, \tag{3.12}$$

$$\xi_{z_f} \sim -i s^{(\nu^2/\kappa)-(m/2)} \exp\left[-\frac{\kappa}{2} s \right] W_f(s), \quad s \to \infty, \tag{3.13}$$

where the coefficients U_f and W_f are both asymptotic to unity as $s \to \infty$, and we have assumed that $\mathrm{Re}(\kappa) \geq 0$. The leading behaviours (3.12) and (3.13) are, in fact, the consistent

asymptotic behaviours for the fast MAG wave solution of the governing equations (3.8) and (3.9) with the magnetic terms included. For complex κ, the asymptotic behaviour of the fast MAG wave is somewhat wave-like. However, it can be verified that the associated wave energy flux vanishes as $s \to \infty$, so our choice of branch $(\operatorname{Re}(k) \geq 0)$ is valid (wave energy flux is discussed in more detail in §4.5).

For $m = 3/2$, in a similar fashion to CB93, the coefficients U_f and W_f may be expanded in asymptotic power series in non-positive half integer powers of s. The details of the series expansions can be found in Appendix C.1. As an indication of their general nature, the first few terms of the series are

$$U_f(s) \sim 1 - \frac{a}{2\kappa}(2a - 1)s^{-1} - \frac{a\kappa^2}{6\nu^2}(\cos\theta + i\sin\theta)^2 s^{-3/2} + \ldots, \qquad (3.14)$$

$$W_f(s) \sim 1 - \frac{a}{2\kappa}(2a - 5)s^{-1} - \frac{a\kappa^2}{6\nu^2}(\cos\theta + i\sin\theta)^2 s^{-3/2} + \ldots, \qquad (3.15)$$

where $a = (3/4) - (\nu^2/\kappa)$. The fast MAG wave is asymptotically a trapped acoustic wave at sufficient depth. The asymptotic leading behaviour of equations (3.12) and (3.13) is exactly that of the trapped non-magnetic p-mode (for details see Appendix A). In fact, the first two non-zero terms of the series U_f (eq. [3.14]) are identical to the non-magnetic p-mode (see eq. [A.4]), and only differ at and above correction terms of order $s^{-3/2}$. Sensitivity to the magnetic field inclination also enters the asymptotic series at terms of order $s^{-3/2}$. Asymptotically the fast MAG wave is unaffected by the magnetic field and, as expected, the field inclination. Hence, the initial assumption for the fast MAG wave solution, that magnetic terms are insignificant relative to the non-magnetic terms, is self-consistent. For $\theta = 0$ the asymptotic leading orders (eqs. [3.12] and [3.13]) and the asymptotic series (eqs. [3.14] and [3.15]) reproduce the vertical field result (CBZ, their eq. [2.12]). It is also worth noting that in the case of exactly horizontal field ($\theta = 90°$) the fast MAG wave asymptotic leading orders (eqs. [3.12] and [3.13]) are well behaved, and yield a valid solution to the second order horizontal field problem.

3.3.2 Slow MAG wave asymptotics

Asymptotically, as $s \to \infty$ where $C_A \ll C_S$, the slow MAG waves are Alfvénic in nature with a vertical wavelength that is very much smaller than the local density scale height. Therefore, in this limit, the propagation of the slow MAG waves is unaffected by the gravitational stratification. For the slow MAG wave solution, this motivates the assumption that the gravitational acceleration vanishes (i.e., $g = 0$) and, therefore, the atmosphere is homogeneous. This assumption must be checked later. In an unstratified atmosphere, we can assume that all perturbed quantities depend on the vertical spatial coordinate, z, according to $\exp(ik_z z)$. Consequently, the governing differential equations (3.2)–(3.4), with $\phi \neq 0$ for the moment, reduce to a set of three linear algebraic equations for the three (unknown) components of the displacement vector, ξ. Nontrivial solutions exist only for specific choices of the frequency, ω, (or phase speed), these are the solutions of the equation

$$\left[\omega^2 - C_A^2 \left(\cos\phi \, \sin\theta \, k + \cos\theta \, k_z\right)^2\right]$$
$$\times \left[\omega^4 - \left(C_A^2 + C_S^2\right)\left(k^2 + k_z^2\right)\omega^2\right.$$
$$\left. +C_A^2 C_S^2 \left(\cos\phi \, \sin\theta \, k + \cos\theta \, k_z\right)^2 \left(k^2 + k_z^2\right)\right] = 0. \tag{3.16}$$

Equation (3.16) is equivalent to the well known dispersion relation for magnetoacoustic and Alfvén waves propagating in a homogeneous magnetofluid (e.g., Ferraro and Plumpton, 1966, pp. 66–89; Priest, 1982, pp. 153–188), except we are using the coordinate system outlined earlier where the z-axis is aligned with the gravitational acceleration (although $g = 0$ in the homogeneous case), the magnetic field vector, $\mathbf{B}$, lies in the (x, z)-plane, and the (lateral) wave-vector, $\mathbf{k}$, lies in the (x, y)-plane (see Fig. 3.1).

The three solutions of equation (3.16) are

$$\omega^2 = \frac{K^2}{2}\left(C_A^2 + C_S^2 \pm \sqrt{C_A^4 + C_S^4 + 2C_A^2 C_S^2 \left(1 - 2\cos^2\psi\right)}\right) \tag{3.17}$$

$$\omega^2 = K^2 C_A^2 \cos^2\psi \tag{3.18}$$

where $K^2 = k^2 + k_z^2$ is the squared magnitude of the total wave-vector, $\mathbf{K} = \mathbf{k} + k_z \hat{\mathbf{e}}_z$, and ψ (defined by $\cos\psi = \left(\cos\phi \, \sin\theta \, k + \cos\theta \, k_z\right)/K$) is the angle between $\mathbf{K}$ and the background magnetic field, $\mathbf{B}$. It is conventional to refer to higher frequency solution of equation (3.17) as the fast magnetoacoustic wave and the lower frequency solution as the slow magnetoacoustic wave. The frequency of solution (3.18) lies between the fast and slow waves and is called the Alfvén wave. In the two-dimensional problem (i.e., $\phi = 0$), the Alfvén waves decouple. However, in the three-dimensional problem (i.e., $\phi \neq 0$, see Chapter 4), the Alfvén waves are required. Therefore, in this subsection, we consider $\phi \neq 0$. We briefly discuss the important properties of the three oscillation modes.

The phase velocity, $\mathbf{v}_p = (\omega/K)\hat{\mathbf{K}}$, for the three oscillation modes is easily derived from equations (3.17) and (3.18). The group velocity for the Alfvén waves is

$$\mathbf{v}_g = \pm C_A \hat{\mathbf{B}}, \tag{3.19}$$

which indicates that energy propagates along the magnetic field lines at the Alfvén speed. It can be shown that the resultant displacement eigenvector for the Alfvén wave solution is

$$\boldsymbol{\xi}_a = -k_y \hat{\mathbf{B}}_\perp + k_\perp \hat{\mathbf{e}}_y \tag{3.20}$$

where $\hat{\mathbf{B}}_\perp = \cos\theta \, \hat{\mathbf{e}}_x - \sin\theta \, \hat{\mathbf{e}}_z$ is the unit vector perpendicular to the background magnetic field, $k_\perp = \mathbf{K} \cdot \hat{\mathbf{B}}_\perp = \cos\phi \, \cos\theta \, k - \sin\theta \, k_z$ is the wavenumber in direction perpendicular to the field, and $k_y = \sin\phi \, k$ is the wavenumber in the y-direction. The displacement eigenvector, $\boldsymbol{\xi}_a$, is perpendicular to both the equilibrium magnetic field, $\mathbf{B}$, and the wave-vector, $\mathbf{K}$, therefore, Alfvén waves are transversely polarised. Alfvén waves are incompressive (i.e., $\nabla \cdot \boldsymbol{\xi}_a = 0$),

and propagate without perturbing the gas or magnetic pressure. The restoring force driving the Alfvén waves is tension along the magnetic field lines.

For the fast and slow magnetoacoustic waves the group velocity is

$$\mathbf{v}_g = \frac{\partial \omega}{\partial k_\parallel}\hat{\mathbf{B}} + \frac{\partial \omega}{\partial k_\perp}\hat{\mathbf{B}}_\perp + \frac{\partial \omega}{\partial k_y}\hat{\mathbf{e}}_y \,,$$

where $k_\parallel = \mathbf{K} \cdot \hat{\mathbf{B}} = \cos\phi \sin\theta\, k + \cos\theta\, k_z$ is the wavenumber in direction parallel to the magnetic field, and

$$\frac{\partial \omega}{\partial k_\perp} = \frac{k_\perp \, (\omega/K)^3}{K \left[2\,(\omega/K)^2 - (C_A^2 + C_S^2) \right]} \,,$$

$$\frac{\partial \omega}{\partial k_y} = \frac{k_y \, (\omega/K)^3}{K \left[2\,(\omega/K)^2 - (C_A^2 + C_S^2) \right]} \,,$$

and

$$\frac{\partial \omega}{\partial k_\parallel} = \frac{k_\parallel \left[(\omega/K)^4 - C_A^2 C_S^2 \right]}{\omega \left[2\,(\omega/K)^2 - (C_A^2 + C_S^2) \right]} \,.$$

The displacement eigenvector for the magnetoacoustic waves is

$$\boldsymbol{\xi}_\pm = \frac{C_S^2 \cos(2\psi) - C_A^2 \pm \sqrt{C_A^4 + C_S^4 - 2C_A^2 C_S^2 \cos(2\psi)}}{2C_S^2 k_\parallel}\hat{\mathbf{B}} + \frac{k_\perp}{K^2}\hat{\mathbf{B}}_\perp + \frac{k_y}{K^2}\hat{\mathbf{e}}_y \,,$$

where the displacement vectors $\boldsymbol{\xi}_+$, $\boldsymbol{\xi}_-$ and $\boldsymbol{\xi}_a$ are mutually orthogonal.

For the stratified atmosphere we are interested in the asymptotic behaviour of the slow magnetoacoustic wave in the region where $C_A \ll C_S$. In this limit, we can expand the slow wave solution (eq. [3.17]) as a Taylor series

$$\omega^2 = K^2 C_A^2 \left(\cos^2\psi + O\left(\frac{C_A^2}{C_S^2}\right) \right) . \tag{3.21}$$

Consequently, in the $C_A \ll C_S$ regime, the group velocity for the slow magnetoacoustic waves is

$$\mathbf{v}_g = \pm C_A \hat{\mathbf{B}} \,, \tag{3.22}$$

illustrating that energy propagates along the magnetic field lines at the Alfvén speed. For slow waves, it can be shown that,

$$\mathbf{K} \cdot \boldsymbol{\xi}_- = O\left(\frac{C_A^2}{C_S^2}\right) , \tag{3.23}$$

39

indicating that slow waves are transversely polarised and incompressive in the limit $C_A \ll C_S$. Also in this limit, it can be shown that the displacement eigenvector, ξ_-, is perpendicular to the equilibrium magnetic field. The dominant term of equation (3.21) and the corresponding group velocity (eq. [3.22]) are identical to the Alfvén wave solution (eq. [3.18] and [3.19], respectively), therefore, in magnetofluids with $C_A \ll C_S$ the slow magnetoacoustic waves are said to be Alfvénic in nature (incompressive oscillations, driven by tension along the magnetic field lines, with displacement eigenvector transverse to the background magnetic field). It is known from §3.3.1 that the vertical wavelength of the fast MAG waves is of similar order to the local density scale height. Therefore, the fast magnetoacoustic wave solution (eq. [3.17]) is not applicable to the stratified atmosphere. The dispersion relation for the slow magnetoacoustic waves in a homogeneous magnetofluid (eq. [3.21]) is valid for a gravitationally stratified atmosphere, where $C_A \ll C_S$, if the vertical wavelength of the oscillations is very much smaller than the local density scale height.

We assume the vertical wavelength of the slow waves is very much smaller than the local density scale height (this must be justified later). With $\phi = 0$, the asymptotic relation for the slow magnetoacoustic-gravity (MAG) waves in a gravitationally stratified atmosphere, consistent with the dispersion relation (3.21), is

$$ C_A^2 \left[\cos\theta \frac{d}{dz} + ik\sin\theta \right]^2 \xi_x(z) \sim -\omega^2 \xi_x(z) , \quad z \to -\infty , $$

which is derived by inverting the $\exp(ik_z z)$ transformation. For convenience, we have chosen ξ_x to be the dependent variable, but any component of the displacement vector would suffice. Adopting the Alfvén speed (eq. [3.6]) and nondimensionalisation (eqs. [3.7]), the asymptotic relation for the slow MAG waves in the complete polytrope is then

$$ \left[\cos^2\theta\, s^{-m} \frac{d^2}{ds^2} - i\kappa\sin\theta\,\cos\theta\, s^{-m} \frac{d}{ds} \right] \xi_x(s) $$
$$ \sim \left(\frac{\kappa^2}{4} \sin^2\theta\, s^{-m} - \nu^2 \right) \xi_x(s) , \quad s \to \infty . \tag{3.24} $$

Applying the method of dominant balance to equation (3.24) yields the two controlling factors $\xi_x \sim \exp\left(\pm 2i\nu \sec\theta\, s^{(m+2)/2} / (m+2) \right)$. The appropriate boundary condition in this case requires that wave-like disturbances be outgoing – retaining the outgoing solution and discarding the incoming solution. This boundary condition is equivalent to that employed by CB93, CBZ and BC97 for vertical field. Further developing the outgoing wave asymptotic solution for equation (3.24) we find

$$ \xi_x \sim s^{-m/4} \exp\left[\tan\theta \frac{i\kappa}{2} s + \sec\theta \frac{2i\nu}{m+2} s^{(m/2)+1} \right] , \quad s \to \infty . \tag{3.25} $$

Unsurprisingly, it can be shown that the exponential part of solution (3.25) is identical to that for a disturbance advecting downward along the magnetic field lines at the Alfvén speed. Asymptotically the vertical wavelength of the slow MAG waves, corresponding to solution (3.25), is

40

$$\lambda \propto \xi_x \left(\frac{d\xi_x}{ds} \right)^{-1} \sim \frac{\cos\theta}{\nu} s^{-m/2}, \quad s \to \infty, \tag{3.26}$$

and the local density scale-height is

$$H = -\rho \left(\frac{d\rho}{dz} \right)^{-1} = \frac{sL}{m}. \tag{3.27}$$

Consequently, the initial assumption that the atmosphere is homogeneous with respect to the slow MAG waves (i.e., the vertical wavelength is very much smaller than the local density scale height) is self-consistent at sufficient depth. This strategy is used only to calculate the leading order terms. For incompressive oscillations,

$$\frac{d\xi_z}{ds} \sim \frac{i\kappa}{2} \xi_x, \quad s \to \infty,$$

hence, for the leading order above (eq. [3.25]), the slow MAG waves require

$$\xi_z \sim \cos\theta \frac{\kappa}{2\nu} s^{-m/2} \xi_x, \quad s \to \infty. \tag{3.28}$$

Applying the leading behaviours for ξ_x and ξ_z (eqs. [3.25] and [3.28], respectively) to the governing equations (3.8) and (3.9), we further develop the asymptotic behaviour for the downward-travelling slow MAG wave:

$$\xi_{x_s} \sim s^{-3/8} \exp\left[\tan\theta \frac{i\kappa}{2} s + \sec\theta \frac{4}{7} i\nu s^{7/4} \right] U_s(s), \quad s \to \infty, \tag{3.29}$$

$$\xi_{z_s} \sim \cos\theta \frac{\kappa}{2\nu} s^{-9/8} \exp\left[\tan\theta \frac{i\kappa}{2} s + \sec\theta \frac{4}{7} i\nu s^{7/4} \right] W_s(s), \quad s \to \infty, \tag{3.30}$$

where the coefficients U_s and W_s are both asymptotic to unity as $s \to \infty$, and we have specialised to the $m = 3/2$ polytrope. For the slow MAG waves the group velocity, and hence the direction of energy propagation, is directed along the magnetic field lines. It may be confirmed that asymptotically, as $s \to \infty$, the wave-energy flux along the field lines is constant (see §4.5 for details). Due to fast-to-slow mode conversion in the region where $C_A \approx C_S$, oscillations (asymptotically composed of fast and slow MAG waves) decay as they propagate in the positive x-direction (Re $(k) \geq 0$). Therefore, for $\theta > 0$ ($\theta < 0$), slow MAG waves travelling along deeper field lines are excited by less (more) energetic waves in the conversion region. Hence, for complex κ, the asymptotic behaviour of the slow MAG wave is exponentially decaying (growing) with increasing depth. For complex κ and $\theta = 0$, the asymptotic behaviour of the slow MAG wave is purely oscillatory.

For $m = 3/2$, in a similar fashion to CB93, the coefficients U_s and W_s may be expanded in asymptotic power series in non-positive quarter integer powers of s. The details of the series expansions can be found in Appendix C.2. As an indication of their general nature, the first few terms of the series are:

$$U_s(s) \sim 1 - \frac{2}{3} i\nu \sin\theta \, \tan\theta \, s^{-3/4} + \dots \, ,$$

$$W_s(s) \sim 1 - \frac{\tan\theta}{6\nu} \left(3\kappa\cos\theta + 4i\nu^2 \sin\theta \right) s^{-3/4} + \dots \, .$$

The asymptotic behaviour of the slow MAG wave (eqs. [3.29] and [3.30]) is dramatically affected by the presence of the non-vertical magnetic field. Both the leading orders (eqs. [3.29] and [3.30]) and the series U_s and W_s are highly sensitive to the field inclination (the second term being absent when the field is vertical). The vertical field slow MAG waves (see CBZ, their eq. [2.11]) can be reproduced by setting $\theta = 0$. As expected the asymptotic behaviour of the slow MAG wave (eqs. [3.29] and [3.30]) breaks down in the horizontal field, singular limit ($\theta \to \pm 90°$).

3.4   The top boundary

At the surface of the complete polytrope, $s = 0$ ($z = 0$), the density, gas pressure and sound speed vanish whereas the Alfvén speed diverges (i.e., $C_A \gg C_S$). There, the two boundary conditions are that both components of the displacement vector, $\boldsymbol{\xi}$, should have a finite magnitude (i.e., the Lagrangian pressure perturbation must vanish at the surface of the atmosphere), and that the magnetic field perturbations match smoothly onto a vacuum potential magnetic field (see Appendix B) that vanishes as $s \to -\infty$ ($z \to \infty$), i.e.,

$$\frac{d\xi_\perp}{ds} = \frac{\kappa}{2}\xi_\perp \quad \text{at} \quad s = 0\,, \tag{3.31}$$

where $\xi_\perp = \cos\theta\,\xi_x - \sin\theta\,\xi_z$ is the component of the displacement in the direction perpendicular to the equilibrium magnetic field. For complex κ, the solutions of equation (3.31) are somewhat wave-like. However, it can be verified that the associated wave energy flux vanishes as $s \to -\infty$, so our choice of branch ($\text{Re}(k) \geq 0$) is valid.

These boundary conditions, the natural choice for the complete polytrope, ignore the possibility of energy escape through the top of the sunspot atmosphere. In their vertical field study CBZ (see also Cally, 1995; Hindman, Zweibel, and Cally, 1996; Lites *et al.*, 1998) relax these boundary conditions. CBZ truncate the polytropic stratification at a finite density (corresponding to optical depth unity), and append an overlying atmosphere consisting of the umbral core model M of Maltby *et al.* (1986) with an isothermal "corona". For frequencies below the acoustic cutoff frequency in the chromosphere (frequency ≈ 4 mHz, $\nu \approx 1.1$), the fast and slow MAG waves are evanescent in the overlying atmosphere. In this case, CBZ found the eigenvalues were almost identical to those of the complete polytrope. On the other hand, for frequencies beyond the acoustic cutoff frequency in the temperature minimum (frequency ≈ 6 mHz, $\nu \approx 1.6$), the eigenvalues differ greatly, with the upward- and downward-escaping slow MAG waves removing comparable levels of wave energy. At these higher frequencies the complete polytrope is no longer a reasonable approximation for the full

atmosphere[6]. However, in light of the exploratory nature of this investigation, the complete polytrope should suffice to indicate the basic features we would expect of a more realistic model atmosphere.

The point $s = 0$ is an irregular singular point of the governing equations (3.8) and (3.9). However, for $m = 3/2$, in terms of the independent variable $\sigma = s^{1/2}$, the governing equations are

$$\cos^2 \theta \left[\frac{d^2}{d\sigma^2} - \frac{1}{\sigma} \frac{d}{d\sigma} - \kappa^2 \sigma^2 \right] \xi_x + \sigma^5 \left(4\nu^2 - \kappa^2 \sigma^2 \right) \xi_x$$
$$= \sin \theta \cos \theta \left[\frac{d^2}{d\sigma^2} - \frac{1}{\sigma} \frac{d}{d\sigma} - \kappa^2 \sigma^2 \right] \xi_z + i\kappa \sigma^5 \left[\sigma \frac{d}{d\sigma} + 3 \right] \xi_z , \qquad (3.32)$$

and

$$\sin^2 \theta \left[\frac{d^2}{d\sigma^2} - \frac{1}{\sigma} \frac{d}{d\sigma} - \kappa^2 \sigma^2 \right] \xi_z + \sigma^5 \left[\frac{d^2}{d\sigma^2} + \frac{4}{\sigma} \frac{d}{d\sigma} + 4\nu^2 \right] \xi_z$$
$$= \sin \theta \cos \theta \left[\frac{d^2}{d\sigma^2} - \frac{1}{\sigma} \frac{d}{d\sigma} - \kappa^2 \sigma^2 \right] \xi_x + i\kappa \sigma^5 \left[\sigma \frac{d}{d\sigma} + 2 \right] \xi_x , \qquad (3.33)$$

and the point $\sigma = 0$ is a regular singular point. Substituting the Frobenius series expansions

$$\xi_x (\sigma) = \sum_{n=0}^{\infty} u_n \sigma^{n+r} , \quad \text{and} \quad \xi_z (\sigma) = \sum_{n=0}^{\infty} w_n \sigma^{n+r} , \qquad (3.34)$$

into equations (3.32) and (3.33) yields four linearly independent solutions. Two solutions have $r = 0$, one solution has $r = 2$ and one solution has $r = -3$. Despite these differing by an integer and containing a double root it may be verified that no logarithmic term is introduced. In the expansions (3.34), r is the same for both ξ_x and ξ_z, therefore, linearly independent solutions can have the same r but the terms in the series will differ.

The $r = -3$ solution is unphysical (as $\delta p \neq 0$ at $\sigma = 0$) and is discarded. Labelling the remaining three finite, linearly independent solutions a, c, and d, the general solution may be written $\xi_x = A\xi_{x_a} + C\xi_{x_c} + D\xi_{x_d}$, and similarly for ξ_z. At this stage, the coefficients A, C and D are arbitrary. Developing the series (see Appendix C.3 for details) and imposing the remaining boundary condition (3.31), it may be shown that

$$D = \frac{1}{10} \left(5\kappa + 2 \tan \theta \left(i\kappa - 2\nu^2 \tan \theta \right) \right) A$$
$$+ \frac{1}{10} \tan \theta \left(3i\kappa \tan \theta - 4\nu^2 - 5\kappa \right) C .$$

The physically acceptable solution is then

$$\begin{pmatrix} \xi_x \\ \xi_z \end{pmatrix} = A \begin{pmatrix} \xi_{x_A} \\ \xi_{z_A} \end{pmatrix} + C \begin{pmatrix} \xi_{x_C} \\ \xi_{z_C} \end{pmatrix} \qquad (3.35)$$

where, reverting to the variable s, the leading terms of each series are:

$$\xi_{x_A} = 1 + \frac{1}{10} \left(5\kappa + 2i\kappa \tan\theta - 4\nu^2 \tan^2\theta \right) s + \dots ,$$

$$\xi_{z_A} = \frac{1}{5} \left(i\kappa - 2\nu^2 \tan\theta \right) s + \dots ; \qquad (3.36)$$

and

$$\xi_{x_C} = \frac{1}{10} \tan\theta \left(3i\kappa \tan\theta - 4\nu^2 - 5\kappa \right) s + \dots ,$$

$$\xi_{z_C} = 1 + \frac{1}{10} \left(3i\kappa \tan\theta - 4\nu^2 \right) s + \dots ; \qquad (3.37)$$

and A and C are the remaining arbitrary constants. The first non-integer powers to appear in these expansions are $s^{7/2}$ in ξ_{x_A} and ξ_{x_C}, and $s^{9/2}$ in ξ_{z_A} and ξ_{z_C}. The vertical field series can be reproduced by setting $\theta = 0$, in this case the first term in the ξ_x expansion in equation (3.37) is $3i\kappa s^{7/2}/35$ (for details see CB93, their eqs. [3.2] and [3.3]). The series expansions (3.36) and (3.37) break down in the horizontal field, singular limit ($\theta \to \pm 90°$), hence for highly inclined fields the solutions will become unreliable. We discuss the convergence properties of the series expansions (3.36) and (3.37) in the next section, §3.5.

3.5 Single fourth order equation

The pair of second order differential equations (3.8) and (3.9) can be written as a single fourth order differential equation,

$$\xi_\perp'''' + p_3(s)\,\xi_\perp''' + p_2(s)\,\xi_\perp'' + p_1(s)\,\xi_\perp' + p_0(s)\,\xi_\perp = 0 , \qquad (3.38)$$

where the coefficients of the derivatives are

$$p_3(s) = \frac{1-m}{s} - \frac{\kappa^2}{s\kappa^2 - 4\nu^2 \sin^2\theta + 2im\kappa \sin\theta \cos\theta} - i\kappa \tan\theta ,$$

$$\begin{aligned} p_2(s) = &\Big\{ 8i\sin\theta \cos^3\theta (1+m)\kappa\nu^2 + 8i\cos\theta \sin\theta \left(ms^{1+m} + 2\sin^2\theta\right)\kappa\nu^2 \\ &+ 2\cos^2\theta \left(2s^{2+m}\kappa^2\nu^2 - \sin^2\theta \left(2(m-2)m\kappa^2 + s^2\kappa^4 - 6s\kappa^2\nu^2 + 8\nu^4\right)\right) \\ &+ \cos^4\theta\,\kappa^2 \left(4m + s\left(4\nu^2 - s\kappa^2\right)\right) + \sin^2\theta \left(s\kappa^2 - 4\nu^2\right)\Big(4s^{1+m}\nu^2 + \sin^2\theta \\ &\times \left(4\nu^2 - s\kappa^2\right)\Big)\Big\} \big/ \left(4\cos^2\theta\,s\left(s\kappa^2 - 4\sin^2\theta\,\nu^2 + 2im\kappa \sin\theta \cos\theta\right)\right) , \end{aligned}$$

$$p_1(s) = \Bigg\{ 4\nu^2 s^m \left(\kappa \left(2im\left(1+m\right)\sin\theta\cos\theta + ms\kappa\right) - 4\nu^2\left(1+m\right)\sin^2\theta\right) \right.$$

$$+ \cos\theta\,\kappa^2 \Big(\kappa(2i\cos^2\theta\,(m-1)\,m\sin\theta + \cos\theta\,ms\,(1-2\sin^2\theta)\,\kappa$$

$$\left. + i\kappa^2\sin\theta\,s^2) - 4\sin^2\theta\,(\cos\theta\,(m-1) + is\sin\theta\,\kappa)\,\nu^2 \Big) \right\}$$

$$\Big/ \left(4\cos^2\theta\,s\,\left(s\kappa^2 - 4\nu^2\sin^2\theta + 2im\kappa\sin\theta\cos\theta\right)\right) ,$$

and

$$p_0(s) = \Bigg\{ \kappa^2 \Bigg(\left(s\kappa^2 - 4\nu^2\right)^2\sin^4\theta - 16i\kappa\nu^2\sin^3\theta\cos\theta - 4\kappa^2\cos^4\theta\,(m + s\nu^2)$$

$$-2i\kappa\sin\theta\cos^3\theta\,\left(ms\kappa^2 + 4\nu^2\left(1+m\right)\right) + \cos^2\theta\sin^2\theta\left(4m\kappa^2\,(m-2)\right.$$

$$\left. + \left(s\kappa^2 - 4\nu^2\right)^2 \right) \Bigg) - 4s^m\nu^2\Big(\kappa^2\left(s^2\kappa^2 + 2m\sin\theta\,(2\sin\theta + i\kappa\cos\theta\,s)\right)$$

$$-4\kappa\left(2i\left(1+m\right)\sin\theta\cos\theta + \kappa s\left(1+\sin^2\theta\right)\right)\nu^2 + 16\nu^4\sin^2\theta\Big) \Bigg\}$$

$$\Big/ \left(16\cos^2\theta\,s\,\left(s\kappa^2 - 4\nu^2\sin^2\theta + 2im\kappa\sin\theta\cos\theta\right)\right) .$$

The analysis of a single ordinary differential equation is somewhat simpler than that for a coupled system. For example, the asymptotic behaviours of the solutions of equation (3.38), as $s \to \infty$, can be derived in the usual way by the method of dominant balance (Bender and Orszag, 1978, Chapter 3). It can be confirmed that these are identical to fast and slow MAG wave solutions derived in §3.3. Asymptotic solutions are not unique (e.g., Bender and Orszag, 1978). Using equation (3.38) we have also pursued the possibility of an improved asymptotic solution for the slow MAG waves (e.g., BC97, their eq. [4.20]), especially in highly inclined fields, but without success.

In addition to $s = 0$ and $s = \infty$, equation (3.38) has a singular point at

$$s = s_c = \frac{4\nu^2}{\kappa^2}\sin^2\theta - \frac{2im}{\kappa}\sin\theta\cos\theta,$$

which is only present if the field is non-vertical ($\theta \neq 0$), and in general, is not on the real s-axis. This singular point may be a critical layer – where the oscillation frequency coincides with a natural frequency of the medium and across which the wave energy flux is discontinuous. The possibility of critical layers in non-vertical magnetic fields has been a point of controversy in the past (e.g., Adam, 1977; Schwartz and Bel, 1984b; Zhugzhda and Dzhalilov, 1984a; Kamp, 1989). Goossens, Poedts, and Hermans (1985) consider the special case of a gravitationally stratified atmosphere permeated by a straight, uniform, non-vertical magnetic field, and conclude that no critical layers (continuous spectra) are present in the two-dimensional case. We must determine the nature of the solutions about $s = s_c$ in order to establish whether the singularity is a critical layer.

The point $s = s_c$ is an irregular singular point of the equation (3.38). However, for $m = 3/2$, in terms of the independent variable σ, the point $\sigma_c = s_c^{1/2}$ is a regular singular point of equation (3.38). Substituting the Frobenius series expansion

$$\xi_\perp(\sigma) = \sum_{n=0}^{\infty} a_n (\sigma - \sigma_c)^{n+r} \,,$$

into equation (3.38) yields the indicial equation,

$$r(r-1)(r-2)(r-4) = 0 \,,$$

which has four distinct roots. These differ by an integer, therefore, one of the solutions may contain a logarithmic term. Further developing each solution, the leading terms of each series are:

$$\xi_{\perp,4}(\sigma) = (\sigma - \sigma_c)^4 + C_4 (\sigma - \sigma_c)^5 + \ldots$$

$$\xi_{\perp,2}(\sigma) = (\sigma - \sigma_c)^2 + C_2 (\sigma - \sigma_c)^3 + \ldots$$

$$\xi_{\perp,1}(\sigma) = (\sigma - \sigma_c) + C_1 (\sigma - \sigma_c)^3 + \ldots$$

$$\xi_{\perp,0}(\sigma) = 1 + C_0 (\sigma - \sigma_c)^3 + \ldots$$

where $\xi_{\perp,r}$ is the series corresponding to the root r, $a_0 = 1$ has been assumed in each case and the coefficients C_r are constants (depending on ν, θ and κ, not shown). The four Frobenius series solutions (about $\sigma = \sigma_c$) are linearly independent and distinct, and none contain a logarithmic term. All four series solutions (about $\sigma = \sigma_c$) are analytic at σ_c, as all the roots of the indicial equation are positive and there is no logarithmic term. Therefore, despite being a singular point of the ODE, the solutions are not singular at σ_c. The implications of this are twofold. Firstly, the energy flux is continuous across $\sigma = \sigma_c$, hence, there is no critical layer (in line with the analysis of Goossens, Poedts, and Hermans, 1985). Secondly, the Frobenius series (3.36) and (3.37) about $\sigma = 0$ ($s = 0$) have infinite radius of convergence[7]. We only use the series (3.36) and (3.37) to start the numerical integrations in the neighbourhood of $s = 0$. In some cases, the series solutions (with full details in Appendix C.3) are applied much deeper. If the numerically evaluated series solution is sufficiently accurate then it can be applied directly at the matching point ($s = s_m$). This avoids integrating from $s = 0$ to $s = s_m$.

---

[7]The radius of convergence is at least the distance to the nearest singular point of the ODE, otherwise, it is either infinite or the distance to another singular point. The radius of convergence will coincide with a singularity of the solution itself.

3.6 Bidirectional shooting method

The complex fourth order boundary value problem, consisting of the fourth order system of differential equations (3.8) and (3.9) and the four boundary conditions, is solved using a bidirectional shooting method. For specified dimensionless frequency, ν, and inclination, θ, the eigenfunction is the linear combination of the four solutions that satisfy the boundary conditions. The associated eigenvalue is the value of the dimensionless wavenumber, κ, for which the linear combination exists. Hence, for given ν, θ and an initial guess for κ, the two Frobenius series solutions (eqs. [3.36] and [3.37]) are independently integrated from $s \approx 0$ to some matching point s_m. Similarly, the fast and slow MAG wave solutions (eqs. [3.12] and [3.13], and eqs. [3.29] and [3.30], respectively) are integrated from some depth, at which the asymptotic solutions are sufficiently accurate, to s_m. The displacements, ξ_x and ξ_z, and their vertical derivatives, ξ_x' and ξ_z', must be continuous at s_m. In general, we must iteratively adjust κ, and re-integrate the solutions, until the resultant linear combination satisfies the continuity requirement.

In the upper regions of the complete polytrope we express the full (physically acceptable) solution as a linear combination of the two Frobenius series solutions (see eq. [3.35]). On the other hand, in the lower regions of the complete polytrope the full solution is a linear combination of the fast and slow MAG wave solutions, i.e.,

$$\begin{pmatrix} \xi_x \\ \xi_z \end{pmatrix} = \begin{cases} \beta_A \begin{pmatrix} \xi_{x_A} \\ \xi_{z_A} \end{pmatrix} + \beta_C \begin{pmatrix} \xi_{x_C} \\ \xi_{z_C} \end{pmatrix}, & \text{if } s < s_m, \\ \beta_s \begin{pmatrix} \xi_{x_s} \\ \xi_{z_s} \end{pmatrix} + \beta_f \begin{pmatrix} \xi_{x_f} \\ \xi_{z_f} \end{pmatrix}, & \text{if } s > s_m. \end{cases} \tag{3.39}$$

Then the matching condition, that ξ_x, ξ_z, ξ_x' and ξ_z' are all continuous at s_m, can be expressed in matrix form as

$$\begin{pmatrix} -\xi_{x_A} & -\xi_{x_C} & \xi_{x_s} & \xi_{x_f} \\ -\xi_{z_A} & -\xi_{z_C} & \xi_{z_s} & \xi_{z_f} \\ -\xi_{x_A}' & -\xi_{x_C}' & \xi_{x_s}' & \xi_{x_f}' \\ -\xi_{z_A}' & -\xi_{z_C}' & \xi_{z_s}' & \xi_{z_f}' \end{pmatrix} \begin{pmatrix} \beta_A \\ \beta_C \\ \beta_s \\ \beta_f \end{pmatrix} = 0, \tag{3.40}$$

where all of the displacements and their derivatives in equation (3.40) are evaluated at $s = s_m$.

The boundary conditions are homogeneous, therefore, we can scale the full solution (3.39) arbitrarily. For simplicity we set $\beta_A = 1$. Equation (3.40) is now over-specified, being four equations in three unknowns. Solutions exist only if the determinant of the 4×4 matrix in equation (3.40) (i.e., the Wronskian of the four solutions) vanishes. Hence, one way to proceed is use a root finder to search for eigenvalues such that the Wronskian vanishes. In practise, we adopt a slightly different but equivalent strategy.

Given ν, θ and an initial guess for κ, we calculate the four solutions at $s = s_m$, then solve the first three rows of equation (3.40) for the β's:

$$\begin{pmatrix} -\xi_{x_C} & \xi_{x_s} & \xi_{x_f} \\ -\xi_{z_C} & \xi_{z_s} & \xi_{z_f} \\ -\xi_{x_C}' & \xi_{x_s}' & \xi_{x_f}' \end{pmatrix} \begin{pmatrix} \beta_C \\ \beta_s \\ \beta_f \end{pmatrix} = \begin{pmatrix} \xi_{x_A} \\ \xi_{z_A} \\ \xi_{x_A}' \end{pmatrix}.$$

47

With these determined, the remaining equation,

$$F(\kappa) = -\xi'_{z_A} - \beta_C \xi'_{z_C} + \beta_s \xi'_{z_s} + \beta_f \xi'_{z_f}$$

must be zero if κ is an eigenvalue, but in general is not. Hence, κ must be iteratively adjusted until $F(\kappa) = 0$ is satisfied to an adequate tolerance. For this purpose we employ Müller's method to iterate to convergence. We use an adaptive Runge-Kutta numerical ODE solver (e.g., Press *et al.*, 1992, Chapter 16) to perform the integrations of the solutions from the boundaries to the matching point.

3.7 Results and discussion

As explained in §3.6 we calculate complex dimensionless wavenumber eigenvalues, κ, for specified real dimensionless frequency, ν, and field inclination, θ. In the vertical field studies (e.g., CBZ) eigencurves or "ridges" were built up in (ν, κ)-space (sequences of eigenvalues, κ, as a function of dimensionless frequency, ν). For non-vertical magnetic fields we have the extra parameter θ, the inclination of the field. Therefore, we build up eigensurfaces of κ over the (ν, θ)-plane. For the sake of brevity and for direct comparison with the vertical field results, we also take slices through the (ν, θ)-plane, holding θ constant and varying ν to build up eigencurves in a similar fashion to CBZ. Conversely, we also take slices holding ν constant and varying θ. Our numerical results suggest that the eigenvalue, κ, depends on the inclination, θ, but not on the sign of θ (i.e., κ is the same for θ and $-\theta$ at a given frequency, ν, whereas the eigenfunctions differ). We have not been able to prove this is generally the case, but do not have a counterexample. Assuming the hypothesis is true, the parameter space search, therefore, only needs to focus on the region $\nu \geq 0$, $0 \leq \theta < 90°$, $\mathrm{Re}(\kappa) \geq 0$ and $\mathrm{Im}(\kappa) \geq 0$.

3.7.1 Eigenvalue topology

Figure 3.3 shows the variation of the real and imaginary parts of κ as a function of dimensionless frequency, ν, when the equilibrium magnetic field is exactly vertical ($\theta = 0$) for the first nine ($n = 0, \ldots, 8$) modes – here $n = 0$ represents the f-mode. This is a reproduction of the results of CBZ (their Figure 1). In the non-magnetic limit ($L \to 0$, i.e., $\nu \to 0$, $\kappa \to 0$ see eq. [3.7]), the eigenvalues of the magnetised complete polytrope can be approximated by the eigenvalues of the unmagnetised complete polytrope. In the unmagnetised ($m = 3/2$) complete polytrope the p-modes satisfy the dispersion relation $\nu^2 = (n + 3/4)\kappa$, where $n = 0, 1, 2, \ldots$ (e.g., Lamb, 1910, see also eq. [A.7]). The resultant eigenvalues are plotted in Figure 3.3 as light dashed lines. It is clear from Figure 3.3(a) that, in the low frequency regime, the magnetic and non-magnetic ridges (eigencurves) are virtually indistinguishable. Our results indicate this is also true when the equilibrium magnetic field is non-vertical. With this in mind, in the graphs presented here, ridges are labelled $n = 0, 1, 2, \ldots$ such that n is the radial order of the non-magnetic p_n-mode whose ridge matches the ridge of the magnetic mode in the low frequency (non-magnetic) regime. It should be noted that n cannot be regarded as the number of nodes in the displacement eigenfunction as in the non-magnetic

case. This is because, in general, the eigenfunctions of the magnetic atmosphere are complex and have no nodes. The ridges presented here are generated by stepping from low frequencies to high frequencies. To initiate the stepping procedure we start in the non-magnetic (low frequency) regime, where the eigenvalues of non-magnetic p-modes can be used as an initial guess.
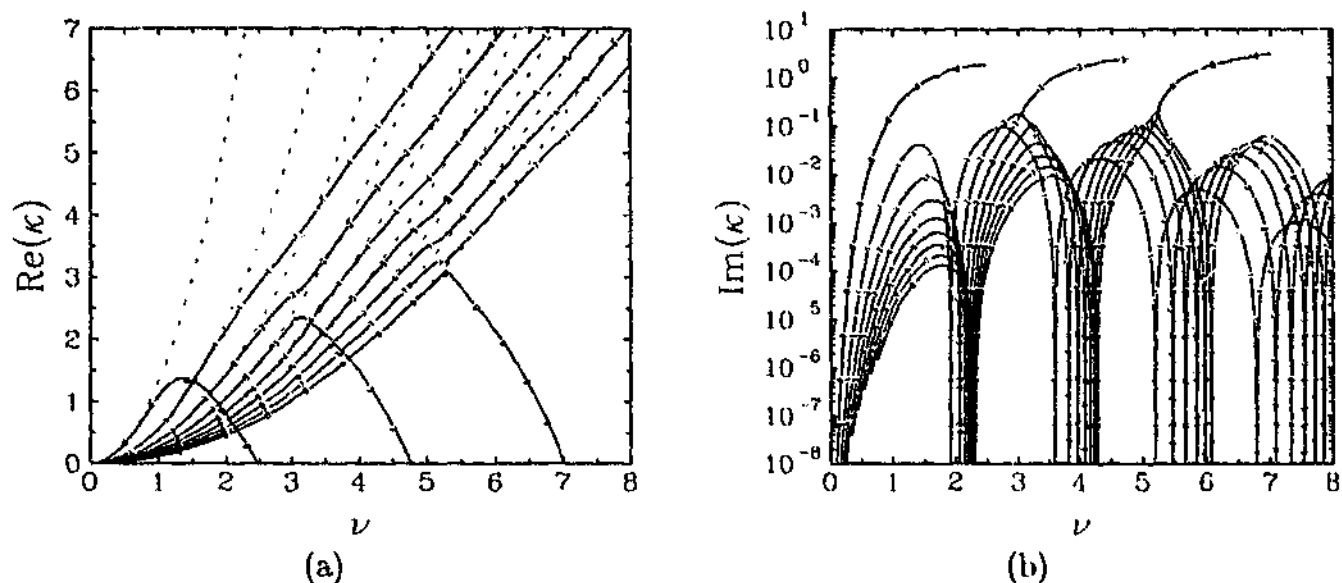

Figure 3.3: (a) Real part of eigenvalue κ as a function of dimensionless frequency ν for the $n = 0, \ldots, 8$ modes (from *top to bottom*, near the origin). At low frequencies these approach the eigencurves of the non-magnetic p-modes, $\kappa = \nu^2 / \left(n + \frac{3}{4} \right)$ (*light dashed lines*). (b) Imaginary part of κ as a function of ν, corresponding to the real part shown on the left. For both of these graphs the equilibrium magnetic field is exactly vertical ($\theta = 0$).

We reiterate the important features of Figure 3.3 (see CBZ for more complete discussion). In general, especially for $\nu \lesssim 1$, for a given frequency along a ridge both the real and imaginary parts of the eigenvalue are largest for the $n = 0$ mode and decrease as n increases. As explained above, at low frequencies ($\nu \ll 1$) the real part of the eigenvalues (Fig. 3.3(a)) are essentially indistinguishable from their non-magnetic counterparts. At higher frequencies the magnetic field has a greater impact; there the ridges diverge from their non-magnetic counterparts. The real part of the eigenvalue still increases monotonically with ν (except for the $n = 0$, 3, and 8 modes) but with a greater horizontal phase speed ($\propto \nu / \mathrm{Re}\,(\kappa)$). For the $n = 0$, 3, and 8 modes the real parts of the eigenvalues do not increase monotonically with ν but turn over and terminate at $\mathrm{Re}\,(\kappa) = 0$. At the frequencies where $\mathrm{Re}\,(\kappa) = 0$ the waves are no longer travelling in the x-direction, but purely decaying, forming a horizontally evanescent mode. Also at these frequencies $\mathrm{Im}\,(\kappa)$ and, hence, the horizontal spatial decay rate of the oscillation is at a maximum. For all modes at low frequencies, $\mathrm{Im}\,(\kappa)$ increases rapidly with increasing frequency. At moderate frequencies ($\nu \approx 1.0 - 1.5$), with the exception of the $n = 0$ mode, $\mathrm{Im}\,(\kappa)$ reaches a local maximum and turns over – this occurs at least once for each mode in the ν-domain presented in Figure 3.3. The sharp troughs, where $\mathrm{Im}\,(\kappa) = 0$ (and $\beta_s = 0$), are frequencies where the π-mode is a trapped normal mode. At these frequencies the slow MAG wave is completely decoupled – no energy escapes down the field lines and the

49

oscillation propagates through the vertically magnetised atmosphere undamped. Away from the sharp troughs there is a non-trivial amount of horizontal spatial decay (i.e., $\text{Im}(\kappa) \neq 0$) as a result of energy being carried down the field lines by the downward-escaping slow MAG waves. For this reason the π-modes are generally referred to as pseudo-modes. For frequencies of observational interest ($\nu \lesssim 2$, depending on the choice of solar parameter $\cdot$ – see §3.7.2) Figure 3.3(b) shows that fast-to-slow MAG wave conversion in vertical field becomes increasingly inefficient with increasing n (radial order). Numerical simulations of p-to-slow mode conversion (e.g., Cally and Bogdan, 1997; Cally, 2000; Rosenthal and Julien, 2000) confirm that this is the case for vertical field monoliths in general.
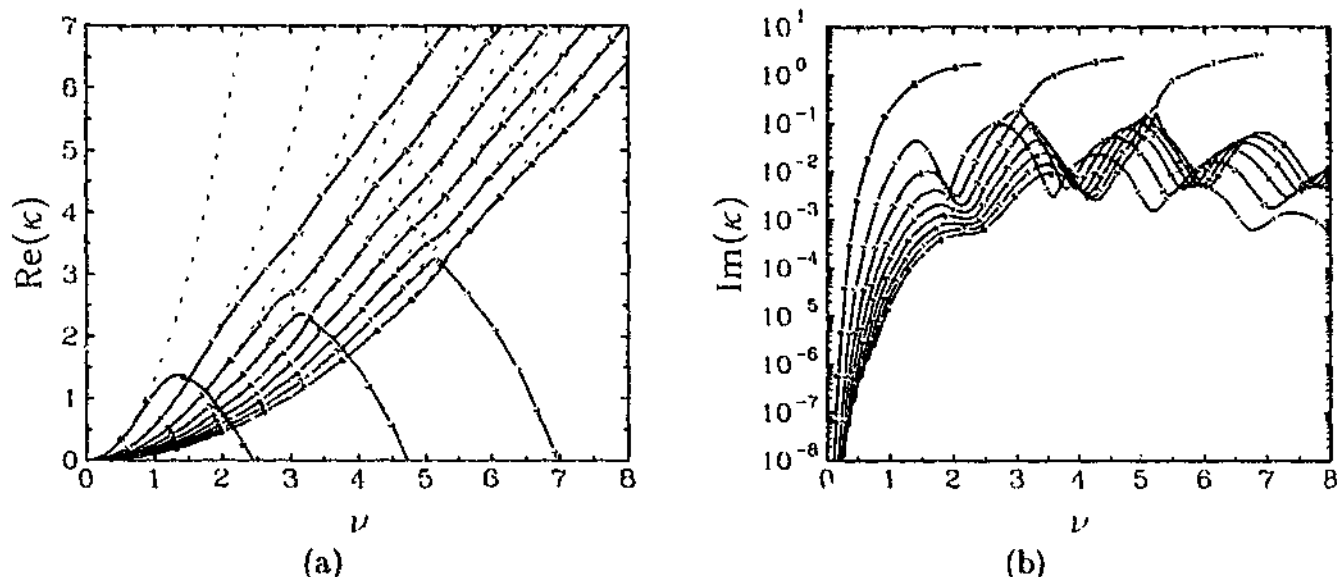
Figure 3.4: Same as Figure 3.3, except $\theta = 5°$.

Figure 3.4 shows the variation of the real and imaginary parts of κ as a function of dimensionless frequency, ν, when $\theta = 5°$ for the first nine ($n = 0, \ldots, 8$) modes. In comparison to the vertical field case (Fig. 3.3), Figure 3.4 shows that at small inclinations there are some important structural changes to the ridges. The real parts of the eigenvalues (Fig. 3.4(a)) are essentially unchanged except that the $n = 7$ mode turns over instead of the $n = 8$ mode (which turns over when $\theta = 0$). In contrast, the imaginary part of the eigenvalues (Fig. 3.4(b)) change rather significantly. In particular, when $\theta \neq 0$ the trapped modes vanish – the sharp troughs (where $\text{Im}(\kappa) = 0$) are not present in non-vertical fields even for very small inclinations. The troughs are still apparent in non-vertical field but only pinch off to $\text{Im}(\kappa) = 0$ in the limit of exactly vertical field (verified by numerical experiment but not pictured). The oscillations in non-vertical magnetic field can no longer arrange themselves to decouple from the escaping slow MAG waves. In vertical field CB93, CBZ and BC97 employ a numbering system for labelling the trapped normal modes according to the number of nodes in their displacement eigenfunction. The disappearance of the trapped modes implies the numbering system is inappropriate in non-vertical magnetic fields. At frequencies away from the trapped modes of the vertical field case, the magnitude of $\text{Im}(\kappa)$ is essentially unaffected by a small inclination in the equilibrium magnetic field. Hence, the efficiency of p-to-slow mode conversion in slightly non-vertical field is basically unchanged in comparison to vertical

50

field. At the frequencies of the vertical field trapped modes, mode conversion is significantly enhanced, however, the enhancement is inconsequential as these frequencies are too sparse.
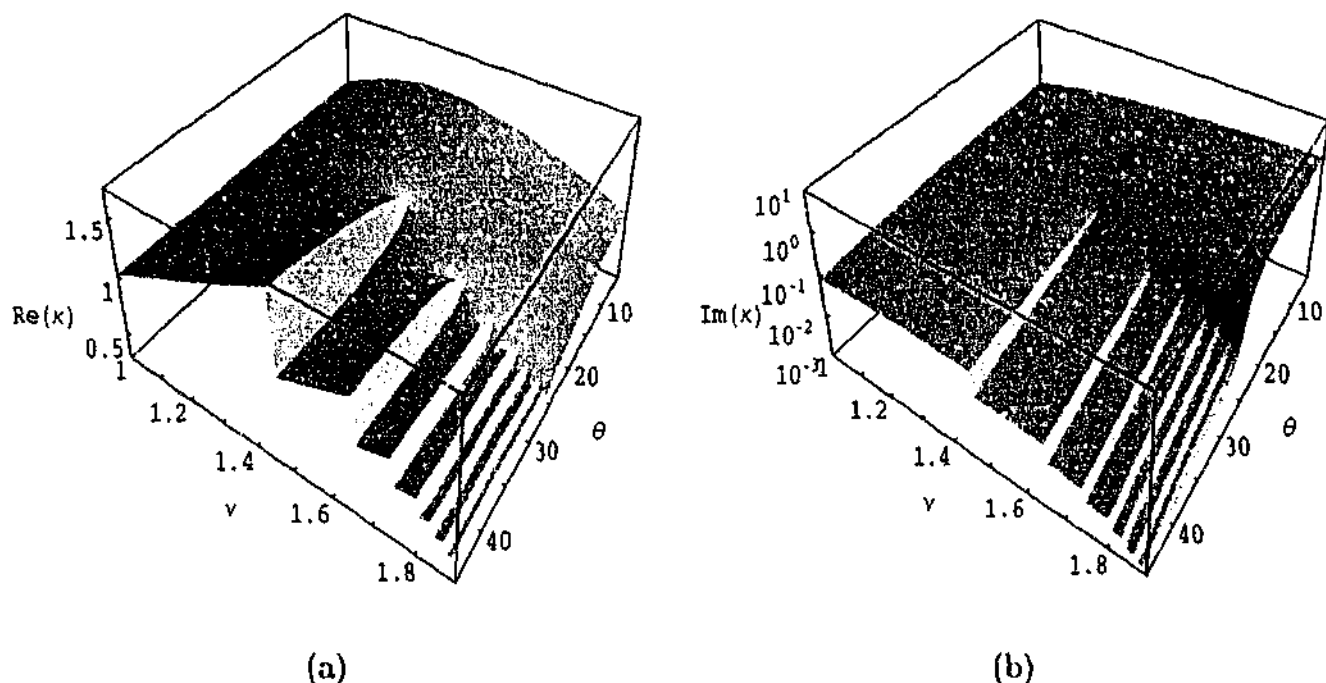

(a)   (b)

Figure 3.5: (a) Real part of the eigenvalue, κ, as a function of field inclination, θ (in degrees), and dimensionless frequency, ν, for the $n = 0$ mode. (b) Imaginary part of κ as a function of θ and ν, corresponding to the real part shown on the left. The domain for both plots is $1 \leq \nu \leq 1.89$, $5° \leq \theta \leq 45°$. The shading of the eigensurfaces is used to highlight contrast only and does not indicate the height of the eigenvalue.

Figure 3.5 shows the variation of the real and imaginary parts of κ as a function of both inclination, θ, and dimensionless frequency, ν, for the $n = 0$ mode. Each point on the eigensurface has been generated starting with the $n = 0$ vertical field mode (e.g., Fig. 3.3) then stepping from $\theta = 0$ to $\theta = 45°$ whilst holding the frequency constant. To clarify, the $n = 0$ ridge of Figure 3.4 could be derived from Figure 3.5 by slicing along $\theta = 5°$. It should be noted that the shading of the eigensurfaces is used to highlight contrast only and does not indicate the height of the eigenvalue. Figure 3.5 shows that for small to moderate inclinations ($5° \lesssim \theta \lesssim 20°$) the eigenvalue is essentially unaffected by the inclination of the magnetic field (both $\mathrm{Re}(\kappa)$ and $\mathrm{Im}(\kappa)$ are essentially constant in the θ-direction). In fact, $\mathrm{Im}(\kappa)$ (Fig. 3.5(b)) decreases slightly as θ increases. At larger inclinations ($\theta \gtrsim 25°$) and lower frequencies ($\nu \lesssim 1.4$), $\mathrm{Re}(\kappa)$ (Fig. 3.5(a)) increases slightly with increasing θ, whereas $\mathrm{Im}(\kappa)$ decreases. The most striking feature of Figure 3.5 occurs in the region $\nu \gtrsim 1.4$ and $\theta \gtrsim 25°$. There the eigensurface undergoes a significant topological transition with a sequence of discontinuities or "cuts" appearing (in decreasing increments of ν). It turns out that these cuts match onto cuts on the surfaces of the higher order modes.

Figure 3.6 shows the variation of the real and imaginary parts of κ as a function of both inclination, θ, and dimensionless frequency, ν, for the $n = 1$ mode. Figure 3.6 is the same as Figure 3.5, except the eigenvalues of the $n = 1$ mode are plotted and the point of view has shifted. The domain in these plots has been truncated at $\theta = 5°$ in order to avoid the
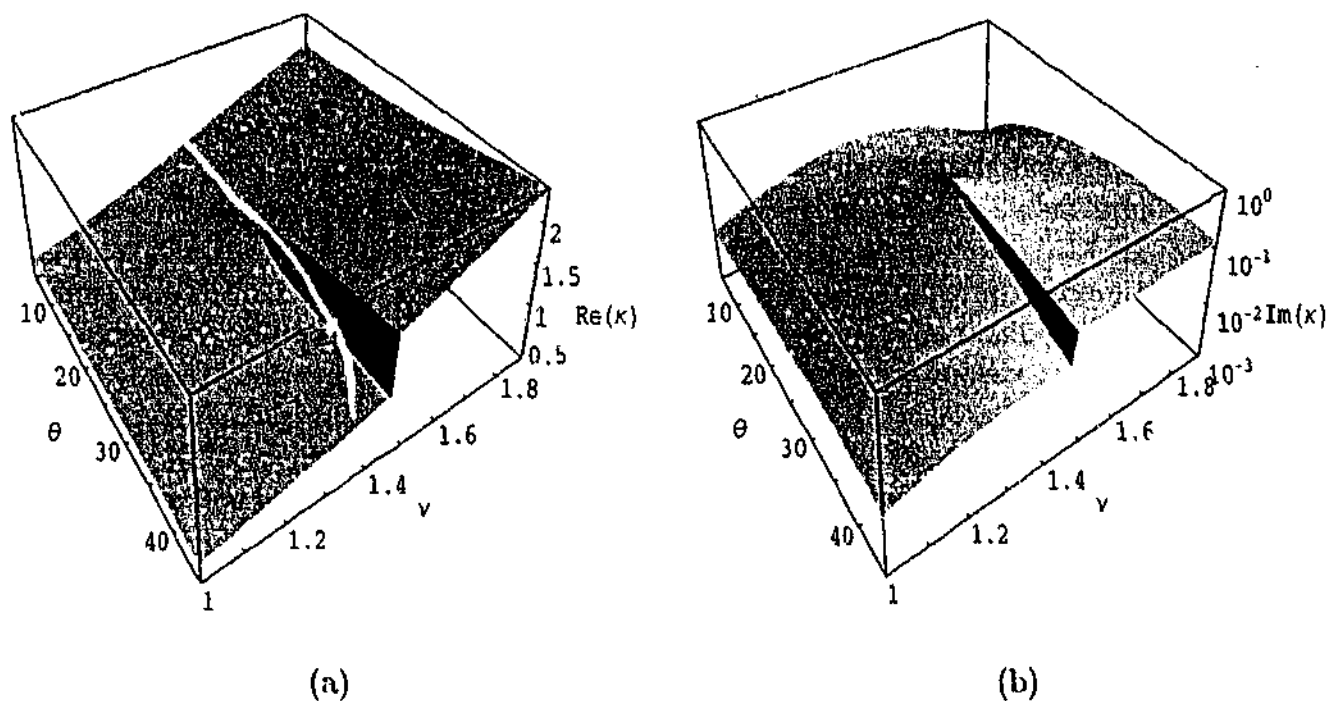
51

Figure 3.6: Same as Figure 3.5 but for $n = 1$ and the point of view has been shifted.

sharp troughs of the vertical field trapped modes ($n \geq 1$). Close inspection of Figure 3.5 and Figure 3.6 reveals that the cut with smallest frequency ($\nu \approx 1.46$) on the $n = 0$ surface (Fig. 3.5) matches onto the single cut on the $n = 1$ surface (Fig. 3.6). There are no further cuts in the $n = 1$ surface outside the pictured domain. It turns out that subsequent cuts in the $n = 0$ surface (Fig. 3.5) match onto cuts in the surfaces in each of the subsequent overtones (not pictured). At higher frequencies ($\nu \gtrsim 1.85$) the cuts in the $n = 0$ surface are not fully resolved in Figure 3.5, but numerical experiments confirm their presence up to at least $n = 8$. This unexpected result reveals that, over the (ν, θ)-plane, the eigenvalues of all the overtones lie on the same surface. The surface displays a bizarre topology (something like a sequence of connected spirals perhaps reminiscent of multivalued functions above the complex plane) which we explore somewhat further shortly. The vertices of the cuts occur at the same location for both the real and imaginary parts of the eigenvalue. Hence, at the vertex of each cut, the eigenvalue exactly coincides with the eigenvalue of another overtone (i.e., a "crossing"). This suggests that labelling of modes is somewhat ambiguous. Certainly, given an atmosphere with field inclination, θ, we can calculate eigenvalues and label modes in the traditional sense (outlined above). However, tracking the changes to a particular mode as θ varies is not strictly possible. The location of the vertices does not coincide with a singularity in any of the coefficients of the governing equations (3.8)-(3.9), as would be the case when a branch cut connects Riemann sheets. The location of the vertices does, however, depend on the boundary conditions (and perhaps other factors such as m, not confirmed). For example, we have run cases (results not displayed) where the polytrope is truncated at some depth and a rigid lid boundary condition is imposed. In this case, the location of the vertices (and the cuts themselves) is highly sensitive to the depth at which the rigid lid is

52

placed.

We now address the important features of Figure 3.6. Figure 3.6(a) shows that for small to moderate inclinations ($5° \lesssim \theta \lesssim 25°$) $\mathrm{Re}(\kappa)$ is essentially unaffected by the inclination of the magnetic field. For larger inclinations and frequencies less than that of the cut, $\mathrm{Re}(\kappa)$ is also essentially unaffected by the inclination, whereas for frequencies beyond the cut, $\mathrm{Re}(\kappa)$ increases slightly with increasing θ ($\mathrm{Re}(\kappa)$ is "bumped up" on the higher frequency side of the cut). The inclination of the field has a more significant affect on $\mathrm{Im}(\kappa)$ (Fig. 3.6(b)). For inclinations less than that of the vertex, $\mathrm{Im}(\kappa)$ increases significantly (more than an order of magnitude) with increasing θ. The imaginary part has a local maximum at $\nu \approx 1.46$ and $\theta \approx 25°$ coinciding with the vertex of the cut. Then for larger inclinations (including those not pictured), $\mathrm{Im}(\kappa)$ decreases monotonically (and rapidly) with increasing θ. This behaviour is indicative of the higher order modes in the domain: $1 \leq \nu \leq 1.89$, $5° \leq \theta \leq 45°$. In particular, mode conversion becomes increasingly efficient for moderate inclinations, reaches a maximum, then becomes increasingly inefficient for larger inclinations. For inclinations approaching horizontal, mode conversion is effectively negligible for all overtones at all frequencies.
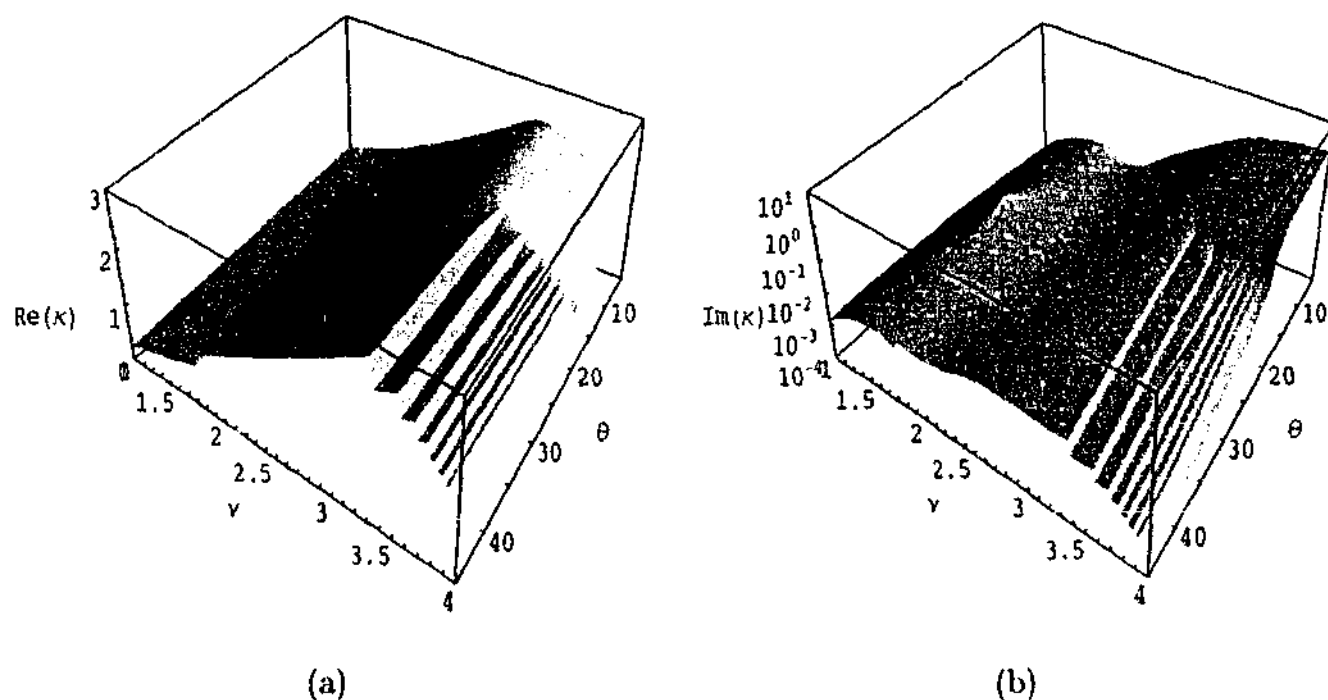

(a)   (b)

Figure 3.7: Same as Figure 3.5 but for $n = 3$ and the domain is $1 \leq \nu \leq 4$, $5° \leq \theta \leq 45°$.

Figure 3.7 shows the variation of the real and imaginary parts of κ as a function of both inclination, θ, and dimensionless frequency, ν, for the $n = 3$ mode. The ν-domain in Figure 3.7 is $1 \leq \nu \leq 4$ (larger than Figs. 3.5 and 3.6). For the lower frequency region of Figure 3.7 the eigensurface shows similar characteristics to $n = 1$ (Fig. 3.6): the surface has a single cut in this region (at $\nu \approx 1.75$) that matches onto the third cut on the $n = 0$ surface (Fig. 3.5). On the higher frequency side of the cut $\mathrm{Re}(\kappa)$ is bumped up, and at the vertex of the cut $\mathrm{Im}(\kappa)$ attains a local maximum. For the higher frequency region of Figure 3.7, where the real part has turned over in the ν-direction (at lower inclinations), the eigensurface

53

shows similar characteristics to $n = 0$, in particular, the sequence of cuts. The vertices of the cuts are situated at $\theta \approx 20°$ (slightly less than those in Fig. 3.5). In a similar fashion to Figure 3.5 these match onto cuts in the eigensurfaces of the higher order modes. The sequence of cuts is a characteristic of the vertical field horizontally evanescent modes when generalised to non-vertical field. When the field is vertical Figure 3.3 shows that the $n = 0, 3,$ and 8 modes are horizontally evanescent modes. It has been confirmed that the eigensurface corresponding to $n = 8$ in Figure 3.3 (not pictured) shows analogous behaviour (evident, for example, as the swapping of the horizontally evanescent mode from $n = 8$ in Fig. 3.3 to $n = 7$ in Fig. 3.4). Since the $n = 3$ sequence is connected to the $n = 0$ sequence via the cut at $\nu \approx 1.75$, and similarly to the $n = 8$ sequence, we are inspired to visualise the shape of the overall eigensurface as a "sequence of connected spirals".

(a)   (b)
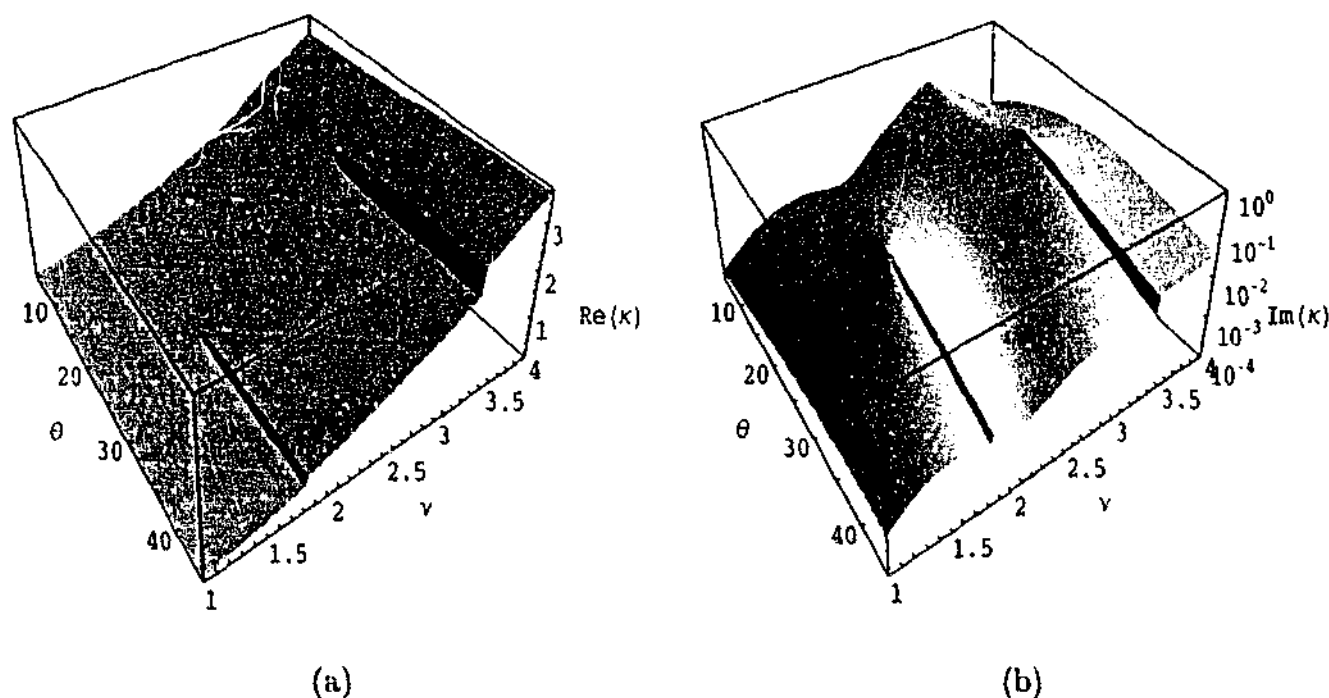
Figure 3.8: Same as Figure 3.7 but for $n = 4$ and the point of view has been shifted.

Figure 3.8 shows the variation of the real and imaginary parts of κ as a function of both inclination, θ, and dimensionless frequency, ν, for the $n = 4$ mode. The eigensurface in Figure 3.8 has two cuts. The lower frequency cut (at $\nu \approx 1.82$) matches onto the fourth cut on the $n = 0$ horizontally evanescent mode (Fig. 3.5). The higher frequency cut (at $\nu \approx 3.4$) matches onto the second cut (the first in the high ν group) on the $n = 3$ horizontally evanescent mode (Fig. 3.7). In the neighbourhood of each cut, Figure 3.8 shows similar characteristics to the $n = 1$ surface (Fig. 3.6): on the higher frequency side of the cut $Re(\kappa)$ is bumped up, and at the vertex of each cut $Im(\kappa)$ attains a local maximum. Figure 3.8 is indicative of higher order modes ($n = 5, 6,$ and 7). All the cuts on the individual eigensurfaces (Figures 3.5–3.8 and those not shown) match onto corresponding cuts on one of the other available eigensurfaces. In the region $\nu \geq 0$, $0 \leq \theta < 90°$, $Re(\kappa) \geq 0$, and $Im(\kappa) \geq 0$, it is therefore apparent that the overall eigensurface is completely filled, and no eigenvalues have

been missed.

Our results quantify the efficiency of fast-to-slow MAG wave conversion in non-vertical field. The efficiency of p-to-slow mode conversion is a much more complicated process to quantify, involving matching oscillations across the interface between the non-magnetic and magnetic regions (e.g., Bogdan and Cally, 1995; Barnes and Cally, 2000). In vertical field studies, eigenvalue analyses (e.g., CB93, CBZ and BC97) agree well with numerical simulation (e.g., Cally and Bogdan, 1997; Rosenthal and Julien, 2000). For this reason we loosely refer to fast-to-slow MAG wave conversion as p-to-slow mode conversion. However, when the field is non-vertical our results show that labelling of modes in the magnetised atmosphere may be more subtle (e.g., Figures 3.5–3.8). The extent to which these results apply to more complicated field geometries, such as spreading field sunspots (e.g., Bogdan, 1999; Cally, 2000), is limited. If these results are valid then matching oscillations across non-vertical sunspot boundaries could be an even more complicated task than anticipated.
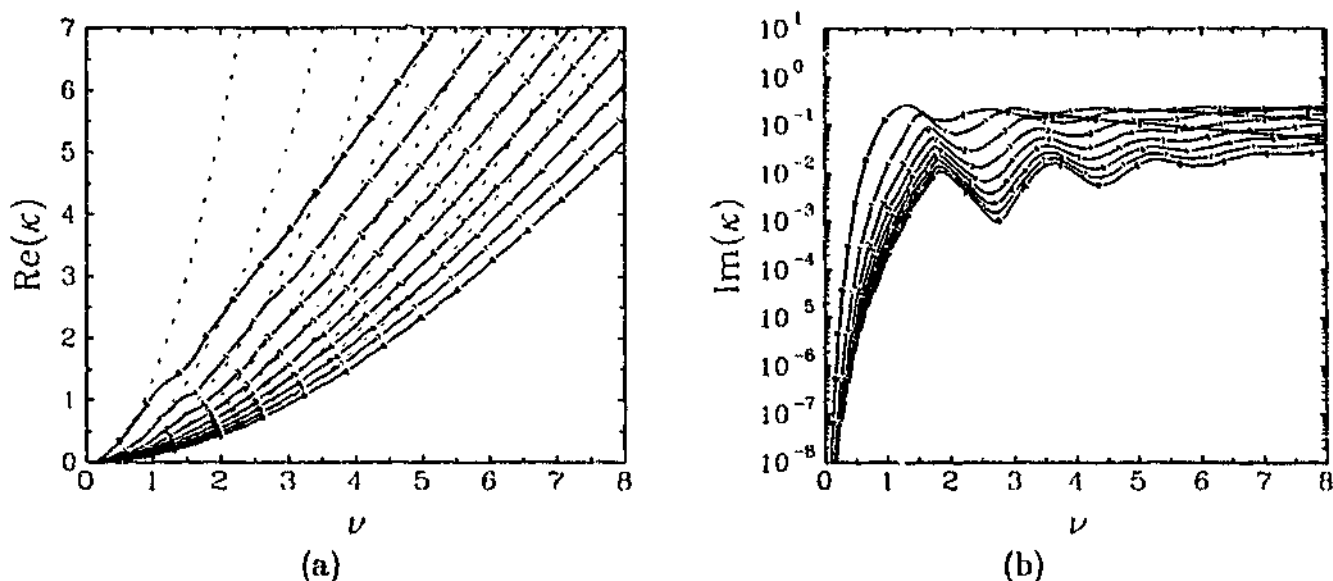
Figure 3.9: Same as Figure 3.3, except $\theta = 30°$.

For purposes of completeness we present two further graphs showing κ as a function of dimensionless frequency, ν, with θ constant. Figure 3.9 shows the variation of the real and imaginary parts of κ as a function of dimensionless frequency, ν, when $\theta = 30°$ for the first nine ($n = 0, \ldots, 8$) modes. The distinctive cuts in Figures 3.5 – 3.8 are not evident in Figure 3.9, this is because the ridges in Figure 3.9 have been generated by stepping from low frequencies (using the non-magnetic modes as initial guess) to high frequencies, holding θ constant (in the same way as Figures 3.3 and 3.4). For example, the ridge labelled $n = 0$ in Figure 3.9 could be derived from the $n = 0$ and $n = 1$ surfaces (Fig. 3.5 and 3.6 respectively) by slicing along $\theta = 30°$. For frequencies less than the cut connecting the two surfaces the $n = 0$ ridge (in Fig. 3.9) lies on the $n = 0$ surface (Fig. 3.5), whereas for frequencies greater than the cut, the $n = 0$ ridge lies on the $n = 1$ surface (Fig. 3.6). Similar observations apply to the higher order modes, so all the ridges in Figure 3.9 appear continuous.

The main features of Figure 3.9 are indicative of the ridges at inclinations near $30°$. In particular, the horizontally evanescent modes (which turn over and terminate at $\mathrm{Re}\,(\kappa) = 0$)

55

vanish for $\theta \gtrsim 30°$. In these cases, Re (κ) (Fig. 3.9(a)) increases monotonically with increasing ν, and at any given frequency Re(κ) decreases with increasing n. Correspondingly, Im (κ) (Fig. 3.9(b)) increases rapidly with increasing ν for low frequencies, and the ridges become almost horizontal for intermediate and higher frequencies. In general, the decoupling troughs of Im (κ) in the vertical field case fade away as θ increases, forming the nearly horizontal curve evident in Figure 3.9(b). This can also be seen on the surfaces in Figures 3.5 ~ 3.8. The sequence of Im (κ) ridges in Figure 3.9(b) form a tightly packed bunch. Hence, at inclinations near the vertex of the cuts (corresponding to a local maximum in Im (κ)), the variation of Im (κ) with n is at a minimum ($\theta \approx 25°$). In the interval $\theta \approx 20° - 30°$ the horizontal section of each ridge (evident in Figure 3.9) reaches a maximum level (Im $(\kappa) \approx 0.1$) before decreasing for larger inclinations $\theta > 30°$.
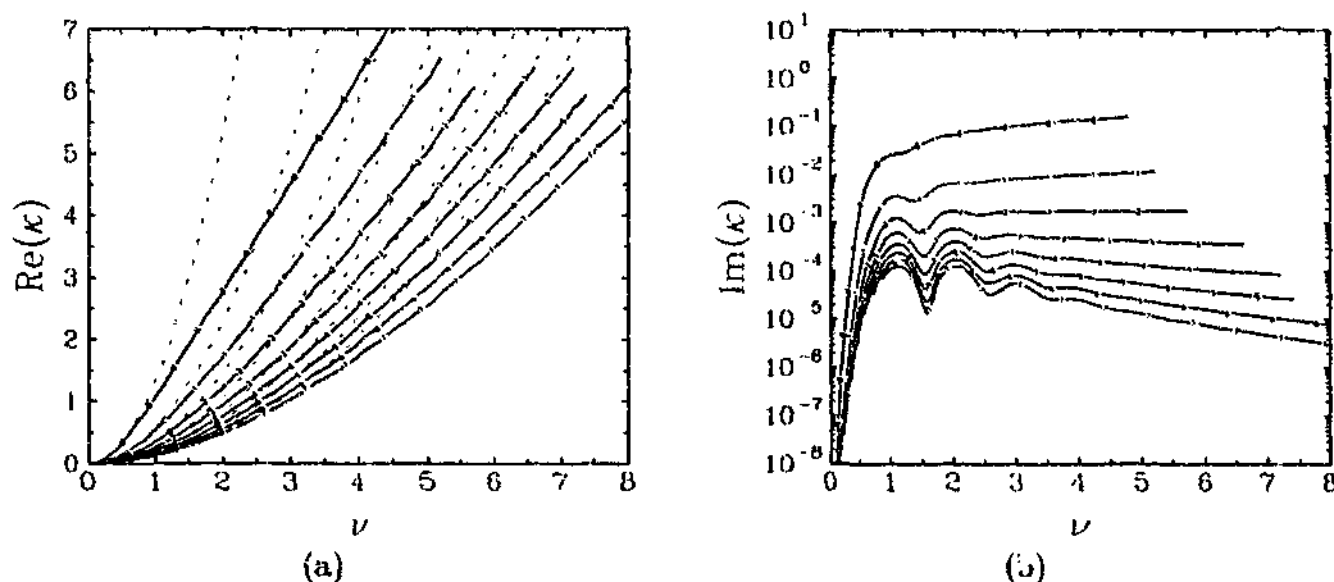
Figure 3.10: Same as Figure 3.3, except $\theta = 60°$ and the n=8 mode has been omitted.

Figure 3.10 shows the variation of the real and imaginary parts of κ as a function of dimensionless frequency, ν, when $\theta = 60°$ for the first eight ($n = 0, \ldots, 7$) modes. In Figure 3.10 some of the ridges terminate prematurely and the $n = 8$ ridge is omitted. The combination of high frequency and large inclination makes the integration of the highly oscillatory slow MAG wave solution very difficult. The possibility of an improved asymptotic solution for the slow MAG waves (e.g., BC97, their eq. [4.20]) has been briefly pursued without success. The eigencurves presented in Figure 3.10 are reliable in the observable frequency range. The main features of Figure 3.10 are indicative of the ridges at angles near 60°. For angles above $\theta \approx 30°$ there is little variation in Re (κ) ridges as a function of θ. There is a strong similarity between the real parts of the ridges of Figure 3.9(a) and Figure 3.10(a), the only difference is a small decrease in phase speed as θ increases. In contrast, the imaginary parts of the eigenvalues vary more dramatically as θ increases. Above $\theta \approx 30°$ the bunch of ridges starts to disperse, increasingly so as θ increases, and the variation of Im (κ) with n increases. This feature is obvious when comparing the Im (κ) ridges between Figure 3.9(b) and Figure 3.10(b). Figure 3.10(b) also illustrates the fact that, above $\theta \approx 45°$, Im (κ) ridges no longer intercept ridges of different n (at least in the range of frequencies covered

56

here). Hence, for any given frequency, $\mathrm{Im}\,(\kappa)$ decreases with increasing n. For the higher order modes, Figure 3.10(b) shows that $\mathrm{Im}\,(\kappa)$ reaches a maximum, and thereafter decreases with increasing ν. This feature is more dramatic for ridges at greater inclinations ($\theta \gtrsim 60°$, graphs not shown). The most important feature of the $\mathrm{Im}\,(\kappa)$ ridges (e.g., Fig. 3.10(b)) at greater inclinations is the rapid decrease of $\mathrm{Im}\,(\kappa)$ as the magnetic field inclination approaches horizontal.

3.7.2 Extinction length

We define the extinction length $L/\mathrm{Im}\,(\kappa) = 1/\mathrm{Im}\,(2k)$ as the distance (in the x-direction) over which the wave energy density decreases by a factor of e (§4.5 provides a detailed discussion of wave-energy flux). To characterise the solar convection zone, we use $g = 274$ m s^{-2} and $L = 400$ km*, so at $z = -L$ the sound speed and the Alfvén speed coincide at 8.55 km s^{-1}. There is some uncertainty in this characterisation. However, in sunspot core models M, L, and E of Maltby et $al.$ (1986) the layers where $C_S \approx 8.55$ km s^{-1} correspond to $\rho \approx (1.2 - 2.0) \times 10^{-3}$ kg m^{-3} and field strengths in the range $3400 - 4200$ G. which is consistent with expectations for subsurface sunspot umbrae.

Figure 3.11 shows the variation of the extinction length as a function of field inclination, θ, for the first nine ($n = 0, \ldots, 8$) modes at four different (fixed) frequencies (a) 3 mHz (b) 4 mHz (c) 5 mHz and (d) 6 mHz. These four frequencies have been chosen as they fall inside the region of observational interest, and they do not coincide with the vertical field trapped modes. The corresponding graphs of the horizontal wavenumber, $\mathrm{Re}\,(k) = \mathrm{Re}\,(\kappa)\,/2L$, are not shown because the variation with θ is only small (as shown in Figures 3.3 – 3.10). It should be noted that the ridge crossings shown in Figure 3.11 are not actual crossings of the eigenvalue. The ridges in Figure 3.11 may be derived by taking constant frequency slices (parallel to the cuts) through the surfaces of Figures 3.5 – 3.8. At all four frequencies Figure 3.11 shows the extinction length of the $n = 0$ mode increases (monotonically) with increasing inclination. This implies that the $n = 0$ mode is most efficiently damped by vertical (or near vertical) field. At all frequencies and $\theta \lesssim 20°$, the extinction length of the $n = 0$ mode is relatively short ($\approx 0.1 - 5$ Mm) and, consequently, will be significantly damped within a sunspot sized region (≈ 10 Mm). For higher field inclinations the efficiency of $n = 0$ mode conversion becomes increasing weak (more rapidly for the higher frequencies). In fact for all modes at all frequencies of observational interest, Figure 3.11 shows that mode conversion becomes increasingly inefficient (extinction length tends to infinity) as the field approaches horizontal (e.g., all modes in field with $\theta \gtrsim 70°$ will show no appreciable damping). This trend is also evident in surfaces in Figures 3.5 – 3.8. Our results are not reliable for inclinations close to the horizontal field singular limit. For inclinations approaching horizontal, the trend evident in Figure 3.11 must be viewed with caution. In the isothermal case, Kamp (1989) suggests singular behaviour will arise for angles only very close to horizontal. For modes with $n \geq 1$, the extinction length initially decreases with increasing inclination, reaching a minimum near $\theta \approx 20° - 60°$, before increasing for larger θ. For the lower frequencies (e.g., Fig. 3.11(a) and 3.11(b)), the minimum is at $\theta \approx 40° - 60°$, whereas, for the higher frequencies (e.g.,

---

*Recent calculations by Cally, Crouch, and Braun (2003, see Appendix F) find the models in best agreement with observations have $L = 600 - 800$ km.
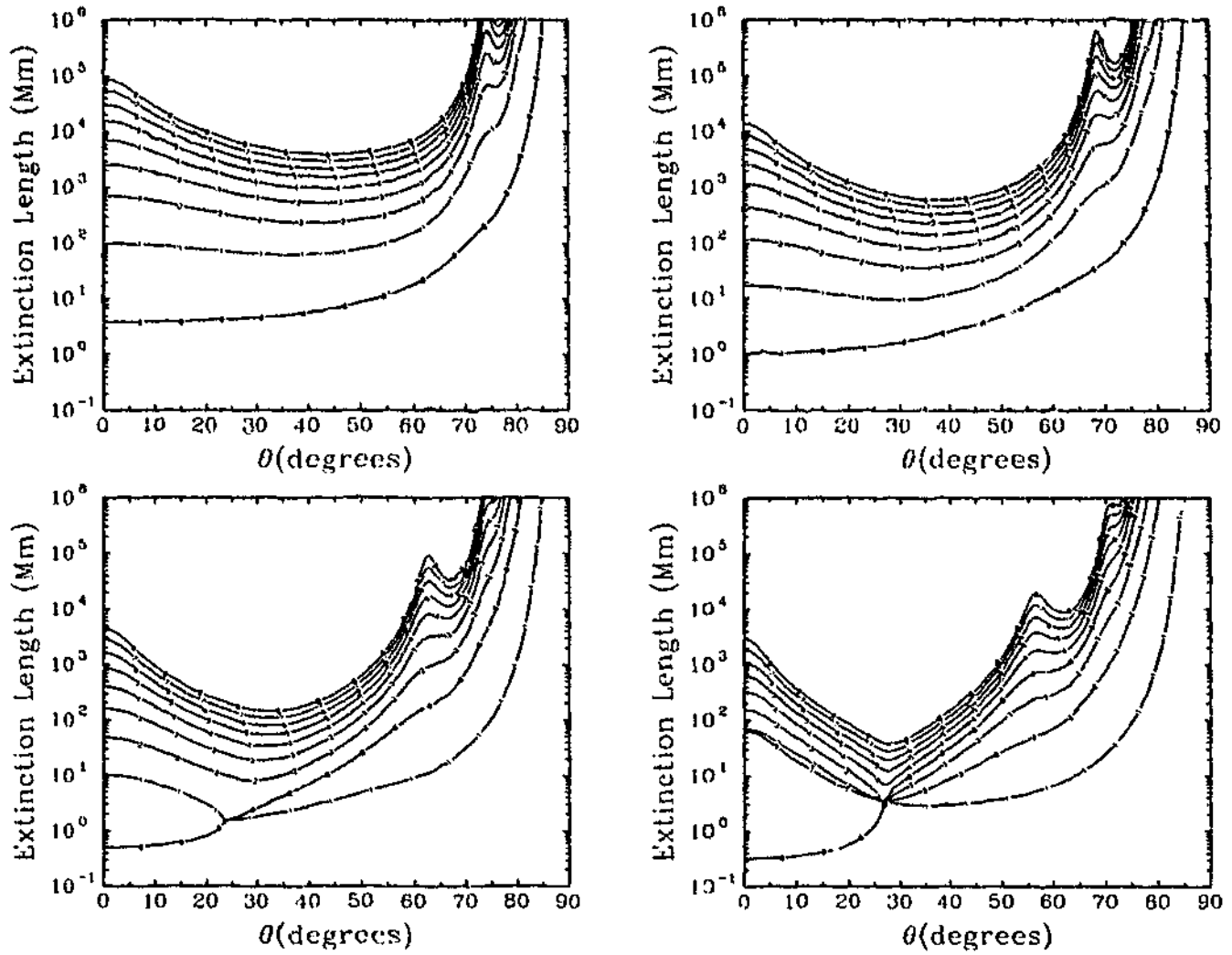
Figure 3.11: Extinction length, $L/\text{Im}(\kappa)$, as a function of angle θ for the $n = 0, \ldots, 8$ modes. (a) *Top left:* the frequency is constant at 3 mHz. (b) *Top right:* 4 mHz. (c) *Bottom left:* 5 mHz. (d) *Bottom right:* 6 mHz.

Fig. 3.11(c) and 3.11(d)), the minimum is at more acute inclinations $\theta \approx 20° - 40°$. The minimum roughly coincides with the vertices of the cuts in the corresponding eigensurfaces (e.g., Figs. 3.5 – 3.8). At these inclinations the efficiency of mode conversion (for $n \geq 1$) is at a maximum. In comparison to vertical field ($\theta = 0$), the enhancement is largest (up to two orders of magnitude) for the higher frequencies (e.g., Fig. 3.11(c) and 3.11(d)). Consequently, π-modes (with $1 \leq n \lesssim 4$ and frequencies $\approx 5 - 6$ mHz) propagating through field inclined at $\theta = 20° - 40°$ will be damped significantly within a sunspot sized region [8].

3.7.3 Eigenfunctions

Figures 3.12 and 3.13 show the displacement eigenfunctions as a function of dimensionless depth, s, corresponding to eigenvalues of the $n = 1$ mode with dimensionless frequency

---

[8] At frequencies near 5 mHz, observations using Hankel analysis Braun (1995) show a remarkable drop in the absorption of p-modes by sunspots. However, using acoustic holography Lindsey and Braun (1999) conclude this is not a property of sunspots, but rather an enhanced emission of p-modes in regions surrounding spots.
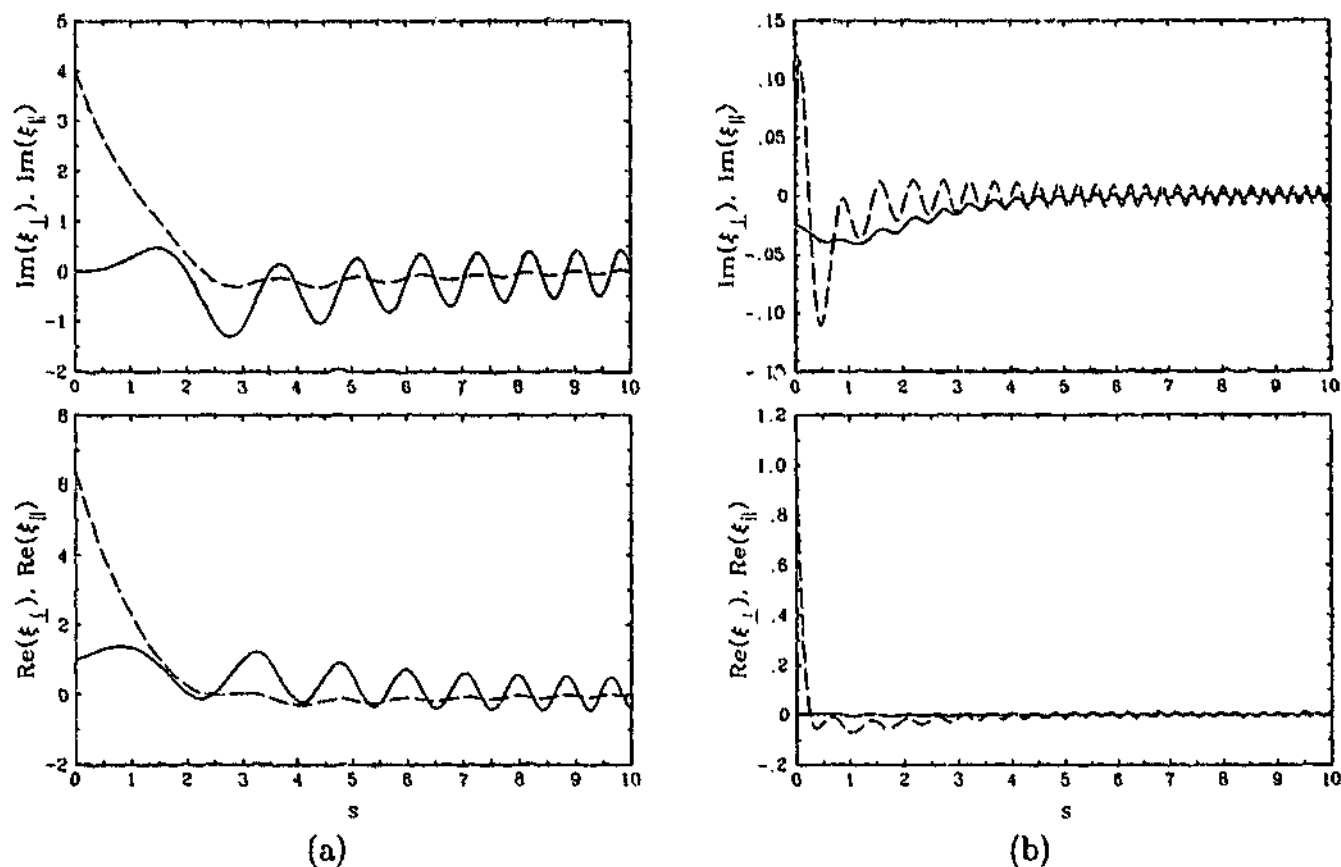
Figure 3.12: Displacement eigenfunctions as a function of dimensionless depth, s, for $\nu = 1.47$ and $n = 1$. The full curve is $\xi_\perp$ and the dashed curve is $\xi_{\parallel}$. On both sides the *top panel* shows the imaginary parts of the displacement and the *bottom panel* shows the real parts. The vertical scaling is arbitrary. Both of the eigenfunctions have eigenvalues, κ, on the $n = 1$ eigensurface (Fig. 3.6) and the $n = 1$ ridge in Figure 3.11(c) ($\nu = 1.47$ corresponds to 5 mHz for the choice of parameters above – see §3.7.2). (a) $\theta = 0$ and $\kappa = 1.258 + 0.039i$. (b) $\theta = 70°$ and $\kappa = 1.932 + 0.013i$.

$\nu = 1.47$ (see Figure 3.6 or the $n = 1$ ridge in Figure 3.11(c), $\nu = 1.47$ corresponds to 5 mHz for the choice of parameters above – see §3.7.2). Figure 3.12(a) shows the displacement eigenfunction for exactly vertical field ($\theta = 0$), Figure 3.12(b) for $\theta = 70°$, Figure 3.13(a) for $\theta = 25°$, and Figure 3.13(b) for $\theta = -25°$. As outlined earlier, the eigenfunctions in Figure 3.13 have the same eigenvalue but the resultant displacements are different. Figure 3.13(a) shows that for $\theta > 0$ the slow mode component of the displacement decays exponentially with depth, whereas for $\theta < 0$ (Fig. 3.13(b)) it grows exponentially with depth; see equations (3.29) and (3.30) for details. Also evident in Figure 3.13 is that the two components of the displacement $\xi_\perp$ (full curve) and $\xi_{\parallel}$ (dashed curve) are in phase for $\theta > 0$, but 180° out of phase for $\theta < 0$. In Figure 3.13, $\mathrm{Im}(\kappa)$ is close to optimal, with a magnitude approximately seven times larger than in Figure 3.12(a). Qualitatively, this is evident as the displacement eigenfunctions in Figure 3.13 clearly have a large (highly oscillatory) slow mode component, whereas in Figure 3.12 the slow mode amplitude is less pronounced. There are two further obvious differences between the displacements at different inclinations that are worth discussing. The first is the decrease of the vertical wavelength of the slow mode component as θ increases – this can be interpreted from the asymptotics (eq. [3.26]). The

59

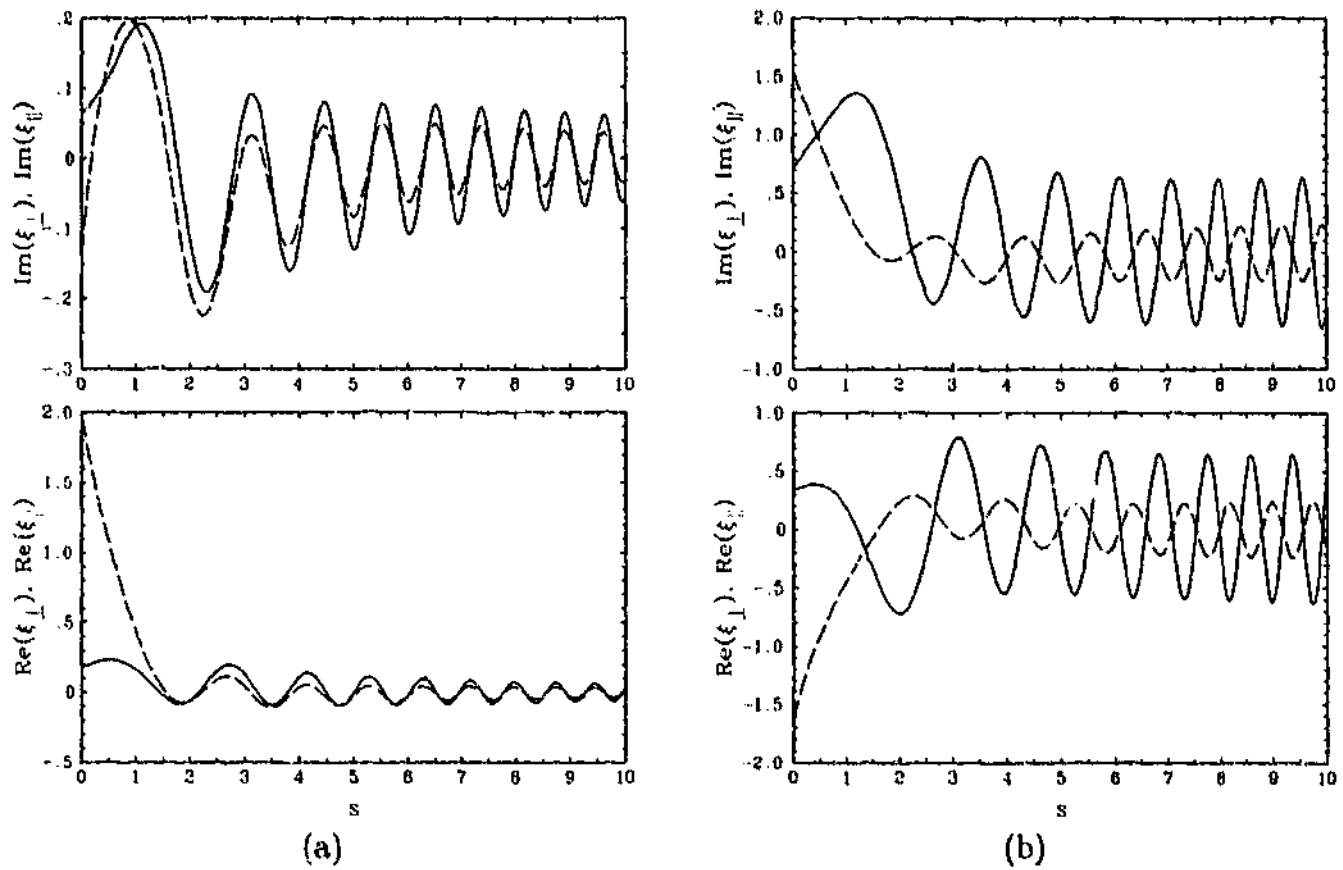*Figure 3.13:* Same as Figure 3.12 except for different inclinations. (a) $\theta = 25°$. (b) $\theta = -25°$. Both eigenfunctions have identical eigenvalues, $\kappa = 1.386 + 0.26i$.

second is the near surface behaviour, the contrast is particularly drastic when comparing displacements in vertical field (Fig. 3.12(a)) with those in highly inclined field (Fig. 3.12(b)). The component of the displacement aligned parallel and perpendicular to the field can be derived from the Frobenius series expansions about $s = 0$ (eqs. [3.36] and [3.37]). The first two terms of each of them are:

$$\xi_{\parallel} = \sin\theta + \frac{1}{10}\left(2i\kappa\sec\theta - 4\nu^2\tan\theta\sec\theta + 5\kappa\sin\theta\right)s + \dots ,$$

$$\xi_{\perp} = \cos\theta\left(1 + \frac{\kappa}{2}s\right) + \dots ,$$

and

$$\xi_{\parallel} = \cos\theta + \frac{1}{10}\sec\theta\left(3i\kappa\tan\theta - 4\nu^2 - 5\kappa\sin^2\theta\right)s + \dots ,$$

$$\xi_{\perp} = -\sin\theta\left(1 + \frac{\kappa}{2}s\right) + \dots .$$

Thus, it can be verified that field aligned motions, $\xi_{\parallel}$, dominate the displacement near the surface when the field is highly inclined. In fact the second terms of both series for $\xi_{\parallel}$ diverge

60

In the horizontal field limit ($\theta \to 90°$). The Lorentz force has no component in the direction along the field. As the magnetic field tips over the influence of gravity parallel to the field diminishes, therefore, large motions are permitted and exhibited near the surface ($s \approx 0$) in Figures 3.12 and 3.13. This is a feature of the complete polytrope, and will not occur to the same extent in the solar convection zone as oscillations there are coupled to oscillations in the chromosphere (and corona).

3.8 Conclusions

We investigated the two dimensional ($\phi = 0$) propagation of oscillations in a complete polytrope permeated by a straight, uniform, non-vertical magnetic field. In particular, we quantified the efficiency of fast-to-slow MAG wave conversion, and subsequent horizontal spatial decay of the oscillation. For modes with $n \geq 1$, we found mode conversion is significantly enhanced (by up to two orders of magnitude) in comparison to vertical field. The enhancement occurs in moderately inclined fields ($\theta \approx 20° - 60°$, depending on the mode and frequency), and is most significant at higher frequencies. At lower frequencies the enhancement is generally negligible. The enhancement appears to be roughly sufficient to explain both the observed p-mode absorption by sunspots (e.g., Braun, 1995; Lindsey and Braun, 1999, see overview in Chapter 1), and the simulated absorption of higher order p-modes by a spreading field sunspot (Cally, 2000). Indeed, recent calculations using the results of this chapter (Cally, Crouch, and Braun, 2003, see Appendix F) indicate the absorption exhibited by non-vertical field is ample to explain the observations. We defer the discussion of these calculations to Chapter 6. However, it should be noted that we adopted $L = 400$ km in this chapter, but Cally, Crouch, and Braun (2003) find the models in best agreement with observations have $L = 600 - 800$ km, in which case, the frequencies quoted in §3.7.2 would be slightly lower (eqn. [3.7]). For the $n = 0$ mode, fast-to-slow MAG wave conversion is most efficient in vertical field (and slightly non-vertical field). For all modes at all frequencies, highly inclined fields ($\theta \gtrsim 70°$) show very inefficient fast-to-slow MAG wave conversion. However, under the assumption that $\phi = 0$, it is not reasonable to conclude that highly inclined field (e.g., flat canopy field in sunspot penumbrae) does not absorb p-modes. For example, the resonant damping of p-modes by horizontal (canopy) field overlying the convection zone (e.g., Vanlommel et al., 2002, and references therein) may also play an important role in p-mode absorption by sunspot penumbrae. In fact, the extent to which these results apply to more complicated geometries (e.g., Bogdan, 1999) is an open question.

Clearly, p-to-slow mode conversion is implicated in the absorption of p-modes by sunspots, our simple two dimensional models are roughly consistent with the observations. In Chapter 4, we shall investigate the effects of propagation in three dimensions ($\phi \neq 0$). In that case, the Alfvén waves are coupled to the MAG waves, raising the possibility of even further absorption.

61

Chapter 4

Mode conversion of solar p-modes in non-vertical magnetic fields: Three-dimensional model

In this chapter, we investigate another promising absorption mechanism – the leakage of energy by Alfvén waves travelling down the field lines. The Alfvén waves decouple in two-dimensional propagation ($\phi = 0$, see Chapter 3). We calculate the efficiency of mode conversion in non-vertical field with three-dimensional propagation (i.e., $\phi \neq 0$), where fast and slow magnetoacoustic-gravity waves and Alfvén waves are coupled. We calculate the resultant decay rates (extinction lengths) and determine the contribution by the slow MAG waves and the Alfvén waves.

4.1 The governing equations

As in Chapter 3, the model atmosphere is taken as a complete isentropic polytrope (eqs. [3.5] and [3.6]), and we adopt the usual nondimensionalisation (eq. [3.7]). The nondimensionalised governing equations with $\phi \neq 0$ are then

$$
s^{-m} \left[\cos^2 \theta \frac{d^2}{ds^2} - \left(\cos^2 \theta + \sin^2 \phi \sin^2 \theta \right) \frac{\kappa^2}{4} \right] \zeta + \left(\nu^2 - \frac{\kappa^2}{4} s \right) \zeta
$$
$$
- \sin \theta \, s^{-m} \left[\cos \phi \cos \theta \frac{d^2}{ds^2} + \frac{i\kappa}{2} \sin^2 \phi \sin \theta \frac{d}{ds} - \cos \phi \cos \theta \frac{\kappa^2}{4} \right] \xi_z
$$
$$
- \frac{i\kappa}{2} \left[s \frac{d}{ds} + m \right] \xi_z = -\frac{i\kappa}{2} \sin \phi \sin \theta \, s^{-m} D_\| \eta \,, \tag{4.1}
$$

$$
\left[s^{-m} D_\|^2 + \nu^2 \right] \eta = - \sin \phi \sin \theta \, s^{-m} D_\| \left[\tilde{\nabla} \cdot \boldsymbol{\xi} \right] \,, \tag{4.2}
$$

$$
\sin^2 \theta \, s^{-m} \left[\frac{d^2}{ds^2} - \cos^2 \phi \frac{\kappa^2}{4} \right] \xi_z + \left[s \frac{d^2}{ds^2} + (m+1) \frac{d}{ds} + \nu^2 \right] \xi_z
$$

62

$$-\sin\theta \, s^{-m} \left[\cos\phi \cos\theta \frac{d^2}{ds^2} + \frac{i\kappa}{2} \sin^2\phi \sin\theta \frac{d}{ds} - \cos\phi \cos\theta \frac{\kappa^2}{4} \right] \zeta$$

$$-\frac{i\kappa}{2} \left[s\frac{d}{ds} + 1 \right] \zeta = \sin\phi \sin\theta \, s^{-m} D_\parallel \left[\frac{d\eta}{ds} \right], \tag{4.3}$$

where $D_\parallel = \frac{i\kappa}{2} \cos\phi \sin\theta - \cos\theta \frac{d}{ds}$ is the nondimensionalised directional derivative along the field lines, and $\tilde{\nabla} \cdot \xi = \frac{i\kappa}{2}\zeta - \frac{d\xi_z}{ds}$ is the nondimensionalised divergence of the displacement vector. With $\phi \neq 0$, the system of differential equations (4.1)–(4.3) is sixth order and completely describes the propagation and linear interaction of all types of MAG waves – the fast and slow MAG waves and the Alfvén waves (where the distinction is valid). In the case of propagation parallel to the x-axis (i.e., $\phi = 0$), equations (4.1) and (4.3) reproduce the fourth order problem (eqs. [3.8] and [3.9], respectively), whereas equation (4.2) decouples and describes the propagation of the Alfvén waves in non-vertical field.

As in Chapter 3, without loss of generality, we assume $\mathrm{Re}\,(\kappa) \geq 0$ throughout the remainder of our analysis (i.e., travelling waves propagate in the positive $\hat{\mathbf{k}}$-direction). We calculate complex wavenumber eigenvalues, κ, for specified real dimensionless frequencies, ν, inclination, θ, and propagation direction ϕ. Again, we restrict our attention exclusively to the case $m = 3/2$.

4.2 The lower boundary

The lower boundary, $s = \infty$, is an intrinsically irregular singular point of the governing equations (4.1)–(4.3). Imposing the appropriate boundary conditions requires knowledge of the asymptotic behaviour of the solutions of governing equations as $s \to \infty$. The analysis is very similar to §3.3, except $\phi \neq 0$, therefore, the Alfvén waves must be included. To avoid repetition some details may be omitted.

As discussed in §3.3, when the sound speed, C_S, and the Alfvén speed, C_A, differ greatly (i.e., $C_A \ll C_S$, as $s \to \infty$) the fast and slow MAG waves and the Alfvén waves decouple. Hence, in the region where $C_A \ll C_S$, we can address the three oscillation modes separately. As in the fourth order case, at great depth, as $s \to \infty$, the fast MAG wave is asymptotically an evanescent acoustic wave (compressive and longitudinally polarised), with a vertical wavelength comparable to the local density scale height. The propagation of the fast MAG wave is asymptotically unaffected by the presence of the magnetic field. On the other hand, the slow MAG wave and the Alfvén wave are strongly affected by the presence of the magnetic field. The slow MAG wave is asymptotically a travelling Alfvén wave (incompressive and transversely polarised), with a vertical wavelength very much smaller than the local density scale height. The physical characteristics of each mode, combined with the method of dominant balance (e.g., Bender and Orszag, 1978, Chapter 3), guide us to consistent asymptotic behaviours for the fast and slow MAG waves and the Alfvén waves.

4.2.1 Fast MAG wave asymptotics

Asymptotically, as $s \to \infty$ where $C_A \ll C_S$, the fast MAG waves are unaffected by the magnetic field. For the fast MAG wave solution, this property motivates the assumption

that, in the governing equations (4.1)-(4.3), the magnetic terms are dominated by the non-magnetic terms. We must check this assumption later. Neglecting the magnetic terms in equations (4.1)–(4.3) leaves

$$\left[s\frac{d^2}{ds^2} + m\frac{d}{ds}\right]\zeta \sim \left(\frac{\kappa^2}{4}s - \nu^2\right)\zeta, \quad s \to \infty, \tag{4.4}$$

$$\frac{d\zeta}{ds} \sim -\frac{i\kappa}{2}\xi_z, \quad s \to \infty, \tag{4.5}$$

and η is very small relative to both ζ and ξ_z, i.e.,

$$\lim_{s\to\infty}\frac{\eta}{\zeta} = 0, \quad \text{and} \quad \lim_{s\to\infty}\frac{\eta}{\xi_z} = 0. \tag{4.6}$$

For the non-magnetic p-modes (see Appendix A for details), the asymptotic relations (4.4) and (4.5) are equalities and η (eq. [4.6]) vanishes exactly.

The method of dominant balance applied to relation (4.4) yields the two controlling factors $\zeta \sim \exp\left(\pm\frac{\kappa}{2}s\right)$. As in §3.3.1, we impose the boundary condition that evanescent modes decrease. Further developing the exponentially decaying asymptotic solution we find:

$$\zeta_f \sim s^{(\nu^2/\kappa)-(m/2)}\exp\left[-\frac{\kappa}{2}s\right]U_f(s), \quad s \to \infty, \tag{4.7}$$

$$
\begin{aligned}
\eta_f \quad \sim \quad & \sin\phi\sin\theta\left(1 - \frac{m\kappa}{2\nu^2}\right)(\cos\phi\sin\theta - i\cos\theta)\\
& \times s^{(\nu^2/\kappa)-(3m/2)-1}\exp\left[-\frac{\kappa}{2}s\right]V_f(s), \quad s \to \infty,
\end{aligned} \tag{4.8}
$$

$$\xi_{z_f} \sim -is^{(\nu^2/\kappa)-(m/2)}\exp\left[-\frac{\kappa}{2}s\right]W_f(s), \quad s \to \infty, \tag{4.9}$$

where the coefficients U_f, V_f and W_f are all asymptotic to unity as $s \to \infty$, and $\text{Re}(\kappa) \geq 0$ is assumed. The leading behaviour for η (eq. [4.8], resulting from eq. [4.2]) clearly shows that η is very much smaller than both ζ and ξ_z, as $s \to \infty$, (consistent with eq. [4.6]). In addition, it can be easily verified, by substituting the leading behaviours (4.7)–(4.9) into the governing equations (4.1)-(4.3), that the magnetic terms are dominated by the non-magnetic terms at sufficient depth. Consequently, the initial assumption for the fast MAG wave solution is self-consistent. As in §3.3.1, for complex κ, the asymptotic behaviour of the fast MAG wave is somewhat wave-like. However, for $\text{Re}(k) \geq 0$, it can be verified that the associated wave energy flux vanishes as $s \to \infty$.

For $m = 3/2$, in a similar fashion to CB93 and §3.3.1, the coefficients U_f, V_f and W_f may be expanded in asymptotic power series in non-positive half integer powers of s. The details of the series expansions are presented in Appendix D.1. The first few terms of the series are:

$$U_f(s) \sim 1 - \frac{a}{2\kappa}(2a-1)s^{-1} - \frac{a\kappa^2}{6\nu^2}(\cos\theta + i\cos\phi\sin\theta)^2 s^{-3/2} + \ldots, \tag{4.10}$$

64

$$V_f(s) \sim 1 - \frac{(a+1)\{(2a-7)\cos\theta + i(2a-3)\cos\phi\sin\theta\}}{2\kappa(\cos\theta + i\cos\phi\sin\theta)} s^{-1}$$

$$- \frac{\kappa^2}{12\nu^2}(2a+3)(\cos\theta + i\cos\phi\sin\theta)^2 s^{-3/2} + \dots, \tag{4.11}$$

$$W_f(s) \sim 1 - \frac{a}{2\kappa}(2a-5)s^{-1} - \frac{a\kappa^2}{6\nu^2}(\cos\theta + i\cos\phi\sin\theta)^2 s^{-3/2} + \dots, \tag{4.12}$$

where $a = (3/4) - (\nu^2/\kappa)$. Unsurprisingly, the asymptotic leading behaviour for the fast MAG wave (eq. [4.7]-[4.9]), and the first two non-zero terms of the series U_f (eq. [4.10]), are exactly that of the trapped non-magnetic p-mode (see Appendix A). Asymptotically, the fast MAG wave is unaffected by the magnetic field strength and inclination, θ, and, as expected, the propagation direction, ϕ. Dependence on both θ and ϕ enter the asymptotic behaviours for ζ and ξ_z in the series U_f and W_f, respectively, at terms of order $s^{-3/2}$. The leading order for η (eq. [4.8]) itself explicitly depends on θ and ϕ, though it is asymptotically dominated by ζ and ξ_z. For $\phi = 0$, $\eta_f = 0$ for all s, and the asymptotic leading orders (eqs. [4.7] and [4.9]) and the asymptotic series (eqs. [4.10] and [4.12]) reproduce the fourth order non-vertical field result (eqs. [3.12]-[3.13] and eqs. [3.14]-[3.15], respectively). For $0 \le \phi \le \pi$ and exactly horizontal field ($\theta = 90°$) the fast MAG wave asymptotic leading orders (eqs. [4.7]-[4.9]) are well behaved, and yield a valid solution to the second order ($\phi \ne 0$) horizontal field problem. With $\theta = 0$, these fast MAG wave solutions reproduce the vertical field solutions (see CBZ, their eq. [2.12]).

4.2.2 Slow MAG wave and Alfvén wave asymptotics

Asymptotically, as $s \to \infty$ (where $C_A \ll C_S$), both the slow MAG waves and the Alfvén waves are transversely polarised, incompressive modes with a vertical wavelength that is very much smaller than the local density scale height (for the sake of conciseness, in the vicinity of the lower boundary, we sometimes refer to both the slow MAG waves and Alfvén waves as the "incompressive modes"; the distinction between the slow MAG waves and Alfvén waves is fully described at the end of this subsection). In the limit where $C_A \ll C_S$, the propagation of the incompressive modes is unaffected by the gravitational stratification. It is therefore reasonable to assume that the atmosphere, as experienced by the incompressive modes at sufficient depth, is homogeneous (i.e., $g = 0$). This assumption must be checked later. The complete solutions for magnetoacoustic and Alfvén waves propagating in a homogeneous magnetofluid with $\phi \ne 0$ were derived in §3.3.2.

In the limit where $C_A \ll C_S$, the dispersion relations for the slow magnetoacoustic wave and the Alfvén wave in a homogeneous magnetofluid are identical (see eqs. [3.18] and [3.21]),

$$\omega^2 = K^2 C_A^2 \cos^2\psi. \tag{4.13}$$

Assuming the vertical wavelength of the incompressive modes is very much smaller than the local density scale height, the asymptotic relation for both the slow MAG waves and Alfvén

waves in a gravitationally stratified atmosphere, consistent with the dispersion relation (4.13), is

$$C_A^2 \left[\cos\theta \frac{d}{dz} + ik\cos\phi\sin\theta \right]^2 \chi(z) \sim -\omega^2\chi(z) , \quad z \to -\infty ,$$

where χ is the dominant component of the displacement vector, $\boldsymbol{\xi}$, for each mode. We leave this general for the moment. The asymptotic relation for the incompressive modes in the complete polytrope (eqs. [3.6] and [3.7]) is then

$$\left[\cos^2\theta\, s^{-m} \frac{d^2}{ds^2} - i\kappa\cos\phi\sin\theta\cos\theta\, s^{-m} \frac{d}{ds} \right] \chi(s)$$
$$\sim \left(\frac{\kappa^2}{4}\cos^2\phi\sin^2\theta\, s^{-m} - \nu^2 \right) \chi(s) , \quad s \to \infty . \tag{4.14}$$

Applying the method of dominant balance to equation (4.14) yields the two controlling factors $\chi \sim \exp\left(\pm 2i\nu\sec\theta\, s^{(m+2)/2}/(m+2) \right)$. As in §3.3.2, we require that wave-like disturbances be outgoing. Further developing the outgoing wave asymptotic solution for equation (4.14) we find

$$\chi \sim s^{-m/4}\exp\left[\cos\phi\tan\theta\frac{i\kappa}{2}s + \sec\theta\frac{2i\nu}{m+2}s^{(m/2)+1} \right] , \quad s \to \infty , \tag{4.15}$$

for both the slow MAG waves and Alfvén waves. Asymptotically the vertical wavelength of the incompressive modes, corresponding to solution (4.15), is

$$\lambda \propto \chi \left(\frac{d\chi}{ds} \right)^{-1} \sim \frac{\cos\theta}{\nu}s^{-m/2} , \quad s \to \infty .$$

Consequently, the initial assumption that the atmosphere is homogeneous with respect to the incompressive modes (i.e., the vertical wavelength is very much smaller than the local density scale height, eq. [3.27]) is self-consistent. The assumption that the atmosphere is homogeneous is used only to calculate the leading order terms. For incompressive oscillations,

$$\frac{d\xi_z}{ds} \sim \frac{i\kappa}{2}\zeta , \quad s \to \infty ,$$

hence, for the leading order above (eq. [4.15]), the slow MAG waves and Alfvén waves require

$$\xi_z \sim \cos\theta\frac{\kappa}{2\nu}s^{-m/2}\zeta , \quad s \to \infty . \tag{4.16}$$

Applying the leading behaviours $\zeta \sim \chi$, $\eta \sim \chi$ and $\xi_z \sim \cos\theta\frac{\kappa}{2\nu}s^{-m/2}\chi$ to the governing equations (4.1)-(4.3) we further develop the resultant asymptotic solutions. Two independent modes can be identified:

$$\zeta_s \sim s^{-3/8}\exp\left[\cos\phi\tan\theta\frac{i\kappa}{2}s + \sec\theta\frac{4}{7}i\nu s^{7/4} \right] U_s(s) , \quad s \to \infty , \tag{4.17}$$

66

$$\eta_s \sim \frac{\sin\phi\,\sin\theta}{6\nu}\left(4i\nu^2\cos\phi\,\tan\theta - 3\kappa\right)s^{-9/8}$$
$$\times \exp\left[\cos\phi\,\tan\theta\,\frac{i\kappa}{2}s + \sec\theta\,\frac{4}{7}i\nu s^{7/4}\right]V_s(s), \quad s\to\infty, \tag{4.18}$$

$$\xi_{z_s} \sim \cos\theta\,\frac{\kappa}{2\nu}s^{-9/8}\exp\left[\cos\phi\,\tan\theta\,\frac{i\kappa}{2}s + \sec\theta\,\frac{4}{7}i\nu s^{7/4}\right]W_s(s), \quad s\to\infty, \tag{4.19}$$

for the downward-travelling slow MAG wave (with the displacement dominated by ζ), and

$$\zeta_a \sim \frac{\sin\phi\,\sin\theta}{6\nu}\left(4i\nu^2\cos\phi\,\tan\theta + 3\kappa\right)s^{-9/8}$$
$$\times \exp\left[\cos\phi\,\tan\theta\,\frac{i\kappa}{2}s + \sec\theta\,\frac{4}{7}i\nu s^{7/4}\right]U_a(s), \quad s\to\infty, \tag{4.20}$$

$$\eta_a \sim s^{-3/8}\exp\left[\cos\phi\,\tan\theta\,\frac{i\kappa}{2}s + \sec\theta\,\frac{4}{7}i\nu s^{7/4}\right]V_a(s), \quad s\to\infty, \tag{4.21}$$

$$\xi_{z_a} \sim \frac{\sin\phi\,\sin\theta\,\kappa}{12\nu^2}\left(4i\nu^2\cos\phi\,\sin\theta + 3\kappa\cos\theta\right)s^{-15/8}$$
$$\times \exp\left[\cos\phi\,\tan\theta\,\frac{i\kappa}{2}s + \sec\theta\,\frac{4}{7}i\nu s^{7/4}\right]W_a(s), \quad s\to\infty, \tag{4.22}$$

for the downward-travelling Alfvén wave (with the displacement dominated by η). All the coefficients U_s, V_s, W_s, U_a, V_a and W_a are asymptotic to unity as $s\to\infty$, and we have specialised to the $m = 3/2$ polytrope. The slow MAG waves (eqs. [4.17]–[4.19]) can be distinguished from the Alfvén waves (eqs. [4.20]–[4.22]) by the direction of the displacement vector (i.e., the polarisation). The group velocity for both the Alfvén waves (eq. [3.19]) and the slow MAG waves (eq. [3.22]), and hence the direction of energy propagation, is directed along the magnetic field lines. It may be confirmed that asymptotically, as $s\to\infty$, the wave-energy flux along the field lines is constant (see §4.5 for details). Due to mode conversion in the region where $C_A \approx C_S$, oscillations (asymptotically composed of fast and slow MAG waves and Alfvén waves) decay as they propagate in the direction parallel to k (for Re$(k) \geq 0$). Therefore, for $0 \leq \theta < \pi/2$ and $0 \leq \phi < \pi/2$ ($\pi/2 < \phi \leq \pi$), slow MAG waves and Alfvén waves travelling along deeper field lines are excited by less (more) energetic waves in the conversion region. Hence, for complex κ, the asymptotic behaviours of both the slow MAG wave and the Alfvén wave are exponentially decaying (growing) with increasing depth. For complex κ, $0 \leq \theta < \pi/2$ and $\phi = \pi/2$, the asymptotic behaviours of both the slow MAG wave and the Alfvén wave are purely oscillatory. Likewise if the field is exactly vertical ($\theta = 0$).

For $m = 3/2$, in a similar fashion to CB93 and §3.3.2, the coefficients U_s, V_s and W_s may be expanded in asymptotic power series in non-positive quarter integer powers of s, and

likewise for the Alfvén wave solution, U_a, V_a and W_a. The details of the series expansions can be found in Appendix D.2. The first few terms of the series are:

$$U_s(s) \sim 1 - \frac{2}{3}i\nu \cos^2 \phi \sin\theta \tan\theta\, s^{-3/4} + \dots,$$

$$V_s(s) \sim 1 - \sec\theta\, s^{-3/4}$$
$$\times \frac{12i\kappa\nu^2 \cos\theta + \cos\phi \sin\theta\, (9\kappa^2 \cos^2\theta + 16\nu^4 \sin^2\theta)}{12\nu\, (3\kappa \cos\theta - 4i\nu^2 \cos\phi \sin\theta)} + \dots,$$

$$W_s(s) \sim 1 - \frac{\cos\phi \tan\theta}{6\nu}\, (3\kappa \cos\theta + 4i\nu^2 \cos\phi \sin\theta)\, s^{-3/4} + \dots,$$

for the slow MAG wave solution, and

$$U_a(s) \sim 1 +$$
$$\frac{12i\kappa\nu^2 \cos 2\theta + \cos\phi \sin\theta\, (16\nu^4 \sin\theta \tan\theta - 9\kappa^2 \cos\theta)}{12\nu\, (3\kappa \cos\theta + 4i\nu^2 \cos\phi \sin\theta)} s^{-3/4} + \dots,$$

$$V_a(s) \sim 1 - \frac{2}{3}i\nu \sin^2 \phi \sin\theta \tan\theta\, s^{-3/4} + \dots,$$

$$W_a(s) \sim 1 + \Big\{ \{12i\kappa\nu^2\, (\cos 2\theta - 2\cos^2\phi \sin^2\theta)$$
$$+ \cos\phi \sin\theta\, (16\nu^4 \sin\theta \tan\theta - 27\kappa^2 \cos\theta)\, \} /$$
$$(12\nu\, (3\kappa \cos\theta + 4i\nu^2 \cos\phi \sin\theta)) \Big\} s^{-3/4} + \dots,$$

for the Alfvén wave solution. The asymptotic behaviours of the slow MAG waves and the Alfvén waves are strongly influenced by both the presence of the non-vertical magnetic field and the propagation direction. The leading orders (eqs. [4.17]–[4.19] and eqs. [4.20]–[4.22], for the slow MAG waves and the Alfvén waves, respectively) and the associated asymptotic series are highly sensitive to the field inclination, θ, and the propagation direction, ϕ. When $\phi = 0$, the Alfvén waves decouple, $\zeta_a = \xi_{z_a} = 0$ (eqs. [4.20] and [4.22]) and $\eta_f = \eta_s = 0$ (eqs. [4.8] and [4.18]) for all s. In this case, the first term (after unity) in the series V_a is $-33i \cos\theta s^{-7/4}/224\nu$. In fact, for $\phi = 0$, V_a may be expanded as an asymptotic power series in non-positive integer powers of $s^{7/4}$. Also, when $\phi = 0$, the slow MAG wave solutions (eqs. [4.17] and [4.19]) reduce to the fourth order solutions (eqs. [3.29] and [3.30]). When $\phi = 90°$, the first term (after unity) in both of the series U_s and W_s is $-\kappa^2 s^{-3/2}/8\nu^2$, and the first θ-dependent term (in both series) is of order $s^{-7/4}$. With $\theta = 0$ equations (4.17) and (4.19), and the series U_s and W_s, reproduce the vertical field slow MAG wave solution (see CBZ, their eq. [2.11]). As expected, for $0 \le \phi \le \pi$, the asymptotic behaviours for both the slow MAG waves (eqs. [4.17]–[4.19]) and the Alfvén waves (eqs. [4.20]–[4.22]) break down in the horizontal field, singular limit ($\theta \to 90°$).

68

4.3 The top boundary

As in Chapter 3, the boundary conditions at the surface of the complete polytrope, $s = 0$, are that all components of the displacement vector, $\boldsymbol{\xi}$, have a finite magnitude, and that the magnetic field perturbations match smoothly onto a vacuum potential magnetic field (see Appendix B) that vanishes as $s \to -\infty$. The relevant equations in the $\phi \neq 0$ case are then:

$$\frac{d\xi_u}{ds} = \frac{\kappa}{2}\xi_u \quad \text{at} \quad s = 0, \tag{4.23}$$

and

$$D_\parallel \eta + \sin\phi \sin\theta \,\tilde{\nabla} \cdot \boldsymbol{\xi} = 0 \quad \text{at} \quad s = 0, \tag{4.24}$$

where $\xi_u = \cos\theta\,\zeta - \cos\phi\sin\theta\,\xi_z$ is the component of the displacement perpendicular to the magnetic field, $\mathbf{B}$, and parallel to the propagation direction, $\mathbf{k}$. When $\phi = 0$, condition (4.23) reproduces the boundary condition imposed in the fourth order case (eq. [3.31]), and condition (4.24) recovers the boundary condition that would be imposed on the Alfvén waves (i.e., $D_\parallel \eta = 0$ at $s = 0$, see BC97 for the vertical field case). An interesting implication of condition (4.24) is that η, the incompressive component of the displacement vector, is coupled to the fluid compressibility, $\tilde{\nabla} \cdot \boldsymbol{\xi} = i\kappa\zeta/2 - \xi_z'$, at $s = 0$, except where the field is exactly vertical ($\theta = 0$) or $\phi = 0$.

In terms of the independent variable $\sigma = s^{1/2}$, the ($m = 3/2$) governing equations are

$$\left[\cos^2\theta \left(\frac{d^2}{d\sigma^2} - \frac{1}{\sigma}\frac{d}{d\sigma} - \kappa^2\sigma^2\right) - \sin^2\phi \sin^2\theta \,\kappa^2\sigma^2\right]\zeta$$
$$+\sigma^5\left(4\nu^2 - \kappa^2\sigma^2\right)\zeta - i\kappa\sigma^5\left[\sigma\frac{d}{d\sigma} + 3\right]\xi_z$$
$$-\sin\theta\left[\cos\phi\cos\theta\left(\frac{d^2}{d\sigma^2} - \frac{1}{\sigma}\frac{d}{d\sigma} - \kappa^2\sigma^2\right) + i\kappa\sin^2\phi\sin\theta\,\sigma\frac{d}{d\sigma}\right]\xi_z$$
$$= i\kappa\sin\phi\sin\theta\,\sigma\left[\cos\theta\frac{d}{d\sigma} - i\kappa\cos\phi\sin\theta\,\sigma\right]\eta, \tag{4.25}$$

$$\left[\cos^2\theta\left(\frac{d^2}{d\sigma^2} - \frac{1}{\sigma}\frac{d}{d\sigma}\right) + 4\nu^2\sigma^5\right]\eta$$
$$-i\kappa\cos\phi\sin\theta\,\sigma\left[2\cos\theta\frac{d}{d\sigma} - i\kappa\cos\phi\sin\theta\,\sigma\right]\eta$$
$$= i\kappa\sin\phi\sin\theta\,\sigma\left[\cos\theta\frac{d}{d\sigma} - i\kappa\cos\phi\sin\theta\,\sigma\right]\zeta$$
$$-\sin\phi\sin\theta\left[\cos\theta\frac{d}{d\sigma} - \left(i\kappa\cos\phi\sin\theta\,\sigma^2 + \cos\theta\right)\frac{1}{\sigma}\right]\frac{d\xi_z}{d\sigma}, \tag{4.26}$$

and

69

$$\sin^2\theta \left[\frac{d^2}{d\sigma^2} - \frac{1}{\sigma}\frac{d}{d\sigma} - \cos^2\phi\,\kappa^2\sigma^2 \right] \xi_z$$

$$+\sigma^5 \left[\frac{d^2}{d\sigma^2} + \frac{4}{\sigma}\frac{d}{d\sigma} + 4\nu^2 \right] \xi_z - i\kappa\sigma^5 \left[\sigma\frac{d}{d\sigma} + 2 \right] \zeta$$

$$-\sin\theta \left[\cos\phi\,\cos\theta \left(\frac{d^2}{d\sigma^2} - \frac{1}{\sigma}\frac{d}{d\sigma} - \kappa^2\sigma^2 \right) + i\kappa\sin^2\phi\,\sin\theta\,\sigma\frac{d}{d\sigma} \right] \zeta$$

$$= -\sin\phi\,\sin\theta \left[\cos\theta\,\frac{d}{d\sigma} - \left(i\kappa\cos\phi\,\sin\theta\,\sigma^2 + \cos\theta \right) \frac{1}{\sigma} \right] \frac{d\eta}{d\sigma}, \qquad (4.27)$$

and the point $\sigma = 0$ ($s = 0$) is a regular singular point (as in §3.4). Substituting the Frobenius series expansions

$$\zeta(\sigma) = \sum_{n=0}^{\infty} u_n \sigma^{n+r}, \quad \eta(\sigma) = \sum_{n=0}^{\infty} v_n \sigma^{n+r}, \quad \text{and} \quad \xi_z(\sigma) = \sum_{n=0}^{\infty} w_n \sigma^{n+r}, \qquad (4.28)$$

into equations (4.25)-(4.27) yields six linearly independent solutions, none of which contain a logarithm. Three solutions have $r = 0$, two solutions have $r = 2$ and one (unphysical) solution has $r = -3$.

Labelling the five finite, linearly independent solutions a, b, c, d and e, the general solution may be written $\zeta = A\zeta_a + B\zeta_b + C\zeta_c + D\zeta_d + E\zeta_e$, and similarly for η and ξ_z (where A, B, C, D, and E are arbitrary constants). Developing the series (see Appendix D.3 for details) and imposing the two remaining boundary conditions (4.23) and (4.24), it may be shown that

$$D = \frac{1}{10} \left(5\kappa + 2\cos\phi\,\tan\theta \left(i\kappa - 2\nu^2\cos\phi\,\tan\theta \right) \right) A$$

$$+\frac{2}{5}\nu^2\cos\phi\,\sin\phi\,\tan^2\theta\,B$$

$$+\frac{1}{10}\cos\phi\,\tan\theta \left(3i\kappa\cos\phi\,\tan\theta - 4\nu^2 - 5\kappa \right) C,$$

and

$$E = \frac{1}{10}\tan\theta \left\{ \sin\phi \left(4\cos\phi\,\tan\theta\,\nu^2 + 3i\kappa \right) A \right.$$

$$+ \left(5i\kappa\cos\phi - 4\nu^2\sin^2\phi\,\tan\theta \right) B$$

$$\left. + \sin\phi \left(4\nu^2 - 3i\kappa\cos\phi\,\tan\theta \right) C \right\}.$$

The physically acceptable resulting solution is then

$$\begin{pmatrix} \zeta \\ \eta \\ \xi_z \end{pmatrix} = A \begin{pmatrix} \zeta_A \\ \eta_A \\ \xi_{zA} \end{pmatrix} + B \begin{pmatrix} \zeta_B \\ \eta_B \\ \xi_{zB} \end{pmatrix} + C \begin{pmatrix} \zeta_C \\ \eta_C \\ \xi_{zC} \end{pmatrix} \qquad (4.29)$$

where the leading terms of each series, in terms of s, are:

$$\zeta_A = 1 + \frac{1}{10} \left(5\kappa + 2\cos\phi\tan\theta \left(i\kappa - 2\nu^2\cos\phi\tan\theta\right)\right) s + \dots ,$$

$$\eta_A = \frac{1}{10}\sin\phi\tan\theta \left(4\cos\phi\tan\theta\,\nu^2 + 3i\kappa\right) s + \dots , \qquad (4.30)$$

$$\xi_{z_A} = \frac{1}{5}\left(i\kappa - 2\cos\phi\tan\theta\,\nu^2\right) s + \dots ;$$

$$\zeta_B = \frac{2}{5}\nu^2\cos\phi\sin\phi\tan^2\theta\,s + \dots ,$$

$$\eta_B = 1 + \frac{1}{10}\tan\theta \left(5i\kappa\cos\phi - 4\nu^2\sin^2\phi\tan\theta\right) s + \dots , \qquad (4.31)$$

$$\xi_{z_B} = \frac{2}{5}\nu^2\sin\phi\tan\theta\,s + \dots ;$$

and

$$\zeta_C = \frac{1}{10}\cos\phi\tan\theta \left(3i\kappa\cos\phi\tan\theta - 4\nu^2 - 5\kappa\right) s + \dots ,$$

$$\eta_C = \frac{1}{10}\sin\phi\tan\theta \left(4\nu^2 - 3i\kappa\cos\phi\tan\theta\right) s + \dots , \qquad (4.32)$$

$$\xi_{z_C} = 1 + \frac{1}{10}\left(3i\kappa\cos\phi\tan\theta - 4\nu^2\right) s + \dots ;$$

and A, B and C are the remaining arbitrary constants. The first non-integer powers to appear in these expansions are $s^{7/2}$ in ζ_A, η_B and ζ_C, and $s^{9/2}$ in η_A, ξ_{z_A}, ζ_B, ξ_{z_B}, η_C and ξ_{z_C}. When $\phi = 0$, the Alfvén waves decouple, $\zeta_B = \xi_{z_B} = 0$ (eq. [4.31]) and $\eta_A = \eta_C = 0$ (eqs. [4.30] and [4.32]) for all s. Also, when $\phi = 0$, ζ_A and ξ_{z_A} (eq. [4.30]) and ζ_C and ξ_{z_C} (eq. [4.32]) reproduce the fourth order solutions (eqs. [3.36] and [3.37]). When $\phi = 90°$, the first term in the ζ_B expansion (eq. [4.31]) is $2i\kappa\nu^2\sec^2\theta\tan\theta\,s^{9/2}/105$, and the first term in the ζ_C expansion (eq. [4.32]) is $3i\kappa\sec^2\theta\,s^{7/2}/35$. For $0 \le \phi \le \pi$, as in the fourth order case, the series expansions (4.30)-(4.32) break down in the horizontal field, singular limit ($\theta \to 90°$). The system of differential equations (4.1)-(4.3) has singularities only at $s = 0$ and $s = \infty$. Therefore, the Frobenius series (4.30)-(4.32) have infinite radius of convergence. However, as in the fourth order case, the series (4.30)-(4.32) are only used to start the numerical integrations in the neighbourhood of $s = 0$.

4.4 Bidirectional shooting method

The complex sixth order boundary value problem, consisting of the sixth order system of differential equations (4.1)-(4.3) and the six boundary conditions, is solved using a bidirectional shooting method in exactly the same fashion as §3.6. For specified dimensionless frequency, ν, inclination, θ, and propagation direction, ϕ, the eigenfunction is the linear combination

71

of the six solutions that satisfy the boundary conditions. The eigenvalue is the value of the dimensionless wavenumber, κ, for which the linear combination exists.

Throughout the complete polytrope, $s \in [0, \infty)$, we express the full, physically acceptable solution as

$$
\begin{pmatrix} \zeta \\ \eta \\ \xi_z \end{pmatrix} = \begin{cases} \beta_A \begin{pmatrix} \zeta_A \\ \eta_A \\ \xi_{z_A} \end{pmatrix} + \beta_B \begin{pmatrix} \zeta_B \\ \eta_B \\ \xi_{z_B} \end{pmatrix} + \beta_C \begin{pmatrix} \zeta_C \\ \eta_C \\ \xi_{z_C} \end{pmatrix}, & \text{if } s < s_m, \\[3mm] \beta_s \begin{pmatrix} \zeta_s \\ \eta_s \\ \xi_{z_s} \end{pmatrix} + \beta_a \begin{pmatrix} \zeta_a \\ \eta_a \\ \xi_{z_a} \end{pmatrix} + \beta_f \begin{pmatrix} \zeta_f \\ \eta_f \\ \xi_{z_f} \end{pmatrix}, & \text{if } s > s_m, \end{cases}
\tag{4.33}
$$

where s_m is the matching point. The matching conditions, that ζ, η, ξ_z, ζ', η' and ξ_z' are all continuous at s_m, can then be expressed in matrix form as

$$
\begin{pmatrix} -\zeta_A & -\zeta_B & -\zeta_C & \zeta_s & \zeta_a & \zeta_f \\ -\eta_A & -\eta_B & -\eta_C & \eta_s & \eta_a & \eta_f \\ -\xi_{z_A} & -\xi_{z_B} & -\xi_{z_C} & \xi_{z_s} & \xi_{z_a} & \xi_{z_f} \\ -\zeta_A' & -\zeta_B' & -\zeta_C' & \zeta_s' & \zeta_a' & \zeta_f' \\ -\eta_A' & -\eta_B' & -\eta_C' & \eta_s' & \eta_a' & \eta_f' \\ -\xi_{z_A}' & -\xi_{z_B}' & -\xi_{z_C}' & \xi_{z_s}' & \xi_{z_a}' & \xi_{z_f}' \end{pmatrix} \begin{pmatrix} \beta_A \\ \beta_B \\ \beta_C \\ \beta_s \\ \beta_a \\ \beta_f \end{pmatrix} = 0,
\tag{4.34}
$$

where all of the displacements and their derivatives in equation (4.34) are evaluated at $s = s_m$.

As in §3.6, the boundary conditions are homogeneous, therefore, we can set $\beta_A = 1$ for convenience. Given ν, θ, ϕ, and an initial guess for κ, we calculate the six solutions at $s = s_m$, then solve the first five rows of equation (4.34) for the β's:

$$
\begin{pmatrix} -\zeta_B & -\zeta_C & \zeta_s & \zeta_a & \zeta_f \\ -\eta_B & -\eta_C & \eta_s & \eta_a & \eta_f \\ -\xi_{z_B} & -\xi_{z_C} & \xi_{z_s} & \xi_{z_a} & \xi_{z_f} \\ -\zeta_B' & -\zeta_C' & \zeta_s' & \zeta_a' & \zeta_f' \\ -\eta_B' & -\eta_C' & \eta_s' & \eta_a' & \eta_f' \end{pmatrix} \begin{pmatrix} \beta_B \\ \beta_C \\ \beta_s \\ \beta_a \\ \beta_f \end{pmatrix} = \begin{pmatrix} \zeta_A \\ \eta_A \\ \xi_{z_A} \\ \zeta_A' \\ \eta_A' \end{pmatrix}.
$$

With these determined, the remaining equation,

$$
F(\kappa) = -\xi_{z_A}' - \beta_B \xi_{z_B}' - \beta_C \xi_{z_C}' + \beta_s \xi_{z_s}' + \beta_a \xi_{z_a}' + \beta_f \xi_{z_f}'
$$

must be zero if κ is an eigenvalue, but in general is not. Hence, κ must be iteratively adjusted until $F(\kappa) = 0$ is satisfied to an adequate tolerance.

4.5 Wave energy flux

The oscillations (π-modes) lose energy as a result of the slow MAG waves and/or the Alfvén waves travelling out of the bottom of the atmosphere. An interesting question is what fraction

of the energy loss is a consequence of slow MAG waves as distinct from the Alfvén waves. To answer this we calculate the wave energy flux of each mode as $z \to -\infty$.

The instantaneous wave energy flux associated with the linearised MHD equations is (e.g., Bray and Loughhead, 1974, p. 252)

$$\mathbf{F} = \left(p_1 + \frac{1}{\mu_B}\mathbf{B} \cdot \mathbf{B}_1\right)\mathbf{v} - \frac{1}{\mu_B}(\mathbf{B}_1 \cdot \mathbf{v})\mathbf{B}, \tag{4.35}$$

where $\mathbf{B}$ is the background magnetic field (eq. [3.1]), $p_1 = \mathrm{Re}\{\tilde{p}_1(z)\exp[i(\mathbf{k}\cdot\mathbf{r} - \omega t)]\}$ is the Eulerian pressure perturbation, $\mathbf{B}_1 = \mathrm{Re}\{\tilde{\mathbf{B}}_1(z)\exp[i(\mathbf{k}\cdot\mathbf{r} - \omega t)]\}$ is the Eulerian magnetic field perturbation, $\mathbf{v} = -\mathrm{Re}\{i\omega\boldsymbol{\xi}(z)\exp[i(\mathbf{k}\cdot\mathbf{r} - \omega t)]\}$ is the velocity (for convenience, the tilde notation is not used for the Fourier transformed displacement vector, $\boldsymbol{\xi}(z) = \zeta(z)\hat{\mathbf{k}} + \eta(z)\hat{\mathbf{k}}_\perp + \xi_z(z)\hat{\mathbf{e}}_z$), and μ_B denotes the magnetic permeability.

The time-averaged wave energy flux, of an individual mode (overtone) at an individual frequency, is defined as

$$\langle \mathbf{F} \rangle = \frac{\omega}{2\pi}\int_{-\pi/\omega}^{\pi/\omega}\mathbf{F}\,dt.$$

The net flux can be calculated by summing $\langle\mathbf{F}\rangle$ over all modes and integrating over all frequencies. The time-averaged wave energy flux corresponding to equation (4.35) is

$$\langle \mathbf{F} \rangle = \frac{\omega}{2}\,\mathrm{Re}\left[i\left(\tilde{p}_1 + \frac{1}{\mu_B}\mathbf{B}\cdot\tilde{\mathbf{B}}_1\right)\boldsymbol{\xi}^* - \frac{i}{\mu_B}\left(\tilde{\mathbf{B}}_1\cdot\boldsymbol{\xi}^*\right)\mathbf{B}\right]\exp\left(-2\,\mathrm{Im}(k)\hat{\mathbf{k}}\cdot\mathbf{r}\right). \tag{4.36}$$

To calculate the energy carried off by the slow MAG waves and the Alfvén waves it is sufficient to evaluate equation (4.36) asymptotically for $z \to -\infty$. The amplitude of the fast MAG wave component of the π-modes decreases exponentially with depth, and so the fast MAG waves do not contribute to the asymptotic energy flux. In a homogeneous magnetofluid, the Alfvén wave Eulerian gas and magnetic pressure perturbations vanish identically. On the other hand, for the slow magnetoacoustic waves in a homogeneous magnetofluid, with $C_A \ll C_S$, the gas and magnetic pressure perturbations are out of phase and cancel. In the stratified atmosphere the situation is similar, though to gain a complete understanding the leading orders (eqs. [4.17]–[4.19] for the slow MAG waves and eqs. [4.20]–[4.22] for the Alfvén waves) and the associated asymptotic series must be employed. For the slow MAG waves the amplitude of the gas pressure perturbation,

$$\frac{\tilde{p}_1}{\zeta_s} \sim \frac{2}{3}i\nu\rho_0 g\cos\phi\,\sin\theta\,s^{3/4}, \quad s \to \infty,$$

and the magnetic pressure perturbation,

$$\frac{\frac{1}{\mu_B}\mathbf{B}\cdot\tilde{\mathbf{B}}_1}{\zeta_s} \sim -\frac{2}{3}i\nu\rho_0 g\cos\phi\,\sin\theta\,s^{3/4}, \quad s \to \infty,$$

both increase with depth. However, these leading behaviours are out of phase and partially cancel. The resultant total pressure perturbation associated with the slow MAG waves,

73

$$\frac{\tilde{p}_1 + \frac{1}{\mu_B}\mathbf{B} \cdot \tilde{\mathbf{B}}_1}{\zeta_s} \sim \rho_0 g \cos\phi \sin\theta \cos\theta\, s^{-1}, \quad s \to \infty,$$

decreases with depth. Likewise, for the Alfvén waves. The amplitude of the gas pressure perturbation,

$$\frac{\tilde{p}_1}{\eta_a} \sim -\frac{2}{3} i\nu\rho_0 g \sin\phi \sin\theta\, s^{3/4}, \quad s \to \infty,$$

and the magnetic pressure perturbation,

$$\frac{\frac{1}{\mu_B}\mathbf{B} \cdot \tilde{\mathbf{B}}_1}{\eta_a} \sim \frac{2}{3} i\nu\rho_0 g \sin\theta\, s^{3/4}, \quad s \to \infty,$$

both increase with depth, but the resultant total pressure perturbation,

$$\frac{\tilde{p}_1 + \frac{1}{\mu_B}\mathbf{B} \cdot \tilde{\mathbf{B}}_1}{\eta_a} \sim -\rho_0 g \sin\phi \sin\theta \cos\theta\, s^{-1}, \quad s \to \infty,$$

decreases with depth. Consequently, for the slow MAG waves and the Alfvén waves, only the third term of equation (4.36) contributes to the wave energy flux at great depth.

Rewriting the third term of equation (4.36) one obtains

$$\langle \mathbf{F} \rangle \sim -\frac{\omega}{2}\frac{\mathbf{B}^2}{\mu_B} \mathrm{Re}\left[i\left(\zeta^* \partial_\parallel \zeta + \eta^* \partial_\parallel \eta + \xi_z^* \partial_\parallel \xi_z - \xi_\parallel^* \nabla \cdot \boldsymbol{\xi}\right)\right] \exp\left(-2\,\mathrm{Im}\,(k)\,\hat{\mathbf{k}} \cdot \mathbf{r}\right)\hat{\mathbf{B}},$$
$$z \to -\infty, \quad (4.37)$$

where $\xi_\parallel = \sin\theta\, \xi_x + \cos\theta\, \xi_z$ is the component of the displacement parallel to the background magnetic field. Equation (4.37) indicates that, asymptotically as $z \to -\infty$, the direction of the wave energy flux is parallel to the background magnetic field. This was to be expected as the group velocities for both the Alfvén waves (eq. [3.19]) and the slow MAG waves (eq. [3.22]) are directed along the magnetic field.

It is convenient to consider the distance, in the x-direction, from the magnetic field line that passes through the origin. This is given by

$$x' = x - \tan\theta\, z.$$

Hence, two points lying on the same field line have the same x'-coordinate (and y-coordinate). In the asymptotic limit $z \to -\infty$, it can be shown that equation (4.37) yields a wave energy flux that is constant along the magnetic field,

$$\lim_{z \to -\infty} \langle \mathbf{F} \rangle = -F_0 \left(|\beta_s|^2 + |\beta_a|^2\right) \nu^2 \exp\left[-2\,\mathrm{Im}\,(k)\left(\cos\phi\, x' + \sin\phi\, y\right)\right]\hat{\mathbf{B}}, \quad (4.38)$$

74

where $F_0 = 2^{1/2}3^{-3/2}g^{3/2}L^{-1/2}\rho_0$, and β_s and β_a are the complex amplitudes arising from the matching procedure (see eq. [4.33]). The contributions to the asymptotic wave energy flux by the slow MAG waves ($\propto |\beta_s|^2$) and the Alfvén waves ($\propto |\beta_a|^2$) are easily identified from equation (4.38). For $\theta = 0$ or $\phi = 0$ the Alfvén waves decouple (i.e., $\beta_a = 0$) and, therefore, do not contribute to the energy flux. The slow MAG waves and the Alfvén waves are asymptotically independent (non-interacting) modes of oscillation, hence, equation (4.38) contains no cross terms.

For $\text{Im}(k) \neq 0$, the π-modes lose energy as they propagate through the atmosphere due to the slow MAG waves and/or the Alfvén waves travelling down the field lines. Conservation of energy, therefore, requires that the (time-averaged) wave energy density of the π-modes declines in accordance with equation (4.38). The extinction length $1/\text{Im}(2k) = L/\text{Im}(\kappa)$ is the distance in the (x,y)-plane (at fixed depth) over which the wave energy density decays by a factor e. The extinction length is a measure of the energy loss suffered by a π-mode as it travels through the atmosphere. If $\text{Im}(k) = 0$, there is no energy loss (neither the slow MAG waves nor the Alfvén waves are not excited), and consequently, the extinction length is infinite. On the other hand, for $\text{Im}(k) \neq 0$, the extinction length is finite, and shorter extinction lengths are associated with oscillations that lose energy more rapidly than those with longer extinction lengths. The extinction length, for $\phi = 0$, was discussed in §3.7.2.

The fractional contributions by the slow MAG waves and the Alfvén waves to the asymptotic wave energy flux (eq. [4.38]) are

$$F_s = \frac{|\beta_s|^2}{|\beta_s|^2 + |\beta_a|^2}, \quad \text{and} \quad F_a = \frac{|\beta_a|^2}{|\beta_s|^2 + |\beta_a|^2},$$

respectively. Obviously $F_s + F_a = 1$, so it is straightforward to derive one of F_s or F_a from the other. In §4.6 we present the eigenvalues, κ, along with the contribution by the Alfvén waves to asymptotic wave energy flux F_a.

4.6 Results and discussion

As explained in §4.4 we calculate complex dimensionless wavenumber eigenvalues, κ, for specified real dimensionless frequency, ν, field inclination, θ, and propagation direction, ϕ. For propagation parallel to the x-axis ($\phi = 0$) in non-vertical field ($\theta \neq 0$), eigensurfaces were built up over the (ν, θ)-plane (see §3.7). For propagation in directions not parallel to the x-axis (i.e., $\phi \neq 0$), the eigenvalues depend on three independent variables: ν, θ, and ϕ, and an additional dependent variable: the contribution by the Alfvén waves to asymptotic wave energy flux, F_a, must also be considered. Firstly, in §4.6.1, we survey the variation of κ and F_a over the (ϕ, θ)-plane at several fixed frequencies. In §4.6.2, for direct comparison with the two-dimensional non-vertical field results, we present eigensurfaces of κ over the (ν, θ)-plane at fixed ϕ, in a similar fashion to Figures 3.5 – 3.8. We also show "traditional" plots of κ (and F_a) as a function of ν with fixed θ and ϕ. The extinction lengths are examined in §4.6.5. Some additional results are supplied in Appendix D.4. Without loss of generality, the parameter space search only needs to focus on the region $\nu \geq 0$, $0 \leq \theta < 90°$, $0 \leq \phi \leq 180°$, $\text{Re}(\kappa) \geq 0$ and $\text{Im}(\kappa) \geq 0$.

75

4.6.1 Eigenvalue topology: variation with both field inclination and propagation direction

Figure 4.1 shows the variation of $\mathrm{Re}\,(\kappa)$, $\mathrm{Im}\,(\kappa)$, and F_a as a function of both field inclination, θ, and propagation direction, ϕ, at fixed dimensionless frequency, $\nu = 0.5$, for two different modes, $n = 0$ (Fig. 4.1(a)) and $n = 1$ (Fig. 4.1(b)). Each point on these eigensurfaces has been generated starting from the corresponding vertical field mode (i.e., $\theta = 0$ and $\phi = 0$, see Fig. 3.3) then stepping from $\theta = 0$ to $\theta = 85°$ whilst holding the frequency ($\nu = 0.5$) and the propagation direction constant. The shading of the eigensurfaces (upper two panels) is used to highlight contrast only and does not indicate the height of the eigenvalue. For the contour-density plots of F_a, dark areas indicate regions where the asymptotic wave energy flux is dominated by the Alfvén waves, whereas light areas indicate regions where the asymptotic flux is dominated by the slow MAG waves. In an analogous fashion, Figures D.1(a), D.1(b), D.2(a), and D.2(b) show $\mathrm{Re}\,(\kappa)$, $\mathrm{Im}\,(\kappa)$, and F_a as a function of both θ and ϕ for $n = 2, 3, 4$, and 5, respectively (with $\nu = 0.5$). In addition, Figures 4.2 – 4.3 and Figures D.3 – D.6 show the variation of $\mathrm{Re}\,(\kappa)$, $\mathrm{Im}\,(\kappa)$, and F_a as a function of both θ and ϕ at several other fixed frequencies. Figures 4.2(a), 4.2(b), D.3(a), D.3(b), D.4(a), and D.4(b) for $\nu = 1.5$ and $n = 0$, 1, 2, 3, 4, and 5, respectively. Figures 4.3(a), 4.3(b), D.5(a), D.5(b), D.6(a), and D.6(b) for $\nu = 3$ and $n = 1, 2, 3, 4, 5$, and 6, respectively (note: the $n = 0$ vertical field mode does not exist for $\nu \gtrsim 2.5$, e.g., Fig. 3.3).

The symmetry of κ about $\phi = 90°$ is clearly evident in the upper two panels of each of Figures 4.1 – 4.3 and Figures D.1 – D.6, with the eigenvalues in the region $0 \leq \phi \leq 90°$ a mirror image of those in $90° \leq \phi \leq 180°$ (i.e., $\kappa\,(\nu, \theta, \phi) = \kappa\,(\nu, \theta, 180° - \phi)$). This property is consistent with the fourth order results (§3.7). We have not been able to prove the symmetry is generally the case, but do not have a counterexample. On the other hand, F_a (bottom panels) is generally not symmetric about $\phi = 90°$. Subsequently, in what follows, we often refer to the eigenvalues only in the region $0 \leq \phi \leq 90°$, in these cases it is implied that the reference applies identically to the region $90° \leq \phi \leq 180°$ (by the symmetry $\kappa\,(\phi) = \kappa\,(180° - \phi)$).

For each mode, n, the behaviour of the eigenvalues over the (θ, ϕ)-plane when $\nu = 0.5$ (Figs. 4.1, D.1, and D.2, upper two panels) is typical of low frequencies in general ($\nu \lesssim 1$). Likewise, for lower frequencies, the behaviour of the $n = 1$ eigensurface is typical of the higher order modes $n \geq 2$. Hence, we concentrate on the $n = 0$ and $n = 1$ modes and only refer to the higher order modes (see Appendix D.4) where significant differences exist (e.g., in the variation of F_a). For all modes with $\nu \lesssim 1$, $\mathrm{Re}\,(\kappa)$ increases monotonically with increasing ϕ in the interval $0 \leq \phi \leq 90°$. This is true for all $\theta > 0$, but is most pronounced for larger inclinations. For the $n = 0$ mode at fixed propagation direction $\phi \approx 90°$, $\mathrm{Re}\,(\kappa)$ increases monotonically with field inclination; whereas for $\phi \approx 0$, $\mathrm{Re}\,(\kappa)$ decreases with θ, to a minimum at $\theta \approx 40° - 70°$ (depending on ν), and increases with θ for larger inclinations. For modes with $n \geq 1$ at all fixed propagation directions, $\mathrm{Re}\,(\kappa)$ decreases with increasing θ, to a minimum at $\theta \approx 60° - 75°$ (depending on ν and n, the decrease is greatest for $\phi \approx 0$), for larger inclinations $\mathrm{Re}\,(\kappa)$ varies only slightly with θ. The middle panels of Figures 4.1 show that the variation of $\mathrm{Im}\,(\kappa)$ with ϕ is effectively negligible for $\theta \lesssim 70°$. In contrast, for highly inclined field ($\theta \gtrsim 70°$), the variation of $\mathrm{Im}\,(\kappa)$ with ϕ is much greater (relatively speaking).
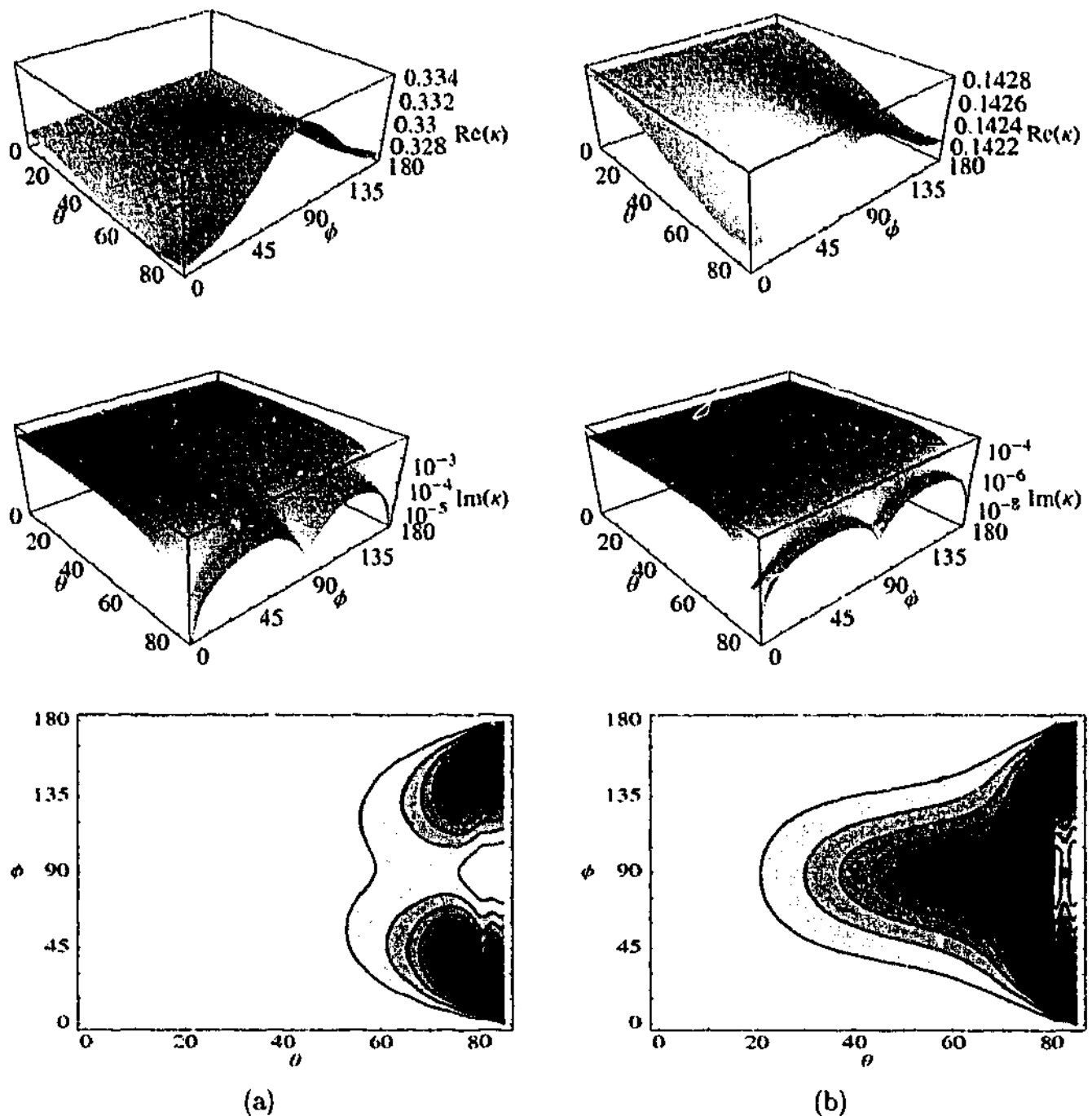
Figure 4.1: Eigenvalues, κ, and the contribution by the Alfvén waves to asymptotic wave energy flux, F_a, as a function of of field inclination, θ, and propagation direction, ϕ (angles are in degrees). On both sides the *top panel* shows the real part of κ as a function of θ and ϕ and the *middle panel* shows the corresponding imaginary part of κ. The shading of the eigensurfaces is used to highlight contrast only and does not indicate the height of the eigenvalue. The *bottom panel* shows F_a as a function of θ and ϕ, corresponding to the eigenvalues shown in the upper two panels. The contours are of $F_a = 0.1, 0.2, \ldots, 0.9$, with the lightest shading indicating $0 < F_a < 0.1$ (i.e., an asymptotic flux dominated by the slow MAG waves) and the darkest $0.9 < F_a < 1$ (dominated by the Alfvén waves). The domain for these plots is $0 \le \theta \le 85°$, $0 \le \phi \le 180°$. For all of these plots the frequency is fixed at $\nu = 0.5$. (a) $n = 0$. (b) $n = 1$.

In the region $\theta \gtrsim 70°$, Im (κ) has a maximum at $\phi \approx 45°$ - several orders of magnitude greater than the $\phi = 0$ case for the largest inclinations, and a minimum at $\phi = 90°$ – also greater than the $\phi = 0$ level for the largest inclinations. For the $n = 0$ mode, Im (κ) decreases monotonically and rapidly with θ for all fixed ϕ. For modes with $n \geq 1$, except for the $n = 1$ mode when $\phi \approx 90°$ (where Im (κ) decreases monotonically with θ), Im (κ) grows with increasing θ to maximum at $\theta \approx 20° - 60°$, up to several orders of magnitude greater than the corresponding vertical field case (most obvious for the higher order modes, e.g., Figs. D.1 – D.2); for larger inclinations Im (κ) decreases rapidly with θ. Therefore, despite the enhancement in the ϕ-direction in highly inclined field ($\theta \gtrsim 70°$), Im (κ) is largest in vertical field for the $n = 0$ mode and moderately inclined field ($\theta \approx 20° - 60°$) for modes with $n \geq 1$, for all propagation directions – a very similar conclusion was reached in the fourth order case, §3.7.

For the $n = 0$ and $n = 1$ eigensurfaces, over the (θ, ϕ)-plane, a dramatic topological transition takes place at frequencies in the interval $1 \leq \nu \leq 1.5$. This is evident in Figure 4.2 with a cut appearing in both the $n = 0$ and $n = 1$ eigensurfaces along $\phi \approx 30°$ (with vertex at $\theta \approx 30°$). Across the cut, the $n = 0$ surface (Fig. 4.2(a)) matches onto the $n = 1$ surface (Fig. 4.2(b)), forming a single sheet. The vertex of the cut occurs at the same location for Re (κ), Im (κ), and F_a. Hence, the vertex represents a "crossing", where the eigenvalues of the two overtones coincide. This type of behaviour was also found in the fourth order case (over the (ν, θ)-plane, see §3.7). The eigenvalues for the higher order modes ($n \geq 2$, e.g., Fig. D.3 – D.4) do not exhibit this complicated topology. Their behaviour is very similar to the corresponding modes at lower frequencies (e.g., Fig. D.1 · D.2, discussed above), except for small inclinations ($\theta \lesssim 20°$), where Re (κ) decreases monotonically with ϕ for modes with $n \geq 1$ in the interval $0 \leq \phi \leq 90°$. For the $n = 0$ and $n = 1$ modes (Fig. 4.2(a) and 4.2(b), respectively) with propagation directions greater than the cut ($30° \lesssim \phi \lesssim 150°$), the variation of both Re (κ) and Im (κ) is broadly similar to the corresponding modes at lower frequencies (e.g., Fig. 4.1, upper two panels). Though there are some exceptions. For the $n = 0$ mode (with $30° \lesssim \phi \lesssim 150°$), Im (κ) still decreases monotonically with θ though less rapidly than at lower frequencies – giving the impression that Im (κ) plateaus at larger inclinations (e.g., Fig. 4.2(a), middle panel). For the $n = 1$ mode, Im (κ) does not vary significantly with ϕ less than the cut, except in highly inclined fields, where Im (κ) actually increases slightly with θ for propagation directions in the range $\phi \approx 20° - 25°$ (this also occurs on the $n = 0$ surface for $\phi \approx 30° - 45°$). Also for the $n = 1$ mode (Fig. 4.2(b), middle panel), the imaginary part attains a local maximum in the neighbourhood of the vertex of the cut ($\theta \approx 25°$, $\phi \approx 30°$), though the peak is not significantly greater than the $\phi = 0$ case; for $30° \lesssim \phi \lesssim 90°$ this Im (κ) peak diminishes gradually with increasing ϕ.

In the interval $1.5 \lesssim \nu \lesssim 3$, the topology of the eigensurfaces over the (θ, ϕ)-plane continues to vary – due the behaviour of the $n = 0$ eigenmode (i.e., the sequence of cuts connecting all eigenmodes, as seen in Fig. 3.5). We do not concern ourselves with the fine details of this here (the topology over the (ν, θ)-plane is considered in detail in the next subsection). When $\nu = 3$, the $n = 0$ vertical field mode does not exist, and each of the $n = 1, 2,$ and 3 eigensurfaces possess two cuts (along $\phi \approx 42°$ and $\phi \approx 138°$, with vertices at $\theta \approx 45°$ for $n = 1$, and at $\theta \approx 20°$ for $n = 2$ and 3). For $20° \lesssim \theta \lesssim 40°$, the $n = 2$ and $n = 3$ surfaces match across both sides of the cut. For larger inclinations ($\theta \lesssim 45°$) the
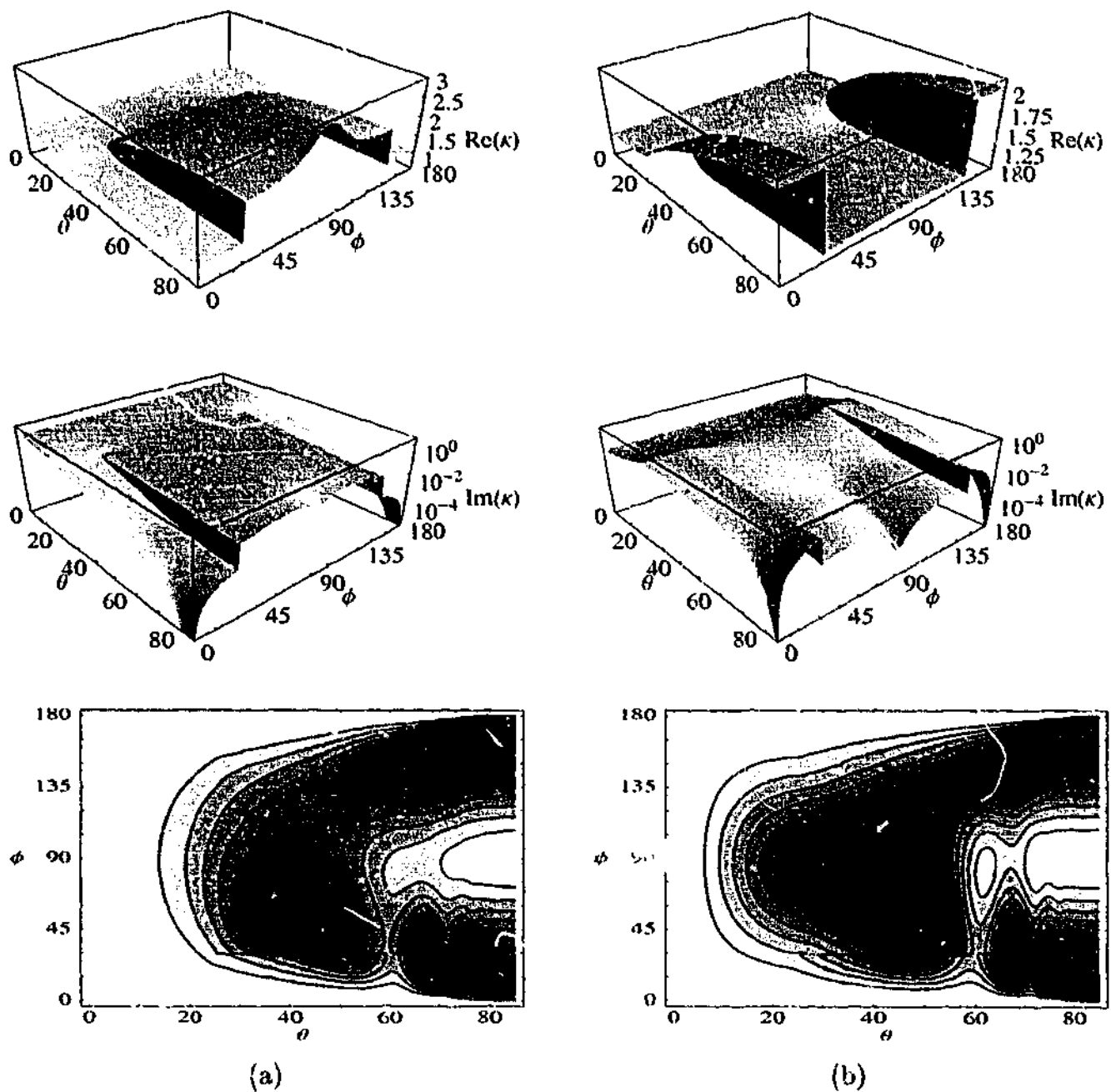
78

Figure 4.2: Same as Figure 4.1 except $\nu = 1.5$. (a) $n = 0$. (b) $n = 1$.

matching is more complicated. The low ϕ side of the cut in the $n = 1$ surface (Fig. 4.3(a)) matches onto the high ϕ side of the cut in the $n = 3$ surface, the low ϕ side of the cut in $n = 2$ (Fig. 4.3(b)) matches onto the high ϕ side of the cut in $n = 1$, and the low ϕ side of the cut in $n = 3$ (Fig. D.5(a)) matches onto the high ϕ side of the cut in $n = 2$. Hence a single surface is formed by the three eigensurfaces. The topology aside, there are several changes to the variation of the eigenvalues (over the (θ, ϕ)-plane) when $\nu = 3$ that warrant discussion. For ϕ less than the cut in the $n = 1$ surface (Fig. 4.3(a)) and above the cut in the $n = 3$ surface (Fig. D.5(a)), at lower inclinations the imaginary parts of the eigenvalues

79
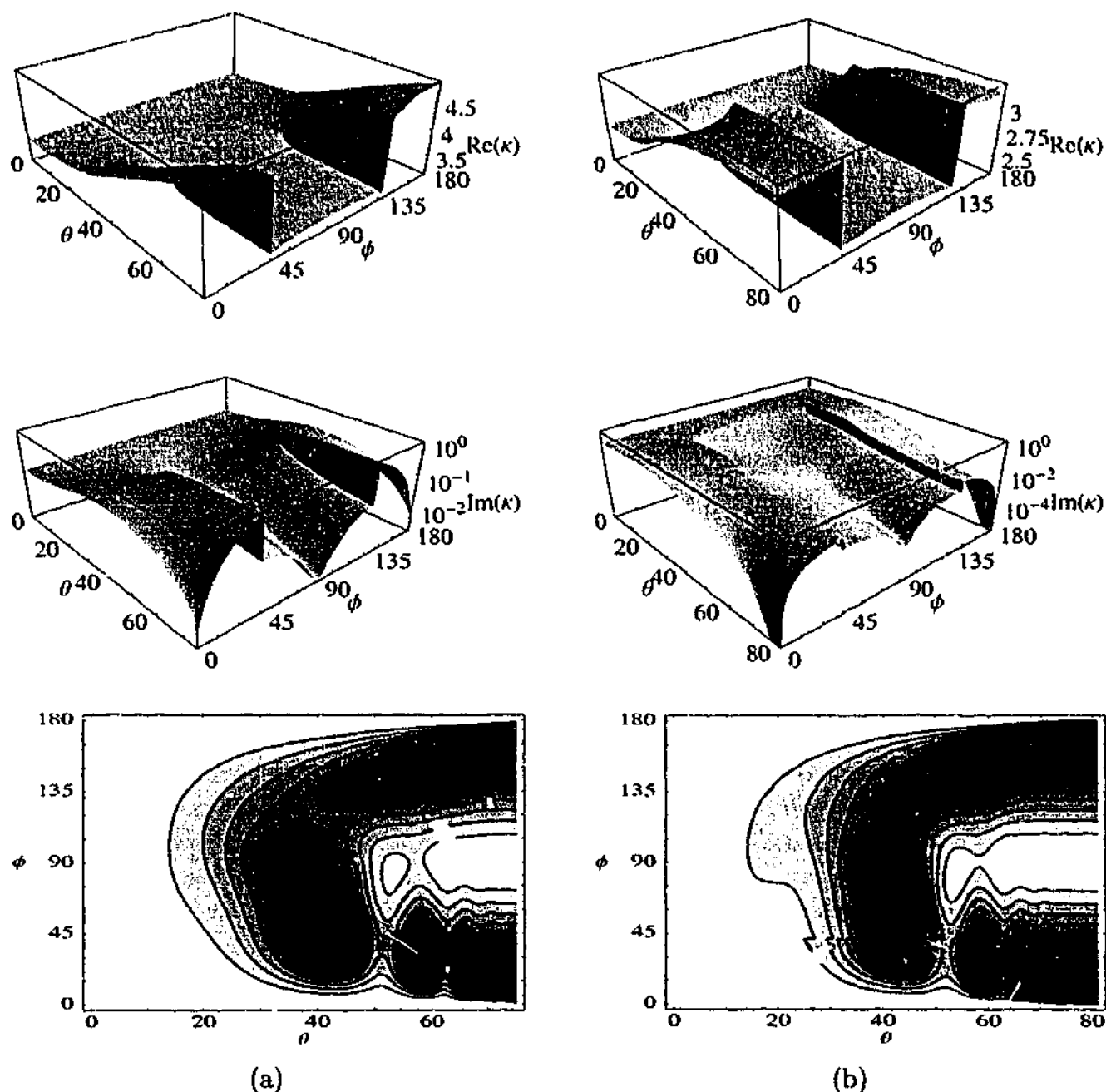
Figure 4.3: Same as Figure 4.1 except $\nu = 3$ and the domains are different. (a) $n = 1$. The domain is $0 \leq \theta \leq 75°$, $0 \leq \phi \leq 180°$. (b) $n = 2$. The domain is $0 \leq \theta \leq 81°$, $0 \leq \phi \leq 180°$.

increase with increasing θ in the usual manner (in the $n = 1$ case a local maximum is attained at the vertex of the cut), but for larger inclinations the imaginary parts tend to plateau (as exhibited by the $n = 0$ and $n = 1$ surfaces when $\nu = 1.5$, Fig. 4.2). This is accompanied by the rapid growth of $\text{Re}(\kappa)$ with increasing inclination at fixed ϕ (as was also the case when $\nu = 1.5$, Fig. 4.2); this is most pronounced at $\phi = 90°$ for $n = 3$ (Fig. D.5(a)). In all other cases, $\text{Im}(\kappa)$ varies in the same fashion as it does at lower frequencies. On the other hand, for the higher order modes ($n \geq 4$), the variation of $\text{Re}(\kappa)$ with inclination is quite different to that at lower frequencies. When $\nu = 3$ for all (fixed) propagation directions, $\text{Re}(\kappa)$ grows

rapidly with increasing inclination to a maximum at $\theta \approx 30°$, and decreases gradually for larger inclinations.

There are two cases where the Alfvén waves decouple (i.e., $\beta_B = 0$ and $\beta_a = 0$, and hence $F_a = 0$): when the magnetic field is exactly vertical ($\theta = 0$), and when the propagation direction is exactly parallel to the x-axis ($\phi = 0$). Consequently, the bottom panels of Figures 4.1 – 4.3 and Figures D.1 – D.6 show, in the neighbourhood of $\theta = 0$, $\phi = 0$, and $\phi = 180°$, that the Alfvén wave contribution to the asymptotic wave energy flux is weak (i.e., $F_a \lesssim 0.1$). When the magnetic field is exactly horizontal ($\theta = 90°$) the slow MAG waves and Alfvén waves do not propagate – resulting in the build up of energy at critical layers (as discussed in §3.1.2, the second order governing equation generally possesses two singularities associated with the Alfvén and cusp resonances). We therefore expect the slow MAG waves and Alfvén waves to decouple as the field inclination approaches horizontal. This does indeed appear to be the case – all of $\mathrm{Im}(\kappa)$, β_a, and β_s drop off rapidly as the inclination approaches horizontal. Though our numerical method is severely limited for $\theta \gtrsim 85°$ – restricting a complete study of the behaviours in highly inclined field. In horizontal field when the propagation direction is exactly perpendicular to the x-axis ($\phi = 90°$), the field aligned component of the displacement, η, is completely decoupled – none of the restoring forces: compressibility, the Lorentz force, or gravity, influence this component. Hence, $\eta = 0$ when $\theta = 90°$ and $\phi = 90°$. In highly inclined field when $\phi \approx 90°$ it is expected that solutions with dominant η components (i.e., the series [4.31] and the Alfvén waves, eqs. [4.20] – [4.22]) will be greatly suppressed (i.e., $\beta_B \approx 0$ and $\beta_a \approx 0$). Indeed, all of Figures 4.1 – 4.3 and Figures D.1 – D.6 show that $F_a \lesssim 0.1$ (i.e., $\beta_a \approx 0$ and $\beta_s \approx 0$, but $|\beta_a| \ll |\beta_s|$) when the field is highly inclined and $\phi \approx 90°$ – though the extent varies with both frequency and radial order. It is also evident that $\beta_B \approx 0$ (and $|\beta_B| \ll \min(1, |\beta_C|)$) in this regime (not displayed).

Broadly speaking, for a given mode n, the range of (θ, ϕ)-space over which the Alfvén waves contribute substantially to the asymptotic energy flux increases with frequency ν. Likewise, for a given frequency ν, the range over which the Alfvén waves contribute increases with radial order n. In general, there is not a strong correlation between the variation of the κ and F_a over the (θ, ϕ)-plane – we give three examples. Firstly, the absence of symmetry in F_a about $\phi = 90°$. Secondly, in vertical and moderately inclined field ($\theta \lesssim 70°$), there are regions where $F_a \geq 0.9$, suggesting the Alfvén waves are dominating the asymptotic flux. However, in these regions ($\theta \lesssim 70°$) the middle panels of Figures 4.1 – 4.3 and Figures D.1 – D.6 show that $\mathrm{Im}(\kappa)$ does not vary in the same manner – in fact $\mathrm{Im}(\kappa)$ is approximately constant in the ϕ-direction in this regime. Thirdly, for all frequencies and all modes when the propagation direction is in the ranges $0 < \phi \lesssim 45°$ and $135° \lesssim \phi < 180°$, the Alfvén waves dominate the asymptotic flux in highly inclined fields ($\theta \gtrsim 70°$); though at fixed propagation direction and $\theta \gtrsim 60°$, F_a fluctuates greatly. However, the middle panels of Figures 4.1 – 4.3 and Figures D.1 – D.6 show that, in highly inclined field ($\theta \gtrsim 70°$), $\mathrm{Im}(\kappa)$ is generally several orders of magnitude less than in vertical and moderately inclined field ($\theta \lesssim 60°$, depending on the mode and frequency) – indicating that both the Alfvén waves and the slow MAG waves are only very weakly excited in highly inclined field. Therefore, regions where $F_a \geq 0.9$ in highly inclined field do not represent a greatly increased Alfvén wave energy flux, but rather almost complete decoupling of the slow MAG waves.

For propagation directions not parallel to the x-axis, it is clearly evident from Figures 4.1 –

81

4.3 and Figures D.1 – D.6, that the Alfvén waves play a significant role in leaking energy from the π-modes in non-vertical field. Generally speaking, except in highly inclined field, the horizontal spatial decay rate of the π-modes varies little with the propagation direction, although the nature of the mode conversion does vary substantially. Hence, rather than radiating great quantities of additional energy, the Alfvén waves tend to compensate in regions of the parameter space where the slow MAG waves are only weakly coupled, and visa versa, keeping the overall damping rate roughly unchanged.

4.6.2 Eigenvalue topology: variation with both frequency and field inclination

Figure 4.4 shows the variation of $\text{Re}(\kappa)$, $\text{Im}(\kappa)$, and F_a as a function of dimensionless frequency, ν, for the first nine ($n = 0, \ldots, 8$) modes when $\theta = 5°$ for two different propagation directions, $\phi = 45°$ (Fig. 4.4(a)) and $\phi = 90°$ (Fig. 4.4(b)). The eigenvalues for the p-modes of the unmagnetised complete polytrope, $\kappa = \nu^2 / (n + 3/4)$, where $n = 0, 1, 2, \ldots$, and $n = 0$ represents the f-mode (e.g., Lamb, 1910, see also eq. [A.7]), are plotted in Figure 4.4 as light dashed lines. The top panels of Figure 4.4 show that in the low frequency regime ($\nu \lesssim 1$), as in the $\phi = 0$ case (see Figs. 3.3, 3.4, 3.9, and 3.10), the magnetic and non-magnetic ridges (eigencurves) are indistinguishable. Hence, we use the mode labelling system that was employed in §3.7, where ridges are labelled $n = 0, 1, 2, \ldots$ such that n is the radial order of the non-magnetic p_n-mode whose ridge matches the ridge of the magnetic mode in the low frequency (non-magnetic) regime. The upper two panels of Figure 4.4(a) and (b), respectively, are the same as Figure 3.4, except the direction of propagation is not parallel to the z-axis. The two propagation directions, $\phi = 45°$ and $\phi = 90°$ (and $\phi = 135°$), are selected because these cases provide a reasonable sample of the variations observed over a broader range of ϕ values (see §4.6.1). It is also worth noting that the $\theta = 5°$ case is typical of slightly inclined fields ($\theta \lesssim 5°$) in general.

In comparison to the $\phi = 0$ case (Fig. 3.4), Figure 4.4 shows that, at small field inclinations, the variation of the eigenvalues with propagation direction ϕ is only subtle. The real parts of the eigenvalues (Fig. 4.4, top panels) are essentially unchanged and the imaginary parts only vary slightly. We briefly discuss the important features of Figure 4.4, some of which were discussed previously in §3.7. In general, especially for $\nu \lesssim 1$, for a given frequency along a ridge both the real and imaginary parts of the eigenvalue are largest for the $n = 0$ mode and decrease as n increases. As explained above, at low frequencies ($\nu \lesssim 1$) the real parts of the eigenvalues (Fig. 4.4, top panels) are indistinguishable from their non-magnetic counterparts. For $\nu \gtrsim 1$, the influence of the magnetic field causes $\text{Re}(\kappa)$ to deviate from the non-magnetic ridges. The real parts of the eigenvalues still increase monotonically with ν (except for the $n = 0, 3$, and 7 modes) but less rapidly than the non-magnetic eigenvalues – corresponding to an increased horizontal phase speed ($\propto \nu/\text{Re}(\kappa)$). For the $n = 0, 3$, and 7 modes the real parts of the eigenvalues do not increase monotonically with ν but turn over and terminate at $\text{Re}(\kappa) = 0$, forming a horizontally evanescent mode. At the frequencies where $\text{Re}(\kappa) = 0$, the imaginary part of the eigenvalue and, hence, the rate of horizontal spatial decay of the π-mode is at a maximum. For all modes at low frequencies, $\text{Im}(\kappa)$ increases rapidly with increasing frequency.
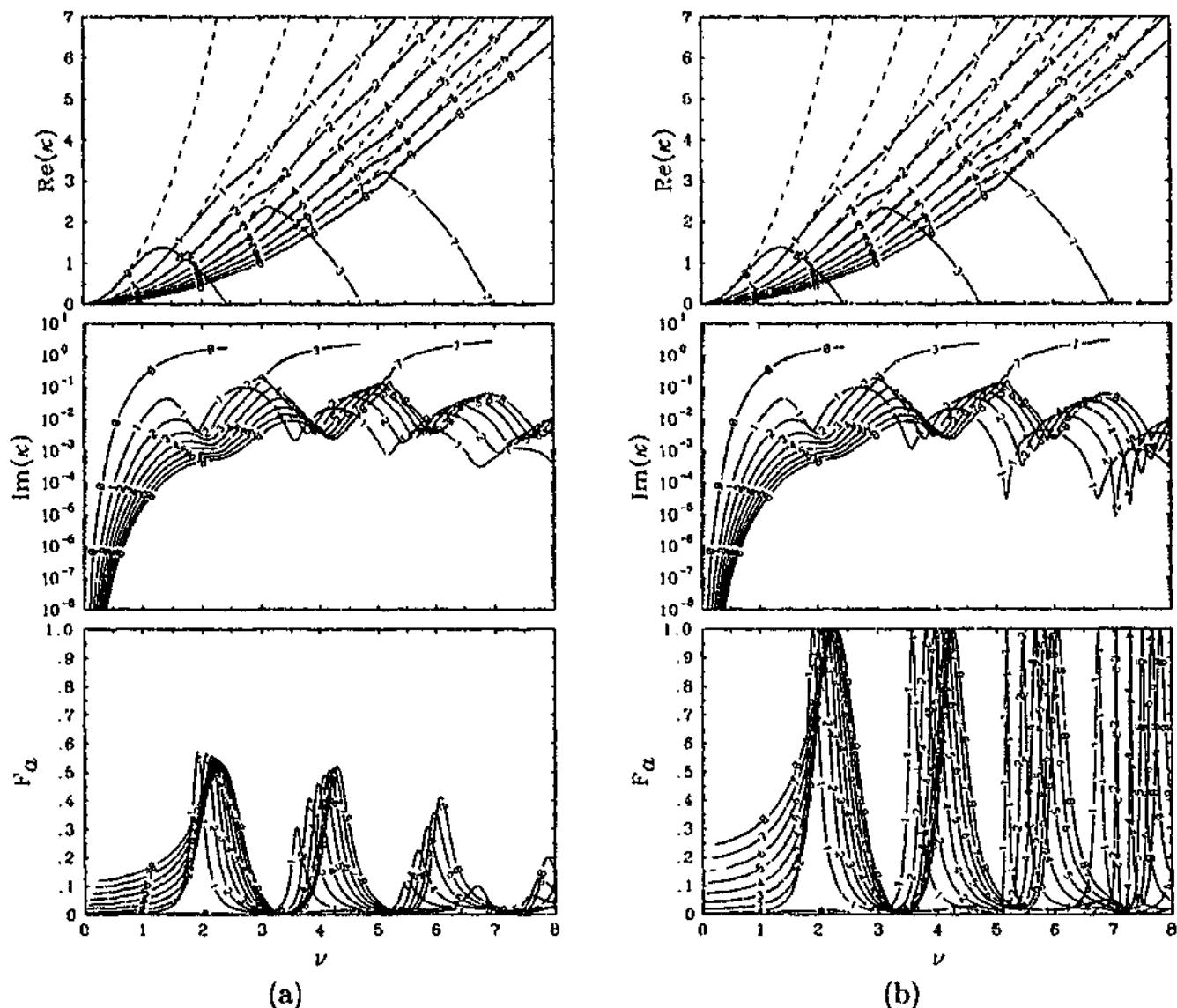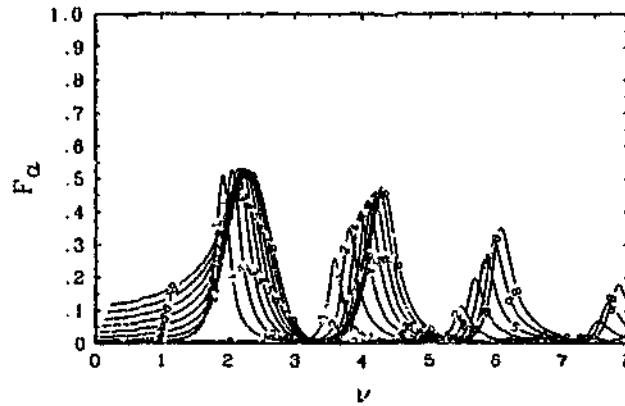
82

Figure 4.4: Eigenvalues, κ, and the contribution by the Alfvén waves to asymptotic wave energy flux, F_a, as a function of dimensionless frequency ν for the $n = 0, \ldots, 8$ modes. On both sides the *top panel* shows the real part of κ as a function of ν. At low frequencies these approach the eigencurves of the non-magnetic p-modes, $\kappa = \nu^2 / \left(n + \frac{3}{4}\right)$ (*light dashed lines*). The *middle panel* shows the imaginary part of κ as a function of ν, corresponding to the real part shown in the *top panel*. The *bottom panel* shows the fractional contribution by the Alfvén waves to the asymptotic wave energy flux, F_a, as a function of ν, corresponding to the eigenvalues displayed in the upper two panels. For all of these graphs the magnetic field inclination is fixed at $\theta = 5°$. The graphs in the upper two panels are the same as Figure 3.4, except the direction of propagation is not parallel to the x-axis. (a) The propagation direction is fixed at $\phi = 45°$. (b) $\phi = 90°$.

When the magnetic field is exactly vertical, CBZ found that for modes with $n \geq 1$ there exists a discrete set of frequencies where the π-modes are trapped normal modes (i.e., $\text{Im}(\kappa) = 0$ and $\beta_s = 0$), evident as the sharp troughs in Figure 3.3(b). When $\phi = 0$, Figure 3.4(b) showed that the trapped normal modes are not present in non-vertical fields even for very small inclinations. The middle panels of Figure 4.4 show this is also the case for oblique propagation ($\phi \neq 0$) in non-vertical fields. However, the $\text{Im}(\kappa)$ troughs, in the neighbourhood of the vertical field trapped normal modes, are slightly deeper (and sharper)

83

when $\phi \neq 0$. In fact, for fixed inclination ($\theta \lesssim 5°$), the depth (and sharpness) of the troughs increases as ϕ approaches $90°$ (verified by numerical experiment but not pictured). This feature is most obvious in the middle panel of Figure 4.4(b), where the troughs at higher frequencies (which are fully resolved) are quite sharp. It is also apparent in the bottom panel of Figure 4.4(b), where F_a is sharply peaked at the frequencies of the vertical field trapped normal modes. These F_a peaks (Fig. 4.4(b), bottom panel) are due to the slow MAG waves decoupling not an enhanced Alfvén wave energy flux (i.e., $\beta_s \approx 0$ and $|\beta_s| \ll |\beta_a|$). For $\phi = 45°$ (Fig. 4.4(a), lower panel) the F_a peaks are smaller and more rounded, especially at higher frequencies (i.e., $\beta_s \approx 0$ but $|\beta_s| \approx |\beta_a|$). This is also the case for $\phi = 135°$ (Fig. 4.5), where the eigenvalues are the same as those displayed in the upper two panels of Figure 4.4(a), but the eigenfunctions, and hence F_a, are different. The increased magnitude and sharpness of the F_a peaks (and $\text{Im}(\kappa)$ troughs) when $\phi = 90°$ suggests that propagation perpendicular to the x-axis is, at some frequencies, least efficient at exciting the slow MAG waves – we explore this possibility later.

Figure 4.5: The contribution by the Alfvén waves to asymptotic wave energy flux, F_a, as a function of dimensionless frequency ν for the $n = 0, \ldots, 8$ modes when $\theta = 5°$ and $\phi = 135°$. In this case, the corresponding eigenvalues are the same as those in the $\phi = 45°$ case (Fig. 4.4(a), upper two panels).

Away from the frequencies of the vertical field trapped normal modes, the π-modes suffer a non-trivial amount of horizontal spatial decay (i.e., $\text{Im}(\kappa) \neq 0$), the amount varies only slightly with propagation direction, ϕ, at the low inclinations (e.g., $\theta = 5°$, Fig. 4.4, also evident at low inclinations in the middle panels of Figs. 4.1 – 4.3 and Figs. D.1 – D.6). It is also true, away from the frequencies of the vertical field trapped normal modes, that F_a varies only slightly with ϕ at the low inclinations (see also Figs. 4.1 – 4.3 and Figs. D.1 – D.6, bottom panels). For frequencies of observational interest $\nu \lesssim 2$ (depending on the choice of solar parameters, see §3.7.2 for discussion), the middle panels of Figure 4.4 show that mode conversion becomes increasingly inefficient with increasing radial order n. This is usually true for all field inclinations and all propagation directions, though there are exceptions which we point out later. In a similar fashion, F_a (bottom panels of Fig. 4.4, and Fig. 4.5) tends to increase with n at low frequencies. Another interesting feature evident in the lower panels of Figure 4.4 is that for oblique propagation the energy flux responsible for the highly damped, horizontally evanescent modes (where $\text{Re}(\kappa) = 0$) is dominated by the slow MAG waves – at these frequencies, F_a is of order a few percent and increases gradually as ϕ approaches

84

90° (verified by numerical experiment but not pictured). It is generally the case, for low inclinations, that the energy flux is dominated by the slow MAG waves (i.e., $F_a \ll 1$), except in the neighbourhood of the vertical field trapped normal modes.

Figure 4.6 shows the variation of $\text{Re}(\kappa)$, $\text{Im}(\kappa)$, and F_a as a function of both dimensionless frequency, ν, and inclination, θ, for the $n = 0$ mode for two different propagation directions, $\phi = 45°$ (Fig. 4.6(a)) and $\phi = 90°$ (Fig. 4.6(b)). Each of Figures 4.6(a) and (b) are the three-dimensional propagation equivalent of Figure 3.5, allowing direct comparison, though the displayed domains are different. Each point on these eigensurfaces has been generated starting with the $n = 0$ vertical field mode (e.g., Fig. 3.3, note ϕ-dependence vanishes from the problem when $\theta = 0$) then stepping from $\theta = 0$ to $\theta = 60°$ whilst holding the frequency and the propagation direction constant. To clarify, the $n = 0$ ridges in Figures 4.4(a) (or (b)) could be derived from Figures 4.6(a) (or (b)) by slicing along $\theta = 5°$. In an analogous fashion, Figures 4.8, 4.10, 4.12 and 4.14 show $\text{Re}(\kappa)$, $\text{Im}(\kappa)$, and F_a as a function of both θ and ν for $n = 1$, 2, 3, and 4, respectively. In each case, the results for two propagation directions are displayed, $\phi = 45°$ (Figs. 4.8(a), 4.10(a), 4.12(a), and 4.14(a)) and $\phi = 90°$ (Figs. 4.8(b), 4.10(b), 4.12(b), and 4.14(b)). Apart from the mode plotted, Figures 4.8, 4.10, 4.12 and 4.14 are the same as Figure 4.6, except the point of view is shifted and the ν-domain is larger. These graphs are can be compared with the $\phi = 0$ cases, though in the $\phi = 0$ case the modes $n = 0$ (Fig. 3.5), $n = 1$ (Fig. 3.6), $n = 3$ (Fig. 3.7), and $n = 4$ (Fig. 3.8) are shown, and the displayed domains are generally larger in both the θ and ν directions in the $\phi \neq 0$ cases. Figures 4.7, 4.9, 4.11, 4.13, and 4.15 show the variation of F_a as a function of ν and θ when $\phi = 135°$ for $n = 0$, 1, 2, 3, and 4, respectively. As mentioned above, when $\phi = 135°$ the eigenvalues are identical to those when $\phi = 45°$ (upper two panels of Figs. 4.6(a), 4.8(a), 4.10(a), 4.12(a), and 4.14(a), respectively), but the eigenfunctions, and hence F_a, are different.

The topology of the eigensurfaces over the (ν, θ)-plane is complicated. We discuss the details separately for each of the two displayed propagation directions. When $\phi = 45°$, in the region $\nu \gtrsim 1.5$ and $\theta \gtrsim 25°$, the $n = 0$ eigensurface (Fig. 4.6(a)) possesses a sequence of cuts (in decreasing increments of ν). These cuts match onto cuts in the surfaces of the higher order modes, in an analogous fashion to the $\phi = 0$ case (Fig. 3.5). When $\phi = 0$, the $n = 1$ surface (Fig. 3.6) and the $n = 2$ surface (not pictured) each possess only a single cut (at $\nu \approx 1.46$ and $\nu \approx 1.65$, respectively). When $\phi = 45°$, the $n = 1$ surface (Fig. 4.8(a)) possesses two cuts (at $\nu \approx 1.56$ and $\nu \approx 2.64$), and the $n = 2$ surface (Fig. 4.10(a)) possesses three cuts (at $\nu \approx 1.76$, $\nu \approx 2.64$, and $\nu \approx 2.98$). In general, we refer to the lowest frequency cut in a given surface as the "first" cut, and cuts at successively greater frequencies are referred to as the second, third, etc. As mentioned above, the first cut in the $n = 0$ surface (Fig. 4.6(a)) matches onto the first cut in the $n = 1$ surface (Fig. 4.8(a)), the second cut in the $n = 0$ surface matches onto the first cut in the $n = 2$ surface (Fig. 4.10(a)), the third cut in the $n = 0$ surface matches onto the first cut in the $n = 3$ surface (Fig. 4.12(a)), and so on up to at least $n = 8$ (at higher frequencies the cuts on the $n = 0$ surface are not fully resolved in Fig. 4.6(a), but numerical experiments confirm their existence up to at least $n = 8$). This is also the case when $\phi = 0$ (as discussed in §3.7). The second cut on the $n = 1$ surface (Fig. 4.8(a)) matches onto the second cut in the $n = 2$ surface (Fig. 4.10(a)). The third cut in the $n = 2$ surface matches onto the second cut in the $n = 3$ surface (Fig. 4.12(a)). When
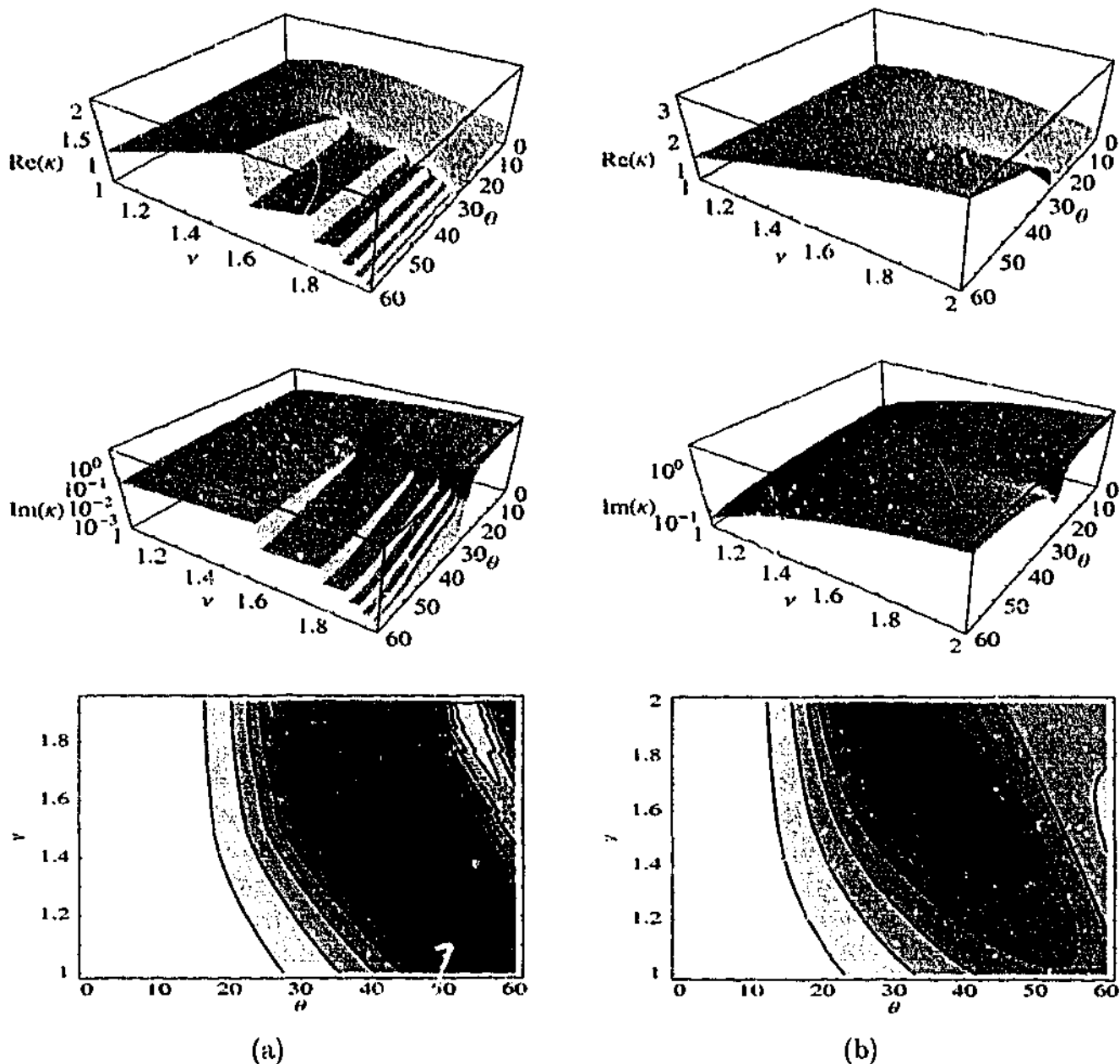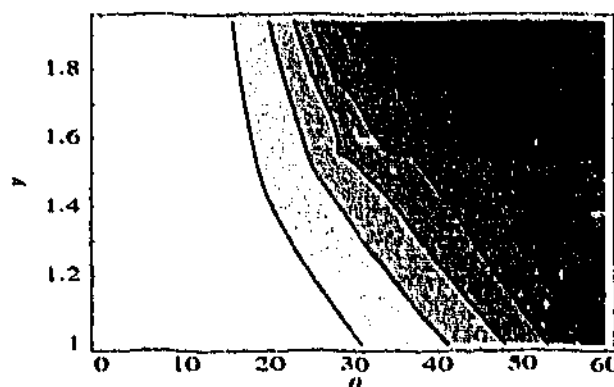
Figure 4.6: Eigenvalues, κ, and the contribution by the Alfvén waves to asymptotic wave energy flux, F_a, as a function of dimensionless frequency, ν, and field inclination, θ (in degrees), for the $n = 0$ mode. On both sides the *top panel* shows the real part of κ as a function of ν and θ the *middle panel* shows the corresponding imaginary part of κ. The shading of the eigensurfaces is used to highlight contrast only and does not indicate the height of the eigenvalue. The *bottom panel* shows F_a as a function of ν and θ, corresponding to the eigenvalues shown in the upper two panels. The contours are of $F_a = 0.1, 0.2, \ldots, 0.9$, with the lightest shading indicating $0 < F_a < 0.1$ and the darkest $0.9 < F_a < 1$. Dark areas indicate regions where the asymptotic flux is dominated by the Alfvén waves, whereas light areas indicate regions where the asymptotic flux is dominated by the slow MAG waves. The graphs in the upper two panels are the same as Figure 3.5, except the direction of propagation is not parallel to the x-axis. (a) The propagation direction is fixed at $\phi = 45°$. The domain is $1 \le \nu \le 1.94$, $0 \le \theta \le 60°$. (b) $\phi = 90°$. The domain is $1 \le \nu \le 2$, $0 \le \theta \le 60°$.

$\phi = 0$, the $n = 3$ surface (Fig. 3.7) has one low frequency cut and a sequence of cuts at higher frequencies. When $\phi = 45°$, the $n = 3$ surface (Fig. 4.12(a)) possesses two low frequency

86

Figure 4.7: The contribution by the Alfvén waves to asymptotic wave energy flux, F_a, as a function of dimensionless frequency, ν, and field inclination, θ, for the $n = 0$ mode. The propagation direction is fixed at $\phi = 135°$. The domain is $1 \leq \nu \leq 1\,94$, $0 \leq \theta \leq 60°$. In this case, the corresponding eigenvalues are the same as those when $\phi = 45°$ (Fig. 4.6(a), upper two panels). The contours are the same as those described in Figure 4.6.

cuts (at $\nu \approx 1.84$ and $\nu \approx 2.98$, with matchings outlined above) and, for $\nu \gtrsim 3.8$, a sequence of cuts (not pictured, but see Fig. 3.7 for similar behaviour). These cuts match onto cuts in the surfaces of the higher order modes, $n \geq 5$. When $\phi = 0$ the $n = 4$ surface (Fig. 3.8) has two cuts, one matches onto the $n = 0$ surface (Fig. 3.5) and the other matches onto the $n = 3$ surface (Fig. 3.7). When $\phi = 45°$ the $n = 4$ surface (Fig. 4.14(a)) only has a single cut (at $\nu \approx 1.89$), in the domain $\nu \leq 8$, that matches onto the $n = 0$ surface (as outlined above). For higher frequencies the $n = 4$ surface possesses no further cuts, and hence, does not match onto the $n = 3$ surface (or any other surface). In all cases, the vertices of the cuts occur at the same location for $\text{Re}(\kappa)$, $\text{Im}(\kappa)$, and F_a. Hence, the vertex of each cut represents a "crossing", where the eigenvalues of two different overtones coincide. However, as in the $\phi = 0$ case, the location of the vertices do not coincide with a singularity in the coefficients of the governing equations (4.1)–(4.3).

When $\phi = 90°$ the topology is completely different. For example, the $n = 0$ surface (Fig. 4.6(b)) does not appear to possess a sequence of cuts. However, very close scrutiny reveals that the sequence of cuts is present in the interval $1.99 < \nu < 2.03$. Practically, this interval is too small to resolve and so the sequence of cuts is not visible in Figure 4.6(b). The $n = 1$ surface (Fig. 4.8(b)) has no cuts (this has been verified numerically up to $\nu = 8$), indicating that when $\phi = 90°$ the $n = 1$ eigensurface is completely disconnected (numerical experiments suggest this is the case for the $n = 1$ mode in the interval $75° \lesssim \phi \lesssim 105°$). The $n = 2$ surface (Fig. 4.10(b)) has two cuts (at $\nu \approx 2$ and $\nu \approx 2.91$), and the $n = 3$ surface (Fig. 4.12(b)) has two cuts in the displayed domain (at $\nu \approx 2$ and $\nu \approx 2.91$). When $\phi = 0$ and $\phi = 45°$, we employed the term "match" to imply that the two surfaces match across both sides of the cut. The matching is identical when $\phi = 90°$. However, due to the very close separation of the cuts in the $n = 0$ surface, the matching appears to be slightly different. At low inclinations ($\theta \lesssim 25°$) and frequencies in the interval $2 \lesssim \nu \lesssim 2.5$, the $n = 0$ surface (Fig. 4.6(b)) terminates as a horizontally evanescent mode (where $\text{Re}(\kappa) = 0$). For $\theta \gtrsim 30°$ and $\nu \approx 2$, the $n = 0$ surface (Fig. 4.6(b)) matches onto the high frequency side of the first cut
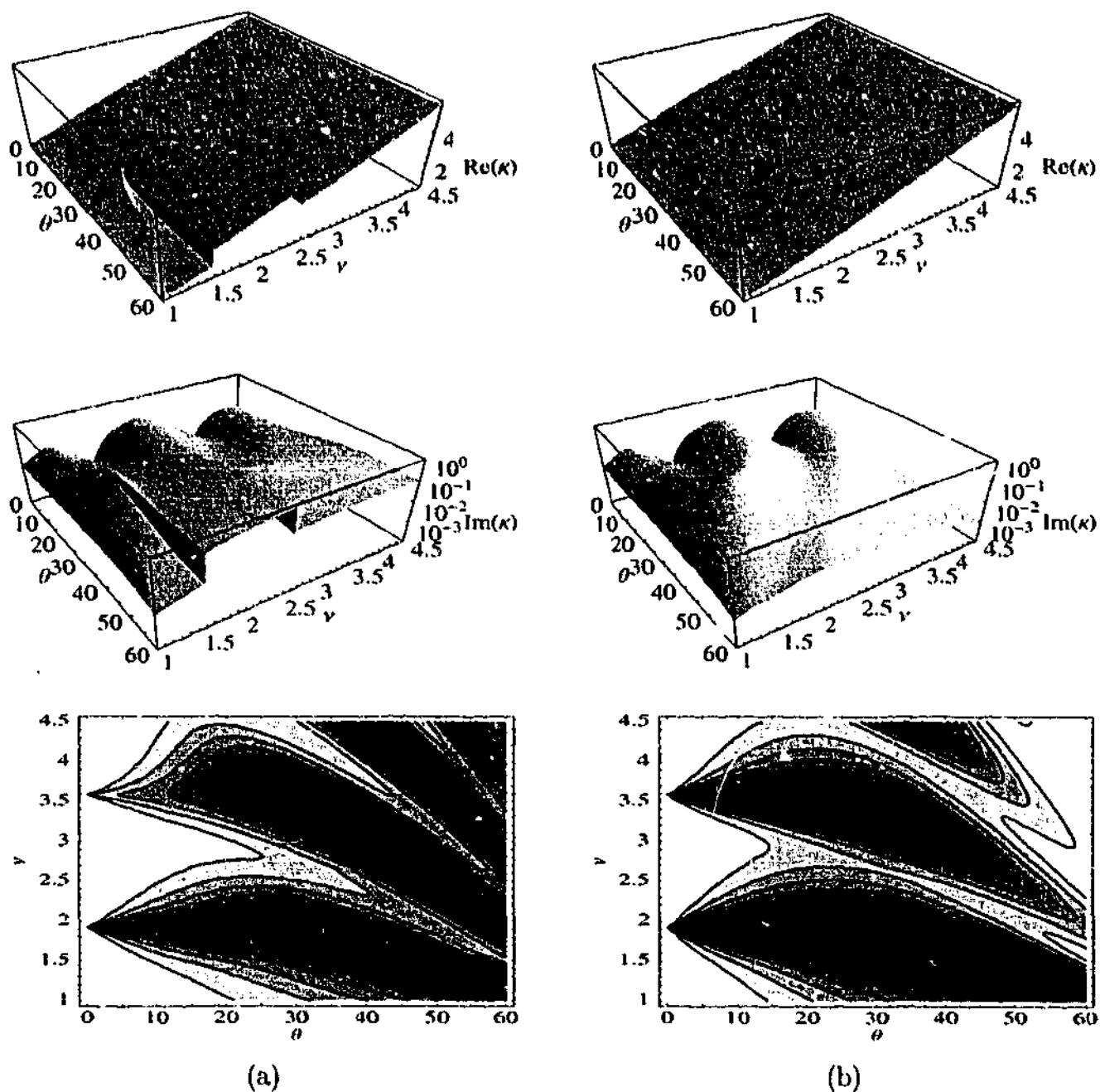
87

Figure 4.8: Same as Figure 4.6, except for $n = 1$. (a) The propagation di~ ~ion is constant, $\phi = 45°$. (b) $\phi = 90°$. The domain for both propagation directions is $1 \leq \nu \leq 4.5$, $0 \leq \theta$

in the $n = 2$ surface (Fig. 4.10(b)), the low frequency side of the first cut in the $n = 2$ surface matches onto the high frequency side of the first cut in the $n = 3$ surface (Fig. 4.12(b)), the low frequency side of the first cut in the $n = 3$ surface matches onto the high frequency side of the single cut in the $n = 4$ surface (Fig. 4.14(b)) and so on up to at least $n = 8$ (verified by numerical experiment). Hence, the spiral-type topology persists at $\phi = 90°$, but each cut, in the sequence on the $n = 0$ surface, occurs at approximately the same frequency. The second cut in the $n = 2$ surface (at $\nu \approx 2.91$, Fig. 4.10(b)) matches (both sides) onto the second cut in the $n = 3$ surface. When $\phi = 90°$, the $n = 3$ surface (Fig. 4.12(b)) possesses two low
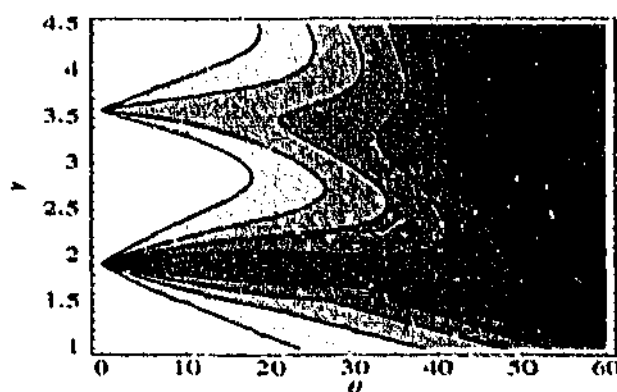
Figure 4.9: Same as Figure 4.7, except for $n = 1$. The corresponding eigenvalues are the same as those when $\phi = 45°$ (Fig. 4.8(a), upper two panels).

frequency cuts (with matchings outlined above) and, for $\nu \gtrsim 4.25$, a sequence of cuts (not displayed). These cuts match onto cuts on the surfaces of the higher order modes, $n \geq 7$. When $\phi = 0$ each of the surfaces $n = 4$ (Fig. 3.8) and $n = 5$ and 6 (not pictured) have two cuts, in each case one matches onto the $n = 0$ surface (Fig. 3.5) and the other matches onto the $n = 3$ surface (Fig. 3.7). When $\phi = 90°$ the $n = 4$ (Fig. 4.14(b)) and $n = 5$ and 6 surfaces (not pictured) only have a single cut each (verified numerically for $\nu \leq 8$) that matches onto the $n = 0$ surface (as outlined above). For higher frequencies these surfaces possess no further cuts, and hence, do not match onto the $n = 3$ surface (or any other surface).

Clearly, the topology of the eigensurfaces varies dramatically with propagation direction. Figures 4.6 - 4.13 and Figures 4.14 - 4.15 (and Figures 3.5 - 3.8) provide only a snapshot of this variation. For example, both the location and the length of the cuts depend on ϕ. We have run cases (results not displayed) for propagation directions other than those displayed. The results suggest that, qualitatively, the eigensurfaces of all modes vary only slightly with ϕ in the interval $0 \leq \phi \lesssim 30°$; topologically any eigensurface in this interval is indistinguishable from its $\phi = 0$ counterpart (with the same radial order n). When $\phi \approx 40°$ a significant topological transition occurs for all eigensurfaces with $n \geq 1$. This is evident when comparing the $\phi = 45°$ case (e.g., Figs. 4.6(a), 4.8(a), 4.10(a), 4.12(a), and 4.14(a)) to the $\phi = 0$ case (e.g., Figs. 3.5 - 3.8) - the eigensurfaces with $1 < n \leq 3$ possess several additional cuts, whereas the $n = 4$ eigensurface (Fig. 4.14(a)) possesses one less cut than in the $\phi = 0$ case (Fig. 3.8). In the interval $40° \lesssim \phi \lesssim 90°$, the topology varies considerably with ϕ for eigensurfaces with $0 \leq n \leq 3$. For example, the distance between the two cuts in the $n = 1$ surface (evident in Fig. 4.8(a) when $\phi = 45°$) decreases and the length of the second cut grows (i.e., the vertex of the cut moves to lower ν) as ϕ increases. In the interval $70° \lesssim \phi \lesssim 75°$, these two cuts collide, and hence, for $75° \lesssim \phi \lesssim 105°$, the $n = 1$ surface has no cuts, as pictured in Figure 4.8(b). A similar type of behaviour is evident for the $n = 2$ surface (Fig. 4.10), with the second cut (evident in Fig. 4.10(a) when $\phi = 45°$) migrating to lower frequencies as ϕ increases. In the interval $70° \lesssim \phi \lesssim 75°$, the first and second cuts in the $n = 2$ surface collide, leaving a single cut at $\nu \approx 2$ when $\phi = 90°$ (Fig. 4.10(b)). As for the $n = 0$ mode, the $\phi = 45°$ case (Fig. 4.6(a)) is qualitatively very similar to the $\phi = 0$ case (Fig. 3.5). In particular, both surfaces possess the sequence of cuts; which, evidently,
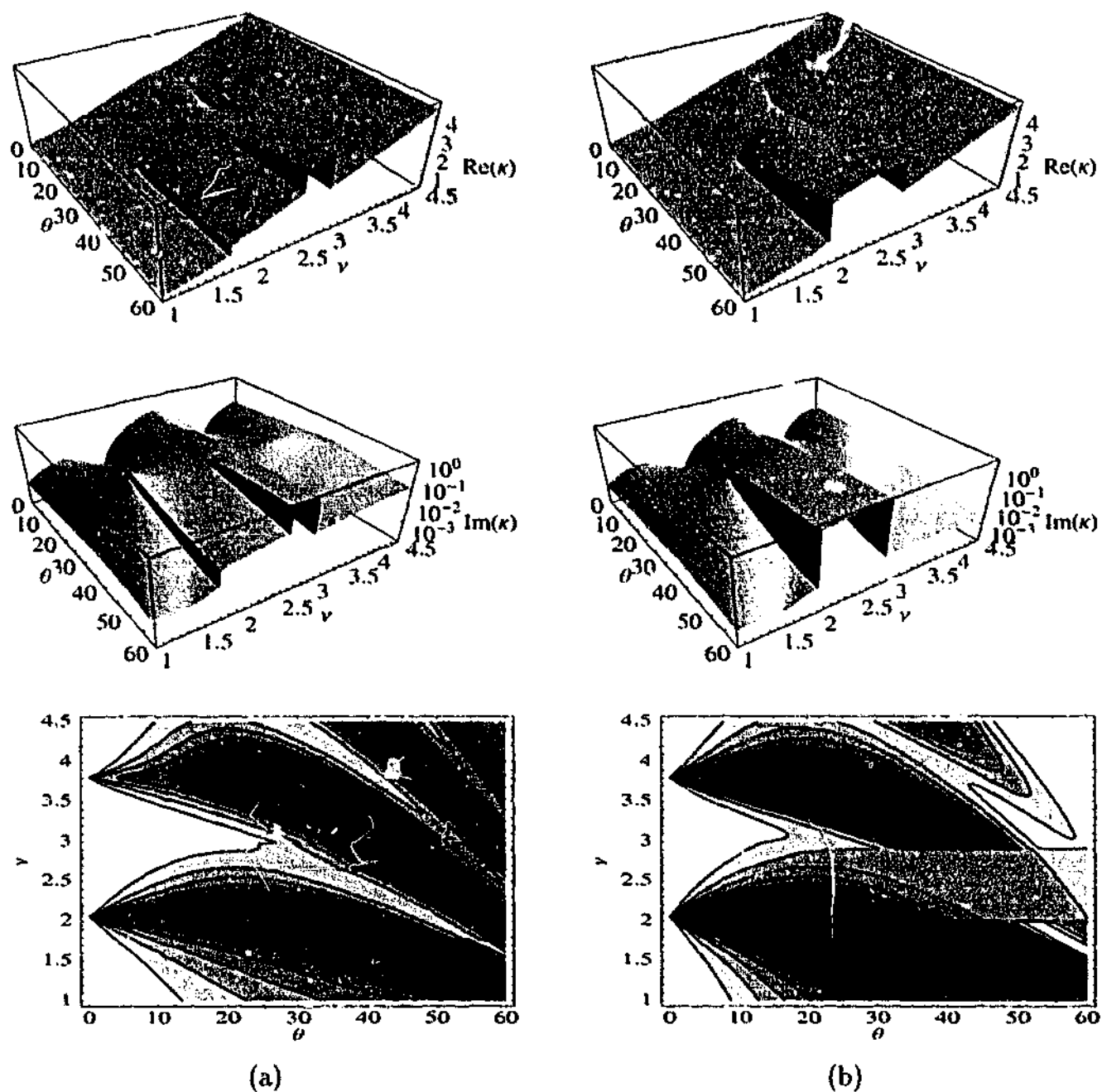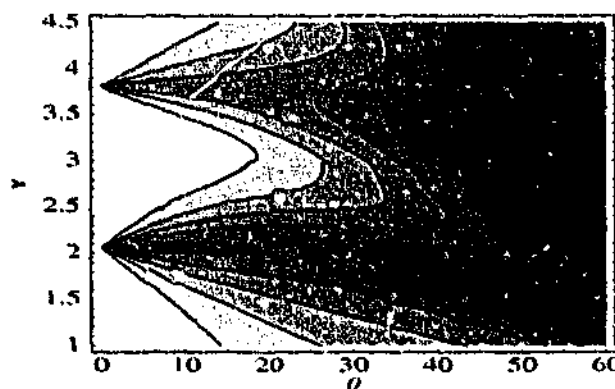
Figure 4.10: Same as Figure 4.6 except for $n = 2$. (a) The propagation direction is constant, $\phi = 45°$. (b) $\phi = 90°$. The domain for both propagation directions is $1 \leq \nu \leq 4.5$, $0 \leq \theta \leq 60°$.

are characteristic of the vertical field horizontally evanescent modes when generalised to non-vertical field (the existence of the sequence of cuts has been confirmed numerically for the $n = 0$ and $n = 3$ eigensurfaces for $0 \leq \phi \leq 180°$, but only for $n = 8$ in a limited domain, not displayed). In the interval $45° \lesssim \phi \lesssim 90°$, each cut in the sequence on the $n = 0$ surface migrates toward $\nu \approx 2$, and the distance between the cuts decreases as ϕ increases – to the extent where the sequence is effectively absent for $75° \lesssim \phi \lesssim 105°$ (e.g., Fig. 4.6(b)). The spiral-type topology is present for all propagation directions. Hence, for $\phi \lesssim 75°$ ($\phi \gtrsim 105°$), the eigenvalues of all overtones, plotted as a function of ν and θ at constant ϕ, lie on the

90

Figure 4.11: Same as Figure 4.7, except for $n = 2$. The corresponding eigenvalues are the same as those when $\phi = 45°$ (Fig. 4.10(a), upper two panels).

same surface, which has a qualitatively similar shape to that described in the $\phi = 0$ case (i.e., a sequence of connected spirals, see §3.7). For $75° \lesssim \phi \lesssim 105°$, the $n = 1$ eigensurface disconnects completely, the sequence of connected spirals remains, but not all eigenvalues lie on the same surface in these cases. As is evident when comparing Figures 4.12(a) and 4.12(b), the topology of the $n = 3$ surface (over the displayed domain) does not evolve dramatically over the interval $45° \lesssim \phi \lesssim 90°$. However, the sequence of cuts (not pictured but evident for $\nu \gtrsim 3$ in Fig. 3.7), does vary significantly with ϕ, in an analogous fashion to $n = 0$ sequence. As was outlined above, depending on the propagation direction, some of the higher order modes disconnect from the sequence of cuts in the $n = 3$ eigensurface. For example, the $n = 4$ surface (Fig. 4.14) is not connected to the $n = 3$ surface for propagation directions in the range $45° \lesssim \phi \lesssim 135°$. Evidently the topology of the $n = 4$ surface does not vary dramatically over this range either. For the sake of brevity, we do not discuss the topology of higher order modes in further detail.

We now turn turn to matters of a quantitative nature. The top panels of Figures 4.6, 4.8, 4.10, 4.12, and 4.14 show that for small to moderate inclinations ($0 \le \theta \lesssim 25°$) $\mathrm{Re}\,(\kappa)$ is only weakly affected by the inclination of the magnetic field and the propagation direction (as indicated by numerical experiments over a range of ϕ, not pictured, see also Figs. 4.1–4.3 and Figs. D.1–D.6). For larger inclinations and frequencies less than that of the first cut in each case, $\mathrm{Re}\,(\kappa)$ is also essentially unaffected by the inclination of the magnetic field. Broadly speaking, for general propagation directions, at frequencies less than that of the first cut in each case, $\mathrm{Re}\,(\kappa)$ grows slightly with increasing inclination for the $n = 0$ mode; whereas for modes with $n \ge 1$ (including those not displayed), $\mathrm{Re}\,(\kappa)$ decreases slightly (in each case this affect is of order a few percent, and is also evident in the top panels of Figs. 4.1, D.1–D.2). For higher frequencies (beyond the first cut in each case), the behaviour of $\mathrm{Re}\,(\kappa)$ is more complicated. For the $n = 0$ mode, $\mathrm{Re}\,(\kappa)$ generally increases slightly with inclination (at fixed frequency), and is "bumped down" on the higher frequency side of each cut. For modes with $n \ge 1$, $\mathrm{Re}\,(\kappa)$ also increases slightly with inclination, and is "bumped up" on the higher frequency side of the first cut in each case; except, of course, in cases where there are no cuts, such as the $n = 1$ surface when $\phi = 90°$ (Fig. 4.8(b)).

As in the $\phi = 0$ case, the middle panels of Figures 4.6, 4.8, 4.10, 4.12, and 4.14 show

91
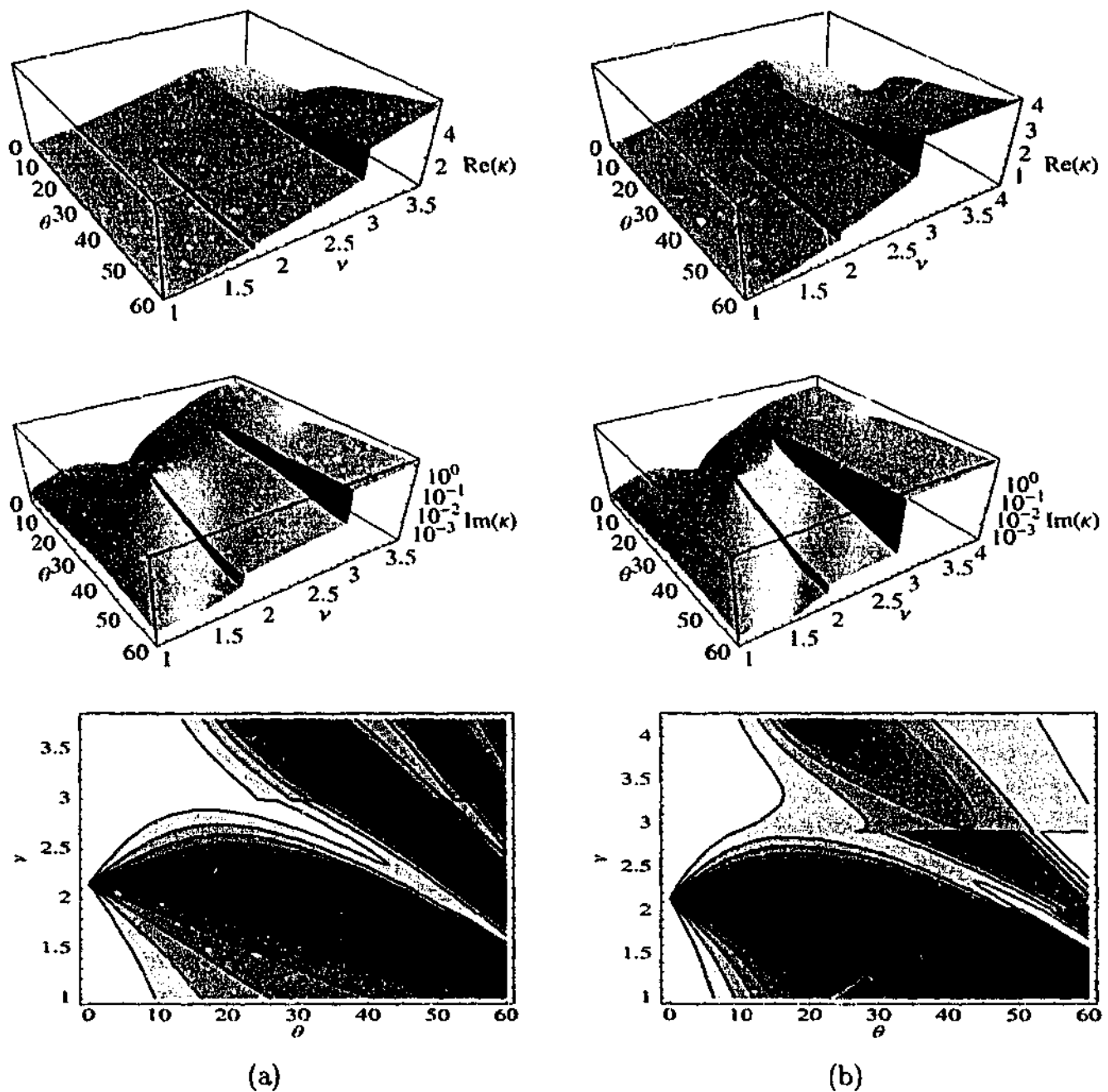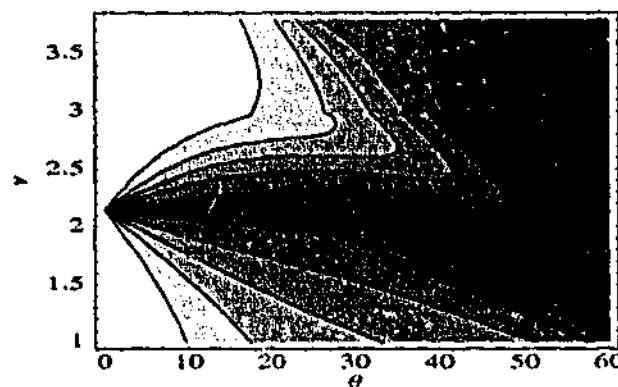
Figure 4.12: Same as Figure 4.6 except for $n = 3$. (a) The propagation direction is constant, $\phi = 45°$. The domain is $1 \le \nu \le 3.8$, $0 \le \theta \le 60°$. (b) $\phi = 90°$. The domain is $1 \le \nu \le 4.2$, $0 \le \theta \le 60°$.

that the inclination has a significant effect on the imaginary part of the eigenvalues. For the $n = 0$ mode at fixed frequency, $\text{Im}(\kappa)$ decreases with increasing θ. This is generally true for all frequencies and all propagation directions (see also Figs. 4.1(a) and 4.2(a), middle panels), except when $\phi \approx 90°$ at the higher displayed frequencies (e.g., Fig. 4.6(b)). For modes with $n \ge 1$, at all displayed frequencies (the effect is less dramatic at low frequencies) and inclinations less than the cuts ($\theta \lesssim 30°$ depending on ν), $\text{Im}(\kappa)$ grows significantly (by more than an order of magnitude) with increasing θ (see also the $n \ge 1$ modes in Figs. 4.1 – 4.3 and D.1 – D.6, middle panels). In each case, with $n \ge 1$, the imaginary parts attain a

Figure 4.13: Same as Figure 4.7, except for $n = 3$. The corresponding eigenvalues are the same as those when $\phi = 45°$ (Fig. 4.12(a), upper two panels).

local maximum (over the (ν, θ)-plane) at the vertex of the first cut (including the $n = 1$ mode when $\phi = 90°$, Fig. 4.8(b), at the location corresponding to vertices in cases with $\phi \lesssim 75°$, e.g., Fig. 4.8(a)). This is also true to some extent for $\text{Im}(\kappa)$ about the vertex of the second and third cuts at higher frequencies, where they exist (including the $n = 4$ surface when $\phi = 45°$, Fig. 4.14(a), at the location corresponding to vertex of the second cut in cases with $\phi \lesssim 45°$, e.g., Fig. 3.8). In general, for inclinations greater than the vertices of the cuts, $\text{Im}(\kappa)$ decreases significantly with increasing θ at fixed frequency and propagation direction. This type of decrease was also found when $\phi = 0$. However, the decrease of $\text{Im}(\kappa)$ with θ (for larger inclinations) is less rapid than in the $\phi = 0$ case – the rate of decrease is least when $\phi = 45°$ and moderate when $\phi = 90°$ (see also Figs. 4.1 – 4.3 and D.1 – D.6, middle panels). We re-address this point later, when considering the extinction lengths. The middle panels of Figures 4.6, 4.8, 4.10, and 4.12 also reveal the existence of an special case, where $\text{Im}(\kappa)$ does not drop off rapidly with increasing inclination, but appears to remain approximately constant (the behaviour of $\text{Re}(\kappa)$ in these cases is equally distinctive). This occurs for frequencies below the first cut in Figures 4.6(a) and (b), between the first and second cuts in Figure 4.8(a), between the second and third cuts in Figure 4.10(a), between the first and second cuts in Figure 4.10(b), and above the second cut in both Figures 4.12(a) and (b) (see also Figs. 4.2(a) and D.5(a), middle panels). Clearly one mode is suffering significantly enhanced damping in comparison to both the corresponding vertical field case ($\theta = 0$) and the $\phi = 0$ case (at the same ν).

In the middle panels of Figures 4.8, 4.10, 4.12, and 4.14, at inclinations near vertical ($\theta \approx 0$), sharp troughs in $\text{Im}(\kappa)$ are evident – these are associated with the vertical field trapped normal modes (as discussed previously in reference to Figs. 4.4 and 4.5 when $\theta = 5°$). Consequently, at lower inclinations ($\theta \approx 0$) for modes with $n \geq 1$, F_a is sharply peaked at the frequencies of the vertical field trapped normal modes – this is particularly evident in the bottom panels of Figures 4.8, 4.10, 4.12, and 4.14 ($\phi = 45°$ and $\phi = 90°$) but less so in Figures 4.9, 4.11, 4.13, and 4.15 ($\phi = 135°$). As discussed earlier (in reference to Fig. 4.4), the F_a peaks are due to the slow MAG waves decoupling, rather than an enhanced Alfvén wave energy flux (the total flux radiated at these frequencies is negligible). Interestingly, for the $n = 4$ mode at low inclinations when $\phi = 45°$ and $\phi = 135°$ (bottom panel of Fig. 4.14(a)
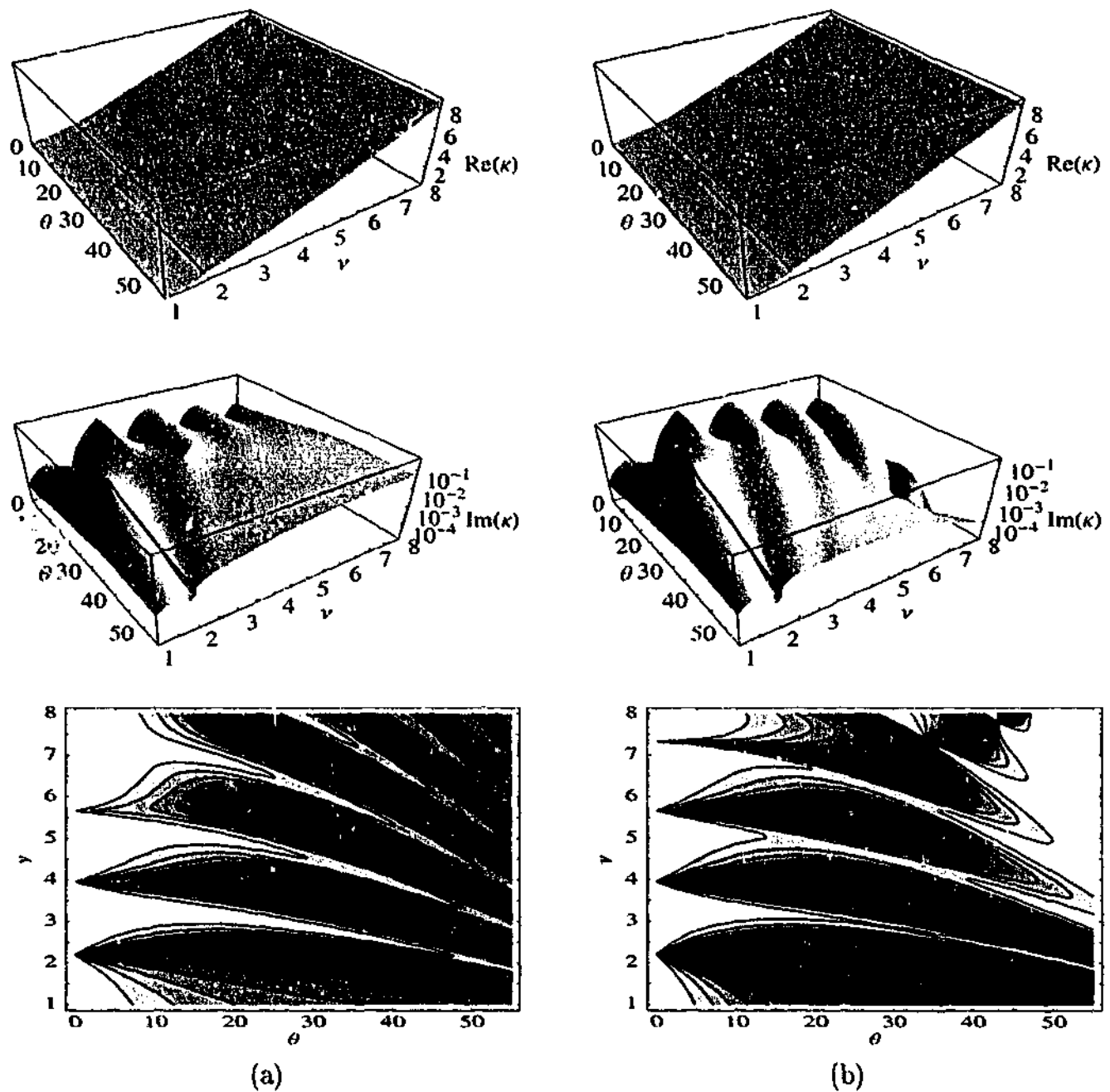
93

Figure 4.14: Same as Figure 4.6 except for $n = 4$. (a) The propagation direction is constant, $\phi = 45°$. (b) $\phi = 90°$. The domain for both propagation directions is $1 \leq \nu \leq 8$, $0 \leq \theta \leq 55°$.

and Fig. 4.15, respectively) there is no peak in F_a at the location of the high frequency vertical field trapped normal mode ($\nu \approx 7.33$) – this is because the Alfvén waves decouple at this frequency (i.e., $\beta_a \approx 0$ and $|\beta_a| \ll |\beta_s|$). For small to moderate inclinations ($\theta \lesssim 30°$), at the frequencies of the vertical field trapped normal modes, the peaks in F_a are moderate ($F_a \lesssim 0.7$) when $\phi = 45°$ (and $\phi = 135°$), but much larger ($0.9 \lesssim F_a \lesssim 1$) when $\phi = 90°$. This feature was discussed earlier (in reference to the $\theta = 5°$ case, Figs. 4.4 and 4.5) and suggests that the slow MAG waves are only weakly coupled at these frequencies when $\phi \approx 90°$ and $\theta \lesssim 30°$.

94
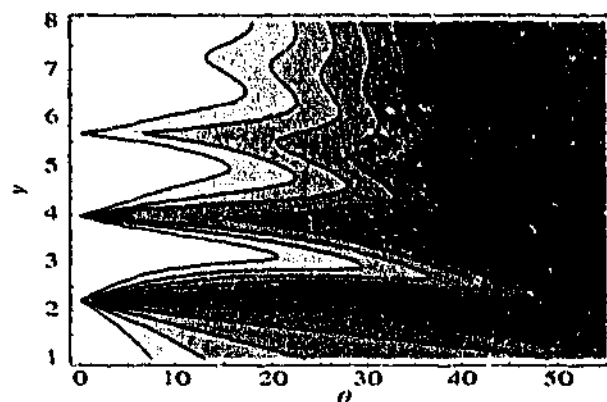
Figure 4.15: Same as Figure 4.7, except for $n = 4$. The corresponding eigenvalues are the same as those when $\phi = 45°$ (Fig. 4.14(a), upper two panels).

The Alfvén waves decouple when $\theta = 0$ or $\phi = 0$ (i.e, $F_a = 0$). Hence, away from the frequencies of the vertical field trapped normal modes, the bottom panels of Figures 4.6, 4.8, 4.10, 4.12, and 4.14 along with Figures 4.9, 4.11, 4.13, and 4.15 show, for small inclinations ($\theta \lesssim 15°$), that $F_a \lesssim 0.1$ and varies only slightly with inclination and propagation direction – indicating the Alfvén waves are only weakly excited in these regions (see also Figs. 4.1 – 4.3 and D.1 – D.6, bottom panels).

In general, for $\phi = 45°$ and $\phi = 90°$, the peaks emanating from the frequencies of the vertical field trapped normal modes dominate the variation of F_a over the $(\nu,\ \theta)$-plane – with the peaks migrating to lower frequencies as θ increases (especially prominent in the $n = 4$ case: Fig. 4.14, bottom panel). On the other hand, when $\phi = 135°$ the peaks in F_a are more diffuse – this type of asymmetry in F_a, about $\phi = 90°$, was also observed in the bottom panels of Figures 4.1 – 4.3 and D.1 – D.6. For $\phi = 90°$ and $n = 4$ (Fig. 4.14(b)) there appears to be a striking correlation between the variations of F_a and Im(κ) over the extended $(\nu,\ \theta)$-plane. However, the topologies of Im(κ) and F_a are generally not strongly correlated (Figs. 4.8 – 4.14, lower two panels). For example, the local maximum in Im(κ) (associated with the vertex of the cuts in the eigensurfaces for $n \geq 1$) does not coincide with any similarly distinctive behaviour in F_a. As concluded in §4.6.1, the Alfvén waves play a significant role in π-mode damping in non-vertical field when propagation is not parallel to the x-axis. However, regions of the parameter space where the Alfvén waves dominate (i.e., $F_a \gtrsim 0.9$) are generally not associated with significantly enhanced horizontal spatial decay dates (i.e., Im(κ)).

Figure 4.16 shows the variation of Re(κ), Im(κ), and F_a as a function of dimensionless frequency, ν, for the first nine ($n = 0, \ldots, 8$) modes when $\theta = 30°$ for two different propagation directions, $\phi = 45°$ (Fig. 4.16(a)) and $\phi = 90°$ (Fig. 4.16(b)). The upper two panels of Figures 4.16(a) and (b), respectively, are equivalent to Figure 3.9, except the propagation direction is not parallel to the x-axis. The inclination $\theta = 30°$ is indicative of the behaviour at moderate inclinations ($\theta \approx 30°$); it also roughly corresponds to the location where Im(κ) attains a local maximum over the $(\nu,\ \theta)$-plane (i.e., the vertex of the cuts in Figs. 4.6 – 4.14). The distinctive cuts seen in Figures 4.6, 4.8, 4.10, 4.12, and 4.14 are not present in Figure 4.16, this is because the ridges in Figure 4.16 have been generated by stepping from low
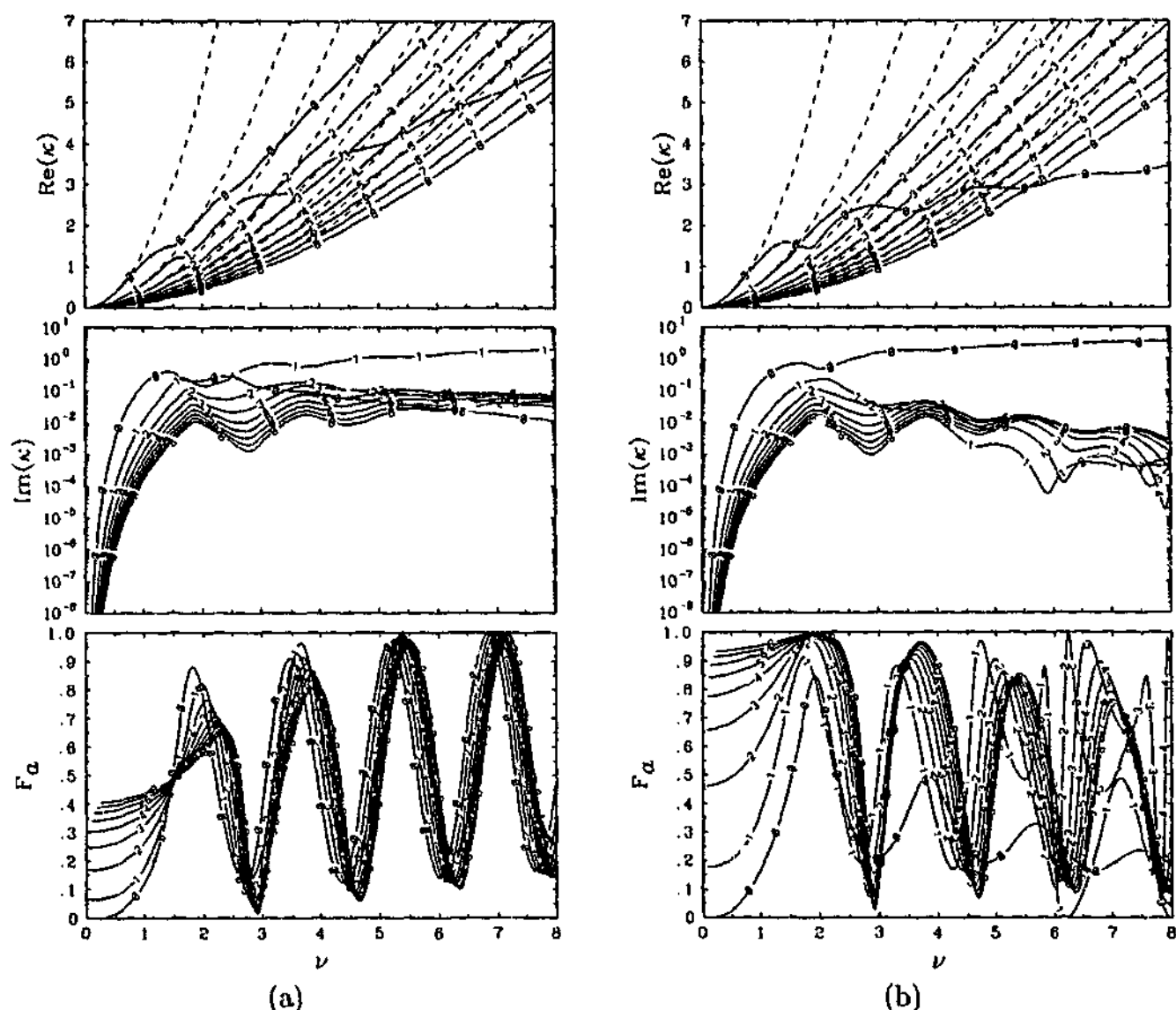
95

Figure 4.16: Same as Figure 4.4, except $\theta = 30°$.(a) $\phi = 45°$. (b) $\phi = 90°$.

frequencies (using the non-magnetic modes as initial guess) to high frequencies, holding θ and ϕ constant (in the same way as Fig. 4.4 and Figs. 3.3 – 3.10). For example, for $\nu \lesssim 4$ (and $\phi = 45°$) the ridge labelled $n = 1$ in Figure 4.16(a) may be derived from the $n = 1$, $n = 0$, $n = 2$, and $n = 3$ surfaces (Figs. 4.8(a), 4.6(a), 4.10(a), 4.12(a), respectively) by slicing along $\theta = 30°$ in the prescribed order. Likewise, the ridge labelled $n = 0$ in Figure 4.16(b) may be derived from the $n = 0$, $n = 2$, and $n = 3$ surfaces (in order, Figs. 4.6(b), 4.10(b), 4.12(b), respectively). The ridges of the other modes may be derived in a similar manner, though the matching between surfaces must be carefully considered (details described above). Hence, all the ridges in Figure 4.16 appear continuous.

Two distinctive features of the ridges in Figure 4.16 can also be observed on the constituent surfaces (Figs. 4.6, 4.8, 4.10, 4.12, and 4.14): the undulations of the real parts exhibited by $n = 1$ in Figure 4.16(a) and $n = 0$ in Figure 4.16(b) – in the neighbourhood of the cuts in the surfaces; and the enhanced imaginary parts for $n = 0$ ($1 \lesssim \nu \lesssim 2.5$) and $n = 1$ ($\nu \gtrsim 2.5$)

96

in Figure 4.16(a) and $n = 0$ in Figure 4.16(b). The latter feature is most pronounced for $n = 0$ in Figure 4.16(b) and was also noted in the discussion of the eigenvalue topology over both the (ν, θ)-plane (e.g., Figs. 4.8, 4.10, 4.12, and 4.14) and the (θ, ϕ)-plane (e.g., Figs. 4.1 -- 4.3 and D.1 - D.6). In these cases a peculiar solution (eigensurface) was found where $\text{Im}(\kappa)$ does not decrease rapidly with increasing θ at larger inclinations, as is usually the case. Interestingly, F_a does not show any distinctive behaviour for $n = 1$ when $\phi = 45°$ (Figure 4.16(a), bottom panel) or $\phi = 135°$ (Fig. 4.17). On the other hand, for $n = 0$ when $\phi = 90°$ (Fig. 4.16(b), bottom panel) F_a does behave slightly differently to the other modes, indicating the damping of this mode is due mainly to slow MAG wave leakage.
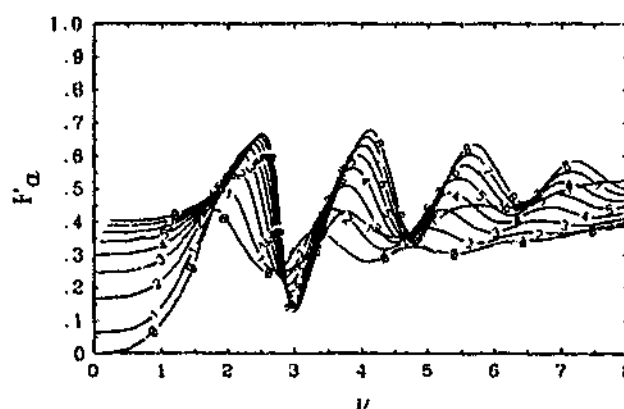
Figure 4.17: Same as Figure 4.5, except $\theta = 30°$. The corresponding eigenvalues are the same as those when $\phi = 45°$ (Fig. 4.16(a), upper two panels).

In the $\phi = 0$ case (Fig. 3.9) the variation of $\text{Im}(\kappa)$ with n is approximately at a minimum -- this is not true when $\phi \neq 0$ as one of the ridges deviates substantially from the general trend in each case ($n = 1$ in Fig. 4.16(a) and $n = 0$ in Fig. 4.16(b)). Apart from this, however, the behaviour of the eigencurves is very similar to Figure 3.9. Namely, there are no surfaces modes in the displayed domain -- for all modes, except the $n = 0$ mode in Figure 4.16(b), $\text{Re}(\kappa)$ increases monotonically with frequency. For the most part, the real parts of the eigenvalues are only weakly affected by the propagation direction. For both displayed propagation directions at low frequencies ($\nu \lesssim 1.5$), $\text{Im}(\kappa)$ increases rapidly with ν in the usual fashion (e.g., Fig. 3.9 and Fig. 4.4). For intermediate and higher frequencies, when $\phi = 45°$ (Fig. 4.16(a)), the $\text{Im}(\kappa)$ ridges are almost horizontal, some gradually decline with ν -- this behaviour is analogous to the $\phi = 0$ case when $\theta = 30°$ (Fig. 3.9(b)). On the other hand, when $\phi = 90°$ (Fig. 4.16(b), middle panel), $\text{Im}(\kappa)$ attains a maximum at $\nu \approx 1.5 - 2$ and decreases with ν for higher frequencies. With the exception of $n = 1$ when $\phi = 45°$ (Fig. 4.16(a), middle panel) and $n = 0$ when $\phi = 90°$ (Fig. 4.16(b), middle panel), the sequence of $\text{Im}(\kappa)$ ridges at both displayed propagation directions form a tightly packed bundle when $\theta = 30°$ -- again, this was the case for all modes when $\phi = 0$ (Fig. 3.9(b)).

At higher frequencies ($\nu \gtrsim 5.5$) when $\phi = 90°$, the $\text{Im}(\kappa)$ ridges of the modes $n = 1$, 2, 3, and 4 each possess a moderately sharp trough (Fig. 4.16(b), middle panel). In the neighbourhood of the troughs, both the slow MAG waves and the Alfvén waves partially decouple -- $|\beta_s| \approx 0$ and $|\beta_a| \approx 0$ and therefore $\text{Im}(\kappa) \approx 0$. However, the decoupling of the slow MAG waves and the Alfvén waves does not occur at the exactly same frequency.

This evident in the bottom panel on Figure 4.16(b), where F_a has a peak slightly to one side of the $\text{Im}(\kappa)$ trough (i.e., $|\beta_s| \approx 0$ and $|\beta_a| \approx 0$ but $|\beta_a| \gtrsim |\beta_s|$ and hence $F_a \approx 1$) and a trough slightly to the other side (i.e., $|\beta_s| \approx 0$ and $|\beta_a| \approx 0$ but $|\beta_s| \gtrsim |\beta_a|$ and hence $F_a \approx 0$) The sharp transition of F_a characterises locations where both the slow MAG waves and the Alfvén waves decouple. These types of decouplings were also found at higher frequencies when $\theta = 5°$ and $\phi = 90°$ (Fig. 4.4(b)), in this case the sharp troughs in $\text{Im}(\kappa)$ are due to the slow MAG waves decoupling (the Alfvén waves are only very weakly coupled at low inclinations). Similarly, $\text{Im}(\kappa)$ troughs accompanied by sharp transitions in F_a are also evident when $\phi = 90°$ at higher frequencies and $\theta \approx 30°$ on the $n = 4$ eigensurface (over the extended (ν, θ)-plane, Fig. 4.14(b), lower panels). On the other hand, when $\phi = 0$ (Fig. 3.9(b)), $\phi = 45°$ (Fig. 4.16(a)) and $\phi = 135°$ (Fig. 4.17) there no sharp troughs in $\text{Im}(\kappa)$ at any frequency. This feature, where the decoupling of the slow MAG waves and the Alfvén waves occurs at a very similar frequency, appears to be a characteristic of the $\phi = 90°$ case.

At moderate inclinations ($\theta \approx 30°$), F_a is highly dependent on frequency. Mode conversion fluctuates from dominant fast-to-slow mode conversion ($F_a \approx 0$) to dominant fast-to-Alfvén mode conversion ($F_a \approx 1$) on several occasions in the displayed domain (Fig. 4.16, bottom panels), though the fluctuation is relatively subdued when $\phi = 135°$ (Fig. 4.17). Both of these features are also evident when taking slices, at $\theta \approx 30°$, through the surfaces in the bottom panels of Figures 4.6, 4.8, 4.10, 4.12, and 4.14 and in Figures 4.7, 4.9, 4.11 4.13, and 4.15. For all propagation directions at low frequencies, the contribution by the Alfvén waves to the asymptotic energy flux, F_a, increases with increasing radial order n – this variation is most pronounced when $\phi \approx 90°$ (Fig. 4.16(b)), see also the $\theta = 5°$ case (Figs. 4.4 and 4.5). At moderate inclinations ($\theta \approx 30°$), the Alfvén waves clearly make a significant contribution the π-mode damping when the direction of propagation is not parallel to the x-axis ($\phi \neq 0$). However, as concluded earlier, rather than radiating vast quantities of additional energy, which would result in a significantly enhanced $\text{Im}(\kappa)$, the Alfvén waves generally compensate at frequencies where the slow MAG waves are only weakly excited (i.e., $F_a \approx 1$), and visa versa for the slow MAG waves where the Alfvén waves decouple (i.e., $F_a \approx 0$). Consequently, $\text{Im}(\kappa)$ does not generally fluctuate in the same manner as F_a. Though there some are exceptions, for instance, the frequencies where both the slow MAG waves and the Alfvén waves are almost completely decoupled and consequently $\text{Im}(\kappa) \approx 0$ (as discussed above).

4.6.3 A singular limit

Before proceeding further, it is instructive to consider a special case. When the magnetic field is exactly horizontal ($\theta = 90°$), the governing equations (4.1)-(4.3) reduce to a second order differential equation that generally possesses two singularities or critical layers – associated with the Alfvén and cusp resonances (as discussed in §3.1.2). However, there is a special case where both critical layers vanish: when the propagation direction is exactly perpendicular to the x-axis ($\phi = 90°$, see e.g., Vanlommel and Goossens, 1999). In this case, the solutions, and hence the displacements, energy fluxes, and other physical quantities are continuous in the interval $0 \leq s < \infty$. The governing equation can be written as

98

$$4\nu^2 s \left(s^{-m} + s\right) Y''(s) + 4\nu^2 \left[(m+2)s - ms^{-m}\right] Y'(s)$$
$$+ \left[m^2\kappa^2 s^{-m} - s\nu^2 \left(\kappa^2 \left(s^{-m} + s\right) - 4\nu^2\right)\right] Y(s) = 0, \tag{4.39}$$

where $Y(s) = \bar{\nabla} \cdot \xi = \frac{i\kappa}{2}\zeta - d\xi_z/ds$ is the nondimensionalised divergence of the displacement vector. As usual we concentrate on the $m = 3/2$ case. The components of the displacement vector in the y- and z-directions subsequently follow from:

$$\xi_y(s) = \zeta(s) = \frac{2i\kappa \left[\left(4\nu^2 \left(1 + s^{5/2}\right) - 15s^{3/2}\right) Y(s) - 6 \left(1 + s^{5/2}\right) Y'(s)\right]}{s^{3/2} \left(9\kappa^2 - 16\nu^4\right)}, \tag{4.40}$$

and

$$\xi_z(s) = \frac{2 \left[\left(3\kappa^2 \left(1 + s^{5/2}\right) - 20\nu^2 s^{3/2}\right) Y(s) - 8\nu^2 \left(1 + s^{5/2}\right) Y'(s)\right]}{s^{3/2} \left(9\kappa^2 - 16\nu^4\right)}, \tag{4.41}$$

respectively. As discussed previously, when $\theta = 90°$ and $\phi = 90°$, the component of the displacement in the x-direction vanishes (i.e., $\xi_x = -\eta = 0$).

Equation (4.39) cannot be solved in terms of tabulated functions, but it may be solved numerically with the assistance of the standard techniques of local analysis. Equation (4.39) has only two singularities: an irregular singularity at $s = \infty$ and a regular singularity at $\sigma = 0$ (where $s = \sigma^2$). At the surface, a stress-free boundary condition is enforced (i.e., $Y = 0$ at $s = 0$). This condition is consistent with the boundary condition imposed in the fourth and sixth order cases (eqs. [4.23]–[4.24]]). The leading terms of the appropriate series solution are

$$Y(s) = s^{5/2} - \frac{9\kappa^2}{56\nu^2}s^{7/2} + \frac{\kappa^2}{36}\left(1 + \frac{81\kappa^2}{224\nu^4}\right)s^{9/2} - s^5 \ldots. \tag{4.42}$$

Subsequently, it can be shown that both components of the displacement (eqs. [4.40] and [4.41]) are finite (and non-zero) at the surface. As $s \to \infty$, the decaying exponential solution is selected,

$$Y(s) \sim s^{(\nu^2/\kappa)-(m/2)-1} \exp\left[-\frac{\kappa}{2}s\right] U(s), \quad s \to \infty, \tag{4.43}$$

where the coefficient U is asymptotic to unity as $s \to \infty$ (and may be expanded in asymptotic power series in non-positive half integer powers of s). The asymptotic leading order (4.43) is identical to the fast MAG waves in non-vertical field (eqs. [4.7]–[4.9]). In this special case ($\theta = 90°$ and $\phi = 90°$), the oscillations are trapped normal modes · propagating without energy loss. Consequently, the eigenvalues, κ, are real. The second order two point boundary value problem is solved numerically in an analogous fashion to the fourth order and sixth order problems (outlined above, §3.6 and §4.4, respectively).

Figure 4.18 shows the variation of the eigenvalues, κ, as function of dimensionless frequency, ν, when $\theta = 90°$ and $\phi = 90°$. Evidently, two classes of solution exist – separated by
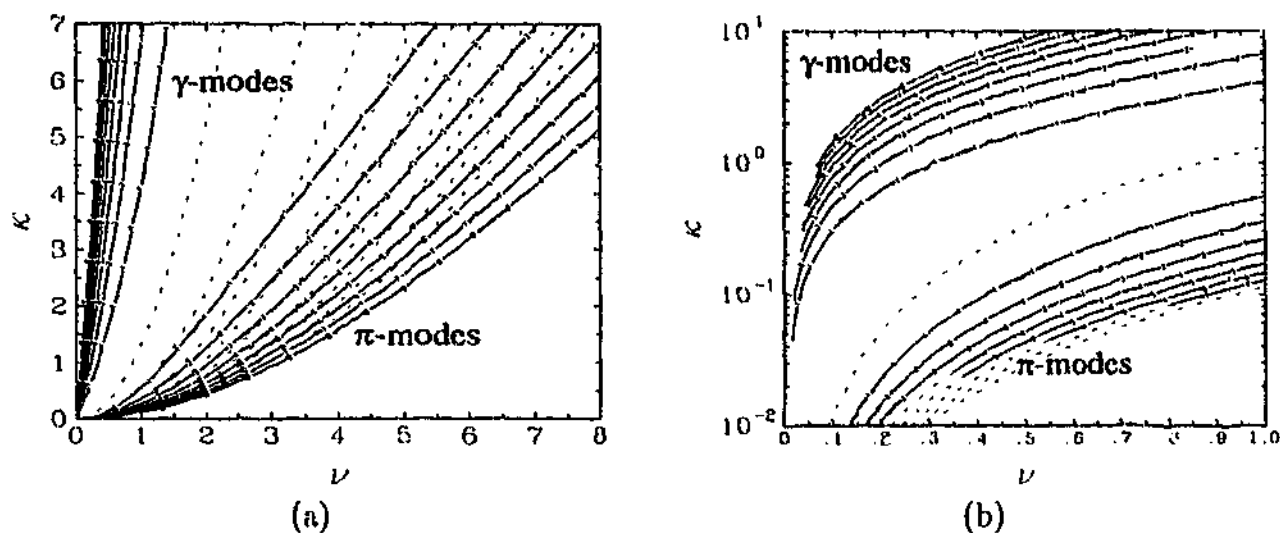
Figure 4.18: (a) Eigenvalue κ as a function of dimensionless frequency ν for the case where the magnetic field is exactly horizontal (i.e., $\theta = 90°$) and the propagation direction is exactly perpendicular to the x-axis (i.e., $\phi = 90°$). Evidently, two classes of solution exist – labelled the π-modes (low wavenumbers) and γ-modes (high wavenumbers). For each set the modes with $n = 1, \ldots, 8$ are plotted. The eigencurves of the non-magnetic p-modes are plotted as *light dashed lines*. (b) Same as (a) except for the domain $0 \le \nu \le 1$ and a logarithmic scale is used on the vertical axis.

the ridge of the non-magnetic f-mode: a low wavenumber set with eigenvalues that match onto the non-magnetic p_n-mode ridges at low frequencies, numbered accordingly $n = 1, 2, 3,\ldots$, and labelled the π-modes (i.e., p-modes modified by the magnetic field); and a high wavenumber set with no non-magnetic counterparts, also numbered $n = 1, 2, 3,\ldots$, and labelled the γ-modes. The expressions for the two components of the displacement (eqs. [4.40] and [4.41]) are singular if $\kappa = 4\nu^2/3$. This condition coincides exactly with the dispersion relation for the non-magnetic f-mode. Figure 4.18 clearly shows that none of the eigencurves intercept the non-magnetic f-mode ridge. Hence, equations (4.40) and (4.41) are valid for all frequencies. In fact, the f-mode, being incompressive in the non-magnetic case, is not described by equation (4.39).

For the π-modes, the displacement eigenfunctions behave very much like the non-magnetic p-modes – three examples are shown in Figure 4.19(a). For the π_1-mode, both components of the displacement eigenfunction have one vertical node. The π_3-eigenfunction has three vertical nodes and the π_5-eigenfunction has five vertical nodes. The π-mode numbering system is identical to that of the non-magnetic p-modes. Figure 4.19(a) shows, for fixed frequency, that the depth of the lower turning point increases (and the horizontal wavenumber decreases, Fig. 4.18) with increasing radial order n. At the surface ($s \approx 0$), the π-mode displacements are dominated by the vertical component, ξ_z (dashed curves in Fig. 4.19(a)).

For the γ-modes, the numbering system is again identical to the non-magnetic p-modes (the radial order n corresponds to the number of vertical nodes in both components of the displacement eigenfunction). In contrast to the p- and π-modes, the depth of the lower turning point for the γ-modes decreases (and the horizontal wavenumber increases, Fig. 4.18) with increasing radial order n, at fixed frequency. Roughly speaking, the γ-mode lower turning points are located at $s \approx 1$ (i.e., in the neighbourhood of the equipartition depth). At the

100

surface, the γ-mode displacements are dominated by the lateral component, ξ_y (full curves in Fig. 4.19(b)). The normalisation adopted in Figure 4.19 requires $\xi_z = 1$ at $s = 0$. It follows, from equations (4.40), (4.41), and (4.42), that $-i\xi_y = 3\kappa/4\nu^2$. This expression again reveals the importance of the non-magnetic f-mode dispersion relation, $\kappa = 4\nu^2/3$, in separating the two classes of solution -- the γ-modes ($\kappa \gg 4\nu^2/3$) and the π-modes ($\kappa \ll 4\nu^2/3$).
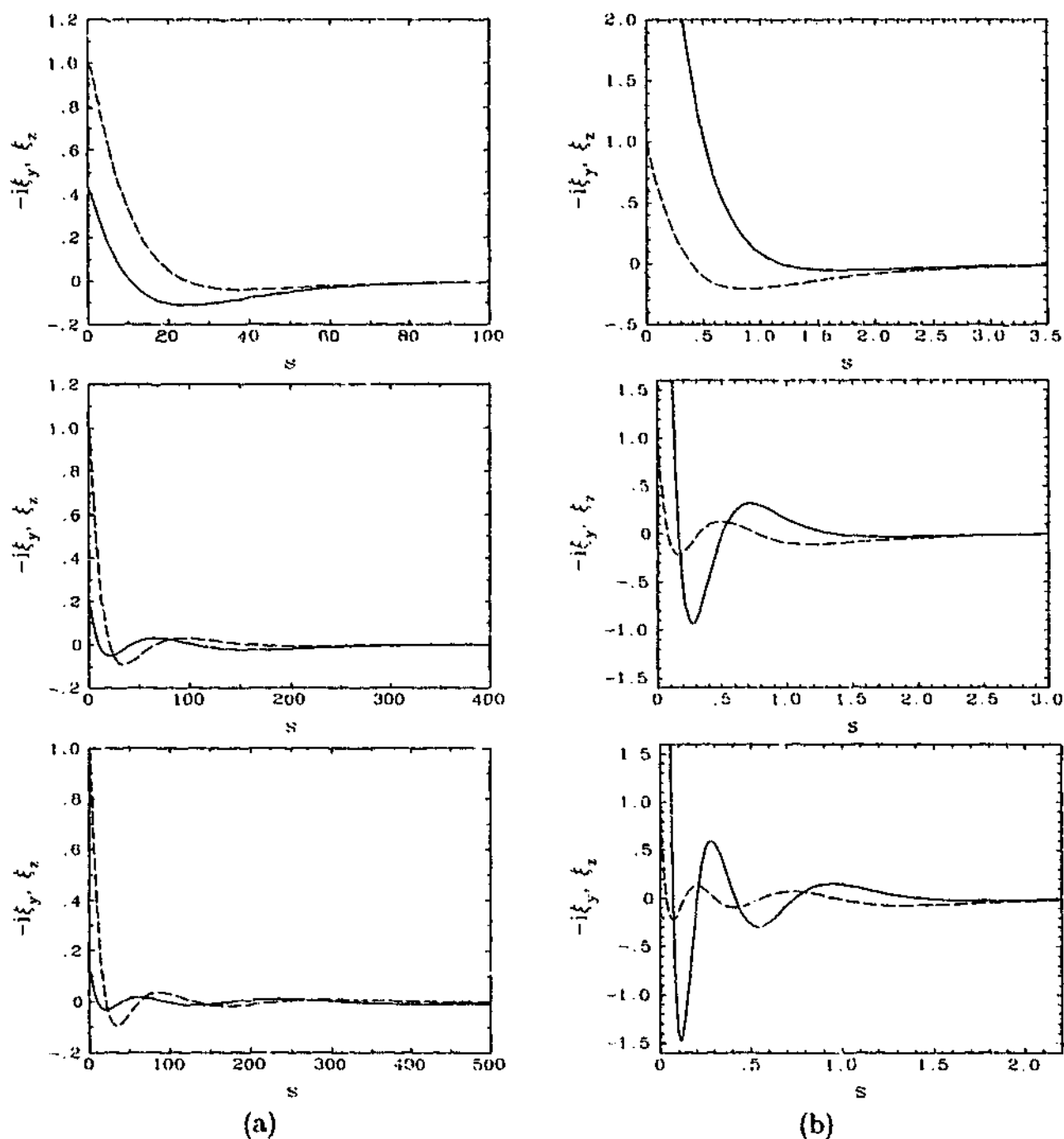
Figure 4.19: Displacement eigenfunctions as a function of dimensionless depth, s, for $\nu = 0.5$ for a selection of π- and γ-modes. The full curve is $-i\xi_y$ and the dashed curve is ξ_z. The normalisation has been chosen such that $\xi_z = 1$ at $s = 0$. On both sides the *top panel* shows the $n = 1$ mode, the *middle panel* shows the $n = 3$ mode, and the *bottom panel* shows the $n = 5$ mode. In each case, the corresponding eigenvalues can be read off from Figure 4.18. (a) π-mode eigenfunctions. (b) γ-mode eigenfunctions.
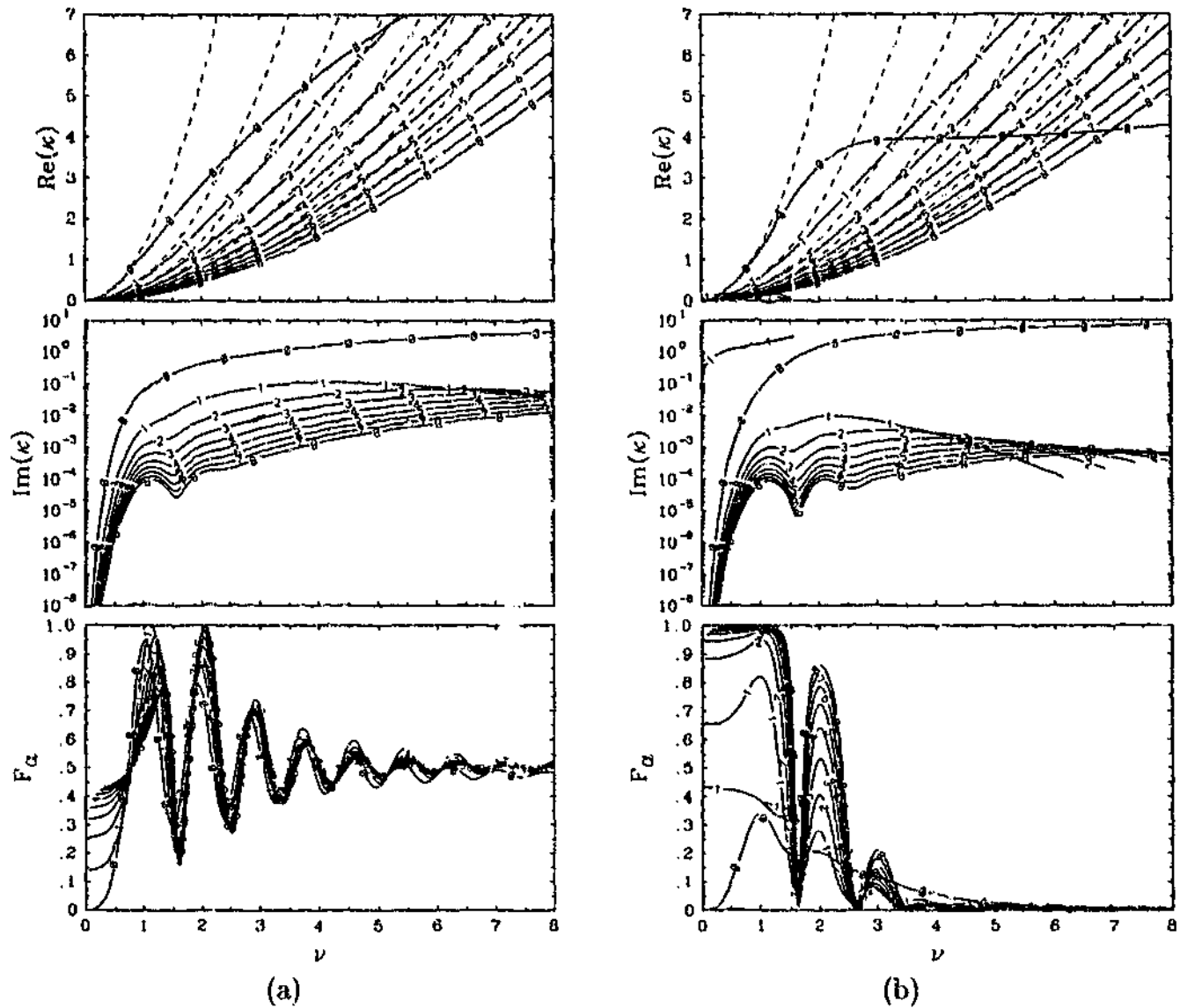
Figure 4.20: Same as Figure 4.4, except $\theta = 60°$.(a) $\phi = 45°$. (b) $\phi = 90°$, also in this case the first γ-mode is included ($n = 1$).

4.6.4 Highly inclined magnetic field cases

Returning to the cases where $\theta \neq 90°$, Figure 4.20 shows the variation of $\text{Re}\,(\kappa)$, $\text{Im}\,(\kappa)$, and F_a as a function of dimensionless frequency, ν, for the first nine ($n = 0, \ldots, 8$) π-modes when $\theta = 60°$ for two different propagation directions, $\phi = 45°$ (Fig. 4.20(a)) and $\phi = 90°$ (Fig. 4.20(b)). The upper two panels of Figure 4.20 are the three-dimensional generalisations of Figure 3.10. In the $\phi = 90°$ case (Fig. 4.20(b)), the ridge for the first γ-mode ($n = 1$) is also shown. Numerical experiments suggest that the γ-modes only exist in highly inclined field ($\theta \gtrsim 50°$) for $\phi \approx 90°$, and the higher order γ-modes exist over smaller range of inclinations than do the lower order modes. Hence, at $\theta = 60°$ only the γ_1-mode is present. Figure 4.21 shows the variation of $\text{Re}\,(\kappa)$, $\text{Im}\,(\kappa)$, and F_a as a function of dimensionless frequency, ν, when $\theta = 80°$. Figure 4.21(a) shows the results for the first nine ($n = 0, \ldots, 8$) π-modes

102

when $\phi = 45°$. Figure 4.21(b) shows the results for the first nine π-modes and the first three $(n = 1, \ldots, 3)$ γ-modes when $\phi = 90°$. Unfortunately, the numerical integration of the γ-mode solutions is troublesome, due to a combination of large inclination, increasing frequency, and large Im (κ). Consequently, the γ-mode ridges terminate prematurely in Figures 4.20(b) and 4.21(b), note this is the case generally for all types of solutions in highly inclined field (e.g., $\theta = 80°$, Fig. 4.21). For the γ-modes, it is evident that Re (κ) decreases rapidly with decreasing inclination (away from $\theta = 90°$). Hence, when plotted as a function of frequency, the real parts of the γ-mode ridges become obscured in some cases (Figs. 4.20(b) and 4.21(b), top panels).
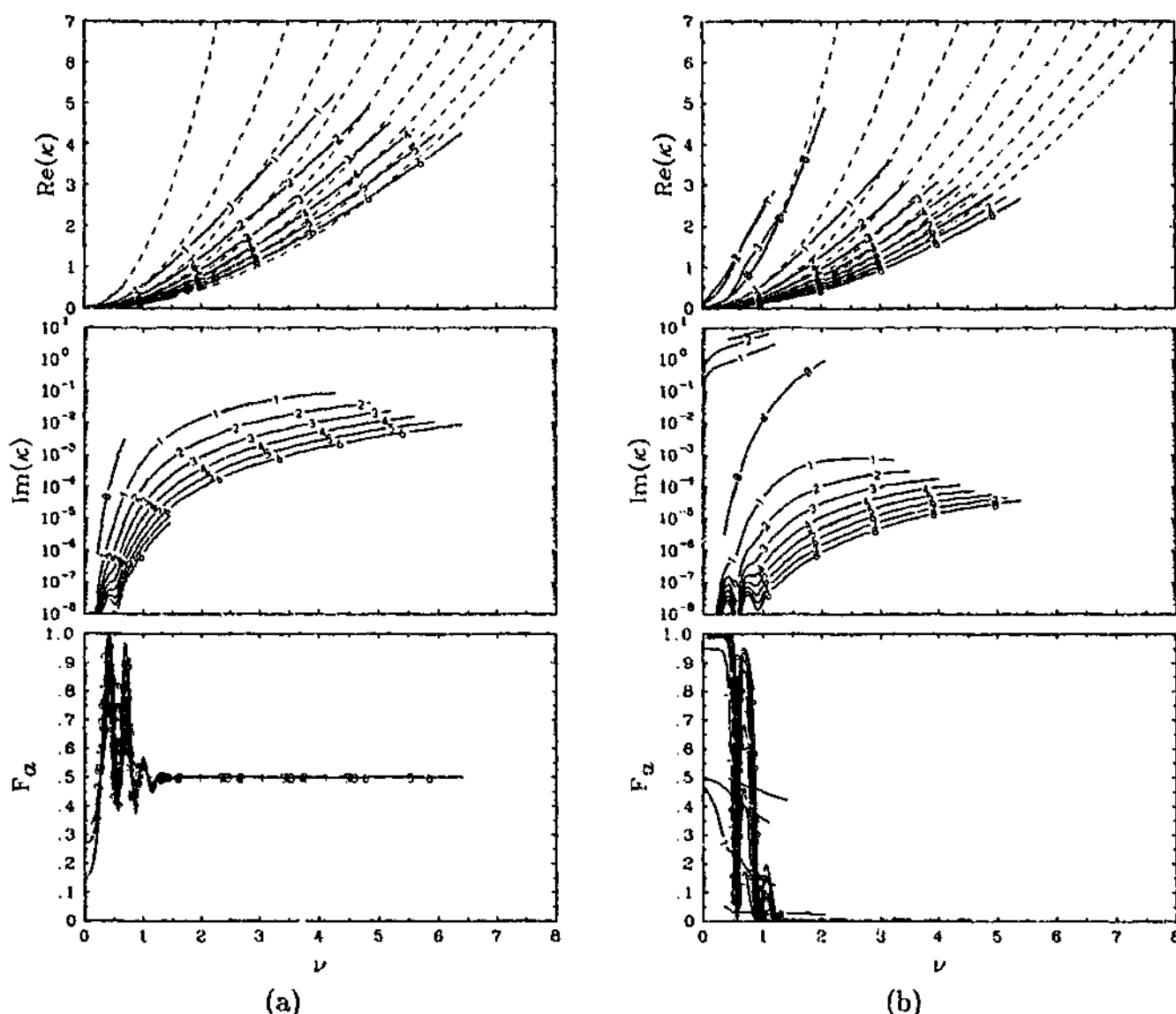
Figure 4.21: Same as Figure 4.4, except $\theta = 80°$. (a) $\phi = 45°$. (b) $\phi = 90°$, also in this case the first three γ-modes are included $(n = 1, \ldots 3)$.

The special case: $\theta = 90°$ and $\phi = 90°$, is a singular limit – the second order governing equation (4.39) does not provide a uniform asymptotic approximation to the true solution of the sixth order MAG wave equations (4.1)–(4.3) in the horizontal field limit, $\theta \to 90°$,

103

when $\phi = 90°$. However, as the inclination of the magnetic field approaches horizontal (when $\phi = 90°$), the real parts of the eigenvalues converge to those of the $\theta = 90°$ case (Fig. 4.18). For example, when overlaid, the real parts of the eigenvalues for π-modes with $n \geq 1$ when $\phi = 90°$, shown in the top panels of Figures 4.20(b) and 4.21(b) when $\theta = 60°$ and $\theta = 80°$, respectively, are indistinguishable from those of the corresponding π-modes in Figure 4.18 (as was shown previously for the π-modes, $\text{Re}(\kappa)$ varies only slightly with inclination, for $\theta \gtrsim 60°$).

On the other hand, the real parts of eigenvalues for the γ-modes vary significantly with inclination. This is obvious when comparing the γ_1-mode at the two displayed inclinations. When $\theta = 80°$, $\text{Re}(\kappa)$ for the γ_1- and γ_2-modes overlap. When $\theta = 60°$, the γ_2- and γ_3-modes do not exist, and $\text{Re}(\kappa)$ for γ_1 is so small that its ridge is obscured by the crowd of π-mode ridges. It appears that the imaginary parts of the γ-mode eigenvalues are less affected by the inclination. However, as the field inclination approaches horizontal the imaginary parts are expected to vanish. Numerically verifying the behaviour in this limit is very difficult. In the singular limit, when $\theta = 90°$ and $\phi = 90°$, the depth of the lower turning point for the γ-mode eigenfunctions is generally very shallow (near $s \approx 1$), and decreases with increasing radial order (as shown in Fig. 4.19(b)). In simple terms, this indicates that a significant fraction of the energy in γ-modes lies in the neighbourhood of the mode conversion region (where $C_S \approx C_A$). Therefore, in highly inclined field, the γ-modes would be expected to undergo very efficient mode conversion. This is indeed the case, the damping rates for the γ-modes (proportional to $\text{Im}(\kappa)$) are several orders of magnitude greater than those for the π-modes (evident in both Figs. 4.20(b) and 4.21(b), middle panels). In addition, the γ-mode damping rates appear to increase with radial order n (see Fig. 4.21(b), middle panel). The bottom panel of Figures 4.20(b) and 4.21(b) show that the γ-mode damping is due to both the slow MAG waves and the Alfvén waves in roughly equal proportions (at least for the displayed frequencies).

In comparison to the $\phi = 0$ case (Fig. 3.10), Figure 4.20 shows that three-dimensional propagation in highly inclined field has a significant influence on the eigenvalues of the π-modes, especially the imaginary parts (middle panels). In a similar fashion to Figure 4.16, one of the modes ($n = 0$) in each case behaves dramatically differently (as observed over the (ν, θ)-plane in Figs. 4.6, 4.8, 4.10, and 4.12). For modes with $n \geq 1$, the real parts of κ, in the top panels of both Figures 4.20(a) and (b), are basically identical to those in Figure 3.10(a). Though comparatively small, the variation of $\text{Re}(\kappa)$ with ϕ is greatest when $\theta \approx 30°$, which roughly coincides with the vertices of the cuts in the surfaces over the (ν, θ)-plane (Fig. 4.6, 4.8, 4.10, 4.12, and 4.14), where $\text{Re}(\kappa)$ is "bumped".

On the other hand, the imaginary parts of κ (Fig. 4.20, middle panels), for π-modes with $n \geq 1$, are significantly different to those in the corresponding $\phi = 0$ case (Fig. 3.10(b)). In particular, in the middle panels of both Figures 4.20(a) and (b), the ridges (with $n \geq 1$) tend to remain bunched up, and do not exhibit the rapid decrease with θ (and n) that is evident in Figures 3.10(b) (and in the extinction length plots of Fig. 3.11). In fact, for $n \geq 1$, at fixed inclination ($\theta \approx 60°$), the $\text{Im}(\kappa)$ ridges increase rapidly with ϕ reach a maximum at $\phi \approx 45°$ (several orders of magnitude above the $\phi = 0$ level) and decrease to a minimum at $\phi = 90°$ (this minimum is above the $\phi = 0$ level). Comparing the middle panels of Figures 4.16(a) and 4.20(a), it is evident that the $\text{Im}(\kappa)$ ridges are at a similar magnitude, suggesting $\text{Im}(\kappa)$ is

does not vary significantly with inclination (in the interval $30° \lesssim \theta \leq 60°$) when $\phi = 45°$. This is not the case when $\phi = 90°$ (Figs. 4.16(b) and 4.20(b)), where for a fixed frequency, $\text{Im}(\kappa)$ decreases by at least an order of magnitude in the interval $30° \leq \theta \leq 60°$. In the $\phi \approx 45°$ case (Fig. 4.20(a)), $\text{Im}(\kappa)$ generally increases monotonically with ν, though the $n = 1$ mode does decrease for higher frequencies. In the $\phi \approx 90°$ case (Fig. 4.20(b)), the $\text{Im}(\kappa)$ ridges peak at low to moderate frequencies (depending on n, but not $n = 0$) and decrease with ν for higher frequencies. For the $n = 0$ mode in both cases, $\text{Im}(\kappa)$ increases monotonically with ν, most rapidly for $\nu \lesssim 2$. It also evident in Figures 3.10 and 4.20 that $\text{Im}(\kappa)$ for the $n = 0$ mode increases with ϕ to a maximum at $\phi = 90°$ (Figure 4.20(b), middle panel). This is also apparent in the eigensurface plots (over the (ν, θ)-plane) shown in Figures 4.6, 4.8, 4.10, and 4.12.
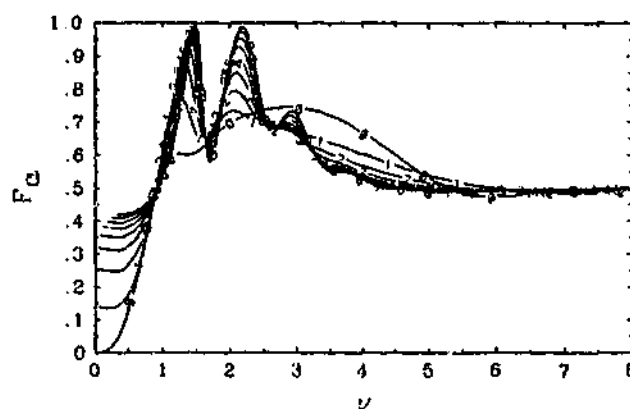
Figure 4.22: Same as Figure 4.5, except $\theta = 60°$. The corresponding eigenvalues are the same as those when $\phi = 45°$ (Fig. 4.20(a), upper two panels).

For all propagation directions when $\theta \approx 60°$, F_a is highly dependent on frequency, but less so than in the $\theta = 30°$ case (Fig. 4.16, lower panels, and Fig. 4.17). For $\phi = 45°$ (Fig. 4.20(a), lower panel), all modes, including the highly damped $n = 0$ π-mode, show a very similar frequency dependence (this is also the case when $\theta = 30°$ and $\theta = 80°$, lower panels of Figs. 4.16(a) and 4.21(a), respectively), fluctuating rapidly for low frequencies. For higher frequencies, the fluctuations decrease to a level where the contribution by slow MAG wave conversion and Alfvén wave conversion are roughly equal (i.e., $F_a \approx 0.5$). This is also the case when $\phi = 135°$ (Fig. 4.22), and especially so when $\theta = 80°$ and $\phi = 45°$ (Fig. 4.21(a), lower panel). For $\phi = 90°$ (Fig. 4.20(b), lower panel), $F_a \approx 0$ at higher frequencies suggesting Alfvén wave conversion is completely overpowered by slow MAG wave conversion in this regime (see also Fig. 4.21(b), lower panel). This behaviour of F_a is also evident at larger inclinations on the eigensurfaces shown in bottom panels Figures 4.6, 4.8, 4.10, 4.12, and 4.14. Again when $\phi = 90°$, the almost simultaneous decoupling of the slow MAG waves and the Alfvén waves is evident in the lower panel of Figure 4.20(b). In this case, the decoupling – characterised by a $\text{Im}(\kappa)$ trough and a sharp transition in F_a – occurs at lower frequencies and is most pronounced for the higher order modes ($n \gtrsim 4$).

4.6.5 Extinction length

In this subsection, we examine the variation of the extinction length as a function of both the propagation direction, ϕ, and the inclination, θ. For the sake of brevity, we focus solely on the π-mode extinction lengths.

Figure 4.23 shows the variation of the extinction length and F_a as a function of propagation direction, ϕ, for the π-modes with $n = 0, \ldots, 8$, at fixed field inclination $\theta = 30°$, and for four different (fixed) frequencies (a) 3 mHz (b) 4 mHz (c) 5 mHz and (d) 6 mHz. The characterisation of the solar convection zone is identical to that discussed in §3.7.2 (i.e., $L = 400$ km*, and $g = 274$ m s^{-2}). The inclination $\theta = 30°$ roughly coincides with location where mode conversion is most efficient, as seen on the surfaces Figures 4.6, 4.8, 4.10, 4.12, and 4.14. Figure 4.23 confirms and clarifies some of the conclusions that were drawn earlier. Firstly, the variation of the π-mode horizontal spatial decay rates with ϕ is effectively negligible at moderate field inclinations ($\theta \approx 30°$). For some of the higher order modes at higher frequencies the extinction length decreases slightly as ϕ approaches 90°. Secondly, broadly speaking, the contribution by the Alfvén waves to asymptotic wave energy flux, F_a, increases with ϕ to a maximum at $\phi \approx 90°$. However, this is not accompanied by a significant decrease of the extinction length, rather the extinction length remains effectively unchanged.

Figure 4.24 shows the variation of the extinction length and F_a as a function of propagation direction, ϕ, for the π-modes with $n = 0, \ldots, 8$, at fixed field inclination $\theta = 80°$, and for four different (fixed) frequencies (a) 3 mHz (b) 4 mHz (c) 5 mHz and (d) 6 mHz. Like Figure 4.23, Figure 4.24 confirms several points that were discussed previously, and shows that the pattern is very similar for higher order modes generally. In highly inclined field, there is a significant variation of the extinction length (i.e., Im(κ)) as a function ϕ. For $\phi = 0$ (or $\phi = 180°$), the Alfvén waves decouple ($F_a = 0$), and in highly inclined field the slow MAG waves are essentially decoupled (the extinction length increases rapidly with inclination, see Fig. 3.11). For all modes at all frequencies, the extinction length decreases with ϕ to a minimum at $\phi \approx 45°$ (the location depends on the radial order), and increases to a local maximum at $\phi = 90°$. For all cases, the extinction length minimum at $\phi \approx 45°$ is generally not short enough to have consequences for p-mode absorption, except for the mode with the shortest extinction length ($n = 0$ in the low frequency cases, and $n = 1$ in the high frequency cases). Figure 4.24 also shows that, in highly inclined field, the behaviour of F_a at all frequencies is very similar for all modes. For $\phi = 0$ (or $\phi = 180°$), $F_a = 0$ but rapidly increases to $F_a \approx 0.9$ near $\phi \approx 10° - 20°$. The Alfvén wave contribution to asymptotic energy flux then steadily decreases to $F_a \approx 0$ at $\phi = 90°$, indicating that the Alfvén waves are essentially decoupled in highly inclined field when $\phi = 90°$ (as discussed previously).

Figure 4.25 shows the variation of the extinction length as a function of field inclination, θ, when $\phi = 45°$ for the first nine ($n = 0, \ldots, 8$) π-modes at four different (fixed) frequencies (a) 3 mHz (b) 4 mHz (c) 5 mHz and (d) 6 mHz. Again, the characterisation of the solar convection zone is identical to that discussed in §3.7.2. Therefore, Figure 4.25 is the same as Figure 3.11, except $\phi = 45°$. The striking contrast between Figures 3.11 and 4.25 is the behaviour of the extinction length in highly inclined field. When $\phi = 0$, Figure 3.11

---

*As noted in §3.7.2, recent calculations by Cally, Crouch, and Braun (2003, see Appendix F) find the models in best agreement with observations have $L = 600 - 800$ km.
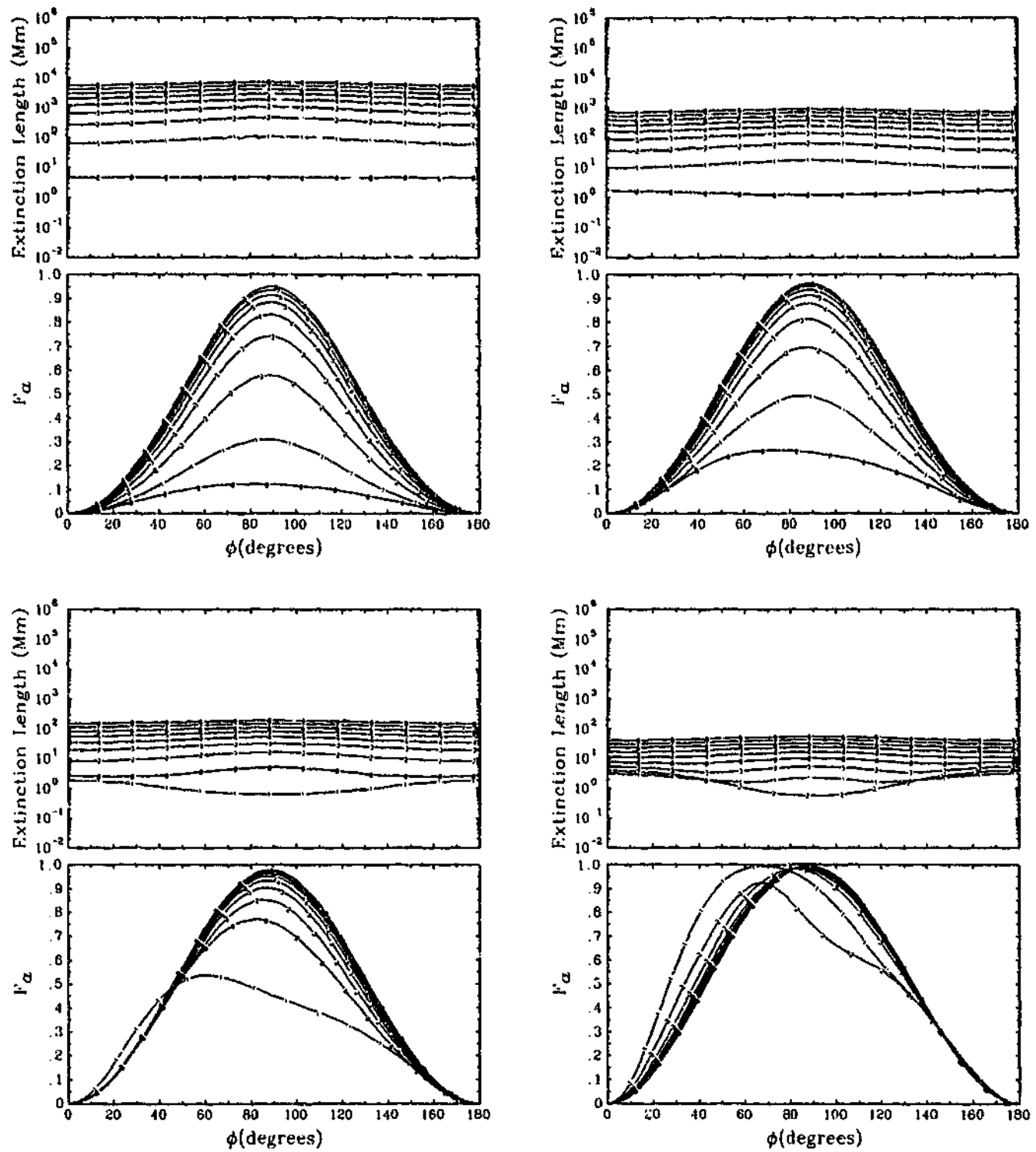
Figure 4.23: Extinction length, $L/\mathrm{Im}\,(\kappa)$, and the contribution by the Alfvén waves to asymptotic wave energy flux, F_a, as a function of propagation direction, ϕ, for the π-modes with $n = 0, \ldots, 8$. This figure is broken into four panels (a) *Top left:* the frequency is constant at 3 mHz. (b) *Top right:* 4 mHz. (c) *Bottom left:* 5 mHz. (d) *Bottom right:* 6 mHz. Within each of the panels, the top graph shows the extinction length as a function of ϕ, the bottom graph displays the corresponding variation of F_a. For all of these plots the field inclination is fixed at $\theta = 30°$.
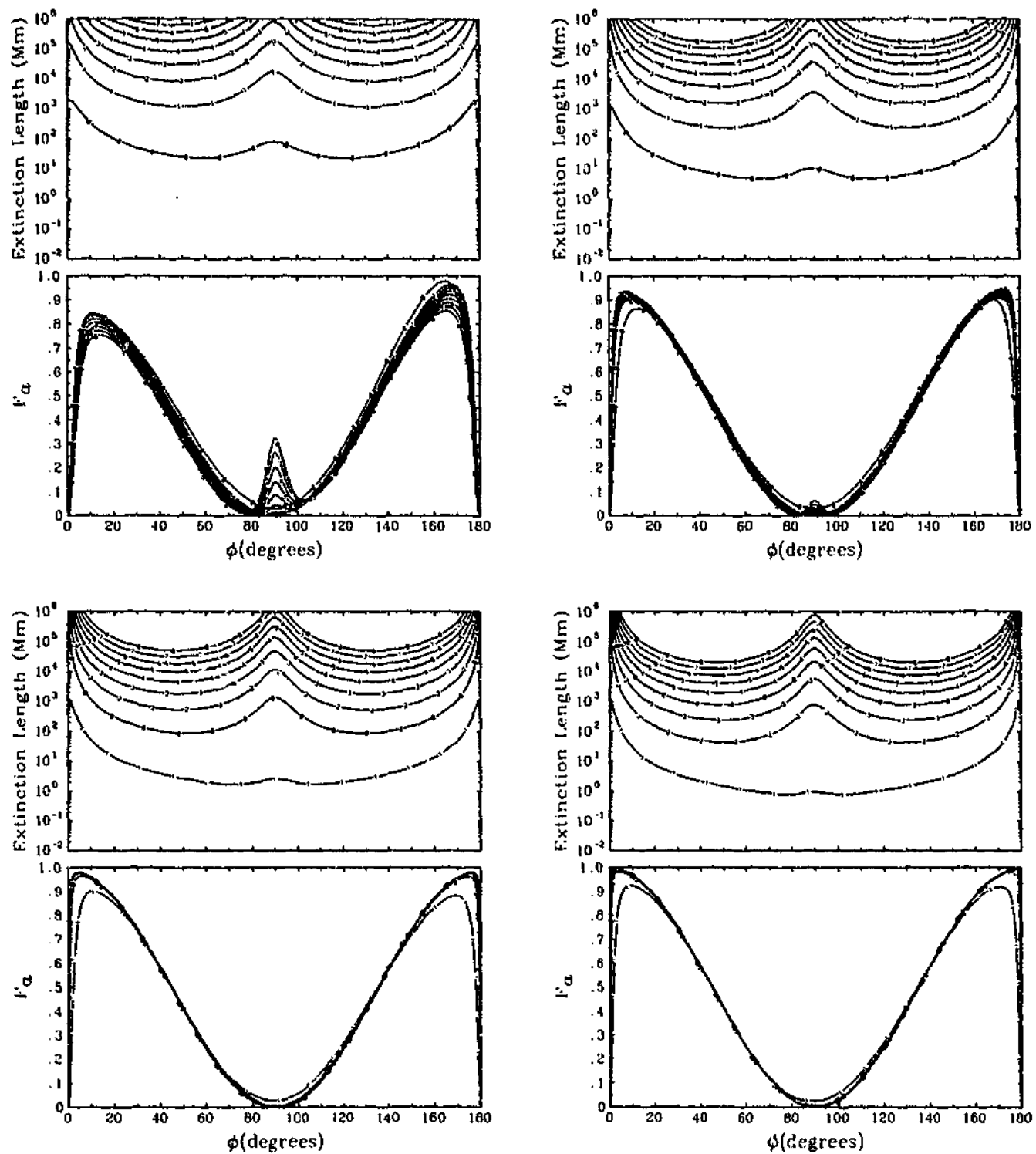
Figure 4.24: Same as Figure 4.23, except $\theta = 80°$.

shows that mode conversion becomes increasingly inefficient (the extinction length tends to infinity) as the field approaches horizontal. In contrast, Figure 4.25 shows that, when $\phi = 45°$, the extinction lengths appear to remain finite as $\theta \to 90°$, for most modes at all displayed frequencies. As the horizontal field singular limit is approached, the numerical integrations

108

become increasingly unreliable, though Figure 4.25 shows the numerical method is reasonably robust in the neighbourhood of $\theta = 90°$. Nevertheless, the results obtained in highly inclined field should be viewed with caution. In particular, the apparent trend shown in Figure 4.25 is probably misleading, but does indicate that solutions of the $(\theta \to 90°)$ perturbation problem (e.g., Kamp, 1989, 1990; Zhukov, 1988, 1989a,b, 1990) could be very useful. Unfortunately, such an approach is beyond the scope of this thesis. As in the $\phi = 0$ case (Fig. 3.11), at all four frequencies Figure 4.25 shows the extinction length of the $n = 0$ mode increases with increasing inclination, though the incre se is much less in magnitude, except in highly inclined field where an apparent, slight c " se is evident at lower frequencies. Also as in the $\phi = 0$ case (Fig. 3.11), for modes with $n \geq 1$, the extinction length initially decreases with increasing inclination, reaching a minimum in the range $\theta \approx 20° - 60°$ (depending on the frequency and the radial order), before increasing for larger θ; though some lower order modes show a slight decrease in highly inclined field at the larger displayed frequencies.

Figure 4.25 shows (the well established result) that in exactly vertical field ($\theta = 0$), the Alfvén waves decouple ($F_a = 0$) and all the energy lost is carried by the slow MAG waves. Figure 4.25 also shows that at inclinations approaching horizontal, the contribution by the Alfvén waves and the slow MAG waves to asymptotic wave energy flux is roughly equal (i.e., $F_a \to 0.5$ as $\theta \to 90°$) for all modes at all frequencies. At intermediate inclinations, F_a changes substantially as θ varies. It is worth noting that $F_a \approx 0.5$ at the locations of the extinction length minima (top graphs in each panel), indicating that Alfvén wave and slow MAG wave leakage contribute to the maximal damping rate in roughly equal proportions, when $\phi = 45°$. Broadly speaking, the behaviour of F_a, when $\phi = 135°$ (Fig. 4.26), is very similar to the case where $\phi = 45°$.

Figure 4.27 shows the variation of the extinction length as a function of field inclination, θ, when $\phi = 90°$ for the first nine ($n = 0, \ldots, 8$) π-modes at four different (fixed) frequencies (a) 3 mHz (b) 4 mHz (c) 5 mHz and (d) 6 mHz. Figure 4.27 is the same as Figure 4.25, except $\phi = 90°$. The behaviour of the extinction length when $\phi = 90°$ (Fig. 4.25) is very similar to that displayed when $\phi = 0$ (Fig. 3.11). In particular, as $\theta \to 90°$, the extinction lengths increase toward infinity. Also, for modes with $n \geq 1$, the extinction length initially decreases with increasing inclination, reaching a minimum near $\theta \approx 20° - 60°$, before increasing for larger θ. For the lower frequencies (e.g., Fig. 4.27(a) and 4.27(b)), the minimum is at $\theta \approx 40° - 60°$, whereas, for the higher frequencies (e.g., Fig. 4.27(c) and 4.27(d)), the minimum is at more acute inclinations $\theta \approx 20° - 40°$. In contrast to the $\phi = 0$ case (Fig. 3.11), at all four frequencies Figure 4.27 shows the extinction length of the $n = 0$ mode is essentially unaffected by the inclination, except at inclinations approaching horizontal where the extinction length of the $n = 0$ mode grows rapidly with increasing inclination. This contrasting behaviour is most pronounced at higher frequencies (e.g., Fig. 4.27(c) and 4.27(d)).

As usual, Figure 4.27 shows that $F_a = 0$ when $\theta = 0$ (and $\phi = 90°$). Figure 4.27 shows that F_a essentially vanishes in highly inclined when $\phi = 90°$, for all modes at all frequencies (due to the suppression of the displacement component, η, as discussed earlier). When $\phi = 90°$, Figure 4.27 shows that F_a attains a maximum (that is largest for the higher order modes) at the inclinations where the extinction length (top graphs in each panel) attains a minimum. For the higher order modes, this suggests that the Alfvén waves are primarily responsible for the damping exhibited in this region (in contrast to the case where $\phi = 45°$, Fig. 4.25).
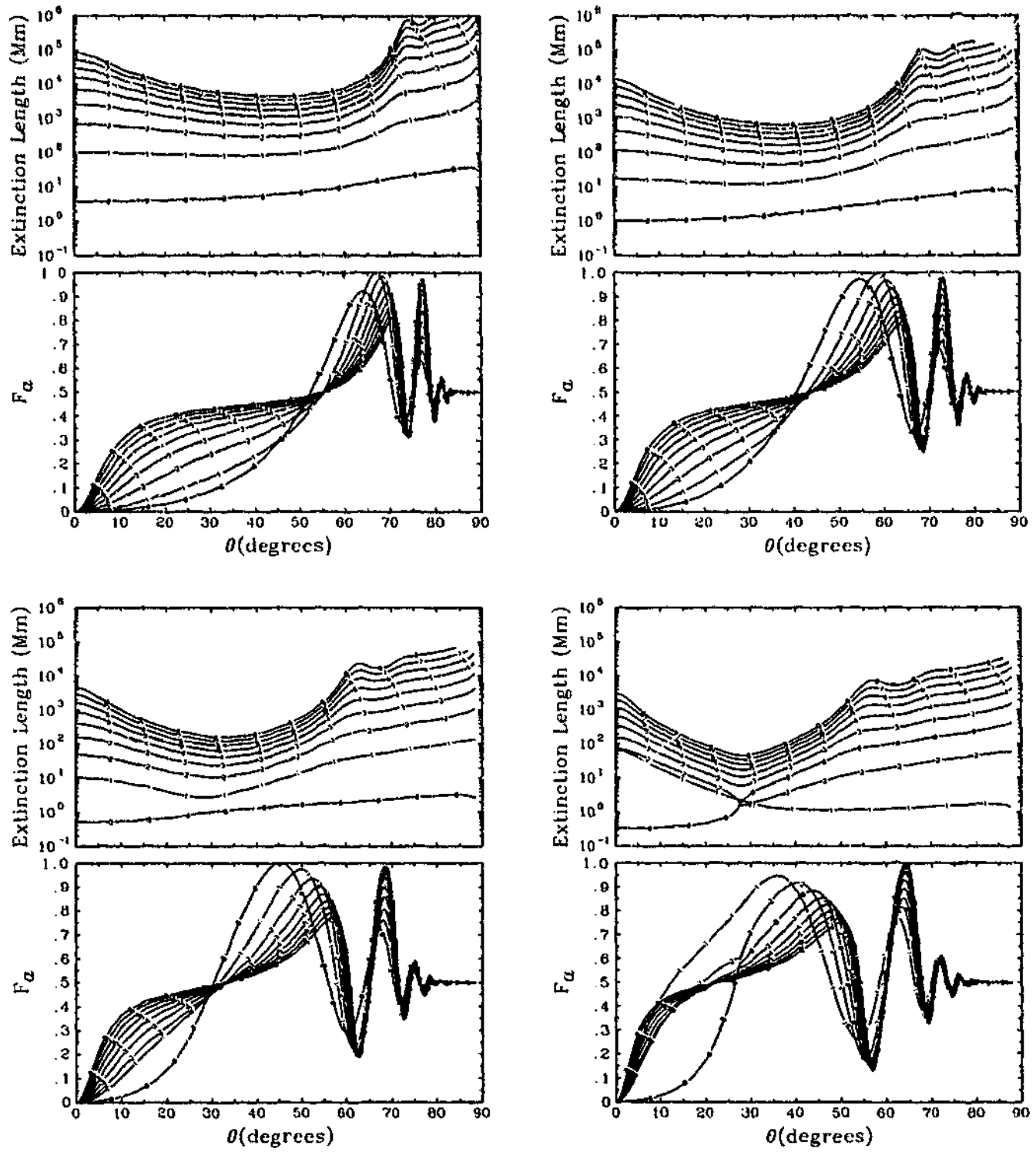
Figure 4.25: Extinction length, $L/\text{Im}(\kappa)$, and the contribution by the Alfvén waves to asymptotic wave energy flux, F_a, as a function of field inclination, θ, for the π-modes with $n = 0, \ldots, 8$. This figure is broken into four panels (a) *Top left*: the frequency is constant at 3 mHz. (b) *Top right*: 4 mHz. (c) *Bottom left*: 5 mHz. (d) *Bottom right*: 6 mHz. Within each of the panels, the top graph shows the extinction length as a function of θ, the bottom graph displays the corresponding variation of F_a. For all of these plots the propagation direction is fixed at $\phi = 45°$. This figure is the same as Figure 3.11, except $\phi = 45°$.

110
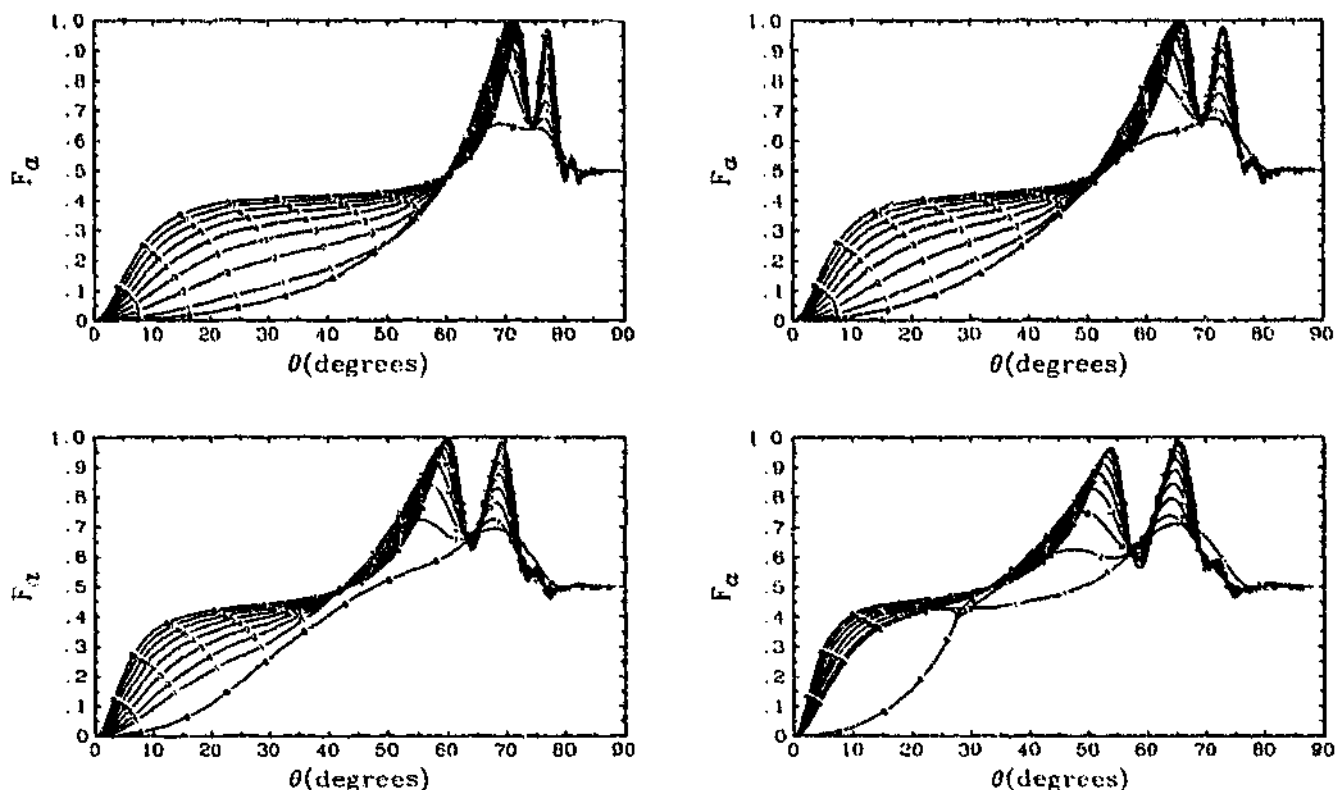
Figure 4.26: Same as Figure 4.25, except $\phi = 135°$. In this case, the extinction lengths are the same as those in Figure 4.25 (i.e., $\phi = 45°$).

4.7 Conclusions

In this chapter, we investigated the three-dimensional ($\phi \neq 0$) propagation of oscillations in a complete polytrope permeated by a straight, uniform, non-vertical magnetic field. We calculated the eigenvalues, κ, and the corresponding contribution by the Alfvén waves to asymptotic wave energy flux, F_a. Several different but complementary approaches were employed in order to gain a complete understanding of the variation of κ and F_a as a function of the three parameters ν, θ, and ϕ. Our findings can be summarised as follows:

- Broadly speaking, except in highly inclined field, the horizontal spatial decay rate of the π-modes (proportional to $\text{Im}(\kappa)$) varies little with the propagation direction, ϕ. However, the nature of the mode conversion (inferred from F_a) does vary substantially. In general, rather than radiating great quantities of additional energy, the Alfvén waves tend to compensate in regions of the parameter space where the slow MAG waves are only weakly coupled, and visa versa, keeping the overall damping rate effectively constant.

- In highly inclined field ($\theta \gtrsim 70°$) at constant frequency, the decay rate has a substantial local maximum at $\phi \approx 45°$. However, this enhancement is still several orders of magnitude less than the values exhibited at lower inclinations with the same ϕ.

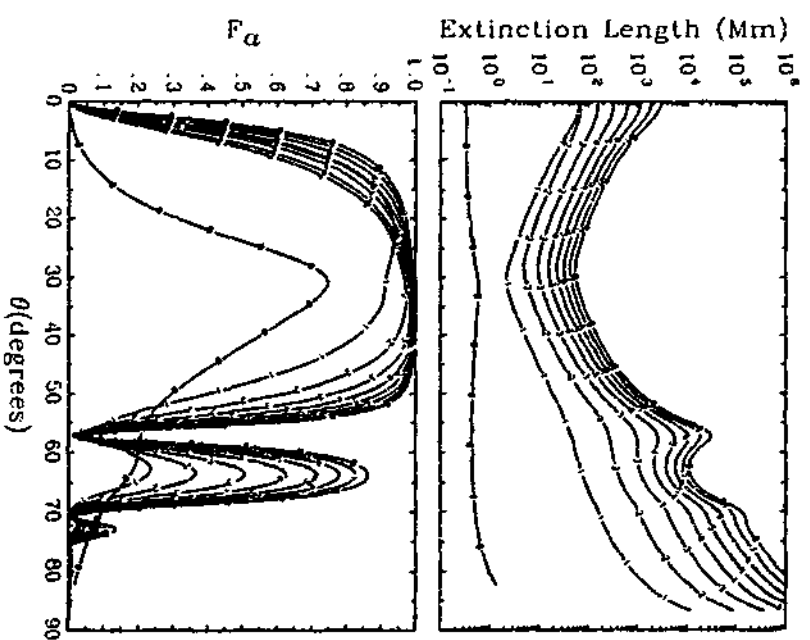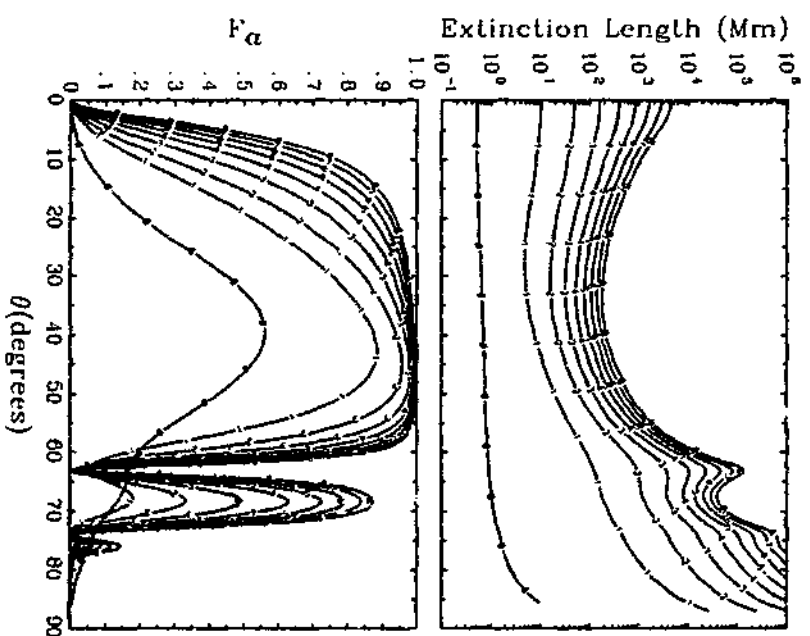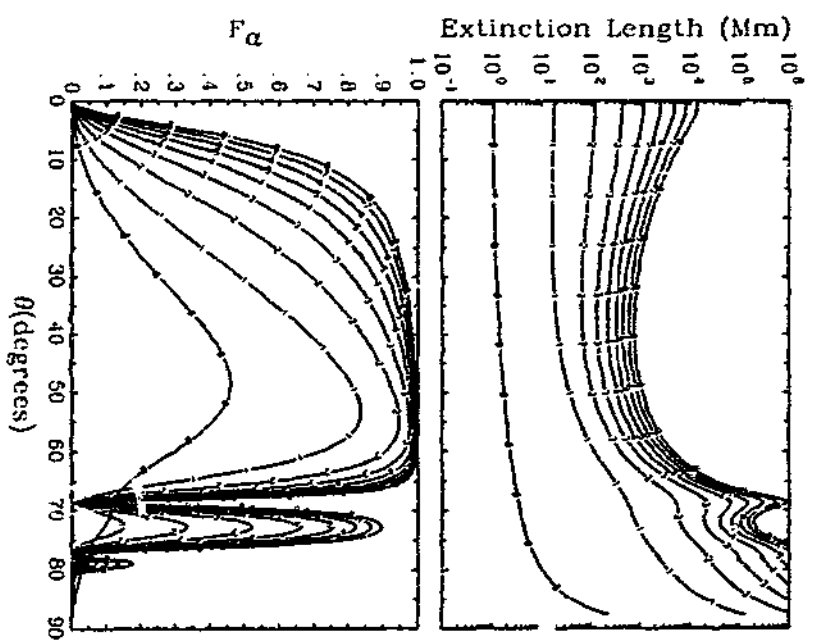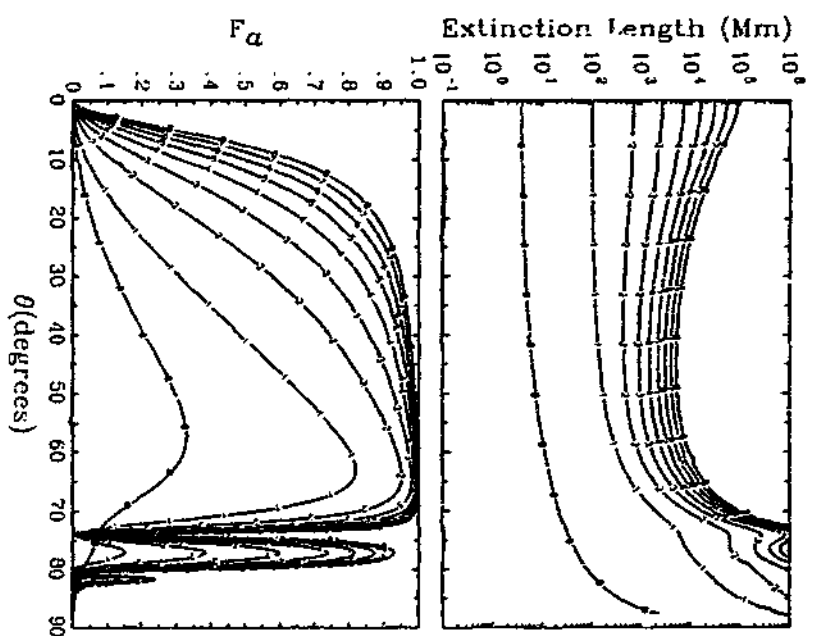- The complicated topology over the (ν, θ)-plane seen in the two-dimensional case (Chap-

111

Figure 4.27: Same as Figure 4.25, except $\phi = 90°$.

112

ter 3) persists for three-dimensional propagation. Indeed, the topology itself varies dramatically with ϕ.

- We found a new type of highly damped solution, the γ-modes, which mainly exist in highly inclined field. Unfortunately, limitations of the numerical method in the highly inclined field regime prevented a complete exploration of the γ-mode solutions. In general, our result tend to suggest highly inclined fields (approaching horizontal) warrant more detailed analysis.

- The horizontal spatial decay rate of the π-modes varies substantially with both frequency and inclination. In comparison to vertical field, we found that π-modes with $n \geq 1$ undergo significantly enhanced mode conversion in moderately inclined fields ($\theta \approx 20° - 60°$, depending on the mode and frequency). As was found in the two-dimensional case (Chapter 3), the enhancement is most pronounced at higher frequencies. For the f-mode ($n = 0$), damping is most efficient in vertical field though in some cases the variation with inclination is weak.

113

Chapter 5

The contribution by thin magnetic flux tubes to p-mode line widths

In the previous two chapters we investigated the fate of oscillations propagating through a slab of uniform, non-vertical magnetic field. In this chapter we focus on highly non-uniform field – an atmosphere threaded by numerous widely spaced, thin magnetic flux tubes. The plasma-β inside the tubes is assumed to be independent of depth. Consequently, conversion of p-modes to tube modes may occur over the entire length of the sub-photospheric tube. We calculate the contribution to p-mode damping resulting from tube modes escaping down into the solar interior and up into the upper solar atmosphere.

5.1 Model and method

In this section we describe each of the components which constitute the model. Firstly, we discuss the model for the non-magnetic convection zone in which the flux tube is embedded, and the oscillations it supports (the p-modes). We then discuss the thin flux tube – both it's static equilibrium configuration and the oscillations it supports (the tube modes, which are driven by the p-modes). The upper boundary condition is discussed in detail, accounting for a previously neglected physical process – the loss of energy to the upper solar atmosphere by the excitation of waves in the chromosphere and corona. Finally, we calculate the p-mode damping rates resulting from the excitation of the tube modes.

5.1.1 Truncated polytrope

The equilibrium structure of the non-magnetic convection zone in which the thin flux tube is embedded is modelled as a plane-parallel, truncated, isentropic polytrope with index m. The vertical variation for the density and pressure have the familiar form:

$$\rho_e(z) = \rho_0 \left(-\frac{z}{z_0}\right)^m \quad \text{and} \quad p_e(z) = p_0 \left(-\frac{z}{z_0}\right)^{m+1},$$

where $p_0 = \rho_0 g z_0 / (m+1)$ and $m = 1/(\gamma - 1)$, the subscript "e" refers to quantities external to the tube, whereas unsubscripted quantities are internal. The truncation depth, $z = -z_0$,

114

taken as the surface of the model convection zone, is assumed to coincide with the $\tau_{0.5} = 1$ level of the photospheric reference model provided in Table 11 of Maltby *et al.* (1986). So $\rho_0 = 2.78 \times 10^{-4}$ kg m^{-3}, $p_0 = 1.21 \times 10^4$ kg m^{-1}s^{-2}, and $g = 2.775 \times 10^2$ m s^{-2} are adopted as the characteristic physical scales at the model photospheric surface. The validity of this model atmosphere was discussed in detail in §3.2.

5.1.2 Oscillations of the truncated polytrope

The solar *p*-modes are modelled as the acoustic oscillations of the truncated polytrope. The acoustic oscillations are assumed to be linear, adiabatic, steady-state and monochromatic with an angular frequency ω (real and non-negative). A detailed discussion of the oscillations supported by a truncated polytrope can be found in Bogdan and Cally (1995). We re-iterate the features vital to our investigation.

The acoustic oscillations of the truncated polytrope are assumed to be adiabatic, therefore, the perturbed fluid density, $\delta\rho(x,t)$, pressure, $\delta p(x,t)$, and the displacement of the fluid element from its rest position, $\xi(x,t)$, may be derived from a velocity potential $\Phi(x,t)$:

$$\xi_e = \nabla\Phi, \quad \delta p_e = -\rho_e \frac{\partial^2 \Phi}{\partial t^2}, \quad \text{and} \quad \delta\rho_e = -\frac{\rho_e}{C_S^2}\frac{\partial^2 \Phi}{\partial t^2}, \tag{5.1}$$

where $C_S = (-gz/m)^{1/2}$ is the adiabatic sound speed. The velocity potential satisfies the partial differential equation (Lamb, 1945, p. 548)

$$\frac{\partial^2 \Phi}{\partial t^2} = C_S^2 \nabla^2 \Phi - g\frac{\partial \Phi}{\partial z}. \tag{5.2}$$

Subject to the boundary conditions; that evanescent modes decrease at the lower boundary (i.e., $\Phi \to 0$, as $z \to -\infty$), and the Lagrangian pressure perturbations vanish at the surface (i.e., $\nabla \cdot \xi_e \to 0$, as $z \to -z_0^-$); it may be verified that

$$\Phi(x,s,t) = A_n s^{-1/2-\mu} W_{\kappa_n,\mu}\left(\frac{s\nu^2}{\kappa_n}\right) \cos(k_n x - \omega t) \tag{5.3}$$

is the relevant solution of equation (5.2), where it is assumed (without loss of generality) that travelling waves propagate in the positive *x*-direction (i.e., $k_n \geq 0$). In equation (5.3), $s = -z/z_0$ is the dimensionless depth, $\nu^2 = m\omega^2 z_0/g$ is the squared dimensionless frequency, $k_n = \nu^2/2\kappa_n z_0$ is the (real) horizontal wavenumber, $W_{\kappa_n,\mu}$ is the Whittaker function (Abramowitz and Stegun, 1964, Chapter 13), $\mu = (m-1)/2$ characterises the stratification, and A_n is the mode amplitude (which is arbitrary but may be specified by some appropriate normalisation). The parameter κ_n is constrained to take on a discrete set of values, being the solutions of

$$W_{\kappa_n,\mu+1}\left(\frac{\nu^2}{\kappa_n}\right) = 0. \tag{5.4}$$

Equation (5.4) is just the requirement that $\nabla \cdot \xi_e \to 0$, as $z \to -z_0^-$ (see Bogdan and Cally, 1995).

The acoustic oscillations satisfy a wave energy conservation law (e.g., Eckart, 1960, Chapter 4),

$$\frac{\partial}{\partial t}\left[\frac{1}{2}\rho_e\left|\frac{\partial\boldsymbol{\xi}_e}{\partial t}\right|^2 + \frac{1}{2\gamma p_e}|\delta p_e|^2\right] + \nabla\cdot\left[\delta p_e\frac{\partial\boldsymbol{\xi}_e}{\partial t}\right] = 0,$$

which is the sum of three terms: the first is the kinetic energy associated with the oscillations ($\propto \rho_e|\partial\boldsymbol{\xi}_e/\partial t|^2$), the second is the internal energy ($\propto |\delta p_e|^2$), and the third is the wave energy flux carried by the perturbations ($\propto \delta p_e(\partial\boldsymbol{\xi}_e/\partial t)$). The time-average p-mode energy underlying a surface area $4\pi R_\odot^2$ (where $R_\odot$ is the solar radius) is then

$$
\begin{aligned}
\langle\mathcal{E}_n\rangle &= 4\pi R_\odot^2\frac{\omega}{2\pi}\int_{-\pi/\omega}^{\pi/\omega}\int_{-\infty}^{-z_0}\left(\frac{1}{2}\rho_e\left|\frac{\partial\boldsymbol{\xi}_e}{\partial t}\right|^2 + \frac{1}{2\gamma p_e}|\delta p_e|^2\right)dz\,dt \\
&= 4\pi R_\odot^2\frac{\rho_0 q\nu^4}{4mz_0^2}A_n^2\mathcal{N}_n,
\end{aligned}
\tag{5.5}
$$

where

$$\mathcal{N}_n = \int_{\nu^2/\kappa_n}^{\infty}\left\{\left(\frac{1}{w}+\frac{1}{4\kappa_n}\right)W_{\kappa_n,\mu}^2(w) + \frac{w^{1+2\mu}}{\kappa_n}\left(\frac{d}{dw}\left[w^{-1/2-\mu}W_{\kappa_n,\mu}(w)\right]\right)^2\right\}dw.\tag{5.6}$$

$\langle\mathcal{E}_n\rangle$ quantifies the amount of p-mode energy available to excite oscillations in the subphotospheric magnetic flux tube.

5.1.3 Thin magnetic flux tubes

The flux tube embedded in the truncated polytrope is modelled as a thin magnetic flux tube (e.g., Defouw, 1976; Roberts and Webb, 1978; Spruit, 1981; Ferriz-Mas and Schüssler, 1989). This means that the radius of the flux tube, $R(z)$, is everywhere small compared to the local density scale height, $H(z) \approx |z|/m$, and the characteristic length scale of the p-mode forcing, $\lambda_\perp \approx g/\omega^2$. The thin flux tube approximation is reasonable for the small-scale intense flux tubes which populate the solar photosphere. These small-scale intense flux tubes have diameters of about 100 km (e.g., Stenflo, 1978) and are embedded in an atmosphere with a density scale height of order a few hundred kilometres. Likewise, the horizontal wavelength of the p-modes is of order several hundred kilometres or more. However, above the photosphere the approximation is unreliable (see BHCC), the model we adopt there is discussed later (§5.1.5). We also assume that the flux tubes are sufficiently separated that the interaction between neighbouring tubes (e.g., multiple scattering) can be neglected. This assumption is reasonable for the solar photosphere, where the surface magnetic filling factor is of order 0.01.

Under the thin flux tube approximation it is possible to neglect the variation of any physical quantity across the lateral extent of the tube. Therefore, the total pressure (gas +

116

magnetic) is constant across the tube, and so for the tube to be in mechanical equilibrium with its surroundings, we must have (e.g., Roberts and Webb, 1978)

$$p_e(z) = p(z) + \frac{1}{2\mu_B} B^2(z) , \qquad (5.7)$$

where $B(z)\,\hat{e}_z$ is the magnetic field inside the tube.

We also assume that the magnetic flux tube is in thermal equilibrium with its surroundings, $T_e(z) = T(z)$. We discuss the validity of this assumption shortly. It then follows (by combining eq. [5.7] with the equations for hydrostatic equilibrium, $dp/dz = -\rho g$, inside and outside the tube) that the plasma-β, defined as

$$\beta = \frac{2\mu_B p(z)}{B^2(z)} ,$$

is independent of depth for a tube in an atmosphere of arbitrary vertical stratification (e.g., Roberts and Webb, 1978). For the sub-photospheric flux tube, embedded in the truncated polytrope, the density, gas pressure, and magnetic field strength inside the tube, respectively, are given by:

$$\rho(z) = \frac{\beta}{\beta+1}\rho_e(z) , \quad p(z) = \frac{\beta}{\beta+1}p_e(z) , \quad \text{and} \quad B(z) = \sqrt{\frac{2\mu_B}{\beta+1}p_e(z)} .$$

Therefore, the stratification inside the flux tube is also an adiabatically stratified polytrope of index m, with a density and gas pressure reduced everywhere by the constant factor $\beta/(\beta+1)$.

We have assumed that a sufficiently thin magnetic flux tube will quickly be brought into thermal equilibrium with its surroundings by radiative diffusion. Below the photosphere the radiative diffusion time-scale for a flux tube is

$$\tau(z) = \frac{R^2(z)}{\kappa(z)} ,$$

where $\kappa = 16\sigma_s T^3/(3c_p\rho^2\tilde{\kappa})$ is the thermal diffusivity ($\sigma_s = 5.67 \times 10^{-8}$ kg s^{-3} K^{-4} is the Stefan-Boltzmann constant, $c_p = \gamma\tilde{R}/(\gamma-1)\mu_g$ is the specific heat of the gas at constant pressure, $\tilde{R} = 8.314 \times 10^3$ m^2 s^{-2} K^{-1} is the universal gas constant, $\mu_g = 0.6$ is assumed, and $\tilde{\kappa}$ is the opacity). The radius of the sub-photospheric constant-β flux tube varies as $R^2(z) \propto B^{-1}(z)$, and we take $R(-z_0) = 150$ km. Therefore, for the thin flux tube embedded in the truncated polytrope (with $m = 3/2$),

$$\tau(z) = \tau_0 \left(-\frac{z}{z_0}\right)^{-13/4} ,$$

where $\tau_0 = 643$ seconds, and we have employed Kramers' opacity law, $\tilde{\kappa} \propto \rho T^{-7/2}$, with $\tilde{\kappa}(-z_0) = 10^{-1}$ m^2 kg^{-1}. Near the photosphere τ is of order several minutes. Below the photosphere τ decreases rapidly with depth, to values of order a few seconds at $z = -5z_0 \approx$ 2 Mm. The observed lifetimes of the flux tubes populating the solar photosphere vary from a

117

few hours to a few days. For example, the elements (flux tubes) of moving magnetic features, in the vicinity of sunspots, have average lifetimes 4 hours (Zhang, Solanki, and Wang, 2003), intranetwork magnetic elements have average lifetimes of 2 hours (Zhang et al., 1998), and magnetic network elements have average lifetimes of 50 hours (Liu et al., 1994). As the lifetimes of the flux tubes greatly exceed the radiative diffusion time-scale, the assumption that flux tube is in thermal equilibrium with its surroundings is plausible.

5.1.4 Oscillations of the thin magnetic flux tube

Spruit (1981) showed that the steady-state, linear oscillations of an isolated, thin, untwisted magnetic flux tube can be completely described by transverse, $\xi_\perp(z,t)$, and longitudinal, $\xi_\parallel(z,t)$, displacements. In the literature, these flux tube oscillations are commonly referred to as kink and sausage modes, respectively. We consider the oscillations of the thin magnetic flux tube (the sausage and kink modes) to be driven by fluctuations associated with incident p-modes. The sausage modes are generated by fluctuations in pressure, whereas the kink modes are produced by lateral velocity shears (i.e., magnetic tension associated with curvature of the flux tube). Figure 5.1 provides a simplified illustration of the tube mode excitation process (for the kink modes). As the flux tube is much thinner than the horizontal wavelength of the p-modes, the tube modes are a result of the temporal driving by the p-modes (i.e., the tube responds to the p-mode frequency, rather than the wavelength).

For a constant-β flux tube embedded in an isentropic polytrope of index m, the PDEs governing the sausage and kink mode displacements, respectively, are:

$$\left[\frac{\partial^2}{\partial t^2} + \frac{2gz}{2m + \beta(m+1)}\frac{\partial^2}{\partial z^2} + \frac{g(m+1)}{2m + \beta(m+1)}\frac{\partial}{\partial z}\right]\xi_\parallel = \frac{(m+1)(\beta+1)}{2m + \beta(m+1)}\frac{\partial^3\Phi}{\partial z\partial t^2}, \qquad (5.8)$$

$$\left[\frac{\partial^2}{\partial t^2} + \frac{2gz}{(m+1)(1+2\beta)}\frac{\partial^2}{\partial z^2} + \frac{g}{1+2\beta}\frac{\partial}{\partial z}\right]\xi_\perp = \frac{2(1+\beta)}{1+2\beta}\frac{\partial^3\Phi}{\partial x\partial t^2}, \qquad (5.9)$$

where Φ is the potential associated with the incident p-mode (eq. [5.3]) evaluated along the equilibrium location of the flux tube axis (taken as $x = 0$). The derivation of the governing PDEs (5.8) and (5.9) is outlined in BHCC (their Appendix A, but see also Defouw, 1976; Ryutov and Ryutova, 1976; Roberts and Webb, 1978, 1979; Spruit, 1981; Ryutova and Priest, 1993a; Hasan, 1997). In the limit of vanishing magnetic field, $\beta \to \infty$, the spatial derivatives on left-hand sides of the PDEs (5.8) and (5.9) vanish, which then implies $\boldsymbol{\xi} = \nabla\Phi$, consistent with the fluid displacements associated with the p-modes (eq. [5.1]). Hence, finite β effects (i.e., non-zero magnetic fields) cause the motions of the flux tube to deviate from that associated with the p-modes, which then causes the p-modes to be scattered and absorbed by the flux tube.

The coefficients of the governing PDEs (5.8) and (5.9) are independent of time, t. Therefore, it is reasonable to use the method of separation of variables and assume the displacements have the form:

$$\xi_\parallel(s,t) = \mathrm{Re}\left[\tilde{\xi}_\parallel(s)e^{-i\omega t}\right] \quad \text{and} \quad \xi_\perp(s,t) = \mathrm{Im}\left[\tilde{\xi}_\perp(s)e^{-i\omega t}\right].$$
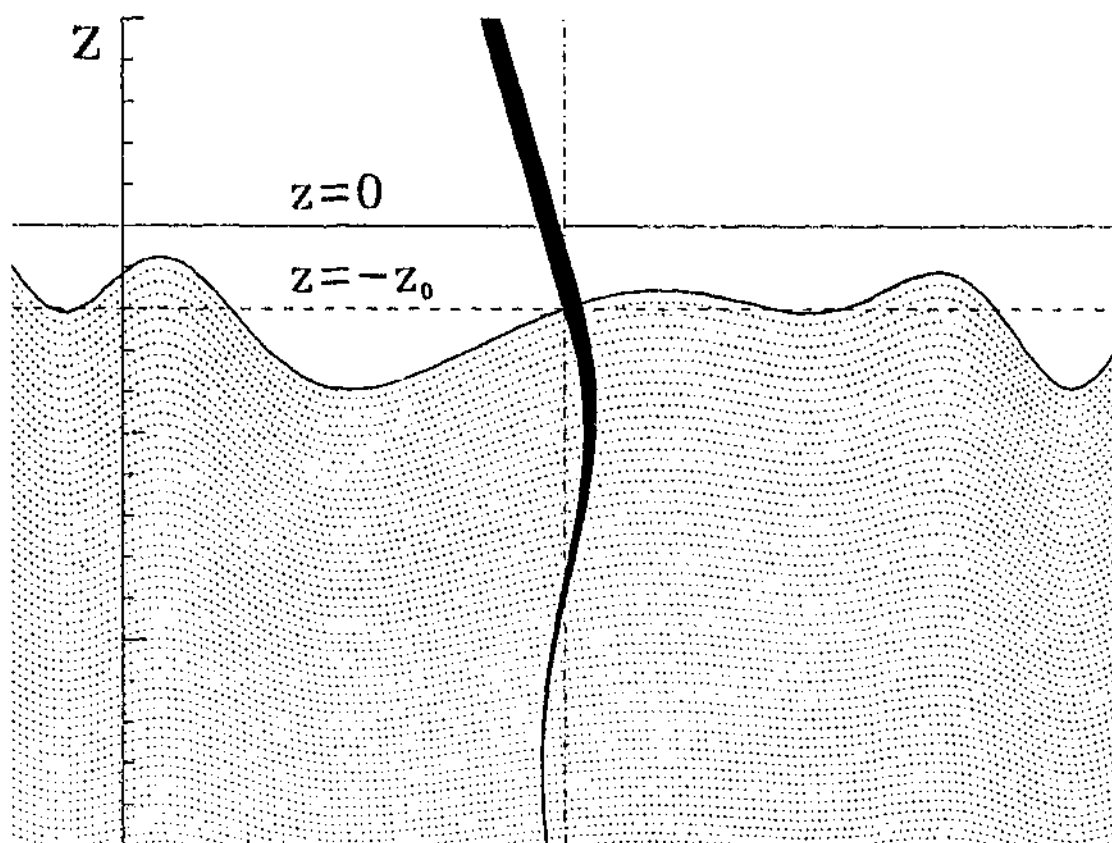
118

Figure 5.1: A sketch of a thin magnetic flux tube being buffeted by *p*-modes. The undisturbed surface of the truncated polytrope is indicated by the horizontal dashed line, and the undisturbed position of the flux tube is represented by the vertical dot-dashed line ($x = 0$). This sketch emphasises the excitation of the kink modes on the tube, induced by lateral velocity shears in the surroundings. Above $z = -z_0$ the thin flux tube approximation breaks down. Hence, the extension of the tube above this level serves as an illustration only. Reproduced courtesy of BHCC.

It can then be shown that the governing PDEs (5.8) and (5.9) for the longitudinal and transverse oscillations reduce to the same inhomogeneous ordinary differential equation,

$$\frac{d^2\tilde{\xi}_\sigma}{ds^2} + \frac{\mu + 1}{s}\frac{d\tilde{\xi}_\sigma}{ds} + \frac{\nu^2\epsilon_\sigma}{s}\tilde{\xi}_\sigma = f_\sigma(s) , \tag{5.10}$$

where σ denotes either $\parallel$ or $\perp$,

$$\epsilon_\parallel = \frac{2m + \beta(m+1)}{2m} \quad \text{and} \quad \epsilon_\perp = \frac{(m+1)(1+2\beta)}{2m} ,$$

and

$$f_\parallel(s) = -\frac{(m+1)(\beta+1)}{2mz_0}\nu^2 A_n \frac{1}{s}\frac{d}{ds}\left[s^{-1/2-\mu}W_{\kappa_n,\mu}\left(\frac{s\nu^2}{\kappa_n}\right)\right]$$

is the driving term for the sausage modes, and

119

$$f_\perp(s) = \frac{i(m+1)(\beta+1)}{2mz_0\kappa_n} \nu^4 A_n s^{-3/2-\mu} W_{\kappa_n,\mu}\left(\frac{s\nu^2}{\kappa_n}\right)$$

is the driving term for the kink modes.

The displacement associated with the sausage and kink modes is required to satisfy boundary conditions at the top ($z = -z_0$) and the bottom ($z \to -\infty$) of the flux tube. At the bottom of the flux tube an outward radiation condition is imposed. At the top of the flux tube both upward- and downward-propagating tube modes are required – an upward-propagating tube mode will partially couple onto waves in the overlying atmosphere, which themselves may be subject to reflection within the chromosphere or corona, or from the transition region. In the case of the kink modes we will consider three distinct models of the corona.

Expressions for the free oscillations of the sub-photospheric flux tube (i.e., eq. [5.10] with $f_\sigma = 0$), satisfying one or other of the bottom and top boundary conditions, are required in constructing the Green's function for the driven tube. We represent the solution satisfying the bottom (outgoing wave) condition by $\psi_\perp$ and $\psi_\parallel$ (horizontal and vertical displacements), and that satisfying the top (as yet unspecified) condition by displacements $\phi_\perp$ and $\phi_\parallel$. These can be expressed concisely in terms of Bessel functions (Abramowitz and Stegun, 1964, eq. [9.1.53]),

$$\psi_\sigma(s) = s^{-\mu/2} H_\mu^{(1)}\left(2\nu\sqrt{\epsilon_\sigma s}\right), \tag{5.11}$$

and

$$\phi_\sigma(s) = s^{-\mu/2}\left[H_\mu^{(2)}\left(2\nu\sqrt{\epsilon_\sigma s}\right) + \lambda_\sigma H_\mu^{(1)}\left(2\nu\sqrt{\epsilon_\sigma s}\right)\right], \tag{5.12}$$

where $H_\mu^{(1)}$ and $H_\mu^{(2)}$ denote the Hankel functions of the first and second kind, respectively.

At the bottom of the flux tube the homogeneous solution ψ_σ (eq. [5.11]) represents a downward-propagating tube mode, as $s \to \infty$, satisfying the outgoing radiation condition. At the top of the flux tube, $s = 1$, the homogeneous solution ϕ_σ (eq. [5.12]) satisfies the condition that both upward- and downward-propagating tube modes be present. The inclusion of the complex parameter, λ_σ (Hindman, 1997), allows a range of boundary conditions to be imposed at the top of the thin magnetic flux tube. The specific form of λ_σ is calculated by matching the particular solution onto upward- and downward-propagating waves in the overlying atmosphere. The details of this matching and the model of the overlying atmosphere will be addressed later (§5.1.5). Provided m is not an odd integer, the Wronskian of the two homogeneous solutions (5.11) and (5.12) is non-zero within the domain of the truncated polytrope. So the two homogeneous solutions are linearly independent for any value of the parameter λ_σ, and the particular solution for the driven tube,

$$\tilde{\xi}_\sigma(s) = -\frac{i\pi}{2}\psi_\sigma(s)\int_1^s r^{\mu+1}\phi_\sigma(r) f_\sigma(r)\,dr - \frac{i\pi}{2}\phi_\sigma(s)\int_s^\infty r^{\mu+1}\psi_\sigma(r) f_\sigma(r)\,dr,$$

is constructed using a Green's function formulation.

5.1.5 Upper boundary conditions

BHCC deliberately neglect the presence of the overlying atmosphere by imposing the stress-free boundary condition at the photosphere. For the sausage modes this requires that the dilation vanishes (i.e., $\nabla \cdot \boldsymbol{\xi} = 0$ at $s = 1$), and for the kink modes the magnetic tension ($\propto \partial^2 \xi_\perp / \partial z^2$) must vanish. The stress-free boundary condition constrains the form of the complex parameters, λ_σ, for the sausage and kink mode respectively,

$$\lambda_\parallel = \frac{-(1+\mu)(1+\beta) H_\mu^{(2)}\left(2\nu\sqrt{\epsilon_\parallel^-}\right) - \nu\sqrt{\epsilon_\parallel^-} H_{\mu+1}^{(2)}\left(2\nu\sqrt{\epsilon_\parallel^-}\right)}{(1+\mu)(1+\beta) H_\mu^{(1)}\left(2\nu\sqrt{\epsilon_\parallel^-}\right) + \nu\sqrt{\epsilon_\parallel^-} H_{\mu+1}^{(1)}\left(2\nu\sqrt{\epsilon_\parallel^-}\right)}$$
$$-\frac{(2i/\pi) W_{\kappa_n,\mu}\left(\frac{\nu^2}{\kappa_n}\right)\left(I_\parallel^{(1)}\right)^{-1}}{(1+\mu)(1+\beta) H_\mu^{(1)}\left(2\nu\sqrt{\epsilon_\parallel^-}\right) + \nu\sqrt{\epsilon_\parallel^-} H_{\mu+1}^{(1)}\left(2\nu\sqrt{\epsilon_\parallel^-}\right)} , \qquad (5.13)$$

$$\lambda_\perp = \frac{\nu\sqrt{\epsilon_\perp^-} H_\mu^{(2)}\left(2\nu\sqrt{\epsilon_\perp^-}\right) - (1+\mu) H_{\mu+1}^{(2)}\left(2\nu\sqrt{\epsilon_\perp^-}\right)}{-\nu\sqrt{\epsilon_\perp^-} H_\mu^{(1)}\left(2\nu\sqrt{\epsilon_\perp^-}\right) + (1+\mu) H_{\mu+1}^{(1)}\left(2\nu\sqrt{\epsilon_\perp^-}\right)}$$
$$-\frac{\left(2i/\left(\pi\nu\sqrt{\epsilon_\perp^-}\right)\right) W_{\kappa_n,\mu}\left(\frac{\nu^2}{\kappa_n}\right)\left(I_\perp^{(1)}\right)^{-1}}{-\nu\sqrt{\epsilon_\perp^-} H_\mu^{(1)}\left(2\nu\sqrt{\epsilon_\perp^-}\right) + (1+\mu) H_{\mu+1}^{(1)}\left(2\nu\sqrt{\epsilon_\perp^-}\right)} , \qquad (5.14)$$

where $I_\parallel^{(1)}$ and $I_\perp^{(1)}$ are defined as

$$I_\parallel^{(1)} = \int_1^\infty r^{\mu/2} H_\mu^{(1)}\left(2\nu\sqrt{\epsilon_\parallel} r\right) \frac{d}{dr}\left[r^{-1/2-\mu} W_{\kappa_n,\mu}\left(\frac{r\nu^2}{\kappa_n}\right)\right] dr , \qquad (5.15)$$

$$I_\perp^{(1)} = \int_1^\infty r^{-\mu/2-1/2} H_\mu^{(1)}\left(2\nu\sqrt{\epsilon_\perp} r\right) W_{\kappa_n,\mu}\left(\frac{r\nu^2}{\kappa_n}\right) dr . \qquad (5.16)$$

In this investigation, we simulate the overlying solar atmosphere with a simple two layer model : chromosphere and corona. The transition region is actually very thin in comparison with the vertical length scales associated with the oscillations involved, so treating it as a discontinuity is reasonable. The chromosphere is modelled as an isothermally stratified layer, with temperature $T_{ch} = 10^4$ K, and with a thickness of ten density scale heights (i.e., $z_{cor} - z_{ch} = 10 H_{ch}$, where H_{ch} is the density scale height in the chromosphere, $z_{ch} = -z_0$ and z_{cor} are the locations of the base of the chromosphere and corona, respectively). The density and pressure inside the flux tube have the familiar form:

$$\rho(z) = \frac{\beta}{\beta+1} \frac{\rho_0 z_0}{(m+1) H_{ch}} \exp\left(\frac{z_{ch} - z}{H_{ch}}\right) , \quad p(z) = \frac{\beta}{\beta+1} p_0 \exp\left(\frac{z_{ch} - z}{H_{ch}}\right) ,$$

for $z_{ch} \leq z \leq z_{cor}$,

where $H_{ch} = RT_{ch}/(\mu_g g)$, R is the gas constant and μ_g is the mean particle weight, and the pressure is continuous across the temperature discontinuities. The corona is modelled as an infinite layer with temperature $T_{cor} = 2 \times 10^6$ K (assuming $\mu_g = 0.6$ throughout the atmosphere). We investigate both sausage and kink modes assuming an isothermally stratified corona, with density and pressure inside the flux tube:

$$\rho(z) = \frac{\beta}{\beta+1} \frac{\rho_0 z_0}{(m+1)H_{cor}} e^{-10} \exp\left(\frac{z_{cor} - z}{H_{cor}}\right), \quad p(z) = \frac{\beta}{\beta+1} p_0 e^{-10} \exp\left(\frac{z_{cor} - z}{H_{cor}}\right),$$

$$\text{for } z \geq z_{cor},$$

where $H_{cor} = RT_{cor}/(\mu_g g)$ is the density scale height in the corona. The Alfvén waves are totally reflected in an infinite, isothermally stratified corona (see e.g., Cally, 1983; An et al., 1989), so for the kink modes we also consider the case where the corona is homogeneous and the Alfvén waves propagate freely. In this case the density and pressure (inside the flux tube),

$$\rho = \frac{\beta}{\beta+1} \frac{\mu_g p_0}{RT_{cor}} e^{-10}, \quad p = \frac{\beta}{\beta+1} p_0 e^{-10}, \quad \text{for } z \geq z_{cor}, \tag{5.17}$$

are constant.

Above the photosphere the magnetic flux tube can no longer be modelled as thin. At the photosphere-chromosphere interface the sausage modes couple onto MAG waves, and the kink modes couple onto Alfvén waves. Cally (1983) studied the propagation of MAG and Alfvén waves in a similar chromosphere-corona system, and found that the energy flux of Alfvén waves propagating into the corona is highly sensitive to the degree of spread of the magnetic field lines of force, whereas the energy flux of MAG waves is not (see also Schwartz, Cally, and Bel, 1984). Consequently, we are justified in neglecting the field spread when discussing MAG waves, i.e.,

$$\mathbf{B} = \sqrt{\frac{2\mu_B p_0}{\beta+1}} \hat{\mathbf{e}}_z, \quad \text{for } z \geq z_{ch}.$$

For the Alfvén waves, however, the magnetic field must be treated carefully - we allow it to spread open with height. In the chromosphere the vertical component decreases exponentially with height,

$$\mathbf{B} = \sqrt{\frac{2\mu_B p_0}{\beta+1}} \exp\left(\frac{z_{ch} - z}{2\alpha H_{ch}}\right) \hat{\mathbf{e}}_z, \quad \text{for } z_{ch} \leq z \leq z_{cor}, \tag{5.18}$$

where α is a free parameter. We take $\alpha = 1.2$, so that the Alfvén speed in the chromosphere increases much less rapidly than the uniform field case. It is assumed that the radial component of the field is negligible. In the corona we consider the magnetic field to be either straight, uniform and vertical,

$$\mathbf{B} = \sqrt{\frac{2\mu_B p_0}{\beta+1}} e^{-5/\alpha} \hat{\mathbf{e}}_z, \quad \text{for } z \geq z_{cor},$$

122

or straight and radial (see Cally, 1983),

$$\mathbf{B} = \sqrt{\frac{2\mu_0 P_0}{\beta + 1}} \, e^{-5/\alpha} \left(\frac{r_{cor}}{r}\right)^2 \hat{\mathbf{e}}_r, \quad \text{for} \quad z \geq z_{cor},$$

where $r_{cor} = R\left(z_{cor}\right)/\sin\theta_m$ (θ_m is the angle at which the field lines are spreading), r is the distance along the field lines, and $\hat{\mathbf{e}}_r$ is the unit vector in the radial direction.

Across the interface at $s = 1$, where the sub-photospheric thin magnetic flux tube matches onto the essentially vertical chromospheric magnetic field, the vertical component of the magnetic field is continuous. It is reasonable to neglect the horizontal component of the sub-photospheric magnetic field since the flux tube is thin, and therefore, the horizontal component is negligible. Across the transition region, for the cases where the coronal magnetic field is straight, uniform and vertical, the direction and magnitude of the magnetic field are continuous. For the Alfvén waves at the transition region, where the essentially vertical chromospheric magnetic field matches onto the straight and radial magnetic field in the corona, the direction of the magnetic field changes discontinuously. This treatment is not entirely self-consistent, and it is possible that this simplification will lead to unphysical Alfvén wave reflection at the transition region. It would be desirable to have a continuous, spreading magnetic field permeating the entire atmosphere (e.g., Bogdan, 1999); however, the complications of such a configuration are not addressed in this simple investigation.

The equations governing the vertically propagating waves in the overlying atmosphere are just equations (3.2)–(3.4) with exactly vertical field ($\theta = 0$) and $k = 0$. In this case, the system (3.2)–(3.4) reduces to three uncoupled equations. The two equations governing the transverse displacements (eqs. [3.2]–[3.3]) are

$$\left[C_A^2 \frac{d^2}{dz^2} + \omega^2\right] \xi_\perp = 0, \tag{5.19}$$

where $\xi_\perp = \zeta$ or η. Equation (5.19) suggests, in addition to the usual Alfvén wave with displacement $\eta \hat{\mathbf{k}}_\perp$, there is a second Alfvénic solution with displacement $\zeta \hat{\mathbf{k}}$. The equation governing the longitudinal displacement (eq. [3.4]) is

$$\left[C_S^2 \frac{d^2}{dz^2} - \gamma g \frac{d}{dz} + \omega^2\right] \xi_\| = 0, \tag{5.20}$$

where $\xi_\| = \xi_z$. Equation (5.20) is just the equation for a vertically propagating sound wave. This is the slow MAG wave solution, for the remainder of this chapter we refer to it simply as the MAG wave solution.

The boundary condition at the photosphere, $z = -z_0 = z_{ch}$, is imposed by matching the sausage (kink) modes onto upward- and downward-propagating MAG (Alfvén) waves in the chromosphere, which in turn match onto only upward-propagating MAG (Alfvén) waves in the corona (e.g., Appendix B of CBZ). An outward radiation condition is imposed as $z \to \infty$. The matching at each temperature discontinuity ($z = z_{ch}$, and the transition region $z = z_{cor}$) ensures that the displacement and its vertical derivative are continuous (Leroy and Schwartz, 1982).

123

In the isothermal stratified chromosphere, the solution of equation (5.20) representing the upward- and downward-propagating waves is

$$
\begin{aligned}
\tilde{\xi}_{\parallel}(z) &= A_{\parallel} \exp\left[\left(1 + i\left(\varpi_{ch}^2 - 1\right)^{1/2}\right)\left(\frac{z - z_{ch}}{2H_{ch}}\right)\right] \\
&+ B_{\parallel} \exp\left[\left(1 - i\left(\varpi_{ch}^2 - 1\right)^{1/2}\right)\left(\frac{z - z_{ch}}{2H_{ch}}\right)\right], \quad \text{for} \quad z_{ch} \leq z \leq z_{cor}, \quad (5.21)
\end{aligned}
$$

where $\varpi_{ch} = \omega/\omega_{ch} = 2\left(H_{ch}/\left(z_0\left(m+1\right)\right)\right)^{1/2}\nu$ is the frequency in units of the chromospheric acoustic cutoff frequency $\omega_{ch} = C_S/2H_{ch}$. In the isothermal stratified corona, the upward-propagating MAG wave solution is

$$
\tilde{\xi}_{\parallel}(z) = C_{\parallel} \exp\left[\left(1 + i\left(\varpi_{cor}^2 - 1\right)^{1/2}\right)\left(\frac{z - z_{cor}}{2H_{cor}}\right)\right], \quad \text{for} \quad z \geq z_{cor}. \quad (5.22)
$$

where $\varpi_{cor} = 2\left(H_{cor}/\left(z_0\left(m+1\right)\right)\right)^{1/2}\nu$. We restrict our attention to the frequency range where $\varpi_{cor}^2 > 1$. The MAG wave solutions of equations (3.2)–(3.4) with exactly vertical field, isothermal stratification, and $k \neq 0$ are well developed: CBZ developed a Frobenius series solution, whereas Cally (2001a, see also Zhugzhda and Dzhalilov, 1982) found an exact analytic solution. The first term in the rapidly convergent series solutions match the $k = 0$ solutions above (eqs.[5.21]–[5.22]).

For an isothermal atmosphere the solutions of equation (5.19) can be written in terms of Bessel functions of the first and second kind, J_0 and Y_0 (e.g., Ferraro and Plumpton, 1958; Hollweg, 1978; Thomas, 1978; Leroy, 1981; Leroy and Schwartz, 1982; An et al., 1989). In the isothermal stratified chromosphere, the solution representing upward- and downward-propagating Alfvén waves is

$$
\tilde{\xi}_{\perp}(z) = A_{\perp} J_0\left[\frac{2\omega L_{ch}}{C_{A,ch}} \exp\left(\frac{z_{ch} - z}{2L_{ch}}\right)\right] + B_{\perp} Y_0\left[\frac{2\omega L_{ch}}{C_{A,ch}} \exp\left(\frac{z_{ch} - z}{2L_{ch}}\right)\right], \quad (5.23)
$$

$$
\text{for } z_{ch} \leq z \leq z_{cor},
$$

where $L_{ch} = \alpha H_{ch}/(\alpha - 1)$, and $C_{A,ch} = \left(2gH_{ch}/\beta\right)^{1/2}$ is the Alfvén speed at the base of the chromosphere (as $z \to z_{ch}^+$). In the chromosphere, we have assumed that the vertical component of the magnetic field decreases exponentially with height (eq. [5.18]). Therefore the radial component of the field is non-zero, and the method of separation of variables (used to derive eqs. [3.2]–[3.4]) is not valid. Consequently, the solution (5.23) is only a first approximation, which is reasonable for the exploratory purposes of this investigation. In the homogeneous corona, with uniform vertical field, the upward-propagating Alfvén wave solution (eq. [3.18]) is

$$
\tilde{\xi}_{\perp}(z) = C_{\perp} \exp\left[i\omega\left(\frac{z - z_{cor}}{C_{A,cor}}\right)\right], \quad \text{for} \quad z \geq z_{cor},
$$

124

where $C_{A,cor} = \left(2g_*H_{cor}\exp\left[-10\left(1-\alpha\right)/\alpha\right]/\beta\right)^{1/2}$ is the Alfvén speed at the base of the corona (as $z \to z_{cor}^+$). In the isothermal stratified corona, with uniform vertical field, the physical solution for the Alfvén waves is

$$\tilde{\xi}_\perp(z) = C_\perp J_0\left[\frac{2\omega H_{cor}}{C_{A,cor}}\exp\left(\frac{z_{cor}-z}{2H_{cor}}\right)\right], \quad \text{for} \quad z \geq z_{cor}.$$

In this case, the Alfvén waves are totally reflected in the infinite corona. Consequently no energy is lost out the top of the tube. In the homogeneous corona, with straight and radial field, Cally (1983) found that the Alfvén wave solutions can be expressed in terms of the Bessel functions $J_{1/6}$ and $J_{-1/6}$. The outward radiating Alfvén wave solution is

$$\tilde{\xi}_\perp(r) = C_\perp\left(\frac{r}{r_{cor}}\right)^{3/2} H_{1/6}^{(1)}\left[\frac{\omega r_{cor}}{3C_{A,cor}}\left(\frac{r}{r_{cor}}\right)^3\right], \quad \text{for} \quad r \geq r_{cor}.$$

The boundary conditions (ensuring continuity of the displacement and its vertical derivative at $z = z_{ch}$ and $z = z_{cor}$) completely constrain the particular solution for the displacement throughout the entire flux tube by fixing the parameter λ_σ and the amplitudes of the MAG and Alfvén waves in the overlying atmosphere A_σ, B_σ, and C_σ. The exact form of the complex parameter λ_σ and the amplitudes of the waves in the overlying atmosphere, A_σ and B_σ, are not particularly illuminating to this discussion, and are therefore not included. The matching coefficients λ_σ and C_σ are, however, required for the calculation of the energy fluxes escaping out of the top and the bottom of the flux tube. Expressions for $C_\parallel$ and $\lambda_\parallel$ can be found in Appendix E.1. Expressions for $C_\perp$ and $\lambda_\perp$, for the three distinct models of the corona, can be found in Appendix E.2 (homogeneous corona, with uniform vertical field), Appendix E.3 (isothermal stratified corona, with uniform vertical field), and Appendix E.4 (homogeneous corona, with straight and radial field).

5.1.6 Mode damping

The power carried by the waves radiating out of the top and the bottom of the tube can be calculated in an identical fashion to BHCC (see their §5 for details). Asymptotically, as $z \to -\infty$, a constant time-averaged power is carried off by the sausage and kink modes,

$$\langle\dot{E}_\sigma^-\rangle = \lim_{z \to -\infty}\left[-\pi R^2\left(z\right)\hat{\mathbf{e}}_z \cdot \frac{\omega}{2\pi}\int_{-\pi/\omega}^{\pi/\omega} \mathbf{F}_\sigma^- dt\right],$$

where $\mathbf{F}_\sigma^-$ is the wave energy flux of the sausage and kink modes (which can calculated using eq. [4.35] and the particular solution for the displacements). Likewise, as $z \to \infty$, the MAG and Alfvén waves carry a constant time-averaged power,

$$\langle\dot{E}_\sigma^+\rangle = \lim_{z \to \infty}\left[\pi R^2\left(z\right)\hat{\mathbf{e}}_z \cdot \frac{\omega}{2\pi}\int_{-\pi/\omega}^{\pi/\omega} \mathbf{F}_\sigma^+ dt\right],$$

where $\mathbf{F}_\sigma^+$ is the wave energy flux of the MAG and Alfvén waves (eq. [4.35]).

125

The oscillations of the flux tube are a direct result of the p-mode forcing, and therefore energy conservation requires that the p-mode energy decline accordingly. This loss of energy translates into a p-mode line width contribution, defined as

$$\Gamma_n(\omega) = \frac{1}{2\pi}\frac{\langle\dot{E}\rangle}{\langle\mathcal{E}_n\rangle},$$

where $\langle\mathcal{E}_n\rangle$ is the time averaged p-mode energy underlying the model solar photosphere (eq. [5.5]). For the longitudinal and transverse components the p-mode line width contributions are, respectively,

$$\Gamma_{n,\|}(\omega) = \omega f\frac{\beta(\beta+1)(m+1)^2}{8m\left(2m+\beta(m+1)\right)}\frac{\left|I_\|^{(2)}+\lambda_\| I_\|^{(1)}\right|^2}{\mathcal{N}_n}+\Gamma_{n,\|}^+(\omega),\qquad(5.24)$$

$$\Gamma_{n,\perp}(\omega) = \omega f\frac{(\beta+1)(m+1)}{8m}\frac{\nu^4}{\kappa_n^2}\frac{\left|I_\perp^{(2)}+\lambda_\perp I_\perp^{(1)}\right|^2}{\mathcal{N}_n}+\Gamma_{n,\perp}^+(\omega),\qquad(5.25)$$

where $\mathcal{N}_n$ is the p-mode energy normalisation integral (eq. [5.6]), and $f = \pi R_0^2/4\pi R_\odot^2$ is the surface magnetic filling factor (R_0 is the radius of the flux tube at $z = -z_o$). The integrals $I_\|^{(2)}$ and $I_\perp^{(2)}$ are defined similarly to $I_\|^{(1)}$ and $I_\perp^{(1)}$ (see eqs. [5.15] and [5.16]), with the $H_\mu^{(1)}$ replaced by $H_\mu^{(2)}$. The upward radiation boundary conditions constrain the parameter λ_σ, and the contributions $\Gamma_{n,\|}^+$ and $\Gamma_{n,\perp}^+$. In that case, the terms $\Gamma_{n,\|}^+$ and $\Gamma_{n,\perp}^+$ correspond to the line width contributions from the MAG and Alfvén waves escaping high into the corona.

The expressions (5.24) and (5.25) are valid for any boundary condition at the top of the photosphere. For the stress-free boundary condition λ_σ take the form of equations (5.13) and (5.14), and $\Gamma_{n,\|}^+$ and $\Gamma_{n,\perp}^+$ are both zero. For the upward radiation boundary conditions, the line width contributions, $\Gamma_{n,\sigma}^+$, are given in Appendix E

5.2 Results

The key results of this investigation are summarised in Figures 5.2–5.4. In these figures, the ratio Γ/ω divided by the magnetic filling factor f is plotted as a function of dimensionless squared frequency $\nu^2 = m\omega^2 z_0/g$ for polytropic index $m = 1.5$ and two different values of the plasma-β. The true p-mode frequency, $\omega/2\pi$, is indicated along the upper axis of each figure. For each figure the line width contribution due to the excitation of the downward-escaping sausage or kink modes alone is plotted as a full curve; the contribution due to the excitation of the upward-escaping MAG or Alfvén waves alone is plotted as a dashed curve. For purposes of comparison the results of BHCC, with the stress-free boundary condition imposed, are also presented (dotted curve).

5.2.1 General Comments

The distinctive feature of Figures 5.2–5.4 is the resonances along the line width curves – a property common to the sausage and kink mode results. The line width contribution of the

126

upward-radiating MAG and Alfvén waves shows the behaviour expected for standing waves setting up resonance in the chromospheric cavity (e.g., Schwartz and Leroy, 1982; Cally, 1983; Schwartz, Cally, and Bel, 1984; Cally, Bogdan, and Zweibel, 1994). The line width contributions for the downward-radiating sausage and kink modes also exhibit resonances – evident as the sharp troughs. At these frequencies, the downward-radiating tube modes (partially) decouple from the p-mode forcing. Both line width contributions from the upward- and downward-radiating waves exhibit similar frequency variation. Such frequency variation is not evident when the stress-free boundary condition is imposed, where the curves tend to flatten out with increasing frequency (see BHCC).

The important result for this investigation is that the line width contribution of tube modes escaping out of the bottom of the tube is more significant (except at decoupling frequencies) than the MAG and Alfvén waves escaping out of the top of the tube. This suggests that modifying the boundary condition at the top of the photosphere has done little to increase the ability of the tube to absorb p-mode energy. In some cases, however, the line width contribution of tube modes escaping out of the bottom of the tube is substantially increased (except at decoupling frequencies) in comparison to the corresponding BHCC result. This somewhat surprising result is explained in detail in the last subsection, §5.2.4.

Overall, the f-mode is damped more than the p-modes, and low order p-modes are damped more than high order ones. This is in qualitative agreement with the observations of Korzennik (1990) and was also clear in the results of BHCC.

Firstly, we examine the sausage and kink modes separately. The important common results, including the reason for the decoupling troughs, are discussed last.

5.2.2 Sausage Modes

Consider first the axisymmetric (sausage) modes (Fig. 5.2). Clearly the f-mode line width is significantly enhanced when the radiation boundary condition is imposed. This is also true for the case with plasma-$\beta = 0.1$ (not pictured). It should be noted that in the cases with the weaker stratification ($m = 1.5$) and stress-free boundary condition imposed (BHCC), the sausage mode excitation by the f-mode was particularly weak, decreasing for large frequencies. In cases with stronger stratification (e.g., $m = 3.85$) and the radiation boundary condition imposed, the enhancement over the BHCC result is less impressive.

The p_1-mode line width is indicative of the p-modes of higher radial order n. It can be seen that the contribution from the upward-escaping MAG waves is at most just above the BHCC result, and the peaks of the contribution from the downward-escaping sausage modes is almost an order of magnitude greater than the BHCC result. For the plasma-$\beta = 0.1$ (not pictured) the sausage mode results are very similar, but the MAG wave contribution is even less significant. The behaviour of the line widths seen here is indicative of the situation with different polytropic stratification (e.g., $m = 3.85$, not pictured).

In all cases the sausage mode results with the radiation condition imposed show similar variation with radial order n to the results of BHCC. For the $\beta = 1$ case, the variation of the line width with radial order is moderate, and for the $\beta = 0.1$ it is very weak. For both values of plasma-β, the troughs for the f-mode occur at frequencies different to those for the p-modes; this is clear in Figure 5.2. The frequency of the MAG wave resonances show no
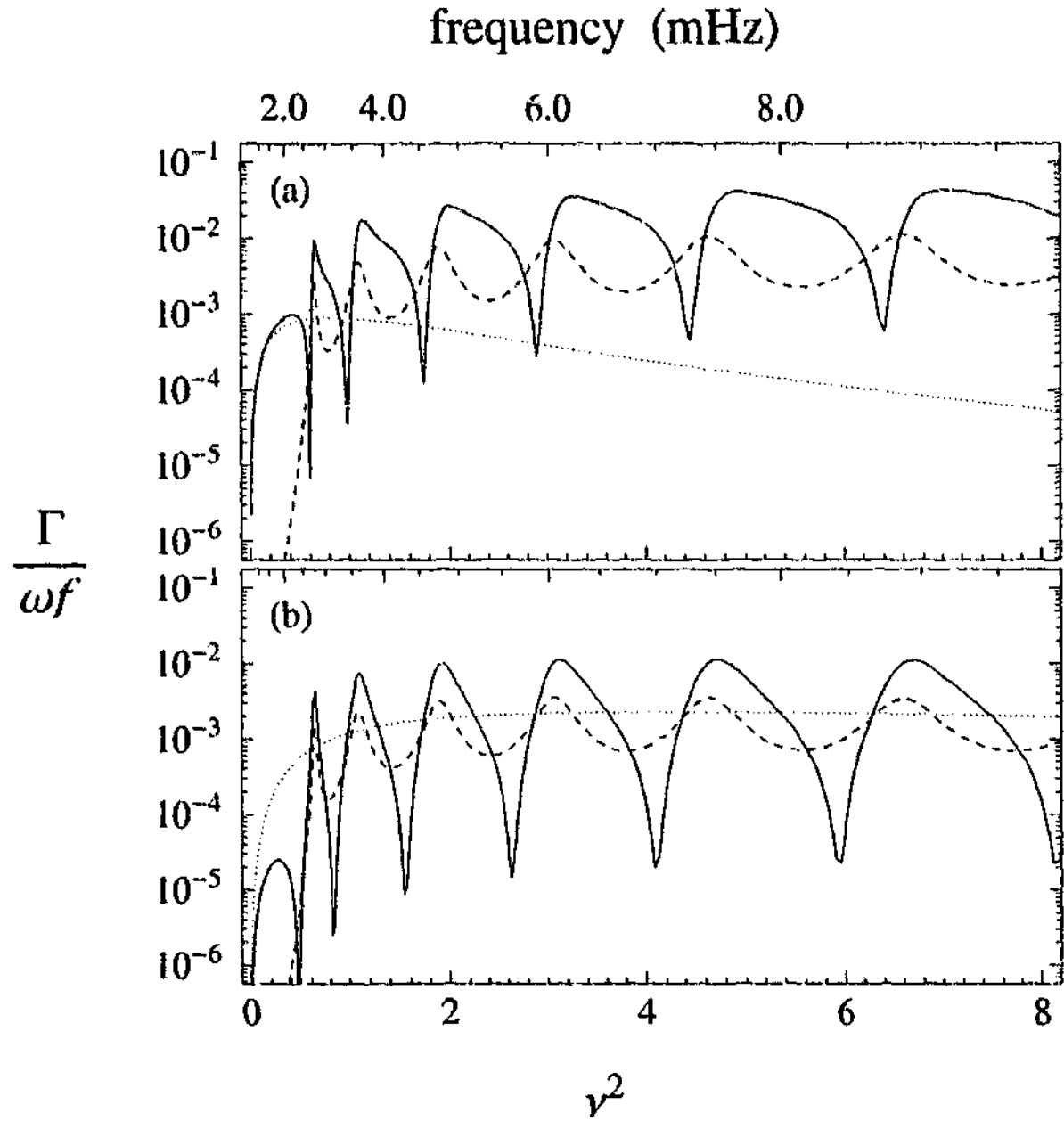
frequency (mHz)

Figure 5.2: Variation of the f- and p_1-mode line width Γ as a function of dimensionless squared frequency $\nu^2 = m\omega^2 z_0/g$ due to the excitation of the sausage modes on thin magnetic flux tubes having a magnetic filling factor f. The dashed curve shows the line width contribution due to the MAG wave excitation alone (wave flux out the top), the full curve shows the line width contribution due to the sausage modes alone (wave flux out the bottom). Note the sharps troughs are not fully resolved. The dotted curve shows the line width contribution due to the sausage modes with the stress-free boundary condition imposed (BHCC). Along the upper horizontal axis the actual p-mode frequency, $\omega/2\pi$, is indicated. For this plot the polytropic index $m = 1.5$ and the plasma-β within the (photospheric) flux tube is unity. The chromosphere and corona are taken as isothermally stratified, permeated by a straight, uniform, vertical magnetic field. (a) The f-mode ($n = 0$), and (b) the p_1-mode ($n = 1$).

variation with radial order. In the case of the kink modes, the frequencies of the resonances also show no variation with radial order.

128

5.2.3 Kink Modes

Figures 5.3 and 5.4 show the key results for the excited transverse modes : kink modes and Alfvén waves. Each plot has a different coronal model. Figures 5.3(a) and 5.4(a) show the results for the homogeneous corona permeated by a straight, uniform, vertical magnetic field. Figures 5.3(b) and 5.4(b) show the results for the isothermally stratified corona with a straight, uniform, vertical magnetic field; in this case there is no energy flux of Alfvén waves as $z \to \infty$ because of total reflection in the infinite isothermal corona. This has been realised elsewhere (e.g., Cally, 1983; An et al., 1989). Figures 5.3(c) and 5.4(c) show the results for the homogeneous corona permeated by a straight, radial magnetic field; the field lines are spreading at an angle of 30° to the vertical, and the radius of the thin magnetic flux tube at the top of the photosphere, $z = -z_0$, is 100 km, in rough agreement with observations (e.g., Stenflo, 1978). In both cases where the corona is assumed homogeneous, the Alfvén waves propagate upward without reflection, as $z \to \infty$. In each case the chromosphere is isothermally stratified, and the vertical component of the magnetic field decreases exponentially with height. It was found that the variation of the chromospheric magnetic field had little effect on the overall damping, and only changed the frequency of the resonances. The frequency of the resonances changes because changing the ambient magnetic field strength changes the wavelength of the Alfvén waves. Variation of the chromospheric field had a small effect on the upward energy loss, but this is inconsequential since the upward energy losses are so small relative to their downward counterparts. In each case the p_1-mode result is plotted since it is indicative of the behaviour exhibited by the modes of higher radial order. It turns out that, relative to the BHCC result, the f-mode damping is slightly suppressed in the case of plasma-$\beta = 0.1$, and is hardly changed (except for the resonance behaviour) for plasma-$\beta = 1$.

Figures 5.3 and 5.4 show that in all cases the line width contribution of upward-radiating Alfvén waves is insignificant (by several orders of magnitude) compared with the contribution of downward-escaping kink modes. It should be noted that this is highly dependent on the temperature of the corona – if the temperature of the model corona is decreased (to perhaps unrealistically low values), the energy flux of upward-propagating waves (both MAG and Alfvén waves) does increase. The interesting result from Figures 5.3 and 5.4 is the similarity in the results for flux tubes with different coronal models. This indicates that the coronal model is relatively insignificant and it is the coupling onto the chromospheric Alfvén waves which is important. It should be noted that in the case of the isothermal corona (Figures 5.3(b) and 5.4(b)) there are extra (weaker) decoupling frequencies due to the total reflection in the corona (see discussion in the next subsection). Figure 5.4 shows that for the tube with $\beta = 0.1$, the kink mode line width contribution is virtually identical to the BHCC result except at decoupling frequencies. For the tube with $\beta = 1$ (Fig. 5.3), the peaks of the kink mode line width contribution are significantly greater (above an order of magnitude) than the BHCC results. For this case ($\beta = 1$), the p-mode excitation of the kink modes is comparable to the sausage modes. The multiple decoupling resonances evident for the sausage modes and the kink modes with $\beta = 1$ are not in the considered frequency range for the kink modes with $\beta = 0.1$. This is a result of the dependence of the Alfvén wavelength on ambient magnetic field strength. The (stronger) decoupling frequencies are the same for both cases
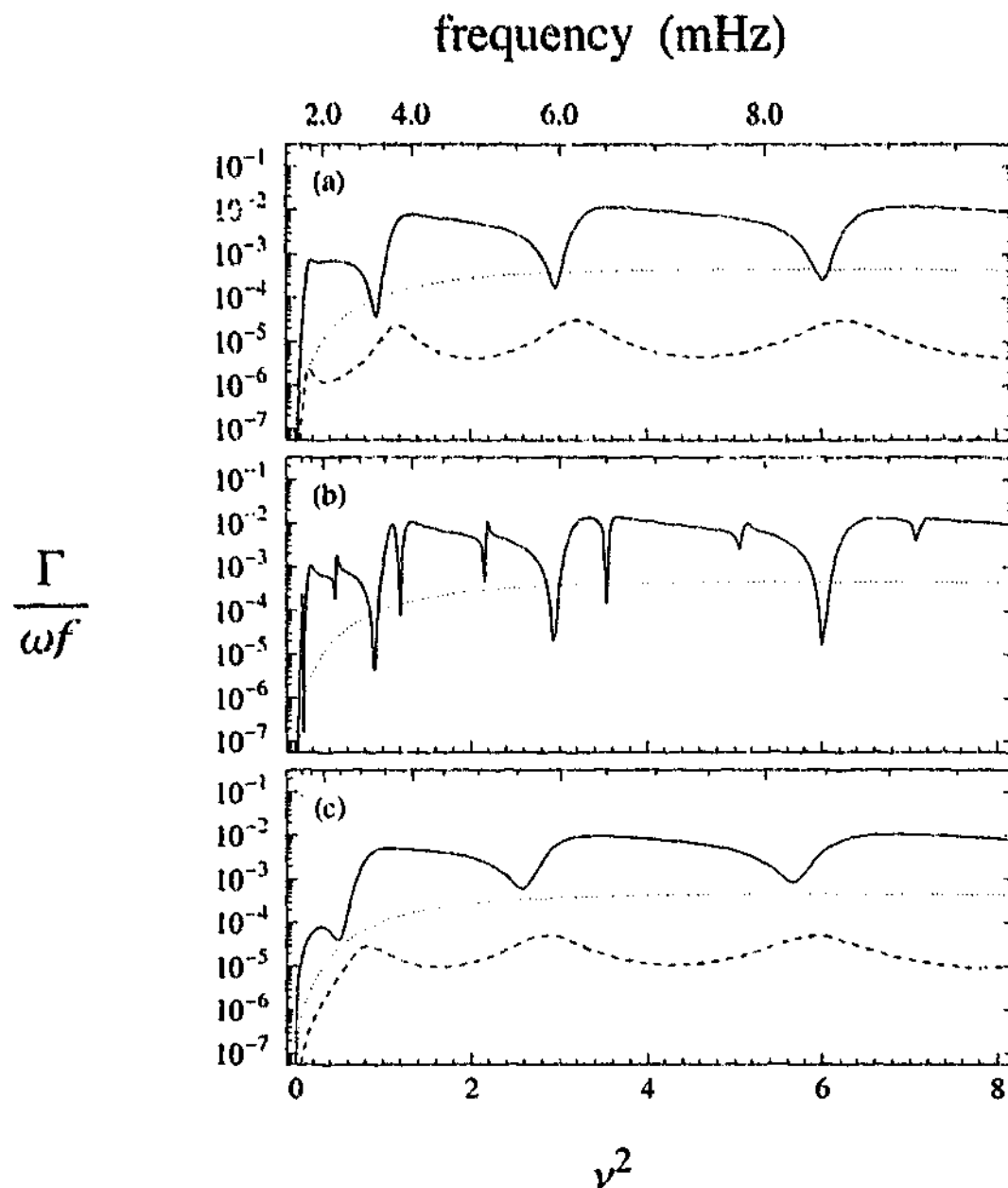
frequency (mHz)

$\dfrac{\Gamma}{\omega f}$

ν^2

Figure 5.3: Variation of the p_1-mode ($n = 1$) line width Γ as a function of dimensionless squared frequency $\nu^2 = m\omega^2 z_0/g$ due to the excitation of the kink modes on thin magnetic flux tubes having a magnetic filling factor f and a plasma-β of unity. The dashed curve shows the line width contribution due to the Alfvén wave excitation alone (wave flux out the top), and the full curve shows the line width contribution due to the kink modes alone (wave flux out the bottom). The dotted curve shows the line width contribution due to the kink modes with the stress-free boundary condition imposed (BHCC). Along the upper horizontal axis the actual p-mode frequency, $\omega/2\pi$, is indicated. For these plots the polytropic index $m = 1.5$. (*a*) The corona is modelled as homogeneous (unstratified) and permeated by a straight, uniform, vertical magnetic field. (*b*) The corona is modelled as isothermally stratified, the magnetic field is straight, uniform and vertical. There is no contribution from upward-escaping Alfvén waves in this case due to complete reflection in the infinite corona. (*c*) The coronal magnetic field is modelled as radial and straight (spreading at 30° to the vertical), the corona is homogeneous (unstratified). Note in each of the cases *a*, *b*, and *c*, the BHCC result (dotted curve) is identical.

130

frequency (mHz)
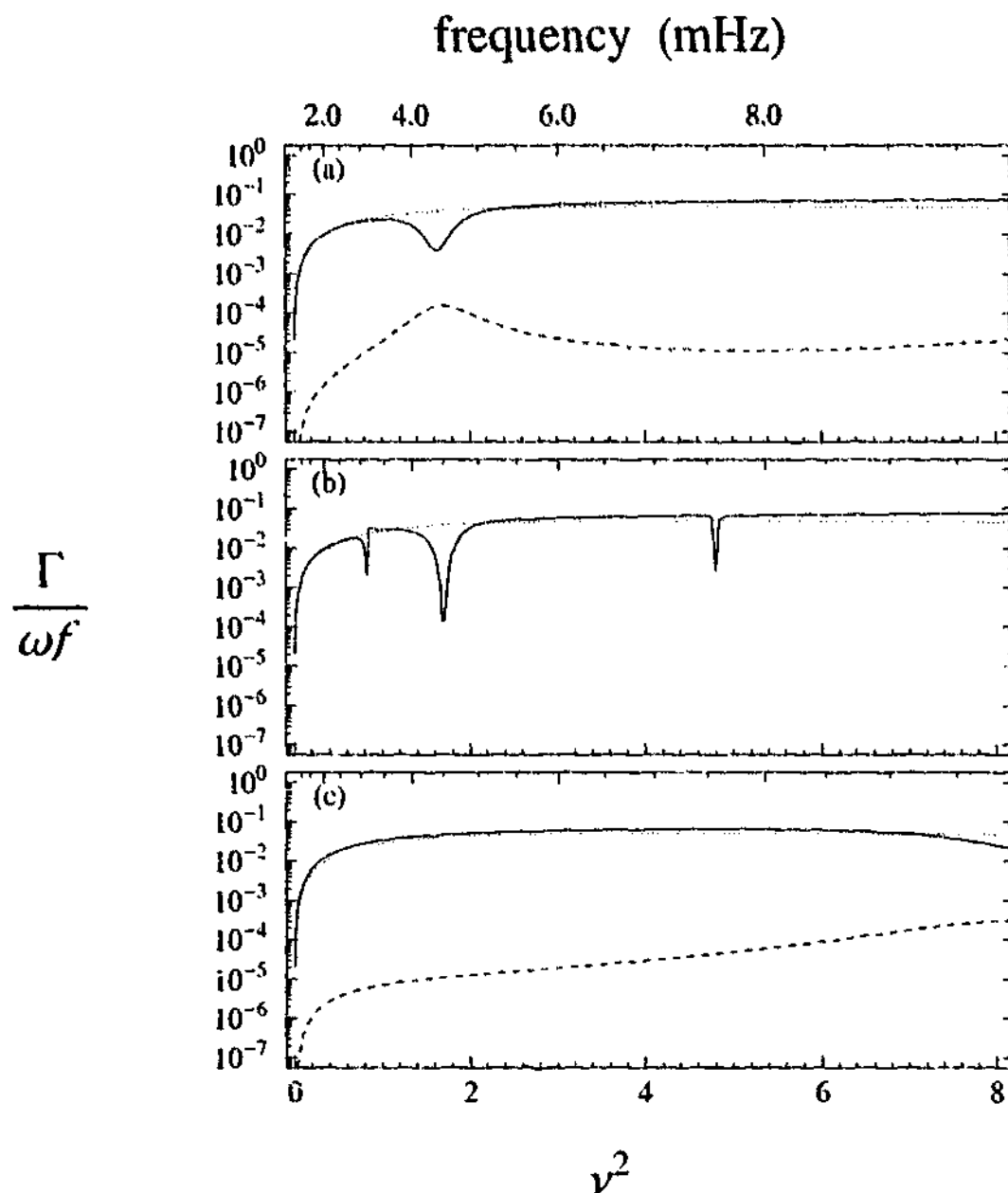
Figure 5.4: Same as Figure 5.3 but for plasma-$\beta = 0.1$ inside the (photospheric) thin magnetic flux tube.

with coronal magnetic field straight, uniform and vertical (Figs. 5.3(a) and (b), and 5.4(a) and (b)). In the case with the coronal magnetic field straight and radial (Figs. 5.3(c) and 5.4(c)), the decoupling frequencies are shifted because of the Alfvén wavelength changing with the character of the magnetic field. Also in the case with the coronal magnetic field straight and radial, the simplification that the magnetic field direction changes discontinuously at the transition region has negligible effect on the results (verified by numerical experiments with the temperature discontinuity removed). For the kink modes, the dependence of the line width on radial order n is weak for the case $\beta = 0.1$, but quite strong for $\beta = 1$, as in BHCC.

5.2.4 Overall Picture

Allowing wave propagation in the overlying atmosphere has changed how the entire thin magnetic flux tube responds to p-mode forcing. In particular, the amplitude of the downward-escaping tube modes has been drastically affected by the boundary condition at the top of the photosphere. Within the flux tube there are upward- and downward-propagating waves. The downward-propagating waves may be a result of reflections at the top of the photosphere or at the transition region, and also tube modes that propagate downward initially. It is the interaction (interference) of all the waves everywhere inside the flux tube that determine the amplitude of the radiating tube modes, along with the correlation between the p-mode forcing (the Whittaker function) and the flux tube response (the Hankel functions). Mathematically, the presence of the integrals $I_\sigma^{(1)}$ and $I_\sigma^{(2)}$ and the parameter λ_σ in equations (5.24) and (5.25) quantify these interactions. The interference of the various tube modes depends on the relative phase of each individual wave – this is highly dependent on the effect that the reflections at the top of the photosphere and the transition region have on the downward-propagating waves. The decoupling troughs are a direct result of the high reflection at the transition region temperature discontinuity; when the discontinuity is removed, the troughs disappear (verified by numerical experiments). The reflected waves are phase shifted relative to the other propagating tube modes. For some frequencies the interference of the waves is destructive, decreasing the amplitude of the downward-radiating tube mode (hence the troughs). In other cases the interference will be constructive (hence the peaks). Evidently the phase shift depends on the properties of the overlying atmosphere; for example, temperature, magnetic field strength, and thickness of the chromospheric cavity.

Reflections at the top of the photosphere ($z = -z_0$) also have a significant effect on the tube mode excitation. It turns out (verified by numerical experiments) that for the $\beta = 1$ case with the stress-free boundary condition imposed, the upward- and downward-propagating kink modes interfere almost completely destructively for the p-modes (less severely for the f-mode). Hence, the kink mode excitation is suppressed considerably in comparison to the tube with the radiation boundary condition where the interference is constructive (away from decoupling resonances). This is also the case for sausage f-mode with $m = 1.5$ (see Fig. 5.2(a)). For the sausage f-mode, when the stress-free boundary condition is imposed upward and downward waves interfere destructively; hence, the line width contribution is strongly suppressed. For the kink modes with $\beta = 0.1$ and the stress-free boundary condition imposed, the interference between upward- and downward-propagating tube modes is is relatively small. Hence, the contrast with the results of the tube with the radiation boundary condition is less pronounced.

The observations of Korzennik (1990) are presented in BHCC (see their Fig. 9) and need not be reproduced here. This graph plots the ratio of the line width Γ divided by the angular frequency ω for the f-mode and the p-modes of radial orders $n = 1 - 5$ (with degree $l \approx 100 - 600$). Broadly speaking, for all modes within the frequency range $\nu \approx 2 - 5$ mHz the ratio Γ/ω lies in the range $5 \times 10^{-4} - 5 \times 10^{-3}$. For each mode, the ratio Γ/ω forms a ridge; along each ridge, Γ/ω increases with frequency. For any given frequency, Γ/ω is largest for the f-mode and decreases as the radial order n of the p-modes increases. The theoretical results of BHCC fall well short of the observations by an order of magnitude or more.

132

The total line width contribution will be a result of damping due to both sausage and kink modes propagating along the magnetic fibril,

$$\Gamma_n\left(\omega\right) = \Gamma_{n,\|}\left(\omega\right) + \Gamma_{n,\perp}\left(\omega\right) ,$$

where $\Gamma_{n,\|}$ and $\Gamma_{n,\perp}$ are defined by equations (5.24) and (5.25), respectively. In all cases the upward-escaping MAG and Alfvén waves have little significance on p-mode damping. The kink mode line width contribution is significantly enhanced in one instance ($m = 1.5$ and $\beta = 1$). But this is not the case that gives closest agreement with the observations of Korzennik (1990), which is $m = 1.5$ and $\beta = 0.1$, with magnetic filling factor $f = 10^{-2}$ (see Fig. 9 of BHCC). We are certainly limited by the frequency ranges of the observations. Figures 5.2 – 5.4 extend above 8 mHz which is substantially beyond the domain of the observations – truncated at approximately 5 mHz. The observations of Korzennik (1990) show no evidence of the resonance behaviour exhibited by line widths in this investigation. It would be expected that the many tubes populating the solar surface would have different properties, for example plasma-β, and different flux tubes would be subject to different conditions – in reality the overlying solar atmosphere would be non-uniform, having a temperature and chromospheric depth which vary over the solar surface. Therefore, resonances from individual tubes would be smeared out and not resolvable. For the p-modes the total line width contribution shows only weak dependence upon radial order n – a result which was presented by BHCC and is evident in the observations of Korzennik (1990). Some of the general behaviour seen here is consistent with observations, but quantitatively the results fall far short of the observational results (Korzennik, 1990). In the favourable cases, the theoretical total line width calculated here (not pictured) can account for only a few percent of the observed line width.

5.3 Conclusions

We investigated the contribution of tube mode oscillations on thin magnetic flux tubes to p-mode line widths. In particular, the effect of the upper solar atmosphere was examined. We found that allowing wave propagation in the upper solar atmosphere certainly affects the response of the thin magnetic flux tube to p-mode forcing. However, the effect is not enough to account for an unmodelled component of p-mode damping. Alone, the line width contributions of MAG and Alfvén waves radiating out of the top of the flux tube are very small, depending on the extent of the temperature discontinuity at the transition region. The tube mode oscillations radiating out of the bottom of the flux tube are more effective at removing energy from the driving p-modes. In some cases the contribution of downward-radiating tube modes is significantly increased relative to the BHCC result, but not in the case in best agreement with observations (Korzennik, 1990).

The simplified models of the upper solar atmosphere may pose limitations on the results presented in this chapter. However, the essential physics has been retained, and the mechanisms at work have been recovered; in addition, the results do not seem to depend strongly on the exact nature of the model. The simple models of this investigation give a good insight into the possibilities of more complicated models of the flux tube above the photosphere. One approach would be to employ the flat canopy approximation for the flux tube beyond the

133

photosphere (e.g., Bogdan, 1999). However, as indicated by the results of this investigation, strong reflection at the temperature discontinuity of the transition region would most likely retard large upward energy fluxes. It would be interesting to see if there was a dramatic change in the downward energy fluxes of the tube modes.

Recently, Rosenthal et al. (2002) have performed numerical simulations of waves propagating through magnetic structures in the solar atmosphere. Their models for the magnetic field in the upper atmosphere are much more sophisticated than those used in this chapter. Rosenthal et al. consider the propagation of waves (generated at the atmospheric base) through both open and closed field structures, and chromospheric network and internetwork regions. The results of Rosenthal et al. provide many important physical insights. Of particular consequence to this chapter, their results indicate that to model the overlying atmosphere properly nonlinear wave propagation must be taken into account.

The recent observations by Komm, Howe, and Hill (2000) found that from solar minimum to solar maximum, the p-mode line widths increase by about 7% on average. The results presented in the previous section and also those of BHCC are less than, but comparable in magnitude to, this amount. This strongly indicates that the origin of the variation found by Komm, Howe, and Hill is magnetic in nature, though we do not perform a detailed comparison here.

Clearly, the mechanism responsible for the damping of p-modes remains unidentified. In the case of damping by small-scale intense magnetic flux tubes, many candidates are yet to be investigated. Dissipative effects such as radiative damping and resonant absorption are also mechanisms that are known to increase the energy absorption from incident p-modes. A dissipation mechanism in the overlying atmosphere would remove some of the energy from the waves reflected within the chromosphere – which could also contribute to the chromosphere's energy budget. To what extent these suggestions could affect p-mode line widths is an open question.

Chapter 6

Discussion and Conclusions

This thesis examined the interaction of solar p-modes with two distinct types of magnetic flux concentration. The first type, a semi-infinite slab of non-vertical field, is applicable to large scale structures such as sunspots and complex active regions. The second type, an isolated thin magnetic flux tube, is a valid approximation to the plethora of widely-spaced, small-scale intense magnetic flux tubes which account for roughly 90% of the magnetic flux threading the solar photosphere.

6.1 Summary

In Chapters 3 and 4 we calculated the efficiency of mode conversion in non-vertical magnetic field. Alone this problem is rather complicated. We broke the problem down into two parts. Firstly, in Chapter 3, we considered two-dimensional propagation where the Alfvén waves are decoupled, and calculated the efficiency of fast-to-slow mode conversion. Secondly, in Chapter 4, with the insight gained in Chapter 3, we extended our attention to the case of three-dimensional propagation. In this case, mode conversion occurs between all three types of waves: fast and slow MAG waves, and Alfvén waves. We calculated the resultant damping rates along with the respective contributions made by the slow MAG waves and Alfvén waves leaking down the magnetic field lines.

In Chapter 3, we investigated the two-dimensional ($\phi = 0$) propagation of oscillations in a complete polytrope permeated by a straight, uniform, non-vertical magnetic field. In particular, we calculated the efficiency of fast-to-slow MAG wave conversion, and subsequent horizontal spatial decay of the π-modes. For modes with $n \geq 1$, we found mode conversion is significantly enhanced (by up to two orders of magnitude) in comparison to vertical field. The enhancement occurs in moderately inclined fields ($\theta \approx 20° - 60°$, depending on the mode and frequency), and is most significant at higher frequencies. At lower frequencies the enhancement is generally negligible. For the f-mode ($n = 0$), fast-to-slow MAG wave conversion is most efficient in vertical field (and slightly non-vertical field). For all modes at all frequencies, highly inclined fields ($\theta \gtrsim 70°$) show very inefficient fast-to-slow MAG wave conversion.

In Chapter 4, we investigated the three-dimensional ($\phi \neq 0$) propagation of oscillations in

a complete polytrope permeated by a straight, uniform, non-vertical magnetic field. Broadly speaking, the results for the π-modes are very similar to those of the two-dimensional ($\phi = 0$) case. For π-modes with $n \geq 1$, we found mode conversion is significantly enhanced in moderately inclined fields ($\theta \approx 20° - 60°$, depending on the mode and frequency), especially at higher frequencies. For the f-mode ($n = 0$), damping is most efficient in vertical field though in some cases the variation with inclination is weak. In general, the π-mode damping rates depend only weakly on the propagation direction ϕ, especially for low to moderate inclinations. In highly inclined field, a substantial enhancement is found centred on $\phi = 45°$, but this enhancement is insignificant in comparison to damping rates at moderate inclinations (with the same ϕ). Broadly speaking, when the direction of propagation is not parallel to the x-axis, both the Alfvén waves and the slow MAG waves make a similar contribution to the π-mode damping. However, the relative contributions vary significantly with frequency, inclination, and to a lesser extent propagation direction. In addition, a new type of highly damped solution (the γ-modes), that mainly exists in highly inclined field, was found. The γ-modes will probably have a significant influence on the absorption of p-modes in the penumbra of sunspots (where the field is highly inclined).

The existence of the γ-modes suggests that highly inclined field is worthwhile examining in closer detail. The numerical integrations employed in Chapter 4 become increasingly unreliable as the horizontal field singular case is approached. We found reliable numerical solutions in the singular case when $\phi = 90°$ (propagation exactly perpendicular to the x-axis). Solutions for the cases where $\phi \neq 90°$ are significantly more complicated and beyond the scope of this thesis. For example, the resonant damping of p-modes by horizontal (canopy) field overlying the convection zone has been investigated by Vanlommel *et al.* (2002) and may also play an important role in p-mode absorption by sunspot penumbrae. Our results suggest that the ($\theta \to 90°$) perturbation problem may indeed be worth addressing (e.g., Kamp, 1989, 1990; Zhukov, 1988, 1989a,b, 1990).

In Chapter 5, we calculated the contribution to p-mode line widths from the excitation of tube mode oscillations on an individual isolated magnetic fibril. An idealised model of the fibril within the convection zone was employed, consisting of a vertical, thin magnetic flux tube embedded in a truncated polytrope. BHCC considered a similar model, but imposed a stress-free boundary condition at the top of the convection zone which acts to completely reflect any upward propagating tube waves back down into the tube. The stress-free boundary condition neglects a possibly important physical process – the loss of energy to the upper solar atmosphere by the excitation of waves in the chromosphere and corona. Using simple models of the solar chromosphere and corona we explored the consequences of applying various boundary conditions. The resultant upward energy fluxes are not large, but surprisingly the more realistic upper boundary conditions lead to a significant increase in kink mode flux out the bottom of the tube. Nevertheless, the sausage mode remains dominant in cases in best agreement with observations, and is essentially unaffected by the more realistic boundary conditions. Consequently, the resultant total p-mode line width computed in Chapter 5 can account for only a few percent of the observed line width. This amount, though relatively small, is roughly consistent with the p-mode line width variation over the solar cycle (from solar minimum to maximum) recently observed by Komm, Howe, and Hill (2000). This tends to suggest that the observed solar cycle variation is indeed magnetic in nature, though further

investigation is required to confirm this hypothesis.

6.2 Comparison with observations

Recent calculations by Cally, Crouch, and Braun (2003) using the results of Chapter 3 have proved to be extremely promising. For the benefit of the reader, their paper is included in Appendix F. Cally, Crouch, and Braun construct a simplified model for the interaction between a sunspot and its surroundings, and use the two-dimensional results of this thesis (Chapter 3). They consider two types of models. The first model is a uniform sunspot where the damping parameter $Im(\kappa)$ and the wavenumber $Re(\kappa)$ apply globally throughout the entire spot (single shell model). The second model is composed of a nested set of piecewise uniform shells (multiple shell model) approximately accounting for the range of inclinations present in real sunspots. Cally, Crouch, and Braun compare their results with the absorption and phase shift data for a real sunspot (NOAA 5254), observed using Hankel analysis by Braun (1995), see Figures 1.4 and 1.5, respectively.

Plotted as a function of azimuthal order m and frequency, Cally, Crouch, and Braun (2003) find excellent agreement between their model and the phase shift observations when $\theta = 30°$ and the equipartition depth $L = 0.8$ Mm for radial orders $1 \leq n \leq 7$. This is also the case for the multiple shell model they present. The absorption produced by their model is generally consistent with observations up to some moderate frequency, dependent on radial order. Thereafter, the absorption is too large, assuming absorbing regions comparable in size to the inferred phase shifting region. Interestingly, both the single and multiple shell models produce a minimum in absorption that coincides approximately with the dip observed by Braun (1995, see also Figure 1.4) at around 5 mHz (depending on radial order). This tends to suggest that the absorption minima observed using Hankel analysis (Braun, 1995) are real. However, the dip does not extend to zero in non-vertical field models. Which indicates that the emission generated by acoustic glories (Donea, Lindsey, and Braun, 2000) still plays a role in the immediate surroundings of sunspots (as suggested by Lindsey and Braun, 1999), though perhaps slightly less significant than originally anticipated.

The excellent agreement of the phase shift predictions with the observations (along with the location of the absorption minimum) allows some degree of probing of subsurface field strengths. Cally, Crouch, and Braun (2003) find the best agreement for $L = 0.6 - 0.8$ Mm which corresponds to magnetic field strengths of $3.6 - 4.8$ kG. These are consistent with expectations for subsurface sunspot umbrae. It should be noted that the optimal equipartition depths found by Cally, Crouch, and Braun are somewhat larger than those used to plot the extinction lengths in §3.7.2 and §4.6.5 (see Fig. 3.11, and Figs. 4.23 – 4.26). If the graphs of the extinction lengths were replotted using the the values found by Cally, Crouch, and Braun the resultant frequencies would decrease slightly and the corresponding extinction lengths would increase.

Most importantly, Cally, Crouch, and Braun (2003) have confirmed that (slow) mode conversion appears to be the predominant mechanism responsible for the observed absorption and phase shifts exhibited by sunspots. And in particular, non-vertical magnetic fields are necessary for the process to work.

6.3 Future directions

For such a crude model, the agreement between the results of Cally, Crouch, and Braun (2003, see Appendix F) and the observed p-mode phase shift and absorption data is remarkable. With this in mind, and with a view to eventually perform quantitative inversions, there are several possible extensions to the current model that warrant consideration. Some are relatively minor increments on the present state of knowledge, others are more significant and pose a considerable – yet likely fruitful – challenge.

The results of Chapter 4 (three-dimensional model) were not incorporated into the Cally, Crouch, and Braun model. Cally, Crouch, and Braun noted that the results of the three-dimensional model (Chapter 4) are generally not substantially different to those of the two-dimensional model (Chapter 3). This is especially true for the π-modes in the cases that are in best agreement with the observations (i.e., $\theta \approx 30°$). Hence, for the sake of simplicity, Cally, Crouch, and Braun just use the data from two-dimensional model (Chapter 3). However, there are some exceptions.

To correctly model the interaction of the p-modes with magnetic flux concentrations the oscillations must match (i.e., total pressure and radial velocity must be continuous) across the boundary between the non-magnetic and magnetic regions. This can be done in a straight-forward fashion for thin magnetic flux tubes (see Chapter 5). On the other hand, for significantly larger magnetic features, such as sunspots, the matching is non-trivial. Because the vertical dependences of the internal and external eigenfunctions are not identical, there will be some degree of mode-mixing (where an incident p-mode with azimuthal and radial orders m and n, will match onto internal π- and γ-modes with the same temporal frequency but different m and/or n). In addition, to perfectly match across the interface the horizontally evanescent jacket modes must be incorporated into the model (e.g., Bogdan and Cally, 1995; Barnes and Cally, 2000). The matching employed by Cally, Crouch, and Braun is only a first a approximation and ignores these complications. For vertical field, this is well justified as the eigenvalue analyses agree very well with the results of numerical simulations (e.g., Cally and Bogdan, 1997; Rosenthal and Julien, 2000), which do adequately account for the matching across the interface. For non-vertical field, the consequences of the approximation utilised by Cally, Crouch, and Braun are less certain. In particular, the oscillations in non-vertical magnetic fields are more complicated than originally anticipated. For example, the labelling of modes is ambiguous, and in Chapter 4 we found an unexpected set of solutions, the γ-modes which are present only in highly inclined field. It would be very interesting, though mathematically very difficult, to incorporate the γ-modes into the Cally, Crouch, and Braun multiple shell models. The γ-modes will be especially important in the outer-most shells where the field is highly inclined in real sunspots (i.e., the penumbra).

Relating to the model atmosphere there are two concerns that should be addressed. Firstly, as discussed in §3.2, the polytrope is only a very crude approximation of the solar convection zone (see Fig. 3.2). Ideally it would be useful to recalculate the eigenvalues of Chapters 3 and 4 for a realistic solar model and then reapply the methods employed by Cally, Crouch, and Braun (2003). However, this is not trivial. The eigenvalue problem is solved numerically, but the eigenvalues depend crucially on the treatment of the lower boundary. The derivation of the asymptotic solutions for large depth, using the method of dominant

138

balance, relies on the stratification being expressed analytically. It is unclear how to do this for a general (tabulated) model. One approach would be to replace the solar model with a polytrope below some depth (in his doctoral thesis, Hunter used this approach in the vertical field case). This approach itself has limitations. The best solar models currently available are for quiet Sun (e.g., Christensen-Dalsgaard, Proffitt, and Thompson, 1993; Christensen-Dalsgaard et al., 1996; Christensen-Dalsgaard, 1997). It is unclear how accurately such a model represents the interior of a sunspot. Unfortunately, the sunspot umbral core models M, L and E of Maltby et al. (1986) are not tabulated to sufficiently large depths below the photosphere.

The second issue with regards to the model atmosphere is the top boundary condition. The boundary conditions employed at the surface in Chapters 3 and 4 are the natural choice for the complete polytrope (for which the density vanishes at the surface). These boundary conditions provide a trustworthy approximation for frequencies below the acoustic cutoff frequency (CBZ). For higher frequencies, it is necessary to account for waves propagating into the upper solar atmosphere. The approach would quite likely be very similar to the work done in Chapter 5 where an upper atmosphere, consisting of an isothermal chromosphere and corona, was appended to a truncated polytrope (see also CBZ; Cally 1995; Hindman, Zweibel, and Cally 1996; Lites et al. 1998 who employed a similar approach for vertical field sunspot models). In the vertical field case, for frequencies below the acoustic cutoff frequency, CBZ found the eigenvalues were almost identical to those of the complete polytrope. On the other hand, for frequencies beyond the acoustic cutoff frequency in the temperature minimum, the eigenvalues differ greatly, with the upward- and downward-escaping slow MAG waves removing comparable levels of wave energy. Cally (2001a) recently found that the governing equations for an isothermal atmosphere permeated by vertical field can be solved exactly in terms of hypergeometric functions, which are much easier to compute in practice than the Meijer G-function solutions found by Zhugzhda and Dzhalilov (1982). In preliminary calculations for the two-dimensional case, we have verified that the governing equations for an isothermal atmosphere permeated by non-vertical field can also be solved in terms of hypergeometric functions in an analogous fashion to Cally (2001a). Such exact analytic solutions allow modelling of the overlying atmosphere to be done with relative ease. The three-dimensional isothermal problem, however, cannot be solved exactly and, therefore, series solutions would need to be employed (see Zhugzhda and Dzhalilov, 1984a). The precise consequences of relaxing the top boundary condition in the non-vertical field cases remains an open question.

Another obvious limitation of the current model is the magnetic field geometry. In reality, the magnetic field strength is not uniform but varies with depth. The task of calculating eigenvalues for more complex magnetic field geometries is mathematically very difficult – complicated by the presence of both vertical and radial gradients. Bogdan (1999) has proposed a method for solving the equations governing the linear, axisymmetric oscillations of a general, axisymmetric, potential, magnetostatic equilibrium. Such a model naturally incorporates the flaring of the magnetic field lines with height, and the concentration of the field with depth. It also naturally accounts for the variation of the field inclination in the radial direction – something which the multiple shell models of Cally, Crouch, and Braun (2003) handle only in a highly simplified fashion. The method outlined by Bogdan (1999)

139

has not been put into practice, though Cally (2000) has run numerical simulations of a very similar model. For advanced forward and inverse modelling to be performed, calculations employing a model similar to that of Bogdan (1999) must be developed. Perhaps a useful first step toward understanding Bogdan's more realistic model would be a simpler problem that accounts for both mode conversion and local resonant absorption, in the presence of gravitational stratification. The combined effect needs to be clarified.

A further complication associated with the magnetic field structure resides in our lack of knowledge of even the basic make up of sunspot magnetic field sub-photosphere. This brings us back to one of the ultimate goals of sunspot seismology (as stated in Chapter 1), namely to discriminate between the monolithic field model and the spaghetti field model (proposed originally by Parker, 1979). To this end, the work done in Chapter 5 may play a vital role. In Chapter 5, the absorption by a single isolated magnetic fibril is computed. An obvious extension of this work is to calculate the scattering phase shifts induced on a p-mode incident upon the thin flux tube. And ultimately, to calculate the effects of multiple scattering from a bundle of closely spaced fibrils, namely Parker's spaghetti model. The recent work by Tirry (2000) showed that resonant frequencies (including multiple scattering resonances exhibited by bundles of closely spaced tubes, see Bogdan and Fox, 1991; Keppens, Bogdan, and Goossens, 1994) are absent in an unstratified cavity when one end of the flux tube is open to wave leakage. Therefore, it would be expected that multiple effects introduced by bundling a collection of fibrils would not show significant enhancements over the simple summation of their respective individual effects. However, as noted by Tirry (2000), the effects of mode mixing (and the jacket modes) and the shielding of the internal tubes from the incident p-modes by the external tubes when gravity is present remain unclear. Nevertheless, it is important to ascertain if such a structure possesses an observable signature that is different from that of the monolithic sunspots.

Appendix A

Non-magnetic p-modes

The equations governing the linear oscillations of a non-magnetic, isentropic polytrope,

$$\left[s\frac{d^2}{ds^2} + m\frac{d}{ds} + \nu^2 - \frac{\kappa^2}{4}s \right] \zeta = 0 , \tag{A.1}$$

$$\frac{d\zeta}{ds} = -\frac{i\kappa}{2}\xi_z , \quad \eta = 0 , \tag{A.2}$$

follow from equations (4.1)–(4.3) by neglecting the magnetic terms (i.e., terms multiplied by the squared Alfvén speed, $C_A^2 \propto s^{-m}$). Equation (A.2) indicates that the displacement associated with the oscillations is irrotational (and may be derived from a potential). The procedure for solving equation (A.1) depends on whether the polytrope is complete (e.g., Lamb, 1945, pp. 545–554) or truncated (e.g., Bogdan and Cally, 1995), however, these only affect the treatment of the top boundary.

A.1   Lower boundary

Here we consider the asymptotic behaviour of the oscillations in the vicinity of the lower boundary ($s = \infty$). The method of dominant balance applied to equation (A.1) yields the two controlling factors $\zeta \sim \exp\left(\pm\frac{\kappa}{2}s\right)$, as $s \to \infty$. We impose the usual boundary condition that evanescent modes be decreasing. Further developing the exponentially decaying solution we find

$$\zeta \sim s^{(\nu^2/\kappa)-(m/2)} \exp\left[-\frac{\kappa}{2}s\right] U_p(s) , \tag{A.3}$$

where $U_p(s)$ is asymptotic to 1 as $s \to \infty$, and may be expanded in an asymptotic power series in negative integer powers of s,

$$U_p(s) \sim \sum_{n=0}^{\infty} u_n s^{-n} ,$$

where $u_0 = 1$. The first few terms of the ($m = 3/2$) series are

141

$$U_p(s) \sim 1 - \frac{a}{2\kappa}(2a-1)s^{-1}$$
$$+ \frac{a}{8\kappa^2}(a+1)(2a-1)(2a+1)s^{-2} + \dots, \tag{A.4}$$

where $a = (m/2) - (\nu^2/\kappa)$. In fact, the general solution for the coefficients u_n is

$$u_n = \left(-\frac{1}{\kappa}\right)^n \frac{(a)_n (1+a-m)_n}{n!}, \tag{A.5}$$

where $(a)_0 = 1$, $(a)_n = a(a+1)\dots(a+n-1)$ is the Pochhammer symbol.

This physically acceptable solution for the p-modes at the lower boundary ($s = \infty$) is well established (e.g., Lamb, 1945; Bogdan and Cally, 1995) and can be written in terms of confluent hypergeometric functions (provided m is not a negative integer),

$$\zeta_b = C_u \exp\left[-\frac{\kappa}{2}s\right] U(a, m, s\kappa),$$

where U is Kummer's function and C_u is an arbitrary constant. It can be easily verified that the asymptotic behaviour of ζ_b, as $s \to \infty$ (Abramowitz and Stegun, 1964, eq. [13.5.2]), is exactly that described above (eqs. [A.3] and [A.5]).

A.2 Solutions for the complete polytrope

In terms of the independent variable $t = s\kappa$, equation (A.1) can be written

$$\left[t\frac{d^2}{dt^2} + (m-t)\frac{d}{dt} - a\right]y = 0, \tag{A.6}$$

where $y(s) = \exp\left(\frac{\kappa}{2}s\right)\zeta(s)$. Equation (A.6) is Kummer's equation (Abramowitz and Stegun, 1964, eq. [13.1.1]) and can be solved in terms of the confluent hypergeometric functions (provided m is not a negative integer). The complete solution is

$$y(t) = A_M M(a, m, t) + A_U U(a, m, t),$$

where A_M and A_U are arbitrary constants.

At the surface of the complete polytrope ($s = 0$) the boundary condition requires that all components of the displacement vector, ξ, have a finite magnitude (i.e., the Lagrangian pressure perturbation must vanish at the surface of the atmosphere). This condition selects $A_U = 0$ and

$$\zeta_t = A_M \exp\left[-\frac{\kappa}{2}s\right] M(a, m, s\kappa).$$

The free modes of oscillation of the atmosphere are associated with the special values of the wavenumber, κ, where the two solutions, ζ_b and ζ_t, are identical up to a multiplicative

constant independent of s. In other words the free oscillations are associated with the zeroes of the Wronskian of the two solutions (Abramowitz and Stegun, 1964, eq. [13.1.22]),

$$W\left\{M\left(a,m,s\kappa\right),U\left(a,m,s\kappa\right)\right\} = -\frac{\Gamma\left(m\right)\left(s\kappa\right)^{-m}\exp\left(s\kappa\right)}{\Gamma\left(a\right)}.$$

The Wronskian of the two solutions will vanish only if the argument of the Gamma function in the denominator is a non-positive integer i.e.,

$$\kappa = \frac{\nu^2}{n+m/2}, \quad n = 0,1,2,3,\dots. \tag{A.7}$$

Equation (A.7) was first published by Lamb (1910), it shows that oscillations of a given frequency, ν, are constrained to propagate with a discrete set of dimensionless horizontal wavenumbers, κ, where $n = 0$ can be identified with the fundamental or f-mode, $n = 1$ with the p_1-mode and so on.

Appendix B

Vacuum potential magnetic field

From the linearised induction equation, the Eulerian magnetic field perturbation is

$$\mathbf{B_1} = \nabla \times (\xi \times \mathbf{B}) .$$

It can be shown that the three components of $\nabla \times \mathbf{B_1}$, in directions $\hat{\mathbf{k}}$, $\hat{\mathbf{k}}_\perp$, and $\hat{\mathbf{e}}_z$, respectively, are:

$$(\nabla \times \mathbf{B_1}) \cdot \hat{\mathbf{k}} = -\mathrm{B} \left(\frac{d}{dz} \left[\partial_\| \eta + \sin\phi \sin\theta \nabla \cdot \xi \right] \right) \exp\left[i \left(\mathbf{k} \cdot \mathbf{r} - \omega t \right) \right] , \qquad (B.1)$$

$$(\nabla \times \mathbf{B_1}) \cdot \hat{\mathbf{k}}_\perp = \mathrm{B} \left(\left[\frac{d^2}{dz^2} - k^2 \right] \xi_u \right) \exp\left[i \left(\mathbf{k} \cdot \mathbf{r} - \omega t \right) \right] , \qquad (B.2)$$

$$(\nabla \times \mathbf{B_1}) \cdot \hat{\mathbf{e}}_z = ik\mathrm{B} \left(\partial_\| \eta + \sin\phi \sin\theta \nabla \cdot \xi \right) \exp\left[i \left(\mathbf{k} \cdot \mathbf{r} - \omega t \right) \right] . \qquad (B.3)$$

For the total magnetic field to be potential the three components (B.1) - (B.3) must vanish.

Appendix C

Mode conversion: Two-dimensional model

C.1 Fast MAG wave asymptotic series

The functions U_f and W_f (eqs. [3.12] and [3.13]) may be expanded as asymptotic power series (in non-positive half integer powers of s):

$$U_f(s) \sim \sum_{n=0}^{\infty} u_n s^{-n/2}, \quad \text{and} \quad W_f(s) \sim \sum_{n=0}^{\infty} w_n s^{-n/2},$$

where (setting $\alpha = (2\nu^2/\kappa) - 3/2 = -2a$)

$$u_0 = w_0 = 1, \quad u_1 = w_1 = 0,$$

$$u_2 = -\frac{\alpha}{4\kappa}(\alpha+1), \quad w_2 = -\frac{\alpha}{4\kappa}(\alpha+5),$$

$$u_3 = w_3 = \frac{\alpha\kappa^2}{12\nu^2}(\cos\theta + i\sin\theta)^2,$$

$$u_4 = \frac{(\alpha-2)(\alpha-1)\alpha(\alpha+1)}{32\kappa^2}, \quad w_4 = \frac{(\alpha-2)\alpha(\alpha+1)(\alpha+7)}{32\kappa^2},$$

and so on. In general, the coefficients u_n and w_n can be calculated from the recurrences:

$$w_n = \frac{3+2\alpha}{64n\nu^4}\left\{(3+n+\alpha)\left(2\kappa(3+2\alpha)\left((n-4-\alpha)u_{n-2}\right.\right.\right.$$

$$\left.\left.-2(n-3)w_{n-2}\right) + 2(n-7-\alpha)\left((4-n+\alpha)(3+2\alpha)w_{n-4}\right.\right.$$

$$+ \sin\theta \, (9 - n + \alpha) \, (3 + 2\,\alpha) \, (\sin\theta \, w_{n-9} - i \cos\theta \, u_{n-9})$$

$$- \kappa \, (\cos\theta \, (n - 5 - \alpha) - 2i\sin\theta \, (3 + 2\alpha)) \, (\cos\theta \, u_{n-7} + i \sin\theta \, w_{n-7}) \Big) \Big)$$

$$+ 2\kappa^2 \Big(2\kappa \, (\cos\theta + i \sin\theta) \, (3 - n + \alpha) \, (\cos\theta \, u_{n-3} + i \sin\theta \, w_{n-3})$$

$$+ (5 - n + \alpha) \Big(\sin\theta \, (\sin\theta \, (3 - n + \alpha) + i \cos\theta \, (3 + 3n + \alpha)) \, w_{n-5}$$

$$- \cos\theta \, ((\cos\theta + i \sin\theta) \, (3 - n + \alpha) - 2 \cos\theta \, (3 + n + \alpha)) \, u_{n-5} \Big) \Big) \Big\} ,$$

and

$$
\begin{aligned}
u_n \;=\; & w_n + \frac{1}{\kappa^2} \cos\theta \, (n - 9 - \alpha) \, (n - 7 - \alpha) \, (\cos\theta \, u_{n-9} + i \sin\theta \, w_{n-9}) \\
& + \frac{1}{\kappa} \Big\{ (3 + 2\,\alpha) \, u_{n-2} + (n - 5 - \alpha) \, w_{n-2} \\
& + 2 \cos\theta \, (n - 7 - \alpha) \, (\cos\theta \, u_{n-7} + i \sin\theta \, w_{n-7}) \Big\} ,
\end{aligned}
$$

where, for the first nine coefficients in particular, coefficients with a negative index are zero (i.e., $u_n = w_n = 0$ for $n < 0$).

Bender and Orszag (1978, Chapters 3 and 8) provides a good discussion of the issues involving gaining an optimal approximation from general asymptotic series. For optimal results, the series are truncated at around their minimum term (in absolute value). In practise the terms in the series tend to jump around wildly in magnitude as n is increased, though with a general downward trend until a minimum is reached and thereafter upward. Therefore, it is important to keep track of the envelope when deciding when the minimum is reached. For the fast mode series we examine successive packets of four terms, taking the maximum in each, and truncating the series when one such maximum exceeds its predecessor.

C.2   Slow MAG wave asymptotic series

The functions U_s and W_s (eqs [3.29] and [3.30]) may be expanded as asymptotic power series (in non-positive quarter integer powers of s):

$$U_s \, (s) \sim \sum_{n=0}^{\infty} u_n s^{-n/4} , \quad \text{and} \quad W_s \, (s) \sim \sum_{n=0}^{\infty} w_n s^{-n/4} ,$$

where

$$u_0 = w_0 = 1 ,$$

$$u_1 = w_1 = u_2 = w_2 = 0 ,$$

146

$$u_3 = -\frac{2}{3}i\nu\sin\theta\tan\theta, \quad w_3 = -\sin\theta\left(\frac{2}{3}i\nu\tan\theta + \frac{\kappa}{2\nu}\right),$$

for the first four terms. For terms $n \geq 4$ we may use the following recurrences:

$$u_n = \Bigg\{ 8\kappa\nu\bigg\{ \cos\theta\,(2n-23)\Big\{ \cos\theta\,(2n-31)\,(\kappa\sin\theta\,w_{n-20} - 2\nu u_{n-17}) $$
$$+8i\kappa\sin\theta\,(2\nu u_{n-13} - \kappa\sin\theta\,w_{n-16})\Big\} + 16\kappa^2\,(2\nu u_{n-9} - \kappa\sin\theta\,w_{n-12})\bigg\}$$
$$+256\kappa\nu^2\sin\theta\,(3i\kappa\cos\theta\,w_{n-3} + (4\nu^2\sin\theta - i\kappa n\cos\theta)\,(2u_{n-3} - w_{n-3}))$$
$$-16\sin\theta\,\kappa^3\,(48\nu^2\sin\theta - i\kappa\cos\theta\,(3+2n))\,w_{n-9} + 8\kappa\cos\theta$$
$$\times\,(16i\nu^2\,(\sin^2\theta\,(2n-17) + 2n - 20) + \kappa\sin\theta\cos\theta\,(2n-17)\,(3+2n))$$
$$\times\,(2\nu u_{n-10} - \kappa\sin\theta\,w_{n-13}) - 32\kappa^2\nu\bigg\{\Big\{ i\kappa\cos\theta\,(2n\,(1-4\sin^2\theta) - 15)$$
$$+16\nu^2\sin\theta\,(1 + 2\sin^2\theta)\Big\}w_{n-6} + (i\kappa\cos\theta\,(3+2n) - 48\nu^2\sin\theta)\,u_{n-6}\bigg\}$$
$$+8\nu\cos\theta\,(3\kappa\cos\theta\,(4n^2 - 24n - 17) + 64i\nu^2\sin\theta\,(n-7))$$
$$\times\,(2\nu u_{n-7} - \kappa\sin\theta\,w_{n-10}) + \cos^2\theta\,(i\kappa\cos\theta\,(3+2n) - 16\nu^2\sin\theta)$$
$$\times\,(425 - 84n + 4n^2)\,(2\nu u_{n-14} - \kappa\sin\theta\,w_{n-17})\Bigg\}/\left(512i\kappa\nu^3\cos\theta\,n\right),$$

and

$$w_n = u_n + \Bigg\{\Big\{ 32i\nu\cos\theta\,(n-11)\,(2\nu u_{n-11} - \kappa\sin\theta\,w_{n-14})$$
$$+(2n-25)\Big\{ \cos^2\theta\,(2n-33)\,(\kappa\sin\theta\,w_{n-21} - 2\nu u_{n-18})$$
$$+8i\kappa\cos\theta\sin\theta\,(2\nu u_{n-14} - \kappa\sin\theta\,w_{n-17})\Big\}$$
$$-4\kappa\,(i\kappa\cos\theta\,(2n-17)\,w_{n-7} + 16\nu^2\sin\theta\,(w_{n-7} - 2u_{n-7})) + 16\kappa^2$$
$$\times\,(2\nu\,(u_{n-10} - 2\sin^2\theta\,w_{n-10}) - \kappa\sin\theta\,(w_{n-13} + w_{n-3}))\Big\}/\left(32\kappa^2\nu\right)\Bigg\},$$

where, for the first twenty-one coefficients in particular, coefficients with a negative index are zero (i.e., $u_n = v_n = w_n = 0$ for $n < 0$). As for the fast modes the terms in the series tend to jump around wildly in magnitude as n is increased. We track the slow mode series in successive packets of twelve terms, truncating the series when the maximum (in a packet) exceeds its predecessor.

147

C.3   Frobenius series

At the regular singular point $\sigma = 0$ ($s = 0$) the displacements may be expanded as Frobenius series, i.e.,

$$\xi_x(\sigma) = \sum_{n=0}^{\infty} u_n \sigma^{n+r}, \quad \text{and} \quad \xi_z(\sigma) = \sum_{n=0}^{\infty} w_n \sigma^{n+r},$$

where the coefficients u_n and w_n for each of the three finite linearly independent solutions, labelled a, c and d, are:

Solution a:

$$r = 0, \quad u_0 = 1, \quad w_0 = u_1 = w_1 = u_2 = 0,$$

$$w_2 = \frac{1}{5}\left(i\kappa - 2\nu^2 \tan\theta\right) ;$$

Solution c:

$$r = 0, \quad w_0 = 1, \quad u_0 = u_1 = w_1 = u_2 = 0,$$

$$w_2 = \frac{1}{10}\left(3i\kappa \tan\theta - 4\nu^2\right) ;$$

Solution d:

$$r = 2, \quad u_0 = 1, \quad w_0 = u_1 = w_1 = 0,$$

$$u_2 = \frac{1}{7}\tan\theta\left(i\kappa - \nu^2 \tan\theta\right) ,$$

$$w_2 = \frac{1}{7}\left(i\kappa - \nu^2 \tan\theta\right) ;$$

for the first two terms. For terms with $n \geq 3$ we may use the following recurrences:

$$w_n = \left\{ \left(i\kappa(n+r) - 4\nu^2 \tan\theta\right) u_{n-2} + \kappa^2 \tan\theta\, u_{n-4} \right.$$
$$\left. + \left(i\kappa(n+r+1)\tan\theta - 4\nu^2\right) w_{n-2} \right\} / \left((n+r)(n+r+3)\right) ,$$

and

$$u_n = \tan\theta\, w_n + \left\{ \left\{\kappa^2\left(u_{n-4} - \tan\theta\, w_{n-4} + \sec^2\theta\, u_{n-9}\right) \right.\right.$$
$$\left.\left. - 4\nu^2 \sec^2\theta\, u_{n-7} + i\kappa \sec^2\theta\,(n+r-4)\, w_{n-7}\right\} / \left((n+r-2)(n+r)\right) \right\} ,$$

where, for the first nine coefficients in particular, coefficients with a negative index are zero (i.e., $u_n = w_n = 0$ for $n < 0$).

148

Appendix D

Mode conversion: Three-dimensional model

D.1   Fast MAG wave asymptotic series

The functions U_f, V_f and W_f (eqs. [4.7]-[4.9]) may be expanded as asymptotic power series (in non-positive half integer powers of s):

$$U_f(s) \sim \sum_{n=0}^{\infty} u_n s^{-n/2}, \quad V_f(s) \sim \sum_{n=0}^{\infty} v_n s^{-n/2}, \quad \text{and} \quad W_f(s) \sim \sum_{n=0}^{\infty} w_n s^{-n/2},$$

where (setting $\alpha = (2\nu^2/\kappa) - 3/2 = -2a$)

$$u_0 = v_0 = w_0 = 1, \quad u_1 = v_1 = w_1 = 0,$$

$$u_2 = -\frac{\alpha}{4\kappa}(\alpha+1), \quad w_2 = -\frac{\alpha}{4\kappa}(\alpha+5),$$

$$v_2 = -\frac{(\alpha-2)\{(\alpha+7)\cos\theta + i(\alpha+3)\cos\phi\sin\theta\}}{4\kappa(\cos\theta + i\cos\phi\sin\theta)},$$

$$u_3 = w_3 = \frac{\alpha\kappa^2}{12\nu^2}(\cos\theta + i\cos\phi\sin\theta)^2,$$

$$v_3 = \frac{\kappa^2}{12\nu^2}(\alpha-3)(\cos\theta + i\cos\phi\sin\theta)^2,$$

$$u_4 = \frac{(\alpha-2)(\alpha-1)\alpha(\alpha+1)}{32\kappa^2}, \quad w_4 = \frac{(\alpha-2)\alpha(\alpha+1)(\alpha+7)}{32\kappa^2},$$

149

$$v_4 = (\alpha - 4)(\alpha - 2)(\alpha + 3)\frac{(\alpha + 9)\cos\theta + i(\alpha + 1)\cos\phi\sin\theta}{32\kappa^2(\cos\theta + i\cos\phi\sin\theta)},$$

and so on. In general, the coefficients u_n, v_n, and w_n can be calculated from the recurrences:

$$
\begin{aligned}
w_n = \frac{1}{64n\nu^4}\Bigg\{ &\kappa^2\bigg\{ 4\sin^2\phi\sin^2\theta\,(\cos\theta + i\cos\phi\,\sin\theta)\,\alpha \\
&\times\Big\{ 2\cos\theta\,(3+\alpha)(5-n+\alpha)\,v_{n-10} - (\cos\theta + i\cos\phi\sin\theta) \\
&\times (2(3+\alpha)\kappa v_{n-8} + (3+n+\alpha)(3+2\alpha)\,v_{n-10})\Big\} \\
&+2(3+2\alpha)\bigg(\sin\theta\Big(\sin^2\phi\sin\theta\,(2-n-\alpha)(3+n+\alpha) \\
&+(5-n+\alpha)(\sin\theta\,(3-n+\alpha) + i\cos\phi\cos\theta\,(3+3n+\alpha))\Big)w_{n-5} \\
&-\Big(\cos\theta\,(\cos\theta + i\cos\phi\sin\theta)(3-n+\alpha)(5-n+\alpha) \\
&-(3+n+\alpha)\big(2\cos^2\theta\,(5-n+\alpha) + \sin^2\phi\sin^2\theta\,(3+2\alpha)\big)\Big)u_{n-5} \\
&-2\kappa\Big(\sin\theta\,\big(n\sin^2\phi\sin\theta + (\sin\theta - i\cos\phi\cos\theta)(3-n+\alpha)\big)w_{n-3} - \\
&\big(\sin^2\phi\sin^2\theta\,(3+\alpha) + \cos\theta\,(\cos\theta + i\cos\phi\sin\theta)(3-n+\alpha)\big)u_{n-3}\Big)\bigg)\bigg\} \\
&+(3+n+\alpha)(3+2\alpha)\bigg\{ 2(3+2\alpha)\kappa\Big((n-4-\alpha)\,u_{n-2} \\
&-2(n-3)\,w_{n-2}\Big) + (n-7-\alpha)\bigg(4\alpha\sin^2\phi\sin^2\theta\,(\cos\theta + i\cos\phi\sin\theta) \\
&\times (\cos\theta\,(9-n+\alpha)\,v_{n-14} - (2\cos\theta + i\cos\phi\sin\theta)\kappa v_{n-12}) \\
&+2\sin\theta\,(9-n+\alpha)(3+2\alpha)(\sin\theta\,w_{n-9} - i\cos\phi\cos\theta\,u_{n-9}) \\
&+2\kappa\Big(\sin\theta\,(i\cos\phi\cos\theta\,(5-n+\alpha) - 2\sin\theta\,(3+2\alpha))\,w_{n-7} \\
&+\big(\cos^2\theta\,(5-n+\alpha) + \sin\theta\,(2i\cos\phi\cos\theta + \sin^2\phi\sin\theta)(3+2\alpha)\big) \\
&\times u_{n-7}\Big) + 2(4-n+\alpha)(3+2\alpha)\,w_{n-4}\bigg)\bigg\}\bigg\}\Bigg\},
\end{aligned}
$$

$$
\begin{aligned}
u_n = w_n &+ \frac{1}{\kappa^2}\cos\theta\,(n-9-\alpha)(n-7-\alpha)(\cos\theta\,u_{n-9} + i\cos\phi\sin\theta\,w_{n-9}) \\
&+\sin^2\phi\sin^2\theta\,(w_{n-5} - u_{n-5}) + \frac{1}{\kappa}\Big\{ (3+2\alpha)\,u_{n-2} + (n-5-\alpha)\,w_{n-2} \\
&+(n-7-\alpha)\Big(\sin\theta\,(2i\cos\phi\cos\theta + \sin^2\phi\sin\theta)\,w_{n-7}
\end{aligned}
$$

150

$$+2\cos^2\theta\, u_{n-7}\Big)\Big\} + \frac{\alpha}{2\nu^2}\sin^2\phi\sin^2\theta\,(\cos\theta + i\cos\phi\sin\theta)$$
$$\times(\cos\theta\,(n-7-\alpha)\,v_{n-12} + (\cos\theta + i\cos\phi\sin\theta)\,\kappa v_{n-10})\,,$$

and

$$
\begin{aligned}
v_n = \frac{1}{4\nu^2}\Big\{&(\cos\theta + i\cos\phi\sin\theta)\Big(\cos\theta\sin^2\phi\sin^2\theta\,(n-5-\alpha)\,\kappa v_{n-10}\\
&+(\cos\theta + i\cos\phi\sin\theta)\,\kappa^2\,(\sin^2\phi\sin^2\theta\,v_{n-8} - v_{n-3})\\
&-2\kappa\cos\theta\,(n-\alpha)\,v_{n-5}\Big) - \cos^2\theta\,(n-2-\alpha)\,(n-\alpha)\,v_{n-7}\Big\}\\
&+\frac{1}{2\alpha\kappa}\Big\{\Big\{\Big\{(\cos\theta\,(n+3+\alpha) + i\cos\phi\sin\theta\,(3+2\alpha))\,\kappa u_n\\
&-(3i\cos\phi\sin\theta + \cos\theta\,(n+3-\alpha))\,\kappa w_n\\
&-\cos\theta\,(n-2-\alpha)\,(n-\alpha)\,w_{n-2}\Big\}/(\cos\theta + i\cos\phi\sin\theta)\Big\}\\
&+(n-5-\alpha)\Big(\cos\theta\,(n-7-\alpha)\,(\cos\theta\,u_{n-7} + i\cos\phi\sin\theta\,w_{n-7})\\
&+\kappa\,(2\cos^2\theta\,u_{n-5} + \sin\theta\,(2i\cos\phi\cos\theta + \sin^2\phi\sin\theta)\,w_{n-5})\Big)\\
&+\sin^2\phi\sin^2\theta\,\kappa^2\,(w_{n-3} - u_{n-3})\Big\}\,,
\end{aligned}
$$

where, for the first fourteen coefficients in particular, coefficients with a negative index are zero (i.e., $u_n = v_n = w_n = 0$ for $n < 0$). As for the two-dimensional fast modes (Appendix C.1) the terms in the series tend to jump around wildly in magnitude as n is increased. We track the three-dimensional fast mode series in successive packets of four terms, truncating the series when the maximum in a packet exceeds its predecessor.

D.2 Slow MAG wave and Alfvén wave asymptotic series

In practise, for the incompressive solutions (the slow MAG wave and the Alfvén wave), we apply the leading behaviours $\zeta \sim \chi$, $\eta \sim \chi$ and $\xi_z \sim \cos\theta\frac{\kappa}{2\nu}s^{-m/2}\chi$ (eqs. [4.15] and [4.16]), i.e.,

$$\zeta \sim s^{-3/8}\exp\left[\cos\phi\tan\theta\frac{i\kappa}{2}s + \sec\theta\frac{4}{7}i\nu s^{7/4}\right]U(s)\,,\quad s\to\infty\,,$$

$$\eta \sim s^{-3/8}\exp\left[\cos\phi\tan\theta\frac{i\kappa}{2}s + \sec\theta\frac{4}{7}i\nu s^{7/4}\right]V(s)\,,\quad s\to\infty\,,$$

$$\xi_z \sim \cos\theta\frac{\kappa}{2\nu}s^{-9/8}$$
$$\times\exp\left[\cos\phi\tan\theta\frac{i\kappa}{2}s + \sec\theta\frac{4}{7}i\nu s^{7/4}\right]W(s)\,,\quad s\to\infty\,,$$

151

where the functions U, V and W may be expanded as asymptotic power series (in non-positive quarter integer powers of s):

$$U(s) \sim \sum_{n=0}^{\infty} u_n s^{-n/4}, \quad V(s) \sim \sum_{n=0}^{\infty} v_n s^{-n/4}, \quad \text{and} \quad W(s) \sim \sum_{n=0}^{\infty} w_n s^{-n/4}.$$

At this stage the series U, V and W are not necessarily asymptotic to unity.

Applying these leading behaviours to the governing equations (4.1)–(4.3) we find two independent solutions:

Slow MAG wave solution:

$$u_0 = w_0 = 1, \quad v_0 = 0,$$

$$u_1 = v_1 = w_1 = u_2 = v_2 = w_2 = 0,$$

$$u_3 = -\frac{2}{3} i\nu \cos^2\phi \sin\theta \tan\theta,$$

$$v_3 = \sin\phi \sin\theta \left(\frac{2}{3} i\nu \cos\phi \tan\theta - \frac{\kappa}{2\nu} \right),$$

$$w_3 = -\cos\phi \sin\theta \left(\frac{2}{3} i\nu \cos\phi \tan\theta + \frac{\kappa}{2\nu} \right);$$

Alfvén wave solution:

$$u_0 = w_0 = 0, \quad v_0 = 1,$$

$$u_1 = v_1 = w_1 = u_2 = v_2 = w_2 = 0,$$

$$u_3 = \sin\phi \sin\theta \left(\frac{\kappa}{2\nu} + \frac{2}{3} i\nu \cos\phi \tan\theta \right),$$

$$v_3 = -\frac{2}{3} i\nu \sin^2\phi \sin\theta \tan\theta,$$

$$w_3 = \sin\phi \sin\theta \left(\frac{\kappa}{2\nu} + \frac{2}{3} i\nu \cos\phi \tan\theta \right),$$

for the first four terms. For terms $n \geq 4$ we may use the following recurrences (which are identical for both the slow MAG wave and Alfvén wave solutions):

152

$$u_n = \left\{ 256\kappa\nu^2 \sin\theta \left\{ \left(3i\kappa\cos\theta - 4\nu^2\cos\phi\sin\theta \right)\left(\sin\phi\, v_{n-3} + \cos\phi\, w_{n-3} \right) \right.\right.$$

$$\left. + 2\cos\phi\left(4\nu^2\cos\phi\sin\theta - i\kappa n\cos\theta \right)u_{n-3} + i\kappa n\cos\phi\cos\theta\, w_{n-3} \right\}$$

$$- 16\sin\theta\,\kappa^3 \left\{ 16\nu^2\sin\theta \left(\cos^2\theta + \cos^2\phi\left(2 + \cos^2\phi\sin^2\theta \right) \right) \right.$$

$$\left. - i\kappa\cos\phi\cos\theta \left(\cos^2\theta\,(3+2n) + \left(12 + \cos^2\phi\,(2n-9) \right)\sin^2\theta \right) \right\} w_{n-9}$$

$$- 16\kappa\nu\cos\theta \left\{ 2\,(2n-17)\sin\phi\sin\theta \left(3\kappa\cos\theta + 4i\nu^2\cos\phi\sin\theta \right)v_{n-10} \right.$$

$$- \left\{ 16i\nu^2 \left(\cos^2\phi\sin^2\theta\,(2n-17) + 2\,(n-10)\left(\cos^2\theta + \cos^2\phi\sin^2\theta \right) \right) \right.$$

$$\left.\left. + \kappa\cos\phi\sin\theta\cos\theta\,(2n-17)(3+2n) \right\} u_{n-10} \right\} + \left(\cos^2\theta + \cos^2\phi\sin^2\theta \right)$$

$$\times 8\kappa\nu \left\{ \cos\theta\,(2n-23) \left\{ \cos\theta\,(2n-31)\left(\kappa\cos\phi\sin\theta\, w_{n-20} - 2\nu u_{n-17} \right) \right.\right.$$

$$\left. + 4i\kappa\sin\theta \left(2\nu\left(2\cos\phi\, u_{n-13} - \sin\phi\, v_{n-3} \right) - \kappa\left(1 + \cos^2\phi \right)\sin\theta\, w_{n-16} \right) \right\}$$

$$\left. + 16\kappa\left(2\kappa\nu u_{n-9} - 4\nu^2\sin\phi\sin\theta\, v_{n-6} - \kappa^2\cos\phi\sin\theta\, w_{n-12} \right) \right\}$$

$$+ 8\nu\cos\theta \left(3\kappa\cos\theta\,(11 + 4\,(n-7)(1+n)) + 64i\nu^2\cos\phi\sin\theta\,(n-7) \right)$$

$$\times \left(2\nu u_{n-7} - \kappa\cos\phi\sin\theta\, w_{n-10} \right) - 32\kappa^2\nu \left\{ \left\{ i\kappa\cos\theta \left(\cos^2\theta\,(2n-15) \right.\right.\right.$$

$$\left.\left. - 3\sin^2\theta\left(4 + \cos^2\phi\,(1+2n) \right) \right) + 16\nu^2\cos\phi\sin\theta\left(1 + 2\cos^2\phi\sin^2\theta \right) \right\}$$

$$\times w_{n-6} + \left\{ i\kappa\cos\theta \left(\cos^2\theta\,(3+2n) + \left(12 + \cos^2\phi\,(2n-9) \right)\sin^2\theta \right) \right.$$

$$\left.\left. - 16\nu^2\cos\phi\sin\theta\left(1 + 2\left(\cos^2\theta + \cos^2\phi\sin^2\theta \right) \right) \right\} u_{n-6} \right\} - 8\kappa^2\sin\theta\cos\theta$$

$$\times \left\{ \left(\left(1 + \cos^2\phi \right)(2n-17)\sin^2\theta + 4\,(n-10)\left(\cos^2\theta + \cos^2\phi\sin^2\theta \right) \right) \right.$$

$$\left. \times 8i\nu^2\cos\phi + \kappa\sin\theta\cos\theta\,(2n-17)\left(6 + \cos^2\phi\,(2n-3) \right) \right\} w_{n-13}$$

$$+ \cos^2\theta\left(425 - 84n + 4n^2 \right)\left(i\kappa\cos\theta\,(3+2n) - 16\nu^2\cos\phi\sin\theta \right)$$

$$\left. \times \left(2\nu u_{n-14} - \kappa\cos\phi\sin\theta\, w_{n-17} \right) \right\} / \left(512 i\kappa\nu^3\cos\theta\, n \right),$$

$$v_n = \left\{ \kappa\cos^2\theta\left(33 - 28n + 4n^2 \right)\left(2\nu v_{n-7} + \kappa\sin\phi\sin\theta\, w_{n-10} \right) \right.$$

$$- 2\sin\phi\sin\theta \left\{ 32i\nu^2\cos\theta\,(n-7)\left(2\nu u_{n-7} - \kappa\cos\phi\sin\theta\, w_{n-10} \right) \right.$$

153

$$+\nu \cos\theta \, (2n - 17) \Big\{ \cos\theta \, (2n - 25) \, (\kappa \cos\phi \sin\theta \, w_{n-17} - 2\nu u_{n-14})$$

$$+4i\kappa \sin\theta \, (2\nu \, (2\cos\phi \, u_{n-10} - \sin\phi \, v_{n-10}) - \kappa \, (1 + \cos^2\phi) \sin\theta \, w_{n-13}) \Big\}$$

$$-2\kappa^2 \Big\{ \sin\theta \, (16 \, (1 + \cos^2\phi) \sin\theta \, \nu^2 - i\kappa \cos\phi \cos\theta \, (2n - 3)) \, w_{n-6}$$

$$+8\kappa\nu \cos\phi \sin\theta \, w_{n-9} - 16\nu^2 u_{n-6} \Big\} + 4\kappa\nu \Big(i\kappa \cos\theta \, (9 + 2n) \, w_{n-3}$$

$$+ \, (32\nu^2 \cos\phi \sin\theta - i\kappa \cos\theta \, (2n - 3)) \, u_{n-3} - 16\nu^2 \sin\theta$$

$$\times \, (\sin\phi \, v_{n-3} + \cos\phi \, w_{n-3}) \Big) \Big\} \Big\} / (64 i\kappa\nu^2 \cos\theta \, n) \; ,$$

and

$$w_n = u_n + \Big\{ \Big\{ 32 i\nu \cos\theta \, (n - 11) \, (2\nu u_{n-11} - \kappa \cos\phi \sin\theta \, w_{n-14})$$

$$+ \, (2n - 25) \Big\{ \cos^2\theta \, (2n - 33) \, (\kappa \cos\phi \sin\theta \, w_{n-21} - 2\nu u_{n-18})$$

$$+4i\kappa \cos\theta \sin\theta \, \Big(2\nu \, (2\cos\phi \, u_{n-14} - \sin\phi \, v_{n-14})$$

$$-\kappa \, (1 + \cos^2\phi) \sin\theta \, w_{n-17} \Big) \Big\} - 4\kappa \Big(i\kappa \cos\theta \, (2n - 17) \, w_{n-7}$$

$$+16\nu^2 \sin\theta \, (\sin\phi \, v_{n-7} + \cos\phi \, w_{n-7} - 2\cos\phi \, u_{n-7}) \Big)$$

$$+16\kappa^2 \Big(2\nu \, (u_{n-10} - (1 + \cos^2\phi) \sin^2\theta \, w_{n-10})$$

$$-\kappa \cos\phi \sin\theta \, (w_{n-13} + w_{n-3}) \Big) \Big\} / (32\kappa^2\nu) \Big\} \; ,$$

where, for the first twenty-one coefficients in particular, coefficients with a negative index are zero (i.e., $u_n = v_n = w_n = 0$ for $n < 0$). It should be noted that for the slow MAG wave solution $U(s) \sim 1$ and $W(s) \sim 1$, as $s \to \infty$, whereas for the Alfvén wave solution $V(s) \sim 1$, as $s \to \infty$. Hence, for a given solution (either the slow MAG wave or the Alfvén wave) to have the coefficients U, V and W all asymptotic to unity, the appropriate factors must be shifted from the series above to the leading orders. The resultant leading orders are presented in equations (4.17)-(4.19) for the slow modes, and equations (4.20)-(4.22) for the Alfvén modes.

As for the fast modes the terms in the series tend to jump around wildly in magnitude as n is increased. We track both the slow MAG wave and Alfvén wave series in successive packets of twelve terms, truncating the series when the maximum in a packet exceeds its predecessor.

D.3 Frobenius series expansions

At the regular singular point $\sigma = 0$ ($s = 0$) the displacements may be expanded as Frobenius series, i.e.,

$$\zeta(\sigma) = \sum_{n=0}^{\infty} u_n \sigma^{n+r}, \quad \eta(\sigma) = \sum_{n=0}^{\infty} v_n \sigma^{n+r}, \quad \text{and} \quad \xi_z(\sigma) = \sum_{n=0}^{\infty} w_n \sigma^{n+r},$$

where the coefficients u_n, v_n, and w_n for each of the five finite linearly independent solutions labelled a, b, c, d and e, are:

Solution a:

$$r = 0, \quad u_0 = 1, \quad v_0 = w_0 = u_1 = v_1 = w_1 = u_2 = v_2 = 0,$$

$$w_2 = \frac{1}{5}\left(i\kappa - 2\nu^2 \cos\phi \tan\theta\right);$$

Solution b:

$$r = 0, \quad v_0 = 1, \quad u_0 = w_0 = u_1 = v_1 = w_1 = u_2 = v_2 = 0,$$

$$w_2 = \frac{2}{5}\nu^2 \sin\phi \tan\theta;$$

Solution c:

$$r = 0, \quad w_0 = 1, \quad u_0 = v_0 = u_1 = v_1 = w_1 = u_2 = v_2 = 0,$$

$$w_2 = \frac{1}{10}\left(3i\kappa \cos\phi \tan\theta - 4\nu^2\right);$$

Solution d:

$$r = 2, \quad u_0 = 1, \quad v_0 = w_0 = u_1 = v_1 = w_1 = 0,$$

$$u_2 = \frac{1}{7}\cos\phi \tan\theta \left(i\kappa - \nu^2 \cos\phi \tan\theta\right),$$

$$v_2 = \frac{1}{28}\sin\phi \tan\theta \left(3i\kappa + 4\nu^2 \cos\phi \tan\theta\right),$$

$$w_2 = \frac{1}{7}\left(i\kappa - \nu^2 \cos\phi \tan\theta\right);$$

Solution e:

$$r = 2, \quad v_0 = 1, \quad u_0 = w_0 = u_1 = v_1 = w_1 = 0,$$

$$u_2 = \frac{1}{28} \sin\phi \tan\theta \left(7i\kappa + 4\nu^2 \cos\phi \tan\theta\right),$$

$$v_2 = \frac{1}{14} \tan\theta \left(7i\kappa \cos\phi - 2\nu^2 \sin^2\phi \tan\theta\right),$$

$$w_2 = \frac{1}{7}\nu^2 \sin\phi \tan\theta;$$

for the first two terms. For terms with $n \geq 3$ we may use the following recurrences:

$$
\begin{aligned}
w_n = \Big\{ & \left(i\kappa(n+r) - 4\nu^2 \cos\phi \tan\theta\right) u_{n-2} + 4\nu^2 \sin\phi \tan\theta \, v_{n-2} \\
& + \left(i\kappa(n+r+1)\cos\phi \tan\theta - 4\nu^2\right) w_{n-2} + \kappa^2 \cos\phi \tan\theta \, u_{n-4} \Big\} / \\
& ((n+r)(n+r+3)),
\end{aligned}
$$

$$
\begin{aligned}
u_n = \cos\phi \tan\theta \, w_n + \Big\{ & \{\kappa^2 \left(1 + \sin^2\phi \tan^2\theta\right) u_{n-4} - 4\nu^2 \sec^2\theta \, u_{n-7} \\
& + \kappa^2 \cos\phi \tan\theta \left(\sin\phi \tan\theta \, v_{n-4} - w_{n-4}\right) + \kappa^2 \sec^2\theta \, u_{n-9} \\
& + i\kappa(n+r-2)\sin\phi \tan\theta(v_{n-2} + \sin\phi \tan\theta \, w_{n-2}) \\
& + i\kappa \sec^2\theta \, (n+r-4) w_{n-7}\} / \left((n+r-2)(n+r)\right) \Big\},
\end{aligned}
$$

and

$$
\begin{aligned}
v_n = -\sin\phi \tan\theta \, w_n + \Big\{ & \{\kappa^2 \cos\phi \tan^2\theta \left(\sin\phi \, u_{n-4} + \cos\phi \, v_{n-4}\right) \\
& + i\kappa(n+r-2)\tan\theta \left(\sin\phi \, u_{n-2} + 2\cos\phi \, v_{n-2} + \sin\phi \cos\phi \tan\theta \, w_{n-2}\right) \\
& - 4\nu^2 \sec^2\theta \, v_{n-7}\} / ((n+r-2)(n+r)) \Big\},
\end{aligned}
$$

where, for the first nine coefficients in particular, coefficients with a negative index are zero (i.e., $u_n = v_n = w_n = 0$ for $n < 0$).

D.4   Additional Results
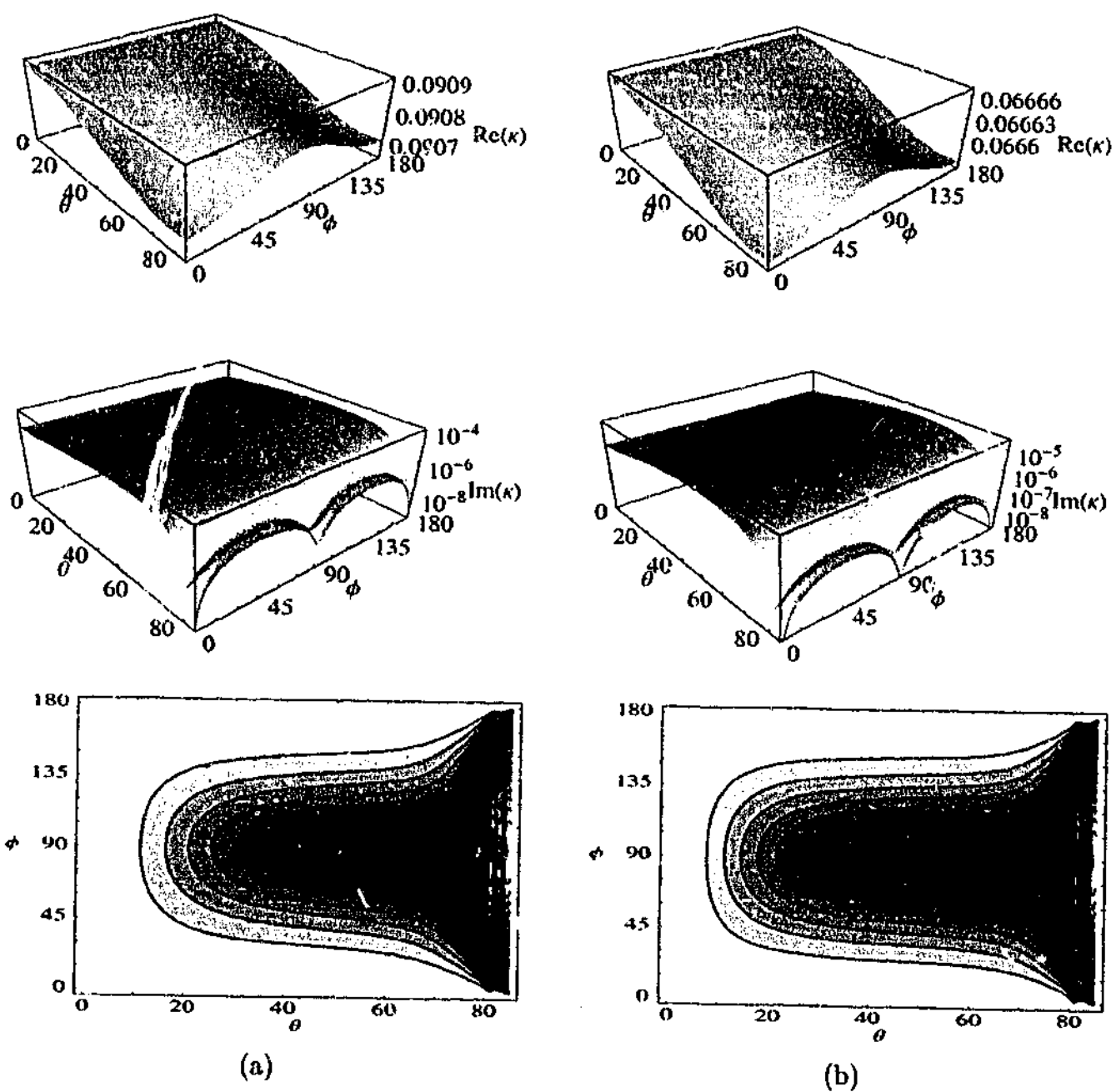
Figure D.1: Same as Figure 4.1, $\nu = 0.5$, but for (a) $n = 2$ and (b) $n = 3$.
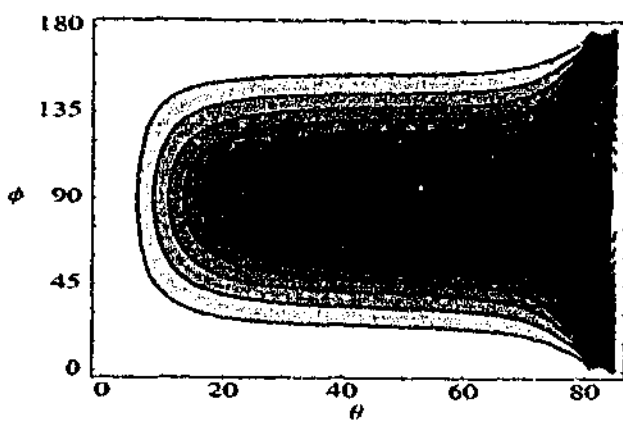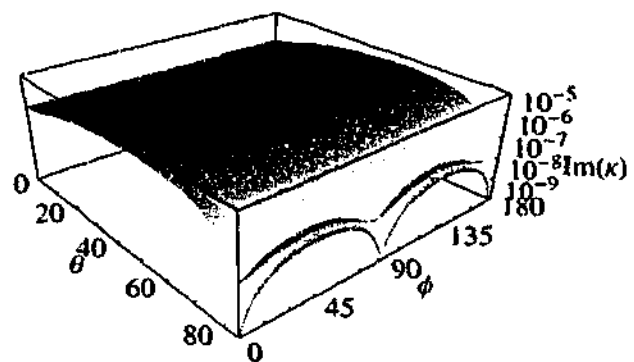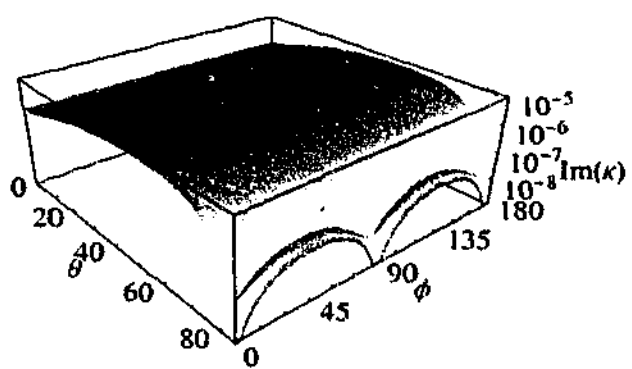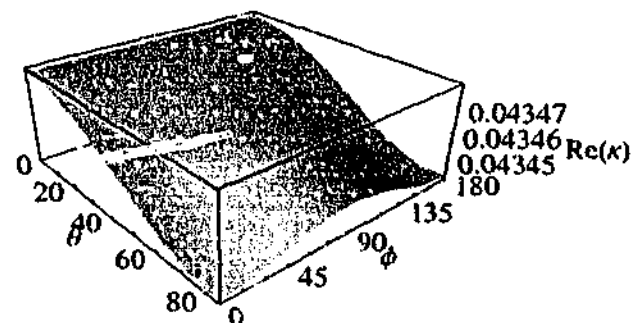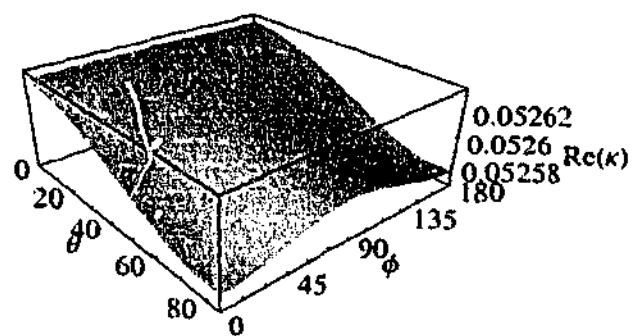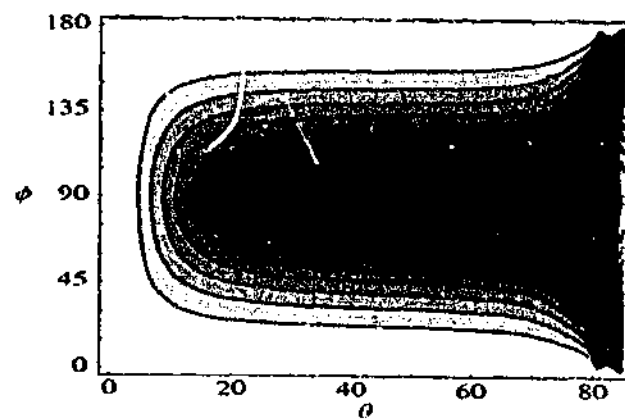
Figure D.2: Same as Figure 4.1, $\nu = 0.5$, but for (a) $n = 4$ and (b) $n = 5$.

158
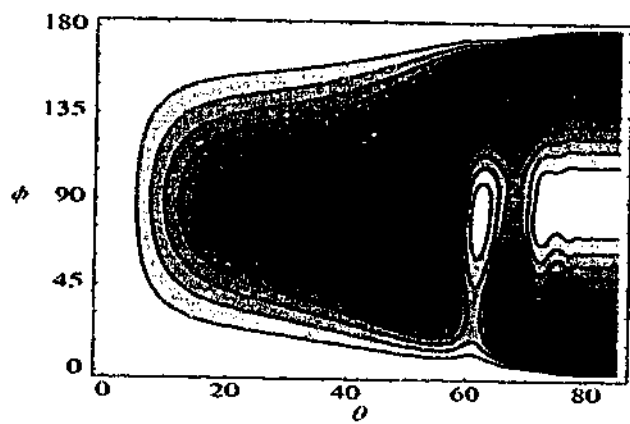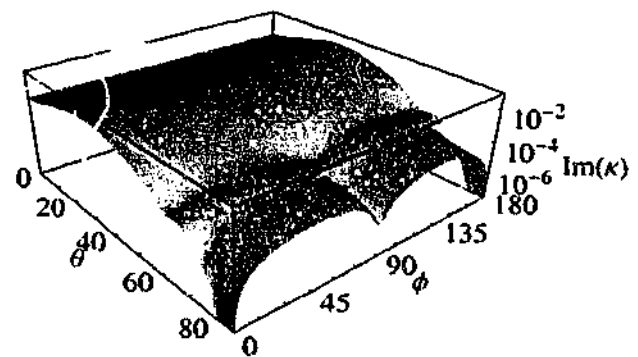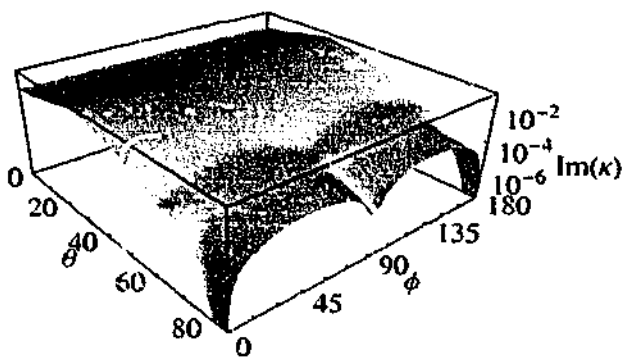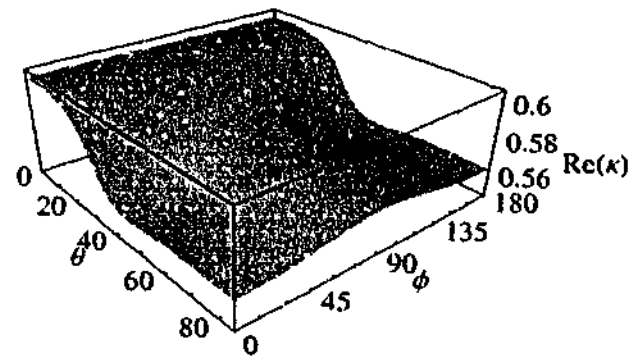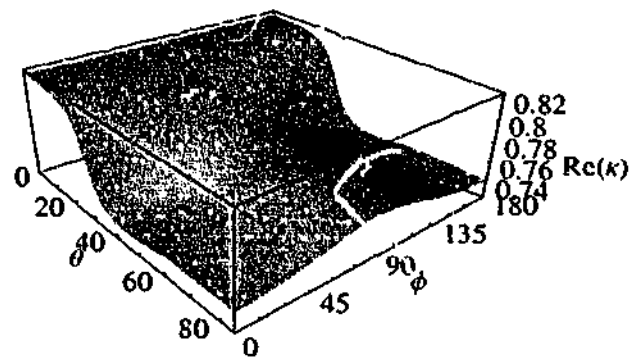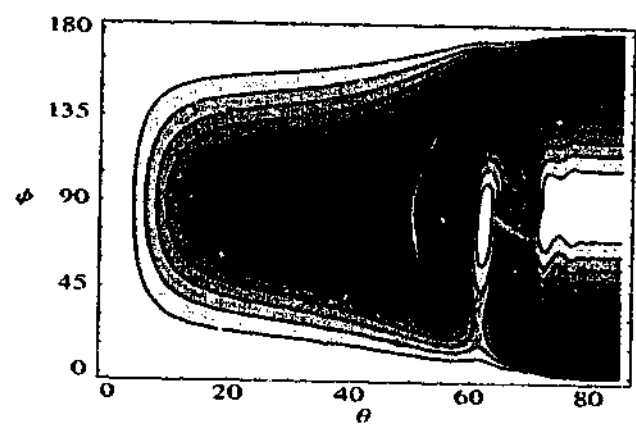
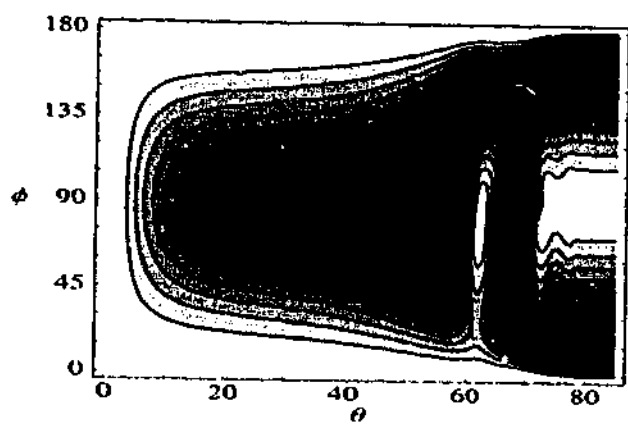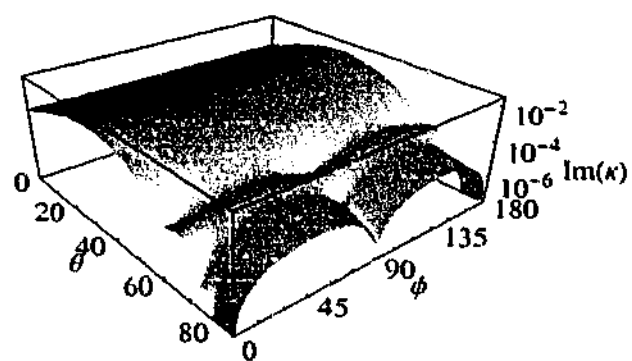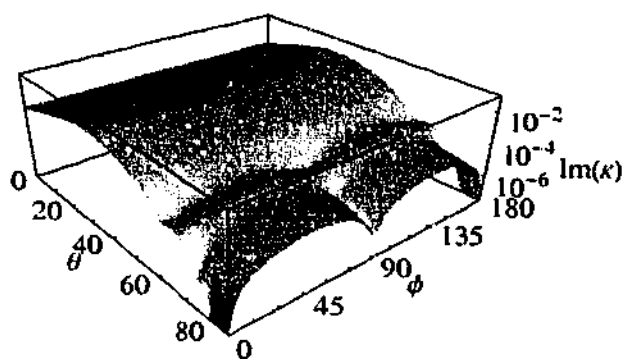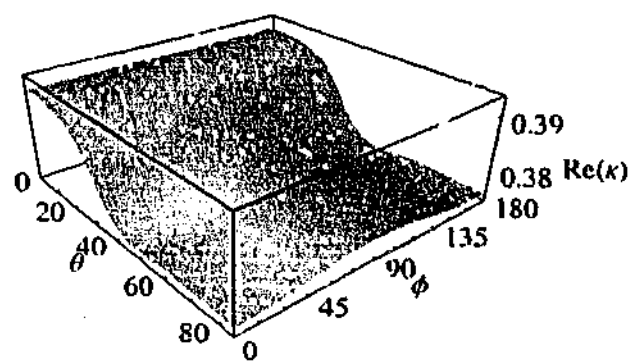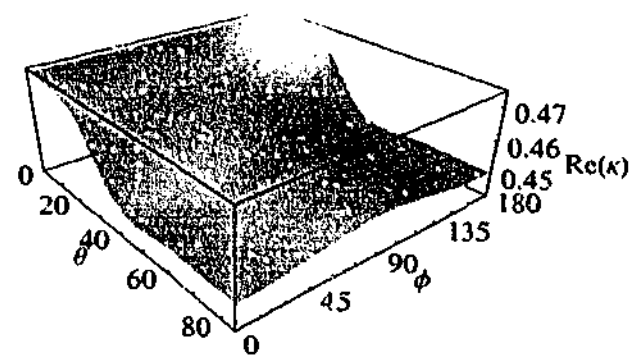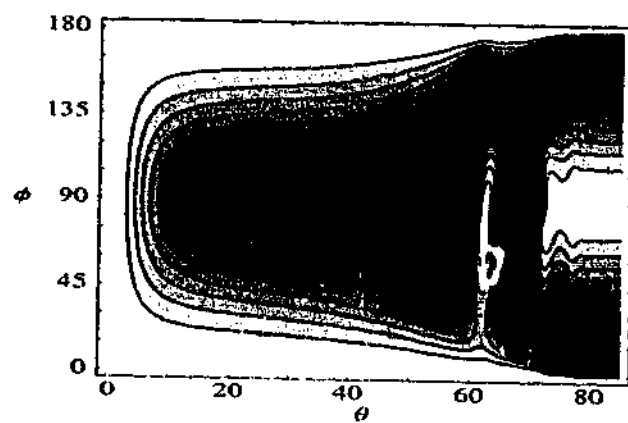*Figure D.3:* Same as Figure 4.2, $\nu = 1.5$, but for (a) $n = 2$ and (b) $n = 3$.

159

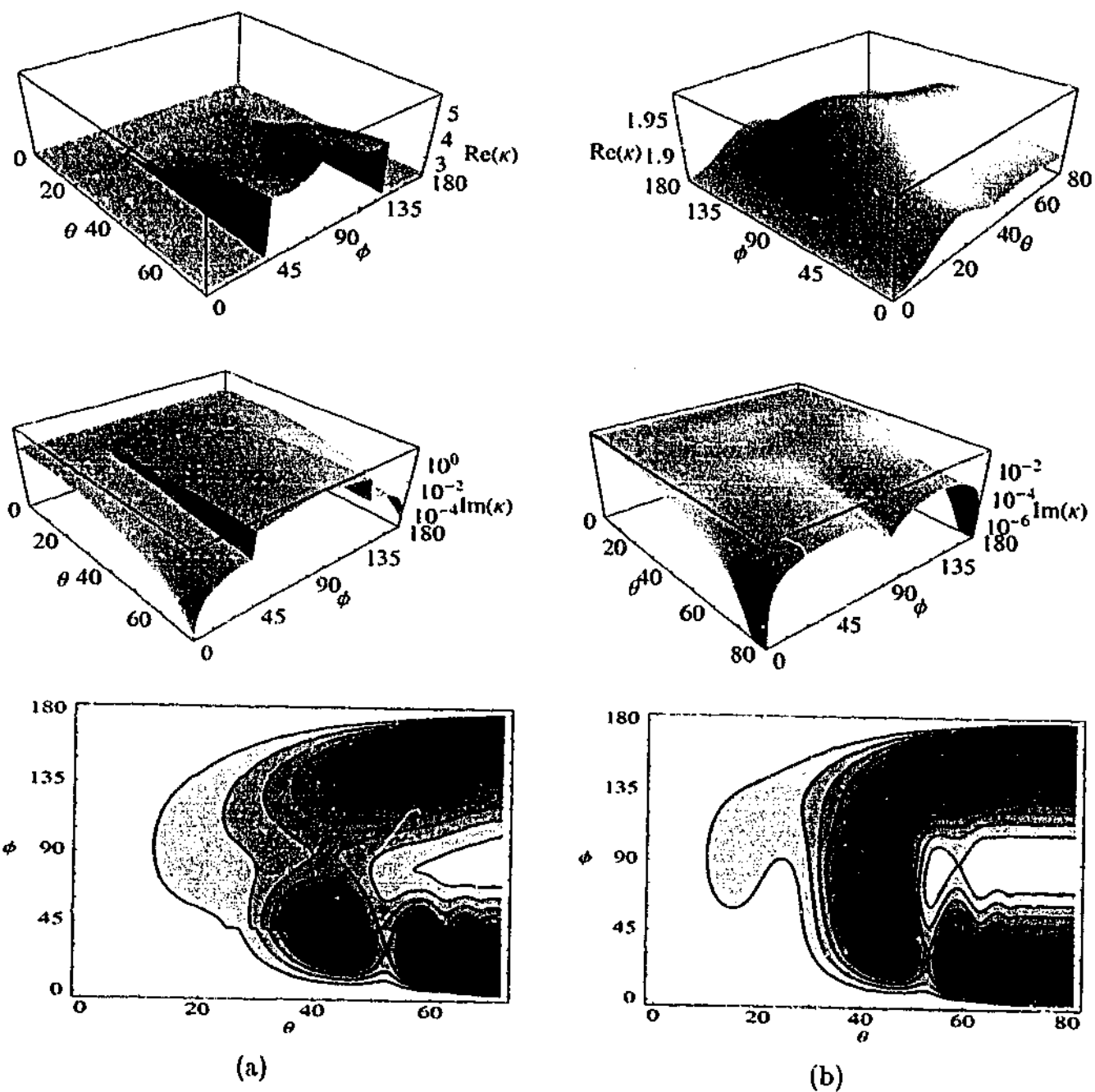*Figure D.4:* Same as Figure 4.2, $\nu = 1.5$, but for (a) $n = 4$ and (b) $n = 5$.

Figure D.5: Same as Figure 4.3, $\nu = 3$, but for (a) $n = 3$ with domain $0 \leq \theta \leq 72°$, $0 \leq \phi \leq 180°$; and (b) $n = 4$ with domain $0 \leq \theta \leq 81°$, $0 \leq \phi \leq 180°$; and the point of view has been shifted for the real parts of $n = 4$ (b, *top panel*).

161
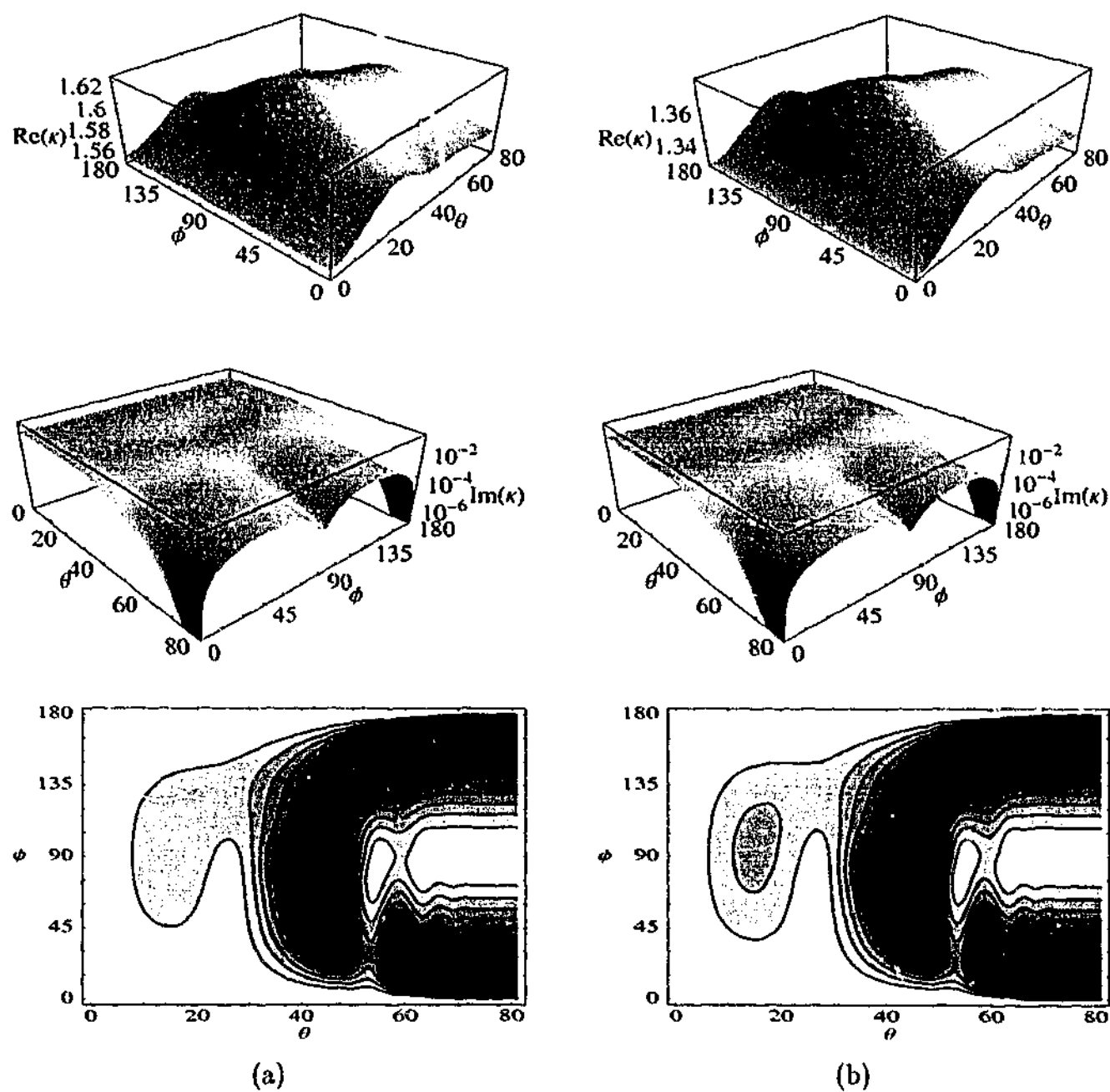
Figure D.6: Same as Figure 4.3, $\nu = 3$, but for (a) $n = 5$ and (b) $n = 6$; and the point of view has been shifted for the real parts in both cases (*top panels*). The domain for both modes is $0 \leq \theta \leq 81°$, $0 \leq \phi \leq 180°$.

162

Appendix E

Thin magnetic flux tubes

E.1   Sausage modes

For the sausage modes the matching coefficients are

$$\lambda_\| = \frac{-a_1 H_{\mu+1}^{(2)}\left(2\nu\sqrt{\epsilon_\|}\right) - a_2 H_\mu^{(2)}\left(2\nu\sqrt{\epsilon_\|}\right)}{a_1 H_{\mu+1}^{(1)}\left(2\nu\sqrt{\epsilon_\|}\right) + a_2 H_\mu^{(1)}\left(2\nu\sqrt{\epsilon_\|}\right)},$$

and

$$C_\| = -A_n I_\|^{(1)} \frac{e^5 \nu\,(m+1)\,(\beta+1)\left(\varpi_{ch}^2-1\right)^{1/2}}{2 m z_0 \sqrt{\epsilon_\|}\left(a_1 H_{\mu+1}^{(1)}\left(2\nu\sqrt{\epsilon_\|}\right) + a_2 H_\mu^{(1)}\left(2\nu\sqrt{\epsilon_\|}\right)\right)},$$

for convenience, we have defined a_1 and a_2 as

$$a_1 = \left[\left(1 + i\left(\varpi_{cor}^2-1\right)^{1/2}\right)\frac{H_{ch}}{H_{cor}} - 1\right]\sin\theta - \left(\varpi_{ch}^2-1\right)^{1/2}\cos\theta,$$

and

$$a_2 = \frac{z_0}{2 H_{ch}\nu\sqrt{\epsilon_\|}}\left\{\left[\varpi_{ch}^2 - \frac{H_{ch}}{H_{cor}}\left(1 + i\left(\varpi_{cor}^2-1\right)^{1/2}\right)\right]\sin\theta\right.$$
$$\left. + \frac{H_{ch}}{H_{cor}}\left(1 + i\left(\varpi_{cor}^2-1\right)^{1/2}\right)\left(\varpi_{ch}^2-1\right)^{1/2}\cos\theta\right\},$$

where $\theta = 5\left(\varpi_{ch}^2-1\right)^{1/2}$. The line width contribution from the upward escaping MAG waves is

$$\Gamma_{n,\|}^+(\omega) = \omega f \frac{g z_0 \mu_g \beta\,(\beta+1)\,(m+1)^2\left(\varpi_{cor}^2-1\right)^{1/2}\left(\varpi_{ch}^2-1\right)\left|I_\|^{(1)}\right|^2}{8\pi\nu^2\epsilon_\| m^2 R T_{cor}\mathcal{N}_n\left|a_1 H_{\mu+1}^{(1)}\left(2\nu\sqrt{\epsilon_\|}\right) + a_2 H_\mu^{(1)}\left(2\nu\sqrt{\epsilon_\|}\right)\right|^2}.$$

163

E.2 Kink modes – homogeneous corona with straight, uniform, and vertical magnetic field

For the kink modes, with a homogeneous (unstratified) corona permeated by straight, uniform, and vertical magnetic field, the matching coefficients are

$$\lambda_\perp = \frac{b_1 b_5 - b_2 b_6}{b_1 b_4 - b_2 b_3} \, ,$$

and

$$C_\perp = \tilde{C}_\perp I \, ,$$

where

$$I = \int_1^\infty r^{\mu+1} \psi_\perp(r) f_\perp(r) \, dr \, ,$$

and

$$\tilde{C}_\perp = \frac{b_1 b_6 - b_3 b_5}{b_1 b_4 - b_2 b_3} \, ,$$

for convenience, b_1, b_2, b_3, b_4, b_5, and b_6 are defined as:

$$b_1 = x_3 J_1(x_1) H_\mu^{(1)}\left(2\nu\sqrt{\epsilon_\perp}\right) - J_0(x_1) H_{\mu+1}^{(1)}\left(2\nu\sqrt{\epsilon_\perp}\right) \, ,$$

$$b_2 = -\frac{2i}{\pi} x_2 x_3 \left[J_1(x_1 x_2) - \left(\frac{iC_{A,ch}}{x_2 C_{A,cor}}\right) J_0(x_1 x_2) \right] \, ,$$

$$b_3 = J_0(x_1 x_2) H_\mu^{(1)}\left(2\nu\sqrt{\epsilon_\perp}\right) \, ,$$

$$b_4 = -\frac{2i}{\pi} J_0(x_1) + \frac{\pi x_1 b_2}{2 x_3} \left(Y_0(x_1) J_0(x_1 x_2) - J_0(x_1) Y_0(x_1 x_2)\right) \, ,$$

$$b_5 = J_0(x_1) H_{\mu+1}^{(2)}\left(2\nu\sqrt{\epsilon_\perp}\right) - x_3 J_1(x_1) H_\mu^{(2)}\left(2\nu\sqrt{\epsilon_\perp}\right) \, ,$$

$$b_6 = -J_0(x_1 x_2) H_\mu^{(2)}\left(2\nu\sqrt{\epsilon_\perp}\right) \, ,$$

where $x_1 = 2\omega L_{ch}/C_{A,ch}$, $x_2 = \exp\left[5(1-\alpha)/\alpha\right]$, and $x_3 = z_0\omega/\left(\nu\sqrt{\epsilon_\perp}C_{A,ch}\right)$. The line width contribution from the upward escaping Alfvén waves is

$$\Gamma_{n,\perp}^+(\omega) = \omega f \left\{ \frac{1}{4\pi} \sqrt{\frac{g}{mz_0}} \frac{\rho(m+1)^2(\beta+1)^2\nu^5}{\rho_0 g m \kappa_n^2} C_{A,cor} \exp(5/\alpha) \frac{\left|\tilde{C}_\perp\right|^2 \left|I_\perp^{(1)}\right|^2}{\mathcal{N}_n} \right\} \, ,$$

where ρ is the constant density in the corona (eq. [5.17]).

164

E.3 Kink modes – isothermal corona with straight, uniform, and vertical magnetic field

For the kink modes, with an isothermal stratified corona permeated by straight, uniform, and vertical magnetic field, the matching coefficients are

$$\lambda_\perp = \frac{c_1 c_5 - c_2 c_6}{c_1 c_4 - c_2 c_3} ,$$

and

$$C_\perp = \tilde{C}_\perp I ,$$

where

$$\tilde{C}_\perp = \frac{c_1 c_6 - c_3 c_5}{c_1 c_4 - c_2 c_3} ,$$

where, for convenience, c_1, c_2, c_3, c_4, c_5, and c_6 are defined as:

$$c_1 = x_3 J_1(x_1) H_\mu^{(1)}(2\nu\sqrt{\epsilon_\perp}) - J_0(x_1) H_{\mu+1}^{(1)}(2\nu\sqrt{\epsilon_\perp}) ,$$

$$c_2 = -\frac{2i}{\pi} x_2 x_3 \left[J_0(x_4) J_1(x_1 x_2) - \left(\frac{C_{A,ch}}{x_2 C_{A,cor}} \right) J_1(x_4) J_0(x_1 x_2) \right] ,$$

$$c_3 = J_0(x_1 x_2) H_\mu^{(1)}(2\nu\sqrt{\epsilon_\perp}) ,$$

$$c_4 = -\frac{2i}{\pi} J_0(x_1) J_0(x_4) + \frac{\pi x_1 c_2}{2x_3} \left(Y_0(x_1) J_0(x_1 x_2) - J_0(x_1) Y_0(x_1 x_2) \right) ,$$

$$c_5 = J_0(x_1) H_{\mu+1}^{(2)}(2\nu\sqrt{\epsilon_\perp}) - x_3 J_1(x_1) H_\mu^{(2)}(2\nu\sqrt{\epsilon_\perp}) ,$$

$$c_6 = -J_0(x_1 x_2) H_\mu^{(2)}(2\nu\sqrt{\epsilon_\perp}) ,$$

where $x_4 = 2\omega H_{cor}/C_{A,cor}$. In this case, the Alfvén waves are totally reflected in the infinite corona. Hence, there is no line width contribution, $\Gamma_{n,\perp}^+(\omega) = 0$.

E.4 Kink modes – homogeneous corona with straight and radial magnetic field

For the kink modes, with a homogeneous (unstratified) corona permeated by straight and radial magnetic field, the matching coefficients are

$$\lambda_\perp = \frac{d_4 d_5 - d_2 d_6}{d_1 d_4 - d_2 d_3},$$

and

$$C_\perp = \tilde{C}_\perp I,$$

where

$$\tilde{C}_\perp = \frac{d_1 d_6 - d_3 d_5}{d_1 d_4 - d_2 d_3},$$

for convenience, d_1, d_2, d_3, d_4, d_5, and d_6 are defined as:

$$d_1 = x_3 J_1(x_1) H_\mu^{(1)}(2\nu\sqrt{\epsilon_\perp}) - J_0(x_1) H_{\mu+1}^{(1)}(2\nu\sqrt{\epsilon_\perp}),$$

$$d_2 = -\frac{2i}{\pi} x_2 x_3 \left[J_1(x_1 x_2) H_{1/6}^{(1)}(x_5) - \left(\frac{C_{A,ch}}{x_2 \omega r_{cor}} \right) J_0(x_1 x_2) \left(2 H_{1/6}^{(1)}(x_5) - 3 x_5 H_{7/6}^{(1)}(x_5) \right) \right],$$

$$d_3 = J_0(x_1 x_2) H_\mu^{(1)}(2\nu\sqrt{\epsilon_\perp}),$$

$$d_4 = -\frac{2i}{\pi} J_0(x_1) H_{1/6}^{(1)}(x_5) + \frac{\pi x_1 d_2}{2 x_3} \left(Y_0(x_1) J_0(x_1 x_2) - J_0(x_1) Y_0(x_1 x_2) \right),$$

$$d_5 = J_0(x_1) H_{\mu+1}^{(2)}(2\nu\sqrt{\epsilon_\perp}) - x_3 J_1(x_1) H_\mu^{(2)}(2\nu\sqrt{\epsilon_\perp}),$$

$$d_6 = -J_0(x_1 x_2) H_\mu^{(2)}(2\nu\sqrt{\epsilon_\perp}),$$

where $x_5 = \omega r_{cor}/3 C_{A,cor}$. The line width contribution from the upward escaping Alfvén waves is

$$\Gamma_{n,\perp}^+(\omega) = \omega f \left\{ \frac{6 z_0 r_{cor} (1 - \cos\theta_m)(m+1)(\beta+1)}{\pi^2 R_0^2} \frac{}{m} \exp(-10/\alpha) \frac{\nu^4}{\kappa_n^2} \frac{\left| \tilde{C}_\perp \right|^2 \left| I_\perp^{(1)} \right|^2}{\mathcal{N}_n} \right\}.$$

Appendix F

Probing Sunspot Magnetic Fields with p-mode Absorption and Phase Shift Data

By P. S. Cally, A. D. Crouch and D. C. Braun

Probing Sunspot Magnetic Fields with p-mode Absorption and Phase Shift Data

P. S. Cally,[1,2] * A. D. Crouch[1]† and D. C. Braun[3]‡

[1] Centre for Stellar and Planetary Astrophysics, School of Mathematical Sciences, Monash University,
Victoria, Australia 3800
[2] High Altitude Observatory, National Center for Atmospheric Research, P.O. Box 3000,
Boulder CO 80307-3000, USA§
[3] NorthWest Research Associates, Inc., Colorado Research Associates Division, 3380 Mitchell Lane,
Boulder CO 80301-5410 USA

8 June 2003

ABSTRACT

Longstanding observations of incoming and outgoing f- and p-modes in annuli around sunspots reveal that the spots partially absorb and substantially shift the phase of waves incident upon them. The commonly favoured absorption mechanism is partial conversion to slow magneto-acoustic waves which disappear into the solar interior channelled by the sunspot's magnetic field. However, up till now, only f-mode absorption could be accounted for quantitatively by this means. Based on vertical magnetic field models, the absorption of p-modes was insufficient. In this paper, we use the new calculations of Crouch & Cally (2003a) for inclined fields, and a simplified model of the interaction between spot interior and exterior. We find excellent agreement with phase shift data assuming field angles from the vertical in excess of 30° and Alfvén/acoustic equipartition depths of around 600-800 km. The absorption of f-modes produced by such models is considerably larger than is observed, but consistent with numerical simulations. On the other hand, p-mode absorption is generally consistent with observed values, up to some moderate frequency dependent on radial order. Thereafter, it too is too large, assuming absorbing regions comparable in size to the inferred phase shifting region. The excess absorption produced by the models is in stark contrast to previous calculations based on vertical magnetic field, and is probably due to finite mode lifetimes and excess emission in acoustic glories. The excellent agreement of phase shift predictions with observational data allows some degree of probing of subsurface field strengths, and opens up the possibility of more accurate inversions using improved models. Most importantly though, we have confirmed that slow mode conversion is a viable, and indeed the likely, cause of the observed absorption and phase shifts.

Key words: Sun: magnetic fields — sunspots — Sun: helioseismology

1 INTRODUCTION

One method of determining how solar oscillations interact with sunspots and other magnetic field concentrations was developed by Braun, Duvall & LaBonte (1987) (see also Bogdan et al 1993; Braun et al. 1992; Braun 1995; Zhang 1997), who observed ingoing and outgoing waves in annuli surrounding spots and plage. This has come to be called Hankel analysis, because of the decomposition into ingoing and outgoing Hankel functions used in most cases. Their unanticipated finding was that sunspots

* E-mail: paul.cally@sci.monash.edu.au
† E-mail: ashley.crouch@maths.monash.edu.au
‡ E-mail: dbraun@cora.nwra.com
§ The National Center for Atmospheric Research is sponsored by the National Science Foundation.

absorb up to half of the incident *p*-mode power at favoured frequencies and horizontal wavenumbers.

More recently, new local helioseismic techniques have been used to probe sunspots and their surroundings. For example, acoustic holography has confirmed the Hankel analysis results (Lindsey & Braun 1999; Braun and Lindsey 2000a; Chou 2000), adding in particular fascinating information about enhanced acoustic emission in regions surrounding sunspots (acoustic glories) (Donea, Lindsey & Braun 2000; Jain & Haber 2002). Acoustic tomography, also known as time-distance helioseismology, has similarly been very successful at imaging subspot regions, (see the well-known "coffee mug" image from the SOHO-9 workshop; Kosovichev, Duvall & Scherrer 2000, Fig. 8). Unlike Hankel analysis, tomography and holography dispense with a modal description altogether in favour of ray or optics formalisms, and are very adept at directly imaging subsurface thermal and flow features. However, despite some progress (Kosovichev & Duvall 1997; Kosovichev, Duvall & Scherrer 2000, 2001), as yet neither holography nor tomography treats magnetic fields entirely satisfactorily. For example, only the fast magnetoacoustic wave is retained in Kosovichev & Duvall (1997), §2.3, and Kosovichev, Duvall & Scherrer (2000), §2.4, and despite the theoretical possibility of disentangling sound and Alfvén speeds, only their sum has so far been reliably measured. (Further questions about the treatment of the acoustic cutoff and Brunt-Väisälä frequencies in the ray approach are discussed by Barnes & Cally 2001).

Indeed, tomography's assumption of a single ray speeding up or slowing down as it meets various features is not appropriate to the mode conversion process commonly envisaged as the cause of wave absorption in sunspots. As first suggested by Spruit (1991) and Spruit & Bogdan (1992), and developed by Cally & Bogdan (1993), Cally, Bogdan & Zweibel (1994), Bogdan & Cally (1997), and Cally (2000), when a *p*-mode encounters magnetic field concentrations characteristic of sunspots, it splits into 'fast' and 'slow' waves which are quite different in nature. Indeed, this coupling is expected to be strongest where the sound speed *c* and Alfvén speed *a* are comparable, in which case the distinction between fast and slow is small. Below this shallow depth though, the sound speed greatly exceeds the Alfvén speed and the two modes decouple. They are then clearly distinguishable: the fast wave is essentially acoustic, and behaves very much like the *p*-mode (it is termed the π-mode by Cally & Bogdan 1993), and the slow mode is nearly transverse, has a wavelength which decreases with depth, and behaves much like an Alfvén wave. This scenario is depicted schematically in Fig. 1.

Although the vertical field model predicts that *f*-modes are substantially absorbed (Cally, Bogdan & Zweibel 1994), *p*-modes of increasing radial order are progressively too weakly affected to account for observations. Based on two dimensional Cartesian simulations, Cally (2000) suggested that spreading
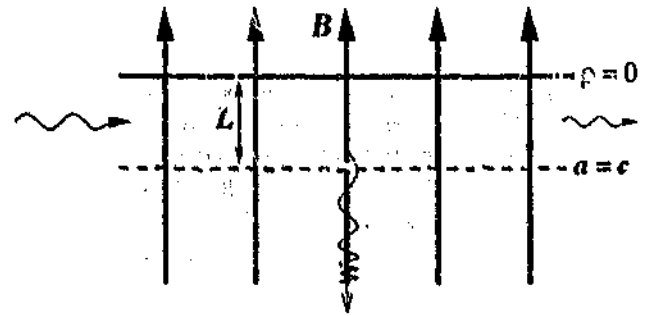

Figure 1. Schematic diagram showing an acoustic wave incident on a vertical magnetic field concentration from the left, and being partially transmitted and partially converted to slow-modes which travel down the magnetic field lines. In reality, there will also be some reflection and scattering. The depth at which the sound and Alfvén speeds coincide is denoted by L. In the simple polytropic model adopted in this paper, the density vanishes at the surface.

magnetic field, as found in sunspots, might be more effective. However, it was unclear whether it was the spreading of the field that had the desired effect, or merely its inclination away from the vertical. To explore this question, Crouch & Cally (2003a) calculated the eigenfunctions and complex eigenvalues of oscillations in an adiabatic polytropic model of index $m_p = 1.5$ (i.e., $\gamma = 5/3$) with uniform inclined magnetic field, and found that indeed substantial enhancements in absorption were found as the field was rotated away from the vertical, with a peak effect at around 30°.

It is the purpose of this paper to explore the extent to which the inclined field results of Crouch & Cally (2003a) can quantitatively explain the Hankel observations. To that end, we shall compare with the absorption and phase shift results presented in Braun (1995), which still represents the highest quality data set of its type. Two sunspot groups, NOAA5254 and NOAA5229 are examined in detail in that reference, each using long data sets collected at the South Pole in 1988 (Braun et al. 1992). The former contains a large nearly circular spot with umbral radius 9 Mm and penumbral radius 18 Mm. The primary spot in NOAA5229 is slightly smaller and less regular. Since the absorption and phase shift results for each are very similar, we shall focus on NOAA5254 here. The annulus used for the Hankel analysis had an inner radius of 30 Mm and an outer radius of 243 Mm. The absorption coefficient α for NOAA5254 is plotted against frequency in Fig. 2, illustrating the points that

(i) α rises from zero at low frequency to a maximum value, and then dips to zero before apparently rising again (see $n = 3$–5 in particular);

(ii) peak absorption diminishes with increasing radial order;

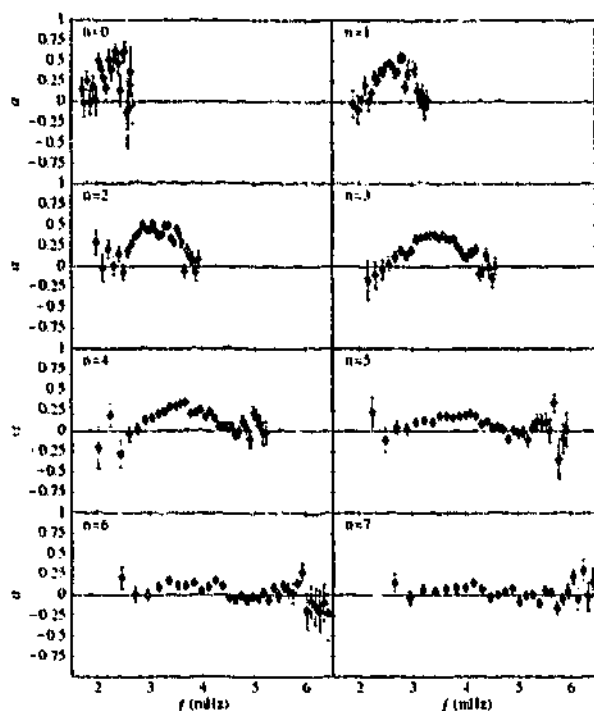(iii) the frequency of the absorption dip is around 5 mHz at larger radial order, but is lower at lower n.

Figure 2. Absorption coefficient α versus frequency for the f- and p-modes in the spot NOAA5254 for different radial order n. The f-mode corresponds to $n = 0$. This figure is a replotting of Fig. 4 of Braun (1995), though against frequency rather than spherical degree ℓ.

Any successful model should reproduce these features.

2 MODEL

Tables resulting from the model of Crouch & Cally (2003a) present the complex eigenvalues κ against real dimensionless frequency ν in a complete adiabatic polytrope of index $m_p = 1.5$ with magnetic inclination angle $\theta = 0°, 5°, 10°, \ldots, 55°$ and p-mode radial index $n = 0, 1, \ldots, 8$ (higher angles are also available, but are not complete in n). Here

$$\nu = \sqrt{\frac{m_p L}{g}}\,\omega \tag{1}$$

where g is the gravitational acceleration, L is the depth at which the sound and Alfvén speeds coincide, and $\kappa = 2kL$ is a dimensionless horizontal wavenumber. In Cartesian geometry, we have assumed an $\exp[i(kx - \omega t)]$ dependence on horizontal position x and time t. Although the eigenvalue tables of Crouch & Cally (2003a) are calculated for a uniform field distribution without bounds, the essence of the model we develop in this paper is to adopt the eigenvalues κ *globally*, i.e., to assume that the damping parameter $Im(\kappa)$ and the local wavenumber $Re(\kappa)$ given by these calculations applies (at least on average) to the spot as a whole, though the field is of course not uniform throughout. (In §3.1 we shall indeed adopt a single value of inclination angle θ and equipartition depth L to be representative of the whole spot, but in §3.2 we relax this by

allowing for a nested set of piecewise uniform shells. Experience with a 2D numerical code (Cally 2000) indicates that absorption and phase shifting are localized over a shallow depth of less than about 1 Mm beneath the spot, and so variation of θ with depth is not important.)

For vertical field, the same equations (and solutions) as are addressed in Cally & Bogdan (1993) and Cally, Bogdan & Zweibel (1994) also result from a cylindrical decomposition in which the three components of velocity take the form (Scheuer & Thomas 1981)

$$u_r = U(z)\left[kZ_{m+1}(kr) - \frac{m}{r}Z_m(kr)\right] \tag{2}$$
$$\times \exp[i(m\vartheta - \omega t)]$$
$$u_\vartheta = -imU(z)\frac{Z_m(kr)}{r}\exp[i(m\vartheta - \omega t)] \tag{3}$$
$$u_z = -ikV(z)Z_m(kr)\exp[i(m\vartheta - \omega t)],$$

where Z represents a Bessel function or linear combination of them $(J, Y,$ or the Hankel functions $H^{(1,2)})$ as appropriate.

In Cartesian geometry, it is assumed that the inclination θ of the uniform magnetic field lies in the x-z plane (the 'fourth-order' problem, because the Alfvén wave decouples in this case leaving a fourth-order system of governing differential equations). Extension to full three-dimensionality (the 'sixth-order' problem), where B makes an angle ϕ with this plane, reveals that the dependence of κ on ϕ is generally weak compared to that on θ (Crouch & Cally 2003b), and we shall ignore it in the simple model presented here. To illustrate the point, Fig. 3 shows the real and imaginary parts of the eigenvalue κ against dimensionless frequency ν for the case $\theta = 30°$ (where . . tion is approximately maximal) and various values of ϕ. It turns out that we are mainly interested in the behaviour for $\nu \lesssim 3$, where indeed ϕ makes little difference, apart from the case of $Re(\kappa)$ for the p_1-mode $(\phi = 45°)$ and the f-mode $(\phi = 90°)$. Since the observational data for f-mode phase shifts is too noisy to be useful, this $Re(\kappa)$ dependence on ϕ does not affect any comparisons we shall make involving the fundamental mode. It may have more effect on p_1 at intermediate ϕ though.

The cylindrical geometry analogue strictly would be a straight-field conical structure (Cally 1983), where θ increases linearly with r, and with only radial $(m = 0)$ oscillations in the 2D case. However, in the spirit of exploration, (and since this is a very difficult problem to solve), we assume a uniform θ throughout the magnetic region, or piecewise uniform in cylindrical shells, and simply adopt the κ eigenvalues from Crouch & Cally (2003a). The essential idea is that κ is a global property of a cylindrical spot, to be read from tables, under the assumption that eqns.(4) are valid. The magnetic field plays no other role than to supply these κ.

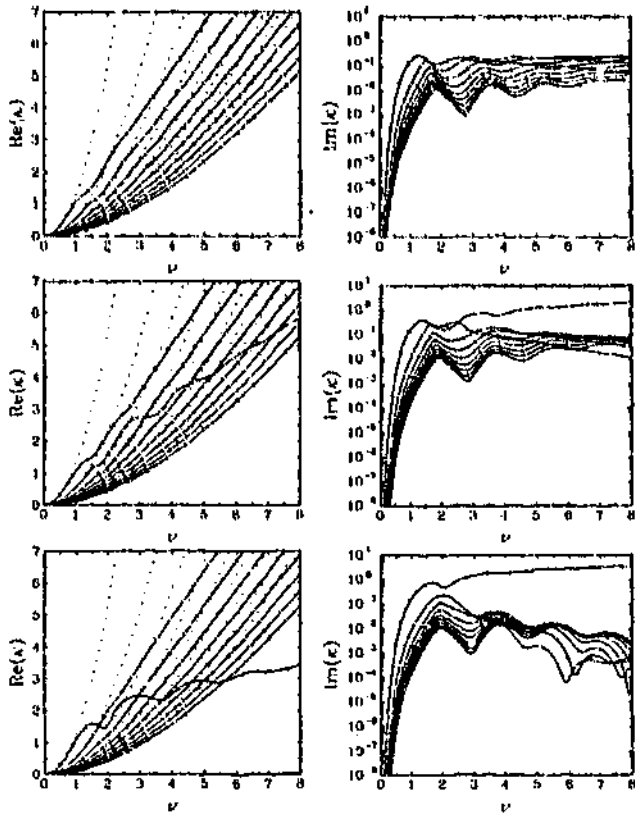In the inner shell, Z_m must be the J_m Bessel function for the solution to be bounded at $r = 0$,

Figure 3. The real (left panels) and imaginary (right panels) parts of the eigenvalues κ against nondimensional frequency ν for the complete $m_p = 1.5$ adiabatic polytrope with uniform magnetic field at angle $\theta = 30°$ and $\phi = 0°$ (top panels), $\phi = 45°$ (middle panels), and $\phi = 90°$ (bottom panels). In the left panels, the dashed lines represent the nonmagnetic case, and correspond to the $f, p_1, \ldots, p_8$ modes respectively, from left to right.

whilst in the outer non-magnetic region, it is a linear combination

$$Z_m(kr) = AH_m^{(1)}(kr) + H_m^{(2)}(kr)$$

corresponding to outgoing and incoming waves respectively. An arbitrary normalization has been applied in which the amplitude of the incoming wave is unity. In any intervening shells, Z_m is an arbitrary combination of J_m and Y_m. Each shell has its own complex k, read from tables. The total pressure and the radial velocity is matched across each shell boundary $r = R_i$, $(0 < R_1 < \ldots < R_N = R)$, i.e., $Z_m(kr)$ and $dZ_m(kr)/dr$ respectively. This allows all the coefficients in the Bessel linear combinations to be determined. Then, from A, we calculate the absorption coefficient α and phase shift δ using

$$\alpha = 1 - |A|^2, \qquad \delta = -\arg(A). \qquad (4)$$

An advance in phase ($\delta > 0$) represents an *increase* in phase speed through the spot. Note that if the internal wavenumber k is the same as that in the external region, k_0 (real), then $A = 1$ and $\alpha = \delta = 0$ as expected.

Limitations of the model are

(i) the magnetic field geometry has been simplified to be piecewise uniform;

(ii) magnetic field variation with depth is not included;

(iii) dependence of κ on the angle ϕ is ignored;

(iv) scattering across radial order n has been neglected (see the discussions in Braun 1995; Barnes & Cally 2000);

(v) the acoustic jacket has been ignored (Bogdan & Cally 1995; Barnes & Cally 2000);

(vi) an $m_p = 1.5$ planar polytrope has been used to calculate the complex κ, though we partially correct for it through the p-mode ridge adjustment procedure discussed later in this section;

(vii) the difference in thermal structure inside and outside the spot has not been explicitly included;

(viii) damping of acoustic emission in sunspots, and enhanced emission in acoustic glories surrounding them, are ignored;

(ix) flows are neglected;

(x) no overlying atmosphere has been included.

Experience with (Cartesian) numerical simulations suggests that none of these is fatal. To some extent, the proof of the pudding will be in the eating; despite these limitations, can Braun's observational Hankel data be adequately matched using the model?

Several of these points warrant further discussion. Regarding Point (ii), our only measure of magnetic field strength is L, the depth in *uniform* field at which $a = c$ (see Fig. 4). In reality, we expect the magnetic field to concentrate with depth. The effect of this is that the best fit to phase shift δ and absorption coefficient α may not occur for the same L and shell radius R. The reason is that phase speed of p or π modes is determined predominantly at the immediate subsurface layers (where the sound speed is lowest), whereas absorption (conversion to slow modes) occurs somewhat lower, presumably around L. Consequently, the magnetic field strength that δ and α 'see' may well be different. Compounding this difference is the observational result from Hankel analysis (Braun 1995) that plage absorbs but does not scatter p-modes,[1] suggesting that the absorbing region may extend beyond the scattering region. This point is addressed further in §3.2.

Points (iv) and (v) are related. Because the vertical dependences of the internal and external eigenfunctions $U(z)$ and $W(z)$ are not identical, there must in reality be some degree of scattering across p-mode ridges. Our model neglects this, and by matching both u_r and total pressure, actually allows for reflection and transmission at $r = R$. When the eigenfunction mismatch is taken into account though, it turns out that it is not possible to match the interior and exterior oscillations using just the discrete sets of f- and p-modes of the given frequency in both regions. Bogdan & Cally (1995) show that a continuous spectrum of horizontally evanescent 'jacket modes' must also be invoked. These supply the 'glue' necessary to perfect the match.

---

[1] However, holgraphy suggests otherwise (Braun and Lindsey 2000b). The reason for the discrepancy is unclear.
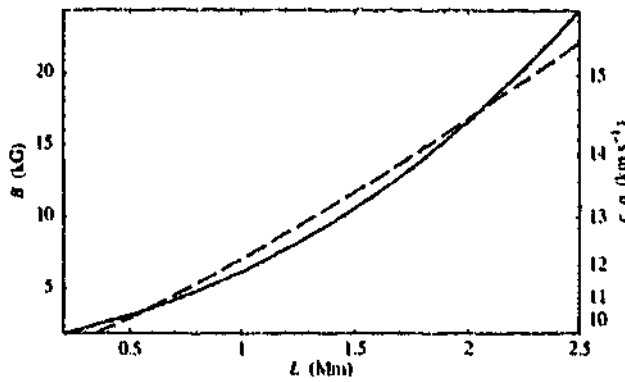
Figure 4. Magnetic field strength B against equipartition depth L for a uniform field in (i) full curve: the realistic solar model fgong.l5bi.d.15 from the Aarhus adiabatic pulsation package (Christensen-Dalsgaard 1997), and (ii) dashed curve: a complete adiabatic polytrope of index $m_p = 1.5$, assuming a density at 1 Mm taken from the Aarhus model. The right hand axis shows the sound and Alfvén speeds at this equipartition depth in the Aarhus model only.

Point (x) is probably unimportant below the chromospheric acoustic cutoff frequency (~ 5 mHz), but above it a more sophisticated model should allow waves to disappear upwards as well as downwards (Cally, Bogdan & Zweibel 1994).

For the single shell model, assuming $k_0 R \gg 1$ and $\Delta k = Re(k) - k_0 \ll R^{-1}$, where k_0 is the (real) wavenumber in the outer nonmagnetic region and k that inside the spot corresponding to the same frequency and p-mode ridge, the boundary matching yields

$$\delta \approx -2 \, Re(\Delta k) \, R \,. \tag{5}$$

For the adiabatic polytrope for example,

$$k_0 = m_p \omega^2 / (2n + m_p) g \,. \tag{6}$$

From the inclined field eigenvalues (see Crouch & Cally 2003a, Figs. 1a, 2a, 7a, and 8a), $Re(\Delta k)$ is nearly always negative, though for $\theta < 30°$ it can be slightly positive at low frequency. So $\delta > 0$, and it initially grows linearly with $Re(\Delta k)$ as frequency increases. Since k_0 increases quadratically with frequency $f = 2\pi\omega$ whilst $Re(k)$ increases only linearly, we expect a superlinear increase in δ with f. This is consistent with the Hankel data (Braun 1995). Equation (5) is also consistent with our basic understanding that an increased phase speed in the spot (decreased wavenumber) gives rise to a positive phase shift when it reemerges. Figure 3 shows the Crouch & Cally (2003a) eigenvalues for $\theta = 30°$, showing that indeed $Re(\Delta k)$ is negative.

However, there is a complication arising from Point (vi) above. Although the polytropic index has little effect on the calculated eigenvalues (see Hunter 1999, for the vertical field case), giving some reassurance about the applicability of the Crouch & Cally (2003a) model to the real sun, it does noticeably affect the location of the p-mode ridges in the f-ℓ plane. If we apply eqn. (6) for a given frequency $f = 2\pi\omega$, there results a considerable distortion in

f. Instead, we proceed as follows: to calculate the model α and δ for a given frequency f, p-mode ridge n, and equipartition depth L, we first determine the corresponding ℓ from the real quiet sun f-ℓ curves, and hence calculate $k_0 = \sqrt{\ell(\ell+1)}/R_\odot$. Then we apply eqn. (6) to find the "polytrope-effective" frequency, and thence ν through eqn. (1). The Crouch & Cally tables are then consulted to find κ. In this way, we compensate for the discrepancy between ridge positions. Our preference for ℓ rather than f as the fundamental quantity allows us to more accurately compare the frequency dependence of α and δ with observations. If we do not apply the correction, similar results are obtained, though for larger L.

3 RESULTS

3.1 Single Shell Models

The radius of the scattering region is most directly probed using a range of azimuthal degree m. The impact parameter $m R_\odot / \sqrt{\ell(\ell+1)}$ is a measure of how directly or glancingly the wave meets the spot. As this approaches the radius of the scattering region, we expect δ to drop towards zero.

To reduce error, Braun (1995) combined phase shift and absorption results into bins in ℓ centered on $\ell = 61, 82, 102, 123, 144, 164, 185, 205, 226, 246, 267, 288, 308, 329, 349, 370, 390, 411, 432, 452, 473, 493, 514, 534, 555, 576, 596, 617, 637, 658, 678, 699,$ and 720. The quality of the data varies considerably across this range, with perhaps the best results at around $\ell = 288$, corresponding to a horizontal wavelength of 15.2 Mm. Figure 5 displays the predicted phase shifts at $\ell = 288$ for a single shell model with $L = 0.8$ Mm, $R = 27.5$ Mm, and field inclination $\theta = 30°$. The comparison with the NOAA5254 data is impressive. Neighbouring values of L (0.6 Mm and 1 Mm) and R (20 Mm and 35 Mm) produce noticeably inferior fits, with $25 \lesssim R \lesssim 30$ Mm being best (c.f., Fan, Braun & Chou 1995). For the most part, we shall fix on $R = 27.5$ Mm from now on.

Models with inclination angles θ below $30°$ yield very poor results because of the negative phase shifts they produce at some frequencies (see the discussion associated with eqn. (5)). On the other hand, the fit degrades comparatively slowly with increasing θ above $30°$ (see Fig. 6). Though $\theta = 30°$ is clearly best, $40°$ may be judged acceptable. Of course, a real sunspot has a wide range of field inclinations, and attempting to model this with a single θ is bound to introduce inaccuracies.

Dependence on ℓ is addressed in Figs. 7 and 8, with $\ell = 205$ and 411 respectively. At the lower ℓ, the fit is still quite good, and in particular the decrease in δ with decreasing ℓ is well modelled. At the larger ℓ, the errors in the observational data are much larger, leaving very few 'reliable' points. There also appears to be more scatter, most notably at $n = 2$, which may reflect the highly spiky behaviour seen in the model curve, or may simply indicate that
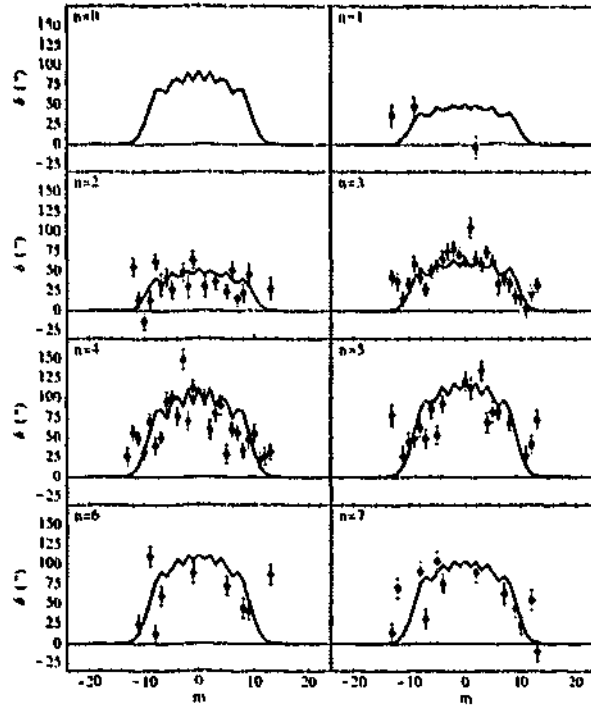
Figure 5. The predicted phase shifts δ (degrees) against angular degree m for a single-shell sunspot model with $L = 0.8$ Mm, $R = 27.5$ Mm, and $\theta = 30°$ at $\ell = 288$ (full curves), for the f-mode ($n = 0$) and first seven p-modes. The points with 1σ error bars represent the Hankel analysis results (binned in ℓ about 288) for the dominant sunspot in the group NOAA5254 (Braun 1995). Only points with error bars below $30°$ are shown.
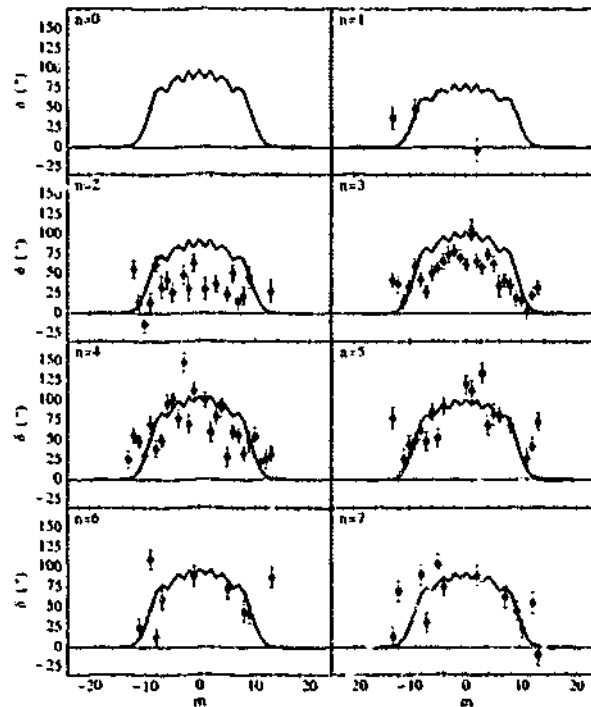

Figure 6. Same as Fig. 5, but for $\theta = 40°$. The fit for $n = 2$ and 3 is clearly inferior.
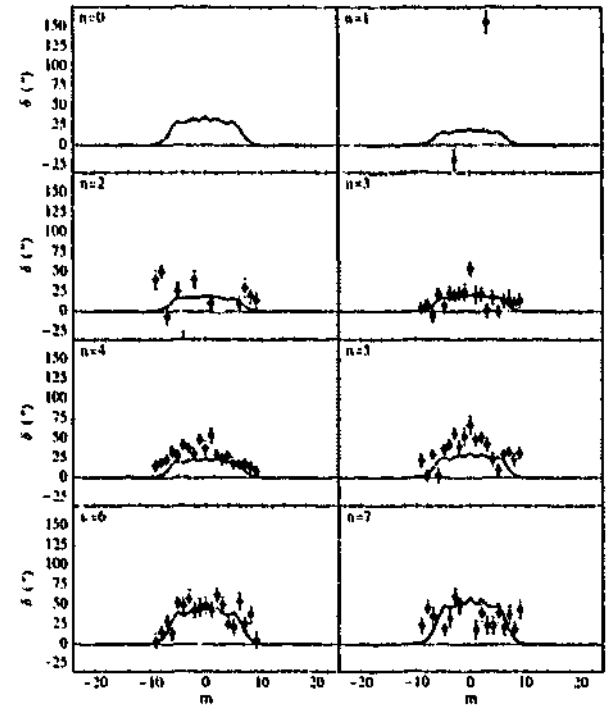
Figure 7. Same as Fig. 5, but for $\ell = 205$.
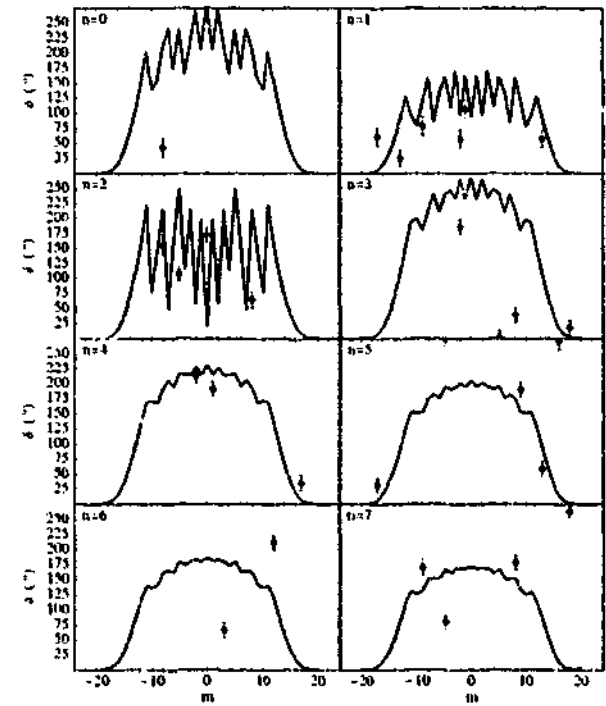
Figure 8. Same as Fig. 5, but for $\ell = 411$. However, all phases have been shifted into the interval $(0°, 360°)$ in this case to avoid jumps when the model δ passes through $180°$.

the data is highly unreliable. On the other hand, these higher ℓ modes may be scattering off smaller scale features in the spot.

Whereas modelling δ against m is fit best with $L \approx 0.8$ Mm, fits of axisymmetric modes against frequency are optimized for somewhat smaller equipartition depths (and slightly larger θ, though this is less significant). Figure 9 depicts phase shift ver-
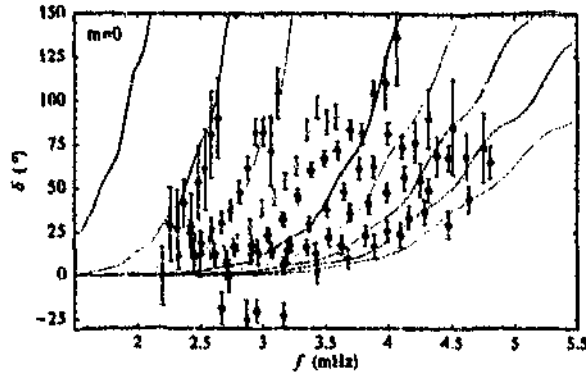
Figure 9. Phase shift δ (curve) as a function of frequency for the single shell model with $L = 0.58$ Mm, $R = 27.5$ Mm, $\theta = 35°$, and for axisymmetric oscillations ($m = 0$). The black curve corresponds to the f-mode, cyan to the p_1-mode, etc. The plotted points of the corresponding colours are the m-averaged values for NOAA5254 (Braun 1995), with only those points plotted which have estimated error bounds $\sigma_\delta \leqslant 30°$. There are no f-mode points of this accuracy. Given the selected values of θ and R, the chosen L represents the least squares best fit to the NOAA5254 phase shift data for p-modes $n = 1, \ldots, 8$.

sus frequency for $m = 0$ and the model $L = 0.58$ Mm, $R = 27.5$ Mm, $\theta = 35°$, compared with the m-averaged δ for NOAA5254. As discussed in Braun (1995), δ is averaged over a small range of m about 0 in order to reduce errors and scatter. The m range varies, but is chosen so as to not intrude far into the 'shoulders' seen in previous figures. Given the limitations of the model discussed earlier, the qualitative agreement in behaviour is pleasing. Better agreement with individual p-mode ridges can be obtained by slightly varying parameters; e.g., reducing L to 0.55 Mm brings the p_1 ridge into almost perfect agreement, though at the expense of the accuracy of the $n \gtrsim 4$ curves. On the other hand, raising L to 0.8 Mm as in previous figures produces comparatively poor results for lower n. Specifically, the ridges are shifted too far to the left (recall that frequency scales as $L^{-1/2}$), though their slopes remain approximately correct. This is clearly a residual effect of the mis-positioning of the p-mode ridges by the polytropic model. It is anticipated that moving to a model based on realistic solar structure instead of a polytrope would improve the match significantly.

Previous attempts to model p-mode absorption in sunspots based on slow-mode conversion and vertical magnetic fields have foundered on the seeming impossibility of obtaining sufficient absorption beyond the f- and perhaps p_1-modes. However, with inclined field, absorption is ample! Figure 10 shows α as a function of m for the case $L = 0.8$ Mm, $R = 27.5$ Mm, $\theta = 40°$. Plotting α as a function of frequency (Fig. 11) reveals a similar picture. Correspondence of the model curves with the dip at 5 mHz may be improved by increasing L (see Fig. 12).

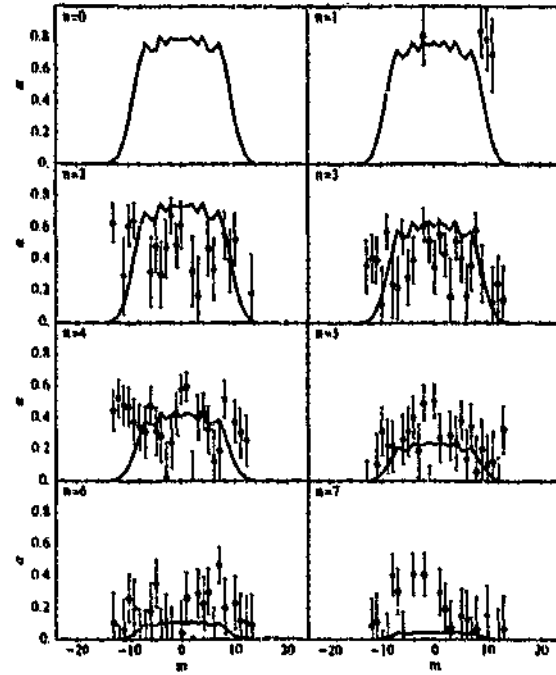Several points should be made about Figs. 11 and 12. First, there is a minimum in α correspond-

Figure 10. Absorption coefficient α versus azimuthal order m for various radial orders n for the model $L = 0.8$ Mm, $R = 27.5$ Mm, $\theta = 40°$, and waves with $\ell = 288$.
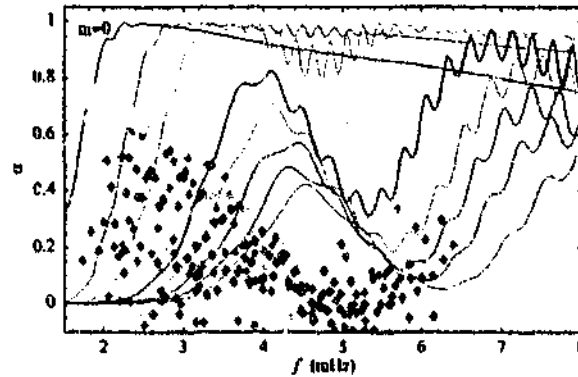

Figure 11. Absorption coefficient α versus frequency for the case of Fig. 9. Again the comparison is with m-averaged Hankel data. Error bars have been suppressed in the interests of clarity, but only those points with $\sigma_\alpha < 0.15$ have been retained.
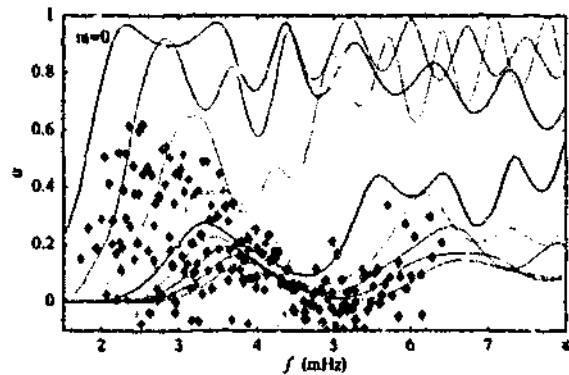

Figure 12. Absorption coefficient α versus frequency for $\theta = 35°$, $L = 0.85$ Mm, and $R = 9$ Mm.

ing to the first dip in the $Im(\kappa)$ curves (see Fig. 3). Although this dip does not extend to zero for $\theta \neq 0$ as it does in the vertical field case (Cally, Bogdan & Zweibel 1994), it is nonetheless substantial (note the logarithmic scale in the figure). At these frequencies, the coupling of fast and slow modes is weak, especially at high radial order. Since $f \propto \nu/\sqrt{L}$, the dip may be moved around in frequency by varying L. If it is believed that the dip in absorption in the Hankel data is actually due to this effect, this gives us a means of fixing L. This is how L was chosen for Fig. 12. Indeed, the tendency for the dip to occur at lower frequency for low radial orders n (most clearly seen in Fig. 2) is matched here.

However, evidence from acoustic holography suggests that the 5 mHz dip may instead be due to an enhancement of emission in this frequency band in a region (the acoustic glory) surrounding the spot (Donea, Lindsey & Braun 2000; Jain & Haber 2002). Nevertheless, the correspondence between the 5 mHz dip and the $Im(\kappa)$ dip at just about the right L seems too great a coincidence to ignore, and we might be lead to believe that both mechanisms are at work here.

Even with the $Im(\kappa)$ dip though, the absorption produced by the model at higher frequencies and low radial order is far too great. A much smaller absorbing radius R can partially rectify this (see Fig. 12), though the discrepancy at low n and large f is still problematic. Cally, Bogdan & Zweibel (1994) argued, in the case of the f-mode, that dissipative mechanisms operate at these frequencies (associated with interaction between the wave and convection) which cause high frequency modes to be local rather than global in nature. The 'memory' of the nearby absorbing spot is therefore rapidly dissipated. The presence of the acoustic glory only amplifies this effect. These mechanisms are not easily modelled at the fundamental level, but reasonable *ad hoc* prescriptions appear capable of substantially reducing the excess absorption. Another possible cause is our neglect of the dependence of $Im(\kappa)$ on the angle ϕ at which the waves meets the vertical plane containing the magnetic field vector B. Although as mentioned earlier, our model assumes no dependence on ϕ, in reality $Im(\kappa)$ does noticeably decrease with frequency for p-modes in field with $\theta \approx 30°$ and $\phi \approx 90°$, contrary to its behaviour at $\phi = 0°$ (Fig. 3).

A final possible reason for the excess absorption in the modes, and possibly the most important one, is that absorption peaks rather sharply around $\theta = 30°$ in the Crouch & Cally (2003a) results (see Fig. 9 of that paper, noting the logarithmic scale), whereas phase shift (i.e., $Re(\kappa)$) varies more gradually. Consequently, whilst an average phase shift associated with $\theta \approx 30°$ does a good job of representing the whole spot, applying this angle everywhere substantially overestimates absorption, which in reality occurs predominantly in regions with that field inclination. This would explain why the absorption vs. frequency curves are too high for parameters

optimized to fit phase shift data, despite having the right general shape.

The oscillations particularly evident in the $p_1, \ldots, p_4$ curves in Fig. 11 are due to leaky resonances in the spot, i.e., partial reflections at $r = R$. Since real sunspots may not have such sharp boundaries, this effect may be smeared in practice.

3.2 Multiple Shell Models

The impact parameter shoulder in the α versus m Hankel data (Fig. 10) is far less clear than it is in δ. This suggests that the absorbing region is actually more extended in radius than is the phase shift region. This is consistent with the result that plage produces a measurable absorption but effectively no phase shift in the Hankel data (Braun 1995). Consequently, we might expect the diffuse magnetic elements surrounding sunspots to continue absorbing beyond the scattering region.

The tendency for δ to be negative for low frequencies when $\theta < 30°$, mentioned in §2, suggests that the umbral core, where the field is presumably close to vertical, should show up as a dip in the δ vs. m graphs at low impact parameter, i.e., low m. Although there is some hint of this in the observational Hankel data for individual m, the scatter makes it unclear whether the effect is really there. Similar comments can be made about α, since it too is greatly reduced in vertical field.

On the one hand, the lack of a shoulder in the α vs. m Hankel data suggests that the absorbing region is large, but on the other, α vs. frequency graphs (Fig. 12) produce best results for R small! Seemingly, one way around this conundrum is to suppose that absorption occurs predominantly in a comparatively thin shell at large radius, thereby presenting a wide target to incoming waves whilst at the same time not absorbing them too much. Alternatively, acoustic glories and finite mode lifetime effects may bring the absorption graphs into line with observations without the need to reduce R.

With that point in mind, Fig. 13 displays δ for $\ell = 288$ and a five shell model consisting of a range of L and θ values. The dips created by the 'umbra' are evident in the model curves. Unfortunately, the quality of the Hankel data is insufficient to usefully probe the umbra in this way. Nevertheless, this somewhat arbitrary model indicates some of the features of a multishell scenario. Figures 13–16 further illustrate the character of this particular five shell model. Overall, it yields a good fit to the phase shift data, and at least a qualitatively correct fit to the absorption data, though as usual α is a little too high and the α shoulder too narrow in m. It would seem that the NOAA5254 spot's absorbing area exceeds 35 Mm, which takes it well into the Hankel annulus.
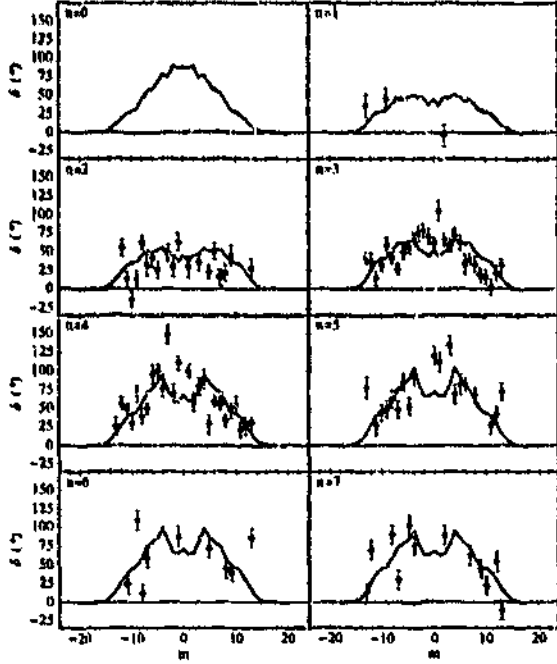
Figure 13. Phase shift δ versus azimuthal order m for various radial orders n for the multishell model $L = \{1,1,0.8,0.6,0.4\}$ Mm, $R = \{6,9,18,25,35\}$ Mm, and $\theta = \{0°,20°,30°,40°,55°\}$, and waves with degree $\ell = 288$.

4 CONCLUSIONS

In this paper, we have explored the consequences of modelling sunspot absorption and phase shift in a crude way using the tabulated eigenvalues of Crouch & Cally (2003a). Overall, given the simplifications made, the correspondence between observational Hankel data and the models is very impressive, especially for δ. Indeed, it is remarkable that the phase shift data can be fitted so well using just magnetic effects, without including internal/external thermal differences. From tomographical inversions, Kosovichev, Duvall & Scherrer (2000) report a typical 0.3–1 km s^{-1} increase in ray-speed in a region as broad as the surface spot and some 10 Mm deep beneath it. As a comparison, the quiet sun sound speed is around 20 km s^{-1} at 4 Mm deep, and 37 km s^{-1} at 10 Mm. They cannot distinguish between sound and fast mode speed, but estimate that it would correspond to a field strength of 18 kG if the increase were entirely magnetic. Given the total sunspot surface magnetic flux though, an 18 kG field at these depths should not fill such a broad region, so we may assume the effect is mostly thermal. But also, judging from their Fig. 8, there is a wave speed *decrease* in the first 2–3 Mm beneath the spot. This is difficult to reconcile with the positive phase shifts found by Hankel analysis, though without more detailed data than can be read from their figure, it is hard to be definitive about this. In any case, we tentatively conclude from our excellent agreement with the Hankel data that the effect on p-mode speeds is predominantly due to magnetoa-
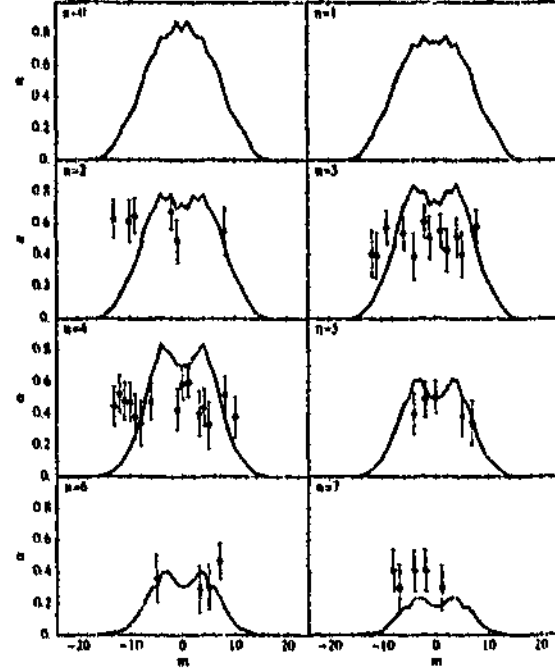
Figure 14. Absorption coefficient α versus azimuthal order m for the five shell model of Fig. 13, again with $\ell = 288$.
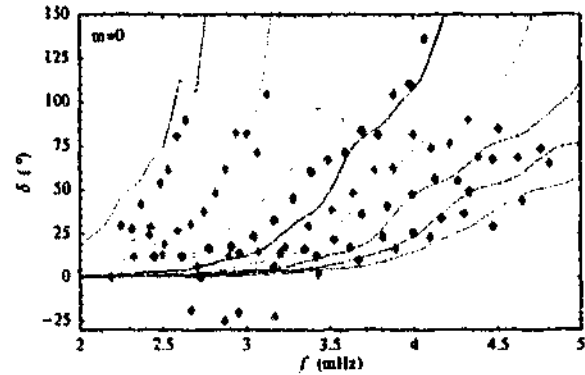

Figure 15. Phase shift δ versus frequency for the five shell model of Fig. 13.
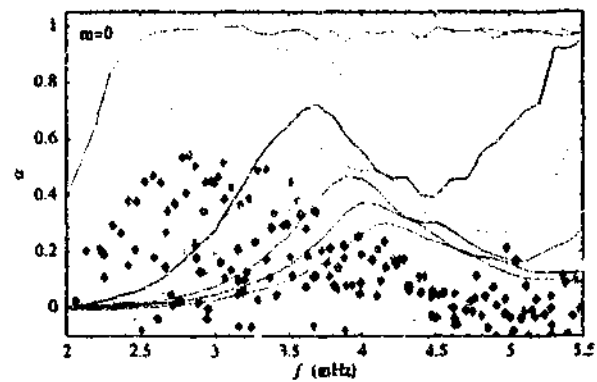

Figure 16. Absorption coefficient α versus frequency for the five shell model of Fig. 13.

coustic coupling at shallow depths (less than 1 Mm) rather than deep thermal perturbations.

Absorption α in our models is consistently somewhat high for values of the parameters L, θ, and R which produce good phase shift fits, though qualitative behaviour is a good match. The discrepancy could be due to several causes, most notably

- inappropriately applying a $\theta \approx 30°$ model, for which absorption is strongly peaked, everywhere in the spot;
- the neglect of convective mode dissipation, depressed acoustic emission inside spots, and enhanced acoustic emission surrounding spots;
- due to sunspot field not being uniform as in the model, the effective magnetic field strength at depths where phase shifting and absorption happen may be quite different, meaning that different parameters may be required in modelling each of the two effects.

Typically, good results are obtained with equipartition depth L between 600 and 800 km roughly, corresponding to Alfvén and sound speeds at $z = -L$ of around 10-11 km s^{-1}, or magnetic field strengths of 3.6-4.8 kG. These are very reasonable numbers.

Indeed, overall, we have been very successful in addressing the list of points to explain set out at the end of §1, as well as others relating to variation with m. However, the polytropic model adopted here is too crude to warrant detailed comparisons with a view to quantitative inversions. It particularly affects the horizontal positioning of curves representing α or δ against frequency. It would be useful to recalculate the Crouch & Cally tables for a realistic solar model, and reapply the procedures developed here to them. However, this is not trivial. Although the eigenvalue differential equations are solved numerically using a shooting method, the eigenvalues rely crucially on the analytic asymptotic solution of the equations for large depth and to high order. This is done using a dominant balance method (which incidentally relies on $4m_p$ being an integer), and it is not clear how to carry this over to a general (tabulated) model. In practice, replacing the solar model by a polytrope below some depth is probably the best way to proceed. Even with a realistic solar model though, the neglect of field strength variation with depth, and thermal differences inside the spot, could preclude exact comparison. Unfortunately, the task of calculating eigenvalues for more complex magnetic geometries is mathematically extremely difficult.

Perhaps the most pertinent lesson to be drawn from our results is that slow mode conversion does indeed seem to be the predominant mechanism responsible for the observed absorption and phase shifts. And in particular, inclined magnetic field is necessary to make the process work.

REFERENCES

Barnes G., Cally P. S., 2000, Solar Phys., 193, 373
Barnes G., Cally P. S., 2000, PASA, 18, 243
Bogdan T. J., Brown T. M., Lites B. W., Thomas J. H., 1993, ApJ, 406, 723
Bogdan T. J., Cally P. S., 1995, ApJ, 453, 919
Bogdan T. J., Cally P. S., 1997, Proc. Roy. Soc. London Ser. A, 453, 943
Braun D. C., 1995, ApJ, 451, 859
Braun D. C., Duvall T. L., LaBonte B. J, 1987, ApJ, 319, L27
Braun D. C., Duvall T. L., LaBonte B. J., Jefferies S. M., Harvey J. W., Pomerantz M. A., 1992, ApJ, 391, L113
Braun D. C., Lindsey, C., 2000a, Solar Phys., 192, 285
Braun D. C., Lindsey, C., 2000b, Solar Phys., 192, 307
Cally P. S., 1983, Solar Phys., 88, 77
Cally P. S., 2000, Solar Phys., 192, 395
Cally P. S., Bogdan T. J., 1993, ApJ, 402, 732
Cally P. S., Bogdan T. J, Zweibel E. G., 1994, ApJ, 437, 505
Crouch A. D., Cally P. S., 2003a, Solar Phys., in press
Crouch A. D., Cally P. S., 2003b, Solar Phys., in preparation
Chou D.-Y., Solar Phys., 192, 241
Christensen-Dalsgaard J., 1997, Aarhus adiabatic pulsation package, http://www.obs.aau.dk/~jcd/adipack.n/
Donea A.-C., Lindsey C., Braun D. C., 2000, Solar Phys., 192, 321
Fan Y., Braun D. C., Chou D.-Y., 1995, ApJ, 451, 877
Hunter I. P., 1999, PhD thesis, Monash University
Jain R., Haber D., 2002, A&A, 387, 1092
Kosovichev A. G., Duvall T. L., Jr., 1997, in Astrophys. Sp. Sci Lib., 225, SCORe'96: Solar Convection and Oscillations and their Relationship, eds J. Christensen-Dalsgaard, F. Pijpers, (Dordrecht: Kluwer), 241
Kosovichev A. G., Duvall T. L., Jr., Scherrer P. H., 2000, Solar Phys., 192, 159
Kosovichev A. G., Duvall T. L., Jr., Scherrer P. H., 2001, in ASP Conference Series, 248, Magnetic Fields across the Hertsprung-Russell Diagram, eds G. Mathys, S. K. Solanki, D. T. Wickramasinghe, 139
Lindsey C., Braun D. C., 1999, ApJ, 510, 494

Scheuer M. A., Thomas J. H., 1981, Solar Phys., 71, 21

Spruit H. C., 1991, in Lecture Notes in Physics, Vol. 388, Challenges to Theories of the Structure of Moderate Mass Stars, eds J. Toomre, D. O. Gough, (Berlin: Springer), 121

Spruit H. C., Bogdan, T. J., 1992, ApJ, 391, L109

Zhang H., 1997, ApJ, 479, 1012

Bibliography

Abdelatif, T. E., Lites, B. W., and Thomas, J. H.: 1986, *Astrophys. J.* **311**, 1015

Abdelatif, T. E. and Thomas, J. H.: 1987, *Astrophys. J.* **320**, 884

Abramowitz, M. and Stegun, I. A.: 1964, *Handbook of Mathematical Functions*, Dover, New York

Adam, J. A.: 1977, *Solar Phys.* **52**, 293

Au, C. -H., Musielak, Z. E., Moore, R. L., and Suess, S. T.: 1989, *Astrophys. J.* **345**, 597

Antia, H. M. and Chitre, S. M.: 1979, *Solar Phys.* **63**, 67

Bachmann, K. T. and Brown, T. M.: 1993, *Astrophys. J.* **411**, L45

Banerjee, D., Hasan, S. S., and Christensen-Dalsgaard, J.: 1995, *Astrophys. J.* **451**, 825

Banerjee, D., Hasan, S. S., and Christensen-Dalsgaard, J.: 1997, *Solar Phys.* **172**, 53

Banerjee, D., O'Shea, E., Goossens, M., Doyle, J. G., and Poedts, S.: 2002, *Astron. Astrophys.* **395**, 263

Barnes, G. and Cally, P. S.: 2000, *Solar Phys.* **193**, 373

Barnes, G. and Cally, P. S.: 2001, *Pub. Astron. Soc. Aust.* **18**, 243

Beckers, J. M. and Schultz, R. B.: 1972, *Solar Phys.* **27**, 61

Beckers, J. M. and Tallant, P. E.: 1969, *Solar Phys.* **7**, 351

Bel, N. and Leroy, B.: 1981, *Astron. Astrophys.* **104**, 203

Bender, C. M. and Orszag, S. A.: 1978, *Advanced Mathematical Methods for Scientists and Engineers*, McGraw-Hill, New York

Bhatnagar, A. and Tanaka, K.: 1972, *Solar Phys.* **24**, 87

Bhatnagar, A., Livingston, W. C., and Harvey, J. W.: 1972, *Solar Phys.* **27**, 80

Birch, A. C., Kosovichev, A. G., Spiegel, E. A., and Tao, L.: 2001, *Solar Phys.* **199**, 291

Birout, D., Goossens, M., Cousens, A., and Mestel, L.: 1982, *Monthly Notices Royal Astron. Soc.* **201**, 619

Bogdan, T. J.: 1987a, *Astrophys. J.* **318**, 888

Bogdan, T. J.: 1987b, *Astrophys. J.* **318**, 896

Bogdan, T. J.: 1989, *Astrophys. J.* **345**, 1042

Bogdan, T. J.: 1992, in J. H. Thomas and N. O. Wiess (eds.), NATO ASIC, Proc. 375, *Sunspots: Theory and Observations*, Kluwer, Dordrecht, p. 345

Bogdan, T. J.: 1997, *Astrophys. J.* **477**, 475

Bogdan, T. J.: 1999, *Astrophys. J.* **512**, 471

Bogdan, T. J.: 2000, *Solar Phys.* **192**, 373

Bogdan, T. J. and Braun, D. C.: 1995, in J. T. Hoeksema, V. Domingo, B. Fleck, and B. Battrick (eds.), Proc. 4th SOHO Workshop, *Helioseismology*, (ESA SP-376), p. 31

Bogdan, T. J. and Cally, P. S.: 1995, *Astrophys. J.* **453**, 919

Bogdan, T. J. and Cally, P. S.: 1997, *Proc. R. Soc. London* **A453**, 943 (BC97)

Bogdan, T. J. and Cattaneo, F.: 1989, *Astrophys. J.* **342**, 545

Bogdan, T. J. and Fox, D. C.: 1991, *Astrophys. J.* **379**, 758

Bogdan, T. J. and Zweibel, E. G.: 1985, *Astrophys. J.* **298**, 867

Bogdan, T. J. and Zweibel, E. G.: 1987, *Astrophys. J.* **312**, 444

Bogdan, T. J., Brown, T. M., Lites, B. W., and Thomas, J. H.: 1993, *Astrophys. J.* **406**, 723

Bogdan, T. J., Hindman, B. W., Cally, P. S., and Charbonneau, P.: 1996, *Astrophys. J.* **465**, 406 (BHCC)

Bogdan, T. J., Braun, D. C., Lites, B. W., and Thomas, J. H.: 1998, *Astrophys. J.* **492**, 379

Braun, D. C.: 1995, *Astrophys. J.* **451**, 859

Braun, D. C.: 1997, *Astrophys. J.* **487**, 447

Braun, D. C. and Duvall, T. L., Jr.: 1990, *Solar Phys.* **129**, 83

Braun, D. C. and Lindsey, C.: 1999, *Astrophys. J.* **513**, L79

Braun, D. C. and Lindsey, C.: 2000a, *Solar Phys.* **192**, 285

Braun, D. C. and Lindsey, C.: 2000b, *Solar Phys.* **192**, 307

Braun, D. C. and Lindsey, C.: 2001, *Astrophys. J.* **560**, L189

Braun, D. C., Duvall, T. L., Jr., and LaBonte, B. J.: 1987, *Astrophys. J.* **319**, L27

Braun, D. C., Duvall, T. L., Jr., and LaBonte, B. J.: 1988, *Astrophys. J.* **335**, 1015

Braun, D. C., LaBonte, B. J., and Duvall, T. L., Jr.: 1990, *Astrophys. J.* **354**, 372

Braun, D. C., Duvall, T. L., Jr., LaBonte, B. J., Jefferies, S. M., Harvey, J. W., and Pomerantz, M. A.: 1992a, *Astrophys. J.* **391**, L113

Braun, D. C., Lindsey, C., Fan, Y., and Jefferies, S. M.: 1992b, *Astrophys. J.* **392**, 739

Braun, D. C., Lindsey, C., Fan, Y., and Fagan, M.: 1998, *Astrophys. J.* **502**, 968

Bray, R. J. and Loughhead, R. E.: 1974, *The Solar Chromosphere*, Chapman and Hall, London

Brown, T. M.: 1990, *Solar Phys.* **128**, 133

Brown, T. M., Christensen-Dalsgaard, J., Dziembowski, W. A., Goode, P., Gough, D. O., and Morrow, C. A.: 1989, *Astrophys. J.* **343**, 526

Cally, P. S.: 1983, *Solar Phys.* **88**, 77

Cally, P. S.: 1984, *Astron. Astrophys.* **136**, 121

Cally, P. S.: 1985, *Aust. J. Phys.* **38**, 825

Cally, P. S.: 1986, *Solar Phys.* **103**, 277

Cally, P. S.: 1995, *Astrophys. J.* **451**, 372

Cally, P. S.: 2000, *Solar Phys.* **192**, 395

Cally, P. S.: 2001a, *Astrophys. J.* **548**, 473

Cally, P. S.: 2001b, in J. L. Ballester and B. Roberts (eds.), *INTAS Workshop on MHD Waves in Astrophysical Plasmas*, pp. 101-110

Cally, P. S. and Adam, J. A.: 1983, *Solar Phys.* **85**, 97

Cally, P. S. and Bogdan, T. J.: 1993, *Astrophys. J.* **402**, 721 (CB93)

Cally, P. S. and Bogdan, T. J.: 1997, *Astrophys. J.* **486**, L67

Cally, P. S., Bogdan, T. J., and Zweibel, E. G.: 1994, *Astrophys. J.* **437**, 505 (CBZ)

Cally, P. S., Crouch, A. D., and Braun, D. C.: 2003, *Monthly Notices Royal Astron. Soc.* submitted, see Appendix F

Campbell, C. G. and Papaloizou, J. C. B.: 1986, *Monthly Notices Royal Astron. Soc.* **220**, 577

Campbell, W. R. and Roberts, B.: 1989, *Astrophys. J.* **338**, 538

Campos, L. M. B. C. and Saldanha, R.: 1991, *Geophys. Astrophys. Fluid Dyn.* **56**, 237

Chang, H. -K., Chou, D. -Y., LaBonte, B., and the TON Team: 1997, *Nature* **389**, 825

Chaplin, W. J., Elsworth, Y., Isaak, G. R., Marchenkov, K. I., Miller, B. A., and New, R.: 2001, *Monthly Notices Royal Astron. Soc.* **322**, 22

Charbonneau, P., Christensen-Dalsgaard, J., Henning, R., Larsen, R. M., Schou, J., Thompson, M. J., and Tomczyk, S.: 1999, *Astrophys. J.* **527**, 445

Chen, H. -R., Chou, D. -Y. and the TON Team: 1997, *Astrophys. J.* **490**, 452

Chen, K. -R., Chou, D. -Y. and the TON Team: 1996, *Astrophys. J.* **465**, 985

Chen, L. and Hasegawa, A.: 1974, *Phys. Fluids* **17**, 1399

Chitre, S. M.: 1992, in J. H. Thomas and N. O. Wiess (eds.), NATO ASIC, Proc. 375, *Sunspots: Theory and Observations*, Kluwer, Dordrecht, p. 333

Chitre, S. M. and Davila, J. M.: 1991, *Astrophys. J.* **371**, 785

Chou, D. -Y.: 2000, *Solar Phys.* **192**, 241

Chou, D. -Y., Chou, H. -Y., Hsieh, Y. -C., and Chen, C. -K.: 1996, *Astrophys. J.* **459**, 792

Christensen-Dalsgaard, J.: 1982, *Monthly Notices Royal Astron. Soc.* **199**, 735

Christensen-Dalsgaard, J., 1997, Aarhus adiabatic pulsation package,
http://astro.phys.au.dk/~jcd/adipack.n/

Christensen-Dalsgaard, J.: 2002, *Rev. Mod. Phys.* **74**, 1073

Christensen-Dalsgaard, J., Gough, D. O., and Thompson, M. J.: 1991, *Astrophys. J.* **378**, 413

Christensen-Dalsgaard, J., Gough, D. O., and Libbrecht, K. G.: 1989, *Astrophys. J.* **341**, L103

Christensen-Dalsgaard, J., Proffitt, C. R., and Thompson, M. J.: 1993, *Astrophys. J.* **403**, L75

Christensen-Dalsgaard, J., Duvall, T. L., Jr., Gough, D. O., Harvey, J. W., and Rhodes, E. J., Jr.: 1985, *Nature* **315**, 378

Christensen-Dalsgaard, J. et al.: 1996, *Science* **272**, 1286

Crouch, A. D. and Cally, P. S.: 1999, *Astrophys. J.* **521**, 878

Defouw, R. J.: 1976, *Astrophys. J.* **209**, 266

Deubner, F. and Gough, D.: 1984, *Ann. Rev. Astron. Astrophys.* **22**, 593

Donea, A.-C., Braun, D. C., and Lindsey, C.: 1999, *Astrophys. J.* **513**, L143

Donea, A.-C., Lindsey, C., and Braun, D. C.: 2000, *Solar Phys.* **192**, 321

D'Silva, S.: 1994, *Astrophys. J.* **435**, 881

D'Silva, S.: 1996, *Astrophys. J.* **469**, 964

D'Silva, S. and Duvall, T. L., Jr.: 1995, *Astrophys. J.* **438**, 454

Duvall, T. L., Jr., Jefferies, S. M., Harvey, J. W., and Pomerantz, M. A.: 1993, *Nature* **362**, 430

Duvall, T. L., Jr., D'Silva, S., Jefferies, S. M., Harvey, J. W., and Schou, J.: 1996, *Nature* **379**, 235

Eckart, C.: 1960, *Hydrodynamics of Oceans and Atmospheres*, Pergamon, New York

Edwin, P. M. and Roberts, B.: 1983, *Solar Phys.* **88**, 179

Elsworth, Y., Howe, R., Isaak, G. R., McLeod, C. P., Miller, B. A., New, R., Speake, C. C., and Wheeler, S. J.: 1994, *Astrophys. J.* **434**, 801

Erdélyi, R. and Goossens, M.: 1994, *Astrophys. Space Sci.* **213**, 273

Evans, J. W. and Michard, R.: 1962, *Astrophys. J.* **136**, 493

Evans, D. J. and Roberts, B.: 1990, *Astrophys. J.* **356**, 704

Fan, Y., Braun, D. C., and Chou, D. -Y.: 1995, *Astrophys. J.* **451**, 877

Ferraro, V. C. A.: 1954, *Astrophys. J.* **119**, 393

Ferraro, V. C. A. and Plumpton, C.: 1958, *Astrophys. J.* **127**, 459

Ferraro, V. C. A. and Plumpton, C.: 1966, *An Introduction to Magneto-fluid Mechanics*, Clarendon Press, Oxford

Ferriz-Mas, A. and Schüssler, M.: 1989, *Geophys. Astrophys. Fluid Dyn.* **48**, 217

Giovanelli, R. G.: 1972, *Solar Phys.* **27**, 71

Goldreich, P. and Kumar, P.: 1991, *Astrophys. J.* **374**, 366

Goldreich, P. and Murray, N.: 1994, *Astrophys. J.* **424**, 480

Goldreich, P., Murray, N., and Kumar, P.: 1994, *Astrophys. J.* **424**, 466

Goossens, M. and Poedts, S.: 1992, *Astrophys. J.* **384**, 348

Goossens, M., Poedts, S., and Hermans, D.: 1985, *Solar Phys.* **102**, 51

Goossens, M., Ruderman, M. S., and Hollweg, J. V.: 1995, *Solar Phys.* **157**, 75

Gore, A.: 1997, *Solar Phys.* **171**, 239

Gore, A.: 1998, *Solar Phys.* **178**, 13

Gough, D. O.: 1984, *Phil. Trans. R. Soc. London* **A313**, 27

Haber, D. A., Hindman, B. W., Toomre, J., Bogart, R. S., Thompson, M. J., and Hill, F.: 2000, *Solar Phys.* **192**, 335

Haber, D. A., Hindman, B. W., Toomre, J., Bogart, R. S., Larsen, R. M., and Hill, F.: 2002, *Astrophys. J.* **570**, 855

Hasan, S. S.: 1997, *Astrophys. J.* **480**, 803

Hasan, S. S. and Bogdan, T. J.: 1996, *Bull. Astron. Soc. India* **24**, 125

Hasan, S. S. and Christensen-Dalsgaard, J.: 1992, *Astrophys. J.* **396**, 311

Hasegawa, A. and Chen, L.: 1976, *Phys. Fluids* **19**, 1924

Hill, F.: 1988. *Astrophys. J.* **333**, 996

Hindman, B. W.: 1997, unpublished manuscript

Hindman, B. W., Zweibel, E. G., and Cally, P. S.: 1996, *Astrophys. J.* **459**, 760

Hollweg, J. V.: 1978, *Solar Phys.* **56**, 305

Hollweg, J. V.: 1988, *Astrophys. J.* **335**, 1005

Howe, R., Komm, R., and Hill, F.: 1999, *Astrophys. J.* **524**, 1084

Hunter, J. P.: 1999, Ph.D. Thesis, Monash University

Ionson, J. A.: 1978, *Astrophys. J.* **226**, 650

Jain, R. and Roberts, B.: 1994a, *Solar Phys.* **152**, 261

Jain, R. and Roberts, B.: 1994b, *Astron. Astrophys.* **286**, 243

Jain, R. and Roberts, B.: 1994c, *Astron. Astrophys.* **286**, 254

Jefferies, S. M., Duvall, T. L., Jr., Harvey, J. W., Osaki, Y., and Pomerantz, M. A.: 1991, *Astrophys. J.* **377**, 330

Kamp, L. P. J.: 1989, *Phys. Fluids* B1, 1385

Kamp, L. P. J.: 1990, *Geophys. Astrophys. Fluid Dyn.* 53, 257

Keppens, R.: 1995, *Solar Phys.* 161, 251

Keppens, R.: 1996, *Astrophys. J.* 468, 907

Keppens, R., Bogdan, T. J., and Goossens, M.: 1994, *Astrophys. J.* 436, 372

Komm, R. W., Howe, R., and Hill, F.: 2000, *Astrophys. J.* 531, 1094

Korzennik, S. G.: 1990, Ph.D. Thesis, Univ. California, Los Angeles

Kosovichev, A. G.: 1996, *Astrophys. J.* 461, L55

Kosovichev, A. G.: 2002, *Astron. Nachr.* 323, 186

Kosovichev, A. G., Duvall, T. L., Jr., and Scherrer, P. H.: 2000, *Solar Phys.* 192, 159

LaBonte, B. J. and Ryutova, M.: 1993, *Astrophys. J.* 419, 388

Lamb, H. C.: 1910, *Proc. R. Soc. London* A84, 551

Lamb, H. C.: 1945, *Hydrodynamics*, Dover, New York

Lazzaro, E., Lontano, M., and Ryutov, D. D.: 2000, *Phys. Rev.* E61, 3069

Leighton, R. B., Noyes, R. W., and Simon, G. W.: 1962, *Astrophys. J.* 135, 474

Leroy, B.: 1980, *Astron. Astrophys.* 91, 136

Leroy, B.: 1981, *Astron. Astrophys.* 97, 245

Leroy, B. and Bel, N.: 1979, *Astron. Astrophys.* 78, 129

Leroy, B. and Schwartz, S. J.: 1982, *Astron. Astrophys.* 112, 84

Libbrecht, K. G.: 1988, *Astrophys. J.* 334, 510

Libbrecht, K. G. and Woodard, M. F.: 1990, *Nature* 345, 779

Lindsey, C. and Braun, D. C.: 1990, *Solar Phys.* 126, 101

Lindsey, C. and Braun, D. C.: 1997, *Astrophys. J.* 485, 895

Lindsey, C. and Braun, D. C.: 1998a, *Astrophys. J.* 499, L99

Lindsey, C. and Braun, D. C.: 1998b, *Astrophys. J.* 509, L129

Lindsey, C. and Braun, D. C.: 1999, *Astrophys. J.* 510, 494

Lindsey, C. and Braun, D. C.: 2000a, *Science*, 287, 1799

Lindsey, C. and Braun, D. C.: 2000b, *Solar Phys.* **192**, 261

Lites, B. W.: 1992, in J. H. Thomas and N. O. Wiess (eds.), NATO ASIC, Proc. 375, *Sunspots: Theory and Observations*, Kluwer, Dordrecht, p. 261

Lites, B. W., Thomas, J. H., Bogdan, T. J., and Cally, P. S.: 1998, *Astrophys. J.* **497**, 464

Liu, Y., Zhang, H., Ai, G., Wang, H., and Zirin, H.: 1994, *Astron. Astrophys.* **283**, 215

Lou, Y. -Q.: 1990, *Astrophys. J.* **350**, 452

Maltby, P., Avrett, E. H., Carlsson, M., Kjeldseth-Moe, O., Kurucz, R. L., and Loeser, R.: 1986 *Astrophys. J.* **306**, 284

Nye, A. H. and Thomas, J. H.: 1974, *Solar Phys.* **38**, 399

Nye, A. H. and Thomas, J. H.: 1976a, *Astrophys. J.* **204**, 573

Nye, A. H. and Thomas, J. H.: 1976b, *Astrophys. J.* **204**, 582

Parker, E. N.: 1979, *Astrophys. J.* **230**, 905

Patrón, J., Hill, F., Rhodes, E. J., Jr., Korzennik, S. G., and Cacciani, A.: 1995, *Astrophys. J.* **455**, 746

Penn, M. J. and Labonte, B. J.: 1993, *Astrophys. J.* **415**, 383

Pintér, B. and Goossens, M.: 1999, *Astron. Astrophys.* **347**, 321

Poedts, S., Goossens, M., and Kerner, W.: 1989, *Solar Phys.* **123**, 83

Poedts, S., Goossens, M., and Kerner, W.: 1990, *Astrophys. J.* **360**, 279

Press, W. H., Teukolsky, S .A., Vetterling, W. T., and Flannery, B. P.: 1992, *Numerical Recipes in FORTRAN : The Art of Scientific Computing*, Cambridge University Press, Cambridge

Priest, E. R.: 1982, *Solar Magnetohydrodynamics*, Reidel, Dordrecht

Proffitt, C. R. and Michaud, G.: 1991, *Astrophys. J.* **380**, 238

Roberts, B. and Webb, A. R.: 1978, *Solar Phys.* **56**, 5

Roberts, B. and Webb, A. R.: 1979, *Solar Phys.* **64**, 77

Roberts, P. H. and Soward, A. M.: 1983, *Monthly Notices Royal Astron. Soc.* **205**, 1171

Roddier, F.: 1975, Academie des Science Paris Comptes Rendus Serie B Sciences Physiques, **281**, 93

Rosenthai, C. S.: 1990, *Solar Phys.* **130**, 313

Rosenthal, C. S.: 1992, *Solar Phys.* **130**, 25

Rosenthal, C. S.: 1995, *Astrophys. J.* **438**, 434

Rosenthal, C. S. and Julien, K. A.: 2000, *Astrophys. J.* **532**, 1230

Rosenthal, C. S., Bogdan, T. J., Carlsson, M., Dorch, S. B. F., Hansteen, V., McIntosh, S. W., McMurry, A., Nordlund, Å., and Stein, R. F.: 2002, *Astrophys. J.* **564**, 508

Ryutov, D. A. and Ryutova, M. P.: 1976, *Soviet Phys. JETP* **43**, 491

Ryutova, M. and Persson, M.: 1984, *Physica Scripta* **29**, 353

Ryutova, M. P. and Priest, E. R.: 1993a, *Astrophys. J.* **419**, 349

Ryutova, M. P. and Priest, E. R.: 1993b, *Astrophys. J.* **419**, 371

Ryutova, M., Kaisig, M., and Tajima, T.: 1991, *Astrophys. J.* **380**, 268

Sakurai, T., Goossens, M., and Hollweg, J. V.: 1991a, *Solar Phys.* **133**, 227

Sakurai, T., Goossens, M., and Hollweg, J. V.: 1991b, *Solar Phys.* **133**, 247

Scharmer, G. B., Gudiksen, B. V., Kiselman, D., Löfdahl, M. G., and Rouppe van der Voort, L. H. M.: 2002, *Nature* **420**, 151

Scheuer, M. A. and Thomas, J. H.: 1981, *Solar Phys.* **71**, 21

Schwartz, S. J. and Bel, N.: 1984a, *Astron. Astrophys.* **137**, 128

Schwartz, S. J. and Bel, N.: 1984b, *Solar Phys.* **92**, 133

Schwartz, S. J. and Leroy, B.: 1982, *Astron. Astrophys.* **112**, 93

Schwartz, S. J., Cally, P. S., and Bel, N.: 1984, *Solar Phys.* **92**, 81

Settele, A., Zhugzhda. Y. D., and Staude, J.: 1999, *Astron. Nachr.* **320**, 147

Settele, A., Staude, J., and Zhugzhda, Y. D.: 2001, *Solar Phys.* **202**, 281

Skartlien, R.: 2001, *Astrophys. J.* **554**, 488

Skartlien, R.: 2002, *Astrophys. J.* **565**, 1348

Small, L. M. and Roberts, B.: 1984, in Proc. 4th European Meeting on Solar Phys., *The Hydromagnetics of the Sun*, European Space Agency, Paris, pp. 257-259

Spruit, H. C.: 1981, *Astron. Astrophys.* **98**, 155

Spruit, H. C.: 1982, *Solar Phys.* **75**, 3

Spruit, H. C. and Bogdan, T. J.: 1992, *Astrophys. J.* **391**, L109

Stenflo, J. O.: 1978, *Rep. Prog. Phys.* **41**, 865

Stenuit, H., Erdélyi, R., and Goossens, M.: 1995, *Solar Phys.* **161**, 139

Stenuit, H., Keppens, R., and Goossens, M.: 1998, *Astron. Astrophys.* **331**, 392

Stenuit, H., Poedts, S., and Goossens, M.: 1993, *Solar Phys.* **147**, 13

Stenuit, H., Tirry, W. J., Keppens, R., and Goossens, M.: 1999, *Astron. Astrophys.* **342**, 863

Thomas, J. H.: 1978, *Astrophys. J.* **225**, 275

Thomas, J. H. and Scheuer, M. A.: 1982, *Solar Phys.* **79**, 19

Thomas, J. H. and Wiess, N. O.: 1992, in J. H. Thomas and N. O. Wiess (eds.), NATO ASIC, Proc. 375, *Sunspots: Theory and Observations*, Kluwer, Dordrecht, p. 3

Thomas, J. H., Cram, L. E., and Nye, A. H.: 1982, *Nature* **297**, 485

Tirry, W. J.: 2000, *Astrophys. J.* **528**, 493

Tirry, W. J., Goossens, M., Pintér, B., Čadež, V., and Vanlommel, P.: 1998, *Astrophys. J.* **503**, 422

Wentzel, D. G.: 1979, *Astron. Astrophys.* **76**, 20

Wilson, P. R.: 1979, *Astron. Astrophys.* **71**, 9

Wilson, P. R.: 1981, *Astrophys. J.* **251**, 756

Woodard, M. F. and Libbrecht, K. G.: 1993, *Astrophys. J.* **402**, L77

Woodard, M. F. and Libbrecht, K. G.: 1991, *Astrophys. J.* **374**, L61

Woodard, M. F. and Noyes, R. W.: 1985, *Nature* **318**, 449

Woodard, M. F., Kuhn, J. R., Murray, N., and Libbrecht, K. G.: 1991, *Astrophys. J.* **373**, L81

Vanlommel, P. and Goossens, M.: 1999, *Solar Phys.* **187**, 357

Vanlommel, P., Debosscher, A., Andries, J., and Goossens, M.: 2002, *Solar Phys.* **205**, 1

Yu, C. P.: 1965, *Phys. Fluids* **8**, 650

Zhang, H.: 1997, *Astrophys. J.* **479**, 1012

Zhang, J., Solanki, S. K., and Wang, J.: 2003, *Astron. Astrophys.* **399**, 755

Zhang, J., Lin, G., Wang. J., Wang, H., and Zirin, H.: 1998, *Solar Phys.* **178**, 245

Zhugzhda, Y. D.: 1984, *Monthly Notices Royal Astron. Soc.* **207**, 731

Zhugzhda, Y. D. and Dzhalilov, N. S.: 1982, *Astron. Astrophys.* **112**, 16

Zhugzhda, Y. D. and Dzhalilov, N. S.: 1984a, *Astron. Astrophys.* **132**, 45

Zhugzhda, Y. D. and Dzhalilov, N. S.: 1984b, *Astron. Astrophys.* **132**, 52

Zhugzhda, Y. D. and Dzhalilov, N. S.: 1984c, *Astron. Astrophys.* **133**, 333

Zhukov, V. I.: 1988, *Astrophys. Space Sci.* **141**, 65

Zhukov, V. I.: 1989a, *Astrophys. Space Sci.* **154**, 247

Zhukov, V. I.: 1989b, *Astron. Astrophys.* **222**, 293

Zhukov, V. I.: 1990, *Astrophys. Space Sci.* **174**, 173

Zhukov, V. I.: 1997, *Astron. Astrophys.* **322**, 302

Zhukov, V. I.: 2002, *Astron. Astrophys.* **386**, 653

Zirin, H. and Stein, A.: 1972, *Astrophys. J.* **178**, L85

Zweibel, E. G. and Bogdan, T. J.: 1986, *Astrophys. J.* **308**, 401

Zweibel, E. G. and Däppen, W.: 1989, *Astrophys. J.* **343**, 994